

ANALYSIS OF THE MAGNETOHYDRODYNAMIC FLOW
OF A FISSIONING GAS IN A
DISK MHD GENERATOR

By

GERARD EDWARD WELCH

A DISSERTATION PRESENTED TO THE GRADUATE SCHOOL
OF THE UNIVERSITY OF FLORIDA IN PARTIAL FULFILLMENT
OF THE REQUIREMENTS OF THE DEGREE OF
DOCTOR OF PHILOSOPHY

UNIVERSITY OF FLORIDA

1992

UNIVERSITY OF FLORIDA



3 1262 08552 4535

Copyright 1992

by

Gerard E. Welch

"My eyes are ever toward the Lord,
for he will free my feet from the snare."

(Psalm 25:15)

*To my parents,
in the name of our Lord Jesus Christ.*

ACKNOWLEDGEMENTS

The author wishes to extend his sincere appreciation and thanks to the members of his supervisory committee, Dr. Edward T. Dugan, Dr. William E. Lear, Jr., Dr. William G. Vernetson, Dr. Alan M. Jacobs, Dr. Calvin C. Oliver, and Dr. Robert J. Hanrahan, for their assistance and direction throughout the course of this work. The author considers it a privilege to have worked under these outstanding academicians.

Special thanks is extended to Dr. Dugan for the hours devoted to reviewing this dissertation, and for his guidance, patience, example, and friendly support over the many years of the author's graduate career. The author thanks Dr. Lear for the many enjoyable hours of discussion on MHD and gas dynamics. Thanks is also extended to Dr. Oliver for his detailed insights into all facets of thermal fluid flow, and for hours of enjoyable and educational conversation.

The author will always be thankful for the support and constant encouragement provided by Dr. Vernetson throughout his graduate career.

Thanks is also extended to Dr. T. I-P. Shih of Carnegie-Mellon University for his time spent in answering detailed questions on computational fluid mechanics, and to Dr. J.G. Appelbaum for the interesting discussions and help on the plasma physics modeling.

Support for the author's graduate work has been provided in part by the University of Florida. The early phase of this dissertation work was supported by the Air force Wright Aeronautical Laboratories for work performed within the Innovative Nuclear Space Power Institute of the University of Florida. The author's masters work was supported by Institute of Nuclear Power Operations. All this support is greatly appreciated.

The author thanks his friends and family in Gainesville for their moral support throughout this work. A special thanks is extended Jean Roach for her true friendship through some of the roughest periods of the author's graduate career and for the many prayers made on the author's behalf by her, and the members of her intercessory prayer group.

Finally, the author thanks his parents, Gerard J. Welch and Mary G. Welch, for their patience and love, for the hope they communicated to the author during these past years, for their many sacrifices in devoting time and financial support during the author's graduate career, and especially for their faithful presence and prayers to the Lord who has sustained the author.

TABLE OF CONTENTS

	<u>page</u>
ACKNOWLEDGMENTS	iv
LIST OF TABLES	viii
LIST OF FIGURES	x
ABSTRACT	xviii
CHAPTERS	
1 INTRODUCTION	1
1.0 Overview	1
1.1 Outflow Disk MHD Generator Power Generation	3
1.2 Background	13
1.3 Problem Statement	17
1.4 Organization of Dissertation	18
2 THEORETICAL MODELING	19
2.0 Introduction	19
2.1 Overview of Assumptions	19
2.2 Fluid Mechanics	26
2.3 Electromagnetics	68
2.4 Plasma Physics Modeling and Transport Properties	83
2.5 Overall MHD Solution	96
3 ANALYSIS	98
3.0 Introduction	98
3.1 Solution Method Modifications for MHD Calculations ..	99
3.2 Duct Geometry Selection	127
3.3 Comparisons with Quasi-One-Dimensional Flow Solver ..	144
3.4 Uniform Plasma Property MHD Solutions	154
3.5 Nonuniform Plasma Transport Properties	180

CHAPTERS	<u>page</u>
3 ANALYSIS (cont.)	
3.6 Nonuniform Fission-Model Plasma Property MHD Solutions	202
3.7 Comparison of Two-Dimensional and Quasi-One- Dimensional Predictions for Reference Equilibrium/ Fission-Model Generator	242
4 SUMMARY, CONCLUSIONS, AND RECOMMENDATIONS	253
4.1 Summary of Results	253
4.2 Conclusions	262
4.3 Recommendations for Future Study	265
APPENDICES	
A QUASI-ONE-DIMENSIONAL DISK MHD FLOW SOLVER	271
B GRID GENERATION	279
C SHOCK CAPTURING	292
LIST OF REFERENCES	300
BIOGRAPHICAL SKETCH	307

LIST OF TABLES

<u>Table</u>	<u>page</u>
1.1 Disk MHD Generator Current Density Component	11
2.1 Governing Equations of Magnetohydrodynamics	20
2.2 Governing Equations of Magnetohydrodynamics with Fission Density Terms in Cylindrical Coordinates with Tangential- Symmetry	30
2.3 Transformed Governing Equations of MHD with Thin-Layer Approximation in Boundary-Fitted Curvilinear Coordinate System (ξ, η)	35
2.4 Pure UF ₄ and He Gas Properties and UF ₄ -(94%)He Working Fluid Mixture Properties	44
2.5 Explicit Method of MacCormack with Generalized Finite- Differencing Sequence	66
2.6 Transformed MHD Electromagnetics Equations in Boundary- Fitted Curvilinear Coordinate System (ξ, η)	73
2.7 Constants of Plasma Physics Transport Property Models	92
3.1 Uniform Plasma Property MHD Generator Parameters	156
3.2 Fluid Property Data for a UF ₄ -(85%)He Working Fluid Mixture for Example Fissioning Plasma Transport Property Calculations	186
3.3 Wall-to-Free Stream Plasma Property Ratios for Hot and Cold Generator Walls with Example Generator Free Stream Flow Conditions	199
3.4 Working Fluid Properties for Equilibrium Electron Temperature/ Fissioning Plasma ($S_{ff} \gg S_{saha}$) MHD Generator Calculations	203

<u>Table</u>	<u>page</u>
3.5 MHD Generator Inlet Conditions and Specified Global Parameters for Nonuniform Fission-Model Plasma Property MHD Generator Calculations	206
3.6 Comparison of Two-Dimensional MHD Solver and Quasi-One-Dimensional Euler Solver Predictions for Reference Fissioning Plasma Generator	245

LIST OF FIGURES

<u>Figure</u>	<u>page</u>
1.1 Schematic Diagram of a Conceptual Space Nuclear Reactor System using Outflow Disk MHD Generator Direct Energy Conversion (Welch et al., 1990)	2
1.2 Top-View and Side-View Schematic Diagrams of the Outflow Disk MHD Generator	8
1.3 Functional Diagram of the Outflow Disk MHD Generator	10
2.1 Schematic Diagram of the Disk MHD Generator Problem Geometry (Top-View)	23
2.2 Side-View Schematic Diagram of Outflow Disk MHD Generator showing a Typical Generator Duct Lofting	28
2.3 Cylindrical (r,z) Coordinate System to Boundary-Fitted (ξ,η) Coordinate System Transformation	32
2.4 Radial Velocity Profile in Turbulent Boundary Layer showing the Laminar Sublayer and Turbulent Regions (after Shapiro, 1954)	55
2.5 Schematic Diagram of Electromagnetics Solver Problem Space	74
2.6 Schematic Diagram showing the Alternating-Direction-Implicit (ADI) Solution Scheme	78
3.1 Schematic Diagram of Lower Wall Corner of Inlet Plane Showing Exaggerated Boundary Layer and Displacement Thicknesses	102
3.2 Static Pressure Contour Plot of Fissioning Flow in Example Duct Geometry of MHD Calculations of Section 3.4	104
3.3 Comparison of Centerline Static Pressure as a function of Radial Position for Code Factors CF = 0, 1, 3.5, and 4.0	111

<u>Figure</u>	<u>page</u>
3.4 Comparison of Centerline Radial Mach Number as a function of Radial Position for Code Factors CF = 0, 1, 3.5, and 4.0	112
3.5 Static Pressure Contour Plot of Fissioning Flow in Example Duct Geometry Considered in Figure 3.2, with Code Factor CF = 3.5	114
3.6 Modified Outflow Pressure Boundary Condition Diagram	117
3.7 Comparison of the Baldwin-Lomax F(z) Distribution for Various Applied B-Fields; F(z) is Plotted as a function of Axial Grid Line Index, from Wall to Center Grid Line	126
3.8 Schematic Diagram of Constant Area Duct Geometry	130
3.9 Comparison of Centerline Radial Mach Number as a function of Radial Position and Neutron Flux Level for Constant Area Duct Geometry	131
3.10 Static Pressure Contour Plot of Fissioning Flow ($\Phi = 10^{16}$ n/cm ² s) in Constant Area Duct Geometry	133
3.11 Comparison of Radial Velocity Component Axial Profiles at the Lower Wall and Radial Position $r = 1.4$ m as a function of Neutron Flux Level for Constant Area Duct Geometry	134
3.12 Comparison of Static Temperature Axial Profiles at the Lower Wall and Radial Position $r = 1.4$ m as a function of Neutron Flux Level for Constant Area Duct Geometry	135
3.13 Comparison of Centerline Radial Mach Number as a function of Radial Position and Neutron Flux Level for Constant Height Duct Geometry	138
3.14 Static Pressure Contour Plot for flow in Constant Height Duct Geometry	139
3.15 Comparison of Radial Velocity Component Axial Profile at Lower Wall and Radial Position $r = 1.25$ m as a function of Neutron Flux Level for Linearly Decreasing Duct Height Geometry	142
3.16 Comparison of Static Temperature Axial Profile at Lower Wall and Radial Position $r = 1.25$ m as a function of Neutron Flux Level for Linearly Decreasing Duct Height Geometry	143

3.17	Schematic Diagram of Linearly Decreasing Duct Height Geometry Typical of Ducts considered in the Remainder of Chapter 3	145
3.18	Comparison of 2-D Navier-Stokes and Q1D Euler Numerical and Analytical Predictions of the Centerline Radial Mach Number as a function of Radial Position for Linearly Decreasing Duct Height Geometry	147
3.19	Comparison of 2-D Navier-Stokes and Q1D Predictions of Centerline Radial Mach Number as a function of Radial Position and Neutron Flux Level in Linear Decreasing Duct Height Geometry	149
3.20	Comparison of 2-D Navier-Stokes and Q1D Predictions of Centerline Swirl Factor as a function of Radial Position and Neutron Flux Level in Linear Decreasing Duct Height Geometry	150
3.21	Comparison of 2-D Navier-Stokes and Q1D Predictions of Centerline Stagnation Temperature as a function of Radial Position and Neutron Flux Level in Linear Decreasing Duct Height Geometry	151
3.22	Comparison of 2-D Navier-Stokes and Q1D Predictions of Centerline Stagnation Pressure as a function of Radial Position and Neutron Flux Level in Linear Decreasing Duct Height Geometry	152
3.23	Schematic Diagram of MHD Generator with Linearly Decreasing Duct Height used for Uniform Plasma Transport Property MHD Calculations	155
3.24	Comparison of Centerline Stagnation Temperature as a function of Radial Position for $B = 0$ T, 3.0 T, 3.5 T and 4 T Generators with Uniform Plasma Transport Properties	157
3.25	Comparison of Centerline Stagnation Pressure as a function of Radial Position for $B = 0$ T, 3.0 T, 3.5 T and 4 T Generators with Uniform Plasma Transport Properties	159
3.26	Current Density Stream Function Contour Plot for Generator with $B = 3.5$ T, $R_L = 0.25$ Ω , and Uniform Plasma Transport Properties ..	160
3.27	Comparison of Centerline Radial Mach Number as a function of Radial Position for $B = 0$ T, 3.0 T, 3.5 T and 4 T Generators with Uniform Plasma Transport Properties	164

3.28	Static Pressure Contour Plot for Generator with $B = 3.5 \text{ T}$, $R_L = 0.25 \Omega$, and Uniform Plasma Transport Properties	165
3.29	Comparison of Radial Component of Velocity as a function of Axial Position at Cathode ($r = 1.25 \text{ m}$) for $B = 3.0 \text{ T}$, 3.5 T , and 4.0 T Generators with Uniform Plasma Transport Properties	167
3.30	Comparison of Tangential Component of Velocity as a function of Axial Position at Cathode ($r = 1.25 \text{ m}$) for $B = 0 \text{ T}$, 3.0 T , 3.5 T , and 4.0 T Generators with Uniform Plasma Transport Properties	170
3.31	Comparison of Static Temperature as a function of Axial Position at Cathode ($r = 1.25 \text{ m}$) for $B = 3.0 \text{ T}$, 3.5 T , and 4.0 T Generators with Uniform Plasma Transport Properties	173
3.32	Comparison of Centerline Stagnation Temperature as a function of Radial Position for $R_L = 0.1 \Omega$, 0.25Ω , and 1.0Ω Generators with Uniform Plasma Properties	175
3.33	Comparison of Centerline Stagnation Pressure as a function of Radial Position for $R_L = 0.1 \Omega$, 0.25Ω , and 1.0Ω Generators with Uniform Plasma Properties	175
3.34	Comparison of Centerline Radial Mach Number as a function of Radial Position for $R_L = 0.1 \Omega$, 0.25Ω , and 1.0Ω Generators with Uniform Plasma Properties	178
3.35	Comparison of Radial Component of Velocity as a function of Axial Position at Cathode ($r = 1.25 \text{ m}$) for $R_L = 0.1 \Omega$, 0.25Ω , and 1.0Ω Generators with Uniform Plasma Properties	179
3.36	Comparison of Tangential Component of Velocity as a function of Axial Position at Cathode ($r = 1.25 \text{ m}$) for $R_L = 0.1 \Omega$, 0.25Ω , and 1.0Ω Generators with Uniform Plasma Properties	181
3.37	Comparison of Static Temperature as a function of Axial Position at Cathode ($r = 1.25 \text{ m}$) for $R_L = 0.1 \Omega$, 0.25Ω , and 1.0Ω Generators with Uniform Plasma Properties	182
3.38	Scalar Electrical Conductivity of Fissioning Plasma as a function of Electron-Heavy Momentum Transfer Cross-Section, \bar{Q}_{eh} , and Nonelastic Scatter Factor, δ	187

<u>Figure</u>	<u>page</u>
3.39 Electron Mobility in Fissioning Plasma as a function of Electron-Heavy Momentum Transfer Cross-Section, \bar{Q}_{eh} , and Nonelastic Scatter Factor, δ	188
3.40 Nonequilibrium Enhanced Scalar Electrical Conductivity of Fissioning Plasma as a Function of Local Swirl Factor and Radial Mach Number	190
3.41 Electron Mobility in Fissioning Plasma, with Nonequilibrium Electron Temperatures, as a function of Local Swirl Factor and Radial Mach Number	191
3.42 Schematic Diagram of MHD Duct with Linear Decreasing Duct Height used for Nonuniform Plasma Property MHD Calculations	205
3.43 Centerline and Lower Wall Radial Profiles of Scalar Electrical Conductivity of Equilibrium Fissioning Plasma in Reference Generator with $B = 5$ T and $R_L = 8 \Omega$	208
3.44 Centerline and Lower Wall Radial Profiles of Electron Mobility of Equilibrium Fissioning Plasma in Reference Generator with $B = 5$ T and $R_L = 8 \Omega$	209
3.45 Static Pressure as a function of Radial Position at Lower Duct Wall of Reference Generator with Equilibrium Fissioning Plasma . . .	210
3.46 Static Temperature as a function of Radial Position at Grid Line 11 (near Lower Wall) of Reference Generator with Equilibrium Fission Plasma	211
3.47 Current Density Stream Function Contour Plot of Reference ($B = 5$ T and $R_L = 8 \Omega$) Generator with Nonuniform Plasma Transport Properties	212
3.48 Static Pressure Contour Plot of Reference ($B = 5$ T and $R_L = 8 \Omega$) Generator with Nonuniform Plasma Transport Properties	213
3.49 Scalar Electrical Conductivity at Anode ($r = 0.79$ m) and Cathode ($r = 1.21$ m) as a function of Axial Position in Reference ($B = 5$ T and $R_L = 8 \Omega$) Generator with Equilibrium Fissioning Plasma	218

3.50	Electron Mobility at Anode ($r = 0.79$ m) and Cathode ($r = 1.21$ m) as a function of Axial Position in Reference ($B = 5$ T and $R_L = 8$ Ω) Generator with Equilibrium Fissioning Plasma	219
3.51	Comparison of Centerline Stagnation Temperature as a function of Radial Position for $B = 0$ T, 5 T, and 6 T Generators with Nonuniform Plasma Transport Properties	220
3.52	Comparison of Centerline Stagnation Pressure as a function of Radial Position for $B = 0$ T, 5 T, and 6 T Generators with Nonuniform Plasma Transport Properties	221
3.53	Comparison of Centerline Radial Mach Number as a function of Radial Position for $B = 0$ T, 5 T, and 6 T Generators with Nonuniform Plasma Transport Properties	223
3.54	Comparison of Radial Component of Velocity as a function of Axial Position at Cathode ($r = 1.21$ m) for $B = 0$ T, 5 T, and 6 T Generators with Nonuniform Plasma Transport Properties	226
3.55	Comparison of Tangential Component of Velocity as a function of Axial Position at Cathode ($r = 1.21$ m) for $B = 0$ T, 5 T, and 6 T Generators with Nonuniform Plasma Transport Properties	228
3.56	Comparison of Static Temperature as a function of Axial Position at Cathode ($r = 1.21$ m) for $B = 0$ T, 5 T, and 6 T Generators with Nonuniform Plasma Transport Properties	231
3.57	Comparison of Centerline Stagnation Temperature as a function of Radial Position for $R_L = 1.8$ Ω , 8 Ω , and 32 Ω Generators with Nonuniform Plasma Transport Properties	233
3.58	Comparison of Centerline Stagnation Pressure as a function of Radial Position for $R_L = 1.8$ Ω , 8 Ω , and 32 Ω Generators with Nonuniform Plasma Transport Properties	235
3.59	Comparison of Centerline Radial Mach Number as a function of Radial Position for $R_L = 1.8$ Ω , 8 Ω , and 32 Ω Generators with Nonuniform Plasma Transport Properties	237
3.60	Comparison of Radial Component of Velocity as a function of Axial Position at Cathode ($r = 1.21$ m) for $R_L = 1.8$ Ω , 8 Ω , and 32 Ω Generators with Nonuniform Plasma Transport Properties ..	238

<u>Figure</u>	<u>page</u>
3.61 Comparison of Tangential Component of Velocity as a function of Axial Position at Cathode ($r = 1.21$ m) for $R_L = 1.8 \Omega$, 8Ω , and 32Ω Generators with Nonuniform Plasma Transport Properties . .	240
3.62 Comparison of Static Temperature as a function of Axial Position at Cathode ($r = 1.21$ m) for $R_L = 1.8 \Omega$, 8Ω , and 32Ω Generators with Nonuniform Plasma Transport Properties	241
3.63 Comparison of 2-D Navier-Stokes MHD Solver and Q1D MHD Solver Predictions of the Centerline Radial Profile of Stagnation Temperature in the Reference ($B = 5$ T and $R_L = 8 \Omega$) Generator with Equilibrium Fissioning Plasma	246
3.64 Comparison of 2-D Navier-Stokes MHD Solver and Q1D MHD Solver Predictions of the Centerline Stagnation Pressure of the Radial Mach Number in the Reference ($B = 5$ T and $R_L = 8 \Omega$) Generator with Equilibrium Fissioning Plasma	248
3.65 Comparison of 2-D Navier-Stokes MHD Solver and Q1D MHD Solver Predictions of the Centerline Radial Profile of the Radial Mach Number in the Reference ($B = 5$ T and $R_L = 8 \Omega$) Generator with Equilibrium Fissioning Plasma	249
3.66 Comparison of 2-D Navier-Stokes MHD Solver and Q1D MHD Solver Predictions of the Centerline Radial Profile of the Swirl Factor in the Reference ($B = 5$ T and $R_L = 8 \Omega$) Generator with Equilibrium Fissioning Plasma	250
A-1 Outflow Disk MHD Generator Schematic Diagram (Top-View)	273
B-1 Schematic Diagram of a Close-up View, Near the Lower Duct Wall, of a Generic Stretched Grid used for MHD Flow Calculations	280
B-2 Example Numerical Grid (used for Nonuniform Plasma Transport Property Generator Calculations in Section 3.6)	290
B-3 Lower Wall Close-up View of Example Numerical Grid Shown in Figure B-2	291
C-1 Static Pressure Contour Plot for Supersonic Flow in Five-Degree Compression Corner Duct Geometry	293

<u>Figure</u>	<u>page</u>
C-2 Centerline Radial Mach Number as a function of Radial Position in Five-Degree Compression Corner Duct Geometry	295
C-3 Centerline Static Pressure as a function of Radial Position in Five-Degree Compression Corner Geometry	296
C-4 Static Pressure Contour Plot for Supersonic Flow in Smooth Five-Degree Compression Turn Duct Geometry	298

Abstract of Dissertation Presented to the Graduate School
of the University of Florida in Partial Fulfillment of the
Requirements for the Degree of Doctor of Philosophy

ANALYSIS OF THE MAGNETOHYDRODYNAMIC FLOW
OF A FISSIONING GAS IN A
DISK MHD GENERATOR

By

Gerard Edward Welch

May, 1992

Chairman: Edward T. Dugan

CoChairman: William E. Lear, Jr.

Major Department: Nuclear Engineering Sciences

The influence of fissioning and magnetohydrodynamic (MHD) interaction on the steady, supersonic flow of a compressible, turbulent, weakly ionized, fissioning gas in an outflow disk MHD generator is investigated in this work. The two-dimensional (r,z) MHD flow is modeled using the thin-layer Navier-Stokes equations with MHD and fission power density source terms, and Maxwell's equations under the MHD Approximations and assuming negligible induced magnetic induction. Simple plasma physics transport property models are developed for the collision-dominated, weakly ionized plasma in which fission-fragment induced ionization provides the dominant source of conduction electrons. The simple plasma physics models used in this work suggest that the the electron number densities ($O 10^{19}/m^3$) and corresponding electrical

conductivity levels (O 1 S/m) obtained from fission-fragment induced ionization alone may be insufficient for practical MHD generator operation.

The MHD flow equations with the fission power density source term, are integrated in boundary-fitted coordinates using the explicit method of MacCormack. The equations of electromagnetics, with variable plasma physics transport properties, are solved using an Alternating-Direction-Implicit (ADI) scheme. A consistent 2-D MHD solution is obtained by iteration between the fluid solver and the electromagnetics solver.

The 2-D MHD solution methodology is used to analyze the influence of duct geometry and fission power density (for neutron flux levels between 0 and 10^{17} n/cm²s) on the behavior of internal supersonic flows (with total Mach numbers less than 3), and to characterize the effects of variable applied magnetic induction levels and generator load resistances on the spatial profiles of important generator variables. The predictions of the 2-D MHD solver developed in this work are compared with those of a quasi-one-dimensional Euler solver with MHD and fission source terms; the agreement between the two approaches suggests that the quasi-one-dimensional Euler solver does an excellent job predicting the behavior of supersonic, fissioning, disk MHD flows.

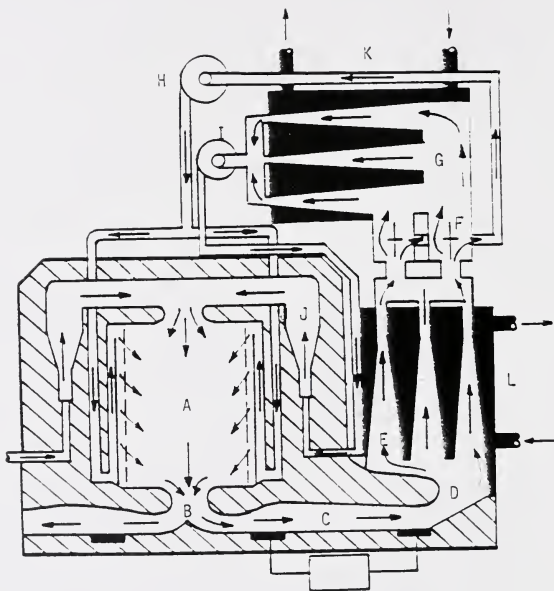
Two-dimensional Hall effect-induced electrode effects are studied. Short-circuit current loops are found to exist over the majority of the electrode area. The generator load current flows through a small fraction ($\leq 10\%$) of the electrode surface, resulting in order-of-magnitude higher localized Joule heating levels which give rise to oblique wave structure.

CHAPTER 1
INTRODUCTION

1.0 Overview

The magnetohydrodynamic (MHD) flow of a fissioning gas in an outflow disk MHD generator is studied in this work. The generator working fluid is a single-phase gas mixture (e.g., uranium-tetrafluoride/helium (UF_4 -He)), containing a significant fraction of a fissionable isotope constituent (e.g., ^{235}U). The disk MHD generator is designed to be an integral part of a nuclear reactor--see the reactor/disk MHD generator configuration of the conceptual space nuclear reactor power system shown in Figure 1.1--so that a high thermal neutron flux level exists throughout the generator duct. The fissioning of the fissionable isotope constituent of the working fluid provides the electrical conductivity necessary for MHD interaction by the mobility of the free electrons arising from fission-fragment induced ionization.

The MHD flow field is modeled using the continuum description of fluid mechanics and electromagnetics. The working fluid is treated as a compressible Navier-Stokes fluid with body force terms arising from MHD interaction and with power density source terms due to both MHD interaction and the fissioning of the working fluid. The fluid flow treated in this work is internal, supersonic (in all



- | | |
|-----------------------|-------------------------|
| A. Gas Core Chamber | G. Secondary Condenser |
| B. Supersonic Nozzle | H. Metal Fluoride Pump |
| C. Disk MHD Generator | I. UF_4 Pump |
| D. Diffuser | J. UF_4 Boiler |
| E. Main Condenser | K. Secondary Radiator |
| F. Separators | L. Primary Radiator |

Figure 1.1 Schematic Diagram of a Conceptual Space Nuclear Reactor System using Outflow Disk MHD Generator Direct Energy Conversion (Welch et al., 1990).

but the narrow region adjacent to the duct walls), compressible, viscous, turbulent, fissioning, MHD flow. Turbulence modeling is included through an eddy viscosity and thermal conductivity model. The generator electromagnetics variables are described by Maxwell's equations and are related through the generalized Ohm's law (constitutive) relationship. Models for plasma transport properties--electrical conductivity and electron mobility--are developed. An overall self-consistent solution methodology for modeling the two-dimensional, steady-state disk MHD generator operation is developed in this work.

This chapter provides a.) an overview of outflow disk MHD power generation, including a detailed description of the disk MHD generator component; b.) the impetus for and objectives of this thesis work; c.) a statement of the problem scope; and d.) an outline of dissertation organization.

1.1 Outflow Disk MHD Generator Power Generation

The operation of an MHD generator may be understood in terms of the macroscopic phenomena associated with the Lorentz forces that arise on the microscopic level in the interaction of the charged particles (electrons and ions) in the weakly ionized plasma working fluid with the local magnetic induction, \underline{B} , and static electric field, \underline{E} . In the continuum description of the MHD generator working fluid, the Lorentz forces on the individual charged particles give rise to macroscopic body forces, \underline{f} , that oppose the bulk flow and an electric power density source, $\underline{J} \cdot \underline{E}$. Using the notation of Mitchner and Kruger (1973), and influenced by similar discussions in classic texts on engineering MHD power

generation (Sutton and Sherman, 1965; Hughes and Young, 1966; and Rosa, 1968) the body forces and power density source terms are developed in the following section.

1.1.1 MHD Interaction Terms

Body force term. The MHD body force against a bulk fluid composed of S constituents ($s = 1, 2, \dots, S$) is given by

$$\underline{f} = \sum_s \underline{f}_s = \sum_s q_s n_s (\underline{u}_s \times \underline{B} + \underline{E}) = \underline{j} \times \underline{B} + \rho^c \underline{E} \quad (1-1)$$

where q_s , n_s , and \underline{u}_s are the charge, number density, and velocity of constituent s , ρ^c ($\equiv \sum q_s n_s$) is the local charge density, and \underline{j} is the total current density, given by

$$\underline{j} = \sum_s \underline{j}_s \equiv \sum_s q_s n_s \underline{u}_s = \sum_s q_s n_s (\underline{u} + \underline{U}_s) = \rho^c \underline{u} + \underline{J} \quad (1-2)$$

where \underline{j}_s is the total current density of constituent s , \underline{U}_s ($\equiv \underline{u}_s - \underline{u}$) is the diffusion velocity of constituent s , \underline{u} ($\equiv \sum \rho_s \underline{u}_s / \sum \rho_s$) is the bulk fluid velocity, and \underline{J}

($\sum \underline{j}_s \equiv \sum q_s n_s \underline{U}_s$) is the conduction current density; the total current density, \underline{j} , is composed of the conduction current density, \underline{J} , and the convection current density, $\rho^c \underline{u}$.

Electric power density term. The electric power density produced in movement of charged particles of constituent s through the static electric field is given by

$$p_s = \frac{d}{dt} \int \underline{f}_s \cdot d\underline{r} = \frac{d}{dt} \int \underline{f}_s \cdot \underline{u}_s dt = \underline{f}_s \cdot \underline{u}_s \quad (1-3)$$

The total local power density term is therefore given by

$$p_e = \sum_s \underline{f}_s \cdot \underline{u}_s = \sum_s q_s n_s (\underline{u}_s \times \underline{B} + \underline{E}) \cdot \underline{u}_s = \underline{j} \cdot \underline{E} \quad (1-4)$$

Alternatively, we can write

$$\sum_s \underline{f}_s \cdot \underline{u}_s = \sum_s \underline{f}_s \cdot (\underline{u} + \underline{U}_s) = \underline{u} \cdot \sum_s \underline{f}_s + \sum_s \underline{f}_s \cdot \underline{U}_s \quad (1-5)$$

Expanding \underline{f}_s with Equation 1-1, it is found that

$$p_e = \underline{j} \cdot \underline{E} = (\underline{j} \times \underline{B} + \rho^c \underline{E}) \cdot \underline{u} + \underline{J} \cdot \underline{E}' \quad (1-6)$$

where $\underline{E}' = \underline{E} + \underline{u} \times \underline{B}$. The local electric power density, $\underline{j} \cdot \underline{E}$, is therefore composed of the flow work--that is the convection of the MHD body force terms--and the Joule heating ($\underline{J} \cdot \underline{E}' = \underline{J} \cdot (\underline{u} \times \underline{B} + \underline{E})$). The conduction current density is related to the electric field strength through the generalized Ohm's law, i.e.,

$$\underline{J} + \mu_e \underline{J} \times \underline{B} = \sigma_e (\underline{u} \times \underline{B} + \underline{E}) = \sigma_e \underline{E}' \quad (1-7)$$

(as used in this work), so that the right-hand-most term in Equation 1-6 is clearly the Joule (or Ohmic or resistance) heating

$$\underline{J} \cdot \underline{E}' = \underline{J} \cdot (\underline{u} \times \underline{B} + \underline{E}) = \frac{\underline{J} \cdot \underline{J}}{\sigma_e} \quad (1-8)$$

For the conditions typical of MHD generators, $|\underline{J}| \gg |\rho^c \underline{u}|$ so that $\underline{j} \approx \underline{J}$. The Lorentz forces arise from movement of both ions and electrons through the electric and magnetic fields. Due to the high mobility of the electrons--that is

relative to the much less mobile ion species ($\mu_e/\mu_s \sim (m_s/m_e)^{1/2}$)--the electrons readily diffuse through the bulk fluid, while the less mobile ions travel with the bulk fluid. The Lorentz forces work to accelerate the electrons; however, as a result of electron-ion and electron-neutral collisions, the electron species reaches a terminal diffusion velocity, \underline{U}_e , and the Lorentz forces attributable to electron current/B-field interaction ($\underline{J}_e \times \underline{B}$) are transferred to the bulk plasma. As a result of relatively large mass (low mobility, $\mu_s \sim (1/m_s)^{1/2}$), the ions species travels nearly with the neutral species (bulk fluid) of the weakly ionized plasma; i.e., at the conditions (temperature and pressure) encountered in MHD power generation, $\underline{U}_i \approx \underline{U}_{s,e} \approx 0$, and therefore $\underline{J} \approx \underline{J}_e$ in the plasmas of interest to this study.

In this dissertation, the MHD interaction terms are included in the Navier-Stokes equations using

$$\underline{f} = \underline{j} \times \underline{B} + \rho^c \underline{E} = \underline{J} \times \underline{B} + \rho^c \underline{E}' \quad (1-9)$$

and

$$\underline{j} \cdot \underline{E} = (\underline{j} \times \underline{B} + \rho^c \underline{E}) \cdot \underline{u} + \underline{J} \cdot \underline{E}' = \underline{J} \cdot \underline{E} + \rho^c \underline{B} \cdot \underline{E} \quad (1-10)$$

Here, it has been assumed that $|\rho^c \underline{E}'| \ll |\underline{J} \times \underline{B}|$ and $|\rho^c \underline{u}| \ll \underline{J}$, which are two of the three "MHD Approximations" (cf. Sutton and Sherman, 1965; Hughes and Young, 1966; and Rosa, 1968) discussed in more detail in Section 2.1.1. The MHD body force terms, $\underline{J} \times \underline{B}$, and electric power density term, $\underline{J} \cdot \underline{E}$, depend therefore on the conduction current, \underline{J} , and not the total current density, \underline{j} , in this work. Note that, therefore, the local charge density need not be known in order

to describe the MHD flow for typical MHD generator conditions. (The charge density may of course be back calculated using Gauss's Law; i.e., $\rho^c = \epsilon_0 \nabla \cdot \underline{E}$.)

1.1.2 Outflow Disk MHD Generator Description

The schematic diagrams in Figure 1.2 provide top and side views of an outflow disk MHD generator. The disk MHD generator is an internal flow device in which a working fluid, containing a finite electrical conductivity, flows predominantly radially from an inlet at the center of the disk, outward between two surfaces (disks), through an applied magnetic field. The high temperature working fluid is exhausted from an upstream plenum (e.g., shock tube, furnace, or reactor core), through a nozzle region, and into the disk MHD generator active volume, as shown. The flow is accelerated in the nozzle region. Typically, the nozzle region contains turning vanes that impart tangential momentum to the flow, imposing a swirl ($S \equiv v/u$) component on the flow; i.e., the flow enters the active generator region flowing radially, at a (tangential) flow angle of $\tan^{-1}(v/u)$.

The disk MHD generator is a Hall device in that (borrowing the terminology of linear generators) the Faraday field (E_θ)--or that component of the electric field normal to both the principal (radial) flow direction and the applied (axial) magnetic field--is zero by design ($E_\theta = 0$). The Faraday (tangential) current density component (J_θ) closes upon itself in a short circuit. The electric power is generated through the radial drift of the electrons in the Hall (radial) current density component (J_r) through the Hall (radial) electric field (of strength E_r).

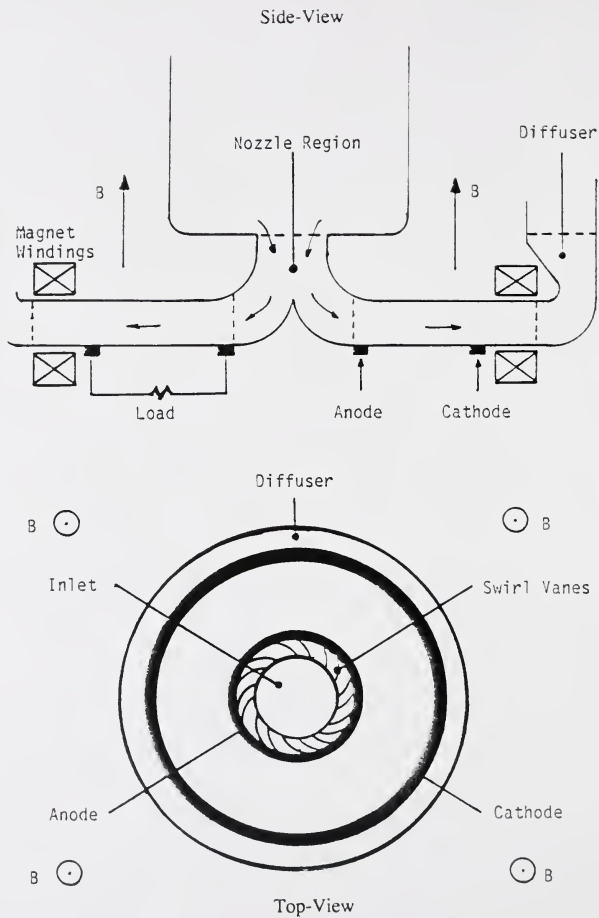


Figure 1.2

Top-View and Side-View Schematic Diagrams of the Outflow Disk MHD Generator.

In order to aid in the description of the disk MHD generator operation, the effects of axial components of fluid velocity (w), current density (J_z), and electric field (E_z) are ignored in the following discussion. (Note that the description is good in that, because the axial components are parallel to the applied magnetic field, the movement of charged particles in the axial direction cause no body forces and, except in the regions very close to the electrodes, contribute very little to the electric power density.)

Consider a working fluid with a finite scalar electrical conductivity, σ_c , which enters the disk MHD generator active volume with velocity $\underline{u} = (u, v, w)$ as shown in Figure 1.3. The free electrons and ions in the fluid interact with the applied magnetic induction $\underline{B} = B \mathbf{e}_z$. The resultant Lorentz forces (then body forces on the fluid) set up an electron drift, reflected in the current density components shown in Table 1.1.

For the sake of discussion, the MHD interaction is decomposed here component-by-component, although in actuality the currents and body forces arise simultaneously as the fluid interacts with the B-field. The working fluid enters the generator radially (disregarding for the moment any swirl component in the flow field); due to the mobility of the free electrons in the plasma, a $-uB$ electromotive force (EMF) drives a short circuit tangential current, $-\sigma_c uB$, and a body force [using Equation (1-9)] $J_\theta B$ is imparted against the flow. The electrons moving tangentially in the Faraday current ($-\sigma_c uB$), interact with the B-field, and give rise to an EMF which forces the electron to drift radially inward (relative to the bulk fluid which is flowing radially outward), setting up the Hall current, J_r ; the Hall

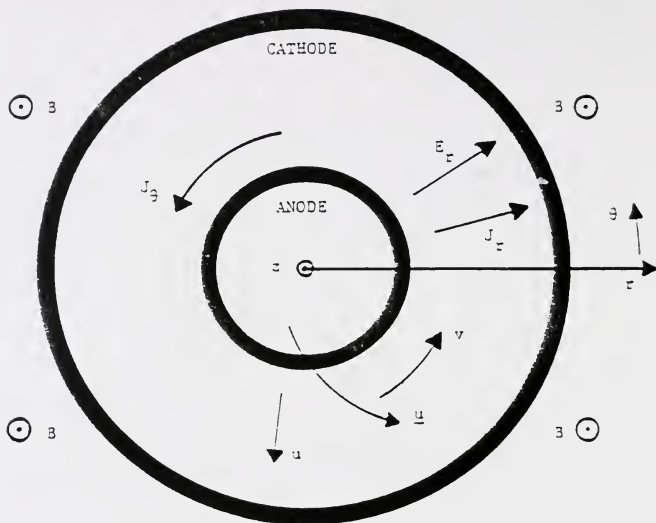


Figure 1.3 Functional Diagram of the Outflow Disk MHD Generator.

Table 1.1 Disk MHD Generator Current Density Components

\underline{J} (Components)	J_r	J_θ
$\sigma_e(\underline{u} \times \underline{B})$	$\sigma_e v B$	$-\sigma_e u B$
$\sigma_e \underline{E}$	$\sigma_e E_r$	0
$-\mu_e(\underline{J} \times \underline{B})^*$	$-\beta_e J_\theta$	$\beta_e J_r$
Total	$J_r = \sigma_\perp ((u\beta_e + v)B + E_r)^\dagger$	$J_\theta = \beta_e J_r - \sigma_e u B^\ddagger$

* Hall Effect

† $\sigma_\perp = \sigma_e / (1 + \beta_e^2)$

‡ or $J_\theta = \sigma_\perp ((\beta_e v - u)B + \beta_e E_r)$

current component caused by this Hall Effect is $-\beta J_\theta$. A body force, $-J_r B$, is imparted tangentially against the flow due to the movement of electrons in the Hall current interacting with the applied magnetic field. The Hall effect is again made manifest as the charged particles in the Hall current interact with the B-field causing a tangential electron drift; the tangential current density component is therefore reduced in magnitude (from $-\sigma_c u B$) by an amount βJ_r .

Recalling that typically the working fluid enters the generator with a tangential velocity (or swirl) component, the electromotive force vB drives a current $\sigma_c v B$ which combines with the Hall effect-induced current component $-\beta J_\theta$. Note that if there is zero load (short circuit) between the electrodes, the Hall field, E_r , is shorted out ($E_r = 0$) and the short circuit Hall current component ($J_{r,short} = \sigma_\perp (u\beta_c + v)B$) exists, where $\sigma_\perp = \sigma_c / (1 + \beta_c^2)$ is the effective (Hall) electrical conductivity in the radial direction. As the load resistance is increased, the radial current density component is reduced in magnitude as the electric field, E_r , develops across the electrodes. If the load is increased to infinite resistance (open circuit), the Hall current goes to zero ($J_r = 0$) and the open circuit Hall field, $(E_r)_{open} = -(u\beta_c + v)B$, exists across the electrodes. For a finite load resistance, both the Hall current density and Hall field exist, and power is produced in the movement of the charged particles through the negative electric field of strength E_r which, by Equation 1-10, is given by $J_r E_r$.

Note that the effect of the positive swirl component is to contribute a positive component to the total Hall current component; this has the effect of reducing the (negative) body force $J_\theta B$ that acts radially against the flow, tending

to decelerate the flow, while increasing the Hall current, and therefore the power density of the generator. The combined effect of reducing the radial body force while enhancing the load current leads to an increase in generator conversion efficiency, as reported in the classic paper on the outflow disk MHD generator by Louis (1968).

In general, the local electric power density ($\underline{J} \cdot \underline{E}$) scales as the square of the radial velocity (u), the square of the magnetic field strength (B), and is proportional to the electrical conductivity of the working fluid (σ_e). It is found in the course of this work that to insure high radial velocity, high swirl factor (for efficiency), and high electron mobility (both for electrical conductivity and Hall parameter), a supersonic flow field is desired.

1.2 Background

The outflow disk MHD generator studied in this work presents an interesting fluid mechanics/electromagnetics problem. The flow is supersonic in all but the boundary layer regions adjacent to the duct walls. Internal supersonic flow fields are potentially complicated in structure: The turning of the flow in any direction is accomplished through the generation of compression or rarefaction waves. In contrast to external flows in which such waves (e.g., a bow shock in front of a blunt body moving at supersonic speeds through a medium) simply project out into space, in internal flow these waves are reflected off the duct walls and in this way propagate downstream. The potential for large spatial gradients exists in the flow field because of these waves, and as a result of compressibility

and viscous effects in the high Reynolds number, turbulent flow fields. (The importance of large gradients in the fluid properties becomes evident in later discussion on the feedback between the plasma transport properties and local thermodynamic conditions.) Further, imposed on the supersonic flow field--for reasons of enhancing generator performance--is a tangential velocity component that decays with radial position in conserving angular-momentum. This added velocity component increases the kinetic energy of the generator flow field, enhances viscous heating and flow losses, while reducing the local thermodynamic properties; i.e., the axial variation in fluid properties is exacerbated by the addition of the swirl component in the flow.

By the nature of the MHD generator, large body forces ($\underline{J} \times \underline{B}$) oppose the flow and perturb the velocity profiles, contributing to adverse pressure gradients, and in some cases causing flow reversal. The body forces, for the most part, act against the flow and tend to decelerate the flow towards Mach one (cf. Shapiro's discussion on Fanno flow in Shapiro, 1953). An interesting phenomenon encountered in MHD generator flows is the distortion of the nominal axial velocity profiles--laminar or turbulent--by the MHD body force terms. A fluid exhibiting these profiles is characterized as a Hartmann flow, after Hartmann and his investigation of incompressible channel flows in the 1930s (reported in standard MHD texts, e.g., Sutton and Sherman, 1965). The Hartmann flow profiles are exhibited in the disk MHD generator as a result of nonuniform axial MHD body force profiles. The axially nonuniform body force profiles--neglecting for the moment any variation in the local magnetic induction, fluid properties,

electrical conductivity, or Hall parameter--result from the axial nonuniformity of the fluid velocity profile. The body force component in the core region of the flow is typically directed against the flow, tending to decelerate the flow; however, in the boundary layer region, where the velocity drops to zero, the body forces may decrease and can change directions. The result of the body force profile is to more greatly decelerate the core flow relative to the flow in boundary layer region causing a distortion in what would be the nominal axial flow profile (uninfluenced by MHD effects). In some cases the flow in the boundary layer region is accelerated by the MHD interaction. In the outflow disk MHD generator, in the case of strong MHD interaction, overshoots near the walls can occur in both the radial and tangential velocity axial profiles. It is noted that in the case of the high Reynolds number (supersonic) turbulent flows studied in this work, the region in which the tangential body forces accelerate the flow is small--possibly less than a percent of the boundary-layer thickness; the flow may be accelerated in a significant portion of a laminar boundary layer.

As described earlier, the generator working fluid in this study is laden with a fissionable isotope, and the active portion of the generator is integral to a nuclear reactor; a significant fission power density source term arises as energy is added to the fluid, locally, as a function of both the local fluid density and neutron flux level. In addition to effecting electrical conductivity by fission-fragment induced ionization, the fission energy addition in the flow tends to diffuse the flow towards Mach one (cf. Shapiro's, 1953, discussion on Rayleigh flow). Therefore, as a result of the decelerating effects of body forces, viscous

losses, the decay of the swirl component in the flow, and heat addition, the tendency of the outflow disk MHD generator is to decelerate supersonic flows to Mach one. Recalling that as a gasdynamic flow approaches Mach one, the rate of change of the flow variables (with respect to Mach number) increases to a maximum, the potential for rapid changes in the flow field variables with space exists in the generator.

In addition to the facets of the disk MHD generator flow dynamics mentioned above, an intimate coupling is seen to exist between the fluid mechanics, fission density, plasma physics properties, and the electromagnetic variables in the MHD flow of a fissioning gas. The number density of free (conduction) electrons available as charge carriers is shown in this work to depend strongly on the local fission density, itself proportional to both the local fluid density and neutron flux level. The electrical conductivity of the working fluid is proportional to the electron number density and the electron mobility, which itself is dependent on the local thermodynamic conditions (e.g., fluid density and static temperature). The electrical conductivity in turn dictates, to a large extent, the magnitudes of the local MHD power density and body forces. The body forces and the electrical and fission power densities affect the flow variable (e.g., velocity, density, etc.) profiles. The axial fission density profile may be expected to follow the axial fluid density profile, because, at the generator operating thermodynamic conditions of interest in this study, the density of the fluid is low enough that no significant neutron flux depression in the axial direction is expected; the neutron flux may be considered axially uniform in the duct region.

(The neutron flux may very well vary radially or tangentially in the generator, this being dependent on the reactor design.) In full circle then, the fission density dictates to a large degree the number density of the conduction electrons.

The discussion above describes the feedback for conditions in which the electrons are in equilibrium with the fluid temperature. In addition to this case, nonequilibrium (enhanced) electron temperatures may be obtained through the heating of the electron "fluid" through the fission-fragment induced ionization of the working fluid and through Joule heating (cf. Kerrebrock, 1961, and see Section 2.4.1 in this work).

1.3 Problem Statement

The discussion in the previous section provides background information indicating that the outflow disk MHD generator provides a plethora of interesting phenomena begging study. The large changes in the fluid thermodynamic variables in a supersonic flow--the contrast between stagnation and static properties, the difference between the core flow and boundary layer flow regions, differences radially through the duct due to the decelerating action of the MHD generator, and changes across waves generated in turning the flow--coupled with the feedback effects between the fission density, local fluid thermodynamic conditions, plasma transport properties, and the electromagnetic variables provide impetus for this work.

The primary objective of this work is to provide a methodology for solving the equations of the MHD flow of a fissioning gas in an outflow disk MHD

generator operating in steady-state. With the developed solution methodology, the effects of fissioning and MHD interaction on the spatial profiles of important fluid dynamic, electromagnetic, and plasma physics variables are studied.

1.4 Organization of Dissertation

Chapter 2 provides the theoretical modeling--governing equations and solution methodology--for the MHD flow of a weakly ionized fissioning plasma in an outflow disk MHD generator. Modifications to the solution methodology that arose in successfully implementing the theory of Chapter 2, and the main body of calculational results, analysis, and discussion are provided in Chapter 3. Chapter 4 provides a summary of results, conclusions, and recommendations for future extensions of this work. Appendix A provides an overview of a separately developed quasi-one-dimensional flow solver. Appendix B provides a description of the grid stretching algorithm used in the work. The shock capturing capability of the developed flow solver is analyzed in Appendix C.

CHAPTER 2

THEORETICAL MODELING

2.0 Introduction

A theoretical model of the MHD flow of a fissioning, compressible, weakly ionized plasma is presented in this chapter. The model is developed in order to predict the two-dimensional (2-D) profiles of important fluid dynamic and electromagnetic variables of a Navier-Stokes fluid with finite electrical conductivity flowing transverse to an applied magnetic field, in a significant neutron flux field, through an outflow disk MHD generator. This chapter presents an overview of the fluid mechanics, electromagnetics, and plasma physics modeling used as a means of predicting the behavior of the MHD generator flow.

2.1 Overview of Assumptions

The equations of magnetohydrodynamics--i.e., the continuum description of fluid mechanics and electromagnetics--governs the behavior of collision-dominated plasma in continua. The "MHD Equations" for this thesis work are presented in Table 2.1. The "MHD Approximations" (see standard textbooks on engineering MHD, e.g., Sutton and Sherman, 1965, Mitchner and Kruger, 1973, or Hughes and Young, 1966) have been imposed in the analysis presented here: It has been

Table 2.1 Governing Equations of Magnetohydrodynamics

Fluid Dynamics

$$\frac{\partial \rho}{\partial t} + \nabla \cdot (\rho \underline{u}) = 0 \quad (2-1)$$

$$\frac{\partial \rho \underline{u}}{\partial t} + \nabla \cdot (\rho \underline{u} \underline{u}) = -\nabla P + \nabla \cdot \underline{\underline{\tau}} + \underline{J} \times \underline{B} \quad (2-2)$$

$$\frac{\partial \rho \bar{e}}{\partial t} + \nabla \cdot (\rho \underline{u} \bar{h}) = \nabla \cdot (\underline{\underline{\tau}} \cdot \underline{u}) - \nabla \cdot \underline{q}'' + \dot{q}_N + \underline{J} \cdot \underline{E} \quad (2-3)$$

Electromagnetics

$$\underline{J} = \frac{1}{\mu_o} \nabla \times \underline{B} \quad (2-4)$$

$$\nabla \times \underline{E} = -\frac{\partial \underline{B}}{\partial t} \quad (2-5)$$

$$\underline{J} + \mu_e \underline{J} \times \underline{B} = \sigma_e (\underline{u} \times \underline{B} + \underline{E}) \quad (2-6)$$

Constitutive Relations

$$\underline{\underline{\tau}} - \tau_{ij} = \mu \left(\frac{\partial u_i}{\partial x_j} + \frac{\partial u_j}{\partial x_i} \right) - \frac{2}{3} \mu \left(\frac{\partial u_k}{\partial x_k} \right) \delta_{ij} \quad (2-7)$$

$$\underline{q}'' = -k \nabla T \quad (2-8)$$

Table 2.1--Continued

Equations of State

$$P = \rho \left(\frac{R_u}{M_w} \right) T \quad (2-9)$$

$$e = c_v T \quad (2-10)$$

Plasma Transport Properties

$$\sigma_e = \sigma_e(\chi_i, P, T, T_e, \Phi, |\underline{B}|) \quad (2-11)$$

$$\mu_e = \mu_e(\chi_i, P, T, T_e) \quad (2-12)$$

Fission Heating

$$\dot{q}_N(\underline{r}) = \rho(\underline{r}) \int_E \alpha(E) \Phi(\underline{r}, E) dE \quad (2-13)$$

Stokes's Relation

$$\lambda = -\frac{2}{3} \mu \quad (2-14)$$

with

$$\tilde{e} = e + \frac{1}{2} \underline{u} \cdot \underline{u} \quad (2-15)$$

$$\tilde{h} = \tilde{e} + \frac{P}{\rho} \quad (2-16)$$

assumed that

$$\begin{aligned} \text{a.) } & \frac{\partial \epsilon_o \underline{E}}{\partial t} \ll \underline{J} & (O10^{-13}\omega) \\ \text{b.) } & \frac{\rho^c \underline{u}}{\underline{J}} \ll 1 & (O10^{-8}) \\ \text{c.) } & \frac{\rho^c (\underline{E} + \underline{u} \times \underline{B})}{\underline{J} \times \underline{B}} \ll 1 & (O10^{-8}) \end{aligned}$$

where ω is the frequency at which the electric field, \underline{E} , varies. The "MHD Approximations" reduce the Ampere-Maxwell relation

$$\frac{\partial}{\partial t} (\epsilon_o \underline{E}) + \rho^c \underline{u} + \underline{J} = \frac{1}{\mu_o} \nabla \times \underline{B} \quad (2-17)$$

to a steady-state (or quasi-steady) relation and remove the explicit dependence of the momentum equation (Equation 2-2) on the net charge density (ρ^c); i.e.,

$$\rho^c \underline{E}' + \underline{J} \times \underline{B} \quad (2-18)$$

2.1.1 Simplifying Assumptions

To further simplify the MHD Equations, the problem is restricted to:

1. Tangential-symmetry ($\partial/\partial\theta = 0$)
2. Negligible induced magnetic induction (\underline{B}')
3. Negligible ion-slip ($\zeta = 0$)
4. Dissociation-free (single component) fluid
5. Perfect Gas
6. Steady-state generator operation.

By reconsidering the disk MHD generator problem geometry shown in Figure 2.1, it is apparent that, at least for this theoretical study of the 2-D (r, z) boundary layers, if the generator inlet flow profiles are tangentially symmetric and if the anode, cathode, and insulated surfaces are uniform (in θ) in composition and

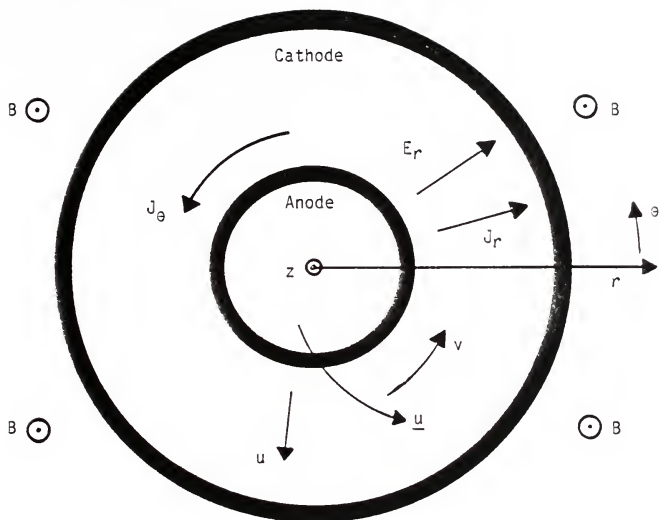


Figure 2.1 Schematic Diagram of the Disk MHD Generator Problem Geometry (Top-View).

temperature--i.e., are symmetric--the flow may also be considered tangentially symmetric. In actual generator operation, one might expect that due to asymmetries in the inlet flow--e.g., induced by turning vanes causing stratified temperature (or electrical conductivity) and velocity streams (wakes)--that the disk generator flow field is not so much tangentially uniform as it is tangentially periodic. The problem of theta-asymmetries has been studied elsewhere; a list of references dealing with non-uniformities induced by the inlet guide vanes is available in Roseman's dissertation (Roseman, 1982). More recently, tangential asymmetry was investigated and simulated by Inui et al. (1989). For the purpose of this study, the ideal case of uniform inlet flow (no temperature or velocity streamers) is considered in order to restrict the cylindrical (r, θ, z) geometry to an (r, z) plane at some (any) arbitrary angle, θ .

The magnetic induction is assumed to be negligible in this study.

Considering the Ampere-Maxwell relation

$$\underline{J} = \frac{1}{\mu_o} \nabla \times \underline{B} = \frac{1}{\mu_o} \nabla \times (\underline{B}^o + \underline{B}^i) \quad (2-19)$$

where \underline{B}^o is the applied magnetic induction and \underline{B}^i is the induced magnetic induction, one can show (see Rosa, 1968, or Sutton and Sherman, 1965) that $|\underline{B}^i|/|\underline{B}^o| \ll 1$ provided that $Re_m \ll 1$ where the magnetic Reynolds number, Re_m is given by

$$Re_m \equiv \mu_o \sigma_c u L \quad [= O(4\pi \times 10^{-7} \cdot 50 \cdot 2000 \cdot 1)] \quad (2-20)$$

($0.01 \leq Re_m \leq 0.1$ in this work). It is assumed that a known, steady-state applied axial magnetic induction exists, uniform throughout the generator duct.

The working fluid is assumed to be a single-phase, single component perfect gas uranium-tetrafluoride (UF_4)-helium (He) mixture. For the sake of this study, the actual identity of the constituents of the working fluid is not so much a factor as the requirement that the ratio-of-specific heats be relatively high ($\gamma \geq 1.3$) and that the fluid contains a significant mole fraction (5 to 6 mole percent) of a fissionable isotope so that significant fissioning occurs in the working fluid in a high thermal neutron flux field ($O 1 \times 10^{16} \text{ n/cm}^2\text{s}$). The stability of the UF_4 gas at temperatures near the 3000 K of interest in this study has not been firmly established; however, it is beyond the scope of this thesis to model the dissociation of the gas mixture. Further, the working fluid is assumed to maintain the same (gas) phase throughout the MHD generator; condensation is not considered in this work.

Under the assumptions discussed above, the MHD Equations can be reduced to a set of steady-state ($\partial/\partial t = 0$) equations; however, as noted in Section 2.2, a time-dependent (marching) solution is used to solve the fluid equations (Equations 2-1 to 2-3) and therefore, the time derivative terms in these equations are maintained, and an asymptotic steady-state solution is obtained (as suggested by Crocco, 1965). It is interesting to note that the time constants of the electromagnetics problem are on the order of the generator RC time constant ($\epsilon_0/\sigma_e \approx 1 \times 10^{-12} - 1 \times 10^{-13} \text{ s}$) and are (nine to ten orders-of-magnitude) smaller than the fluid mechanic time constants ($O L/U \approx 1 \text{ m}/1000 \text{ m/s} - 1 \times 10^{-3} \text{ s}$); the time-dependent fluid solution method coupled with the steady-state (quasi-steady) electromagnetics solution provides an overall consistent solution method that is

valid for time-dependent generator problems given that applied electromagnetic fields (e.g., applied B-field) vary with frequencies much less than 1 to 10 gigahertz (0.10^{12} s^{-1}).

The remainder of this chapter is devoted to a detailed presentation of the theoretical modeling developed to describe the steady-state operation of the outflow disk MHD generator. The fluid mechanics modeling is addressed first, followed by the electromagnetics and plasma physics modeling.

2.2 Fluid Mechanics

The governing equations of fluid mechanics used in this study may be rewritten as

$$\frac{\partial \rho}{\partial t} + \nabla \cdot (\rho \underline{u}) = 0 \quad (2-21)$$

$$\frac{\partial \rho \underline{u}}{\partial t} + \nabla \cdot (\rho \underline{u} \underline{u} + P \underline{I} - \underline{\tau}) = \underline{J} \times \underline{B} \quad (2-22)$$

$$\frac{\partial \rho \underline{e}}{\partial t} + \nabla \cdot (\rho \underline{u} \underline{h} + \underline{q}'' - \underline{\tau} \cdot \underline{u}) = \underline{J} \cdot \underline{E} + \dot{q}_N \quad (2-23)$$

Note that, independent of the chosen coordinate system, the above equations contain actual source terms, $\underline{J} \times \underline{B}$, $\underline{J} \cdot \underline{E}$, and \dot{q}_N arising from the MHD interaction and fission power. As a matter of interest, the MHD source terms could be rewritten in a divergence form--that is included in the divergence term of the left hand side of Equations 2-22 and 2-23--by introducing the Maxwell stress tensor and by making use of the Poynting vector (see, for example, Hughes and Young,

1966). Having neglected the effect of the induced B-field relative to the applied B-field, the formulation presented in Equations 2-21 to 2-23 is used in this study.

Figure 2.2 shows a typical outflow disk MHD generator geometry. The variable generator duct height, or lofting, suggests that the governing equations be mapped into a tangentially symmetric boundary-fitted coordinate system. As a matter of documentation, an attempt was made to transform the Navier-Stokes equations from 3-D Cartesian geometry into a generalized (ξ, η, ζ) coordinate system, with one ignored coordinate (e.g., ζ , as encountered in an axisymmetric flow). It was re-discovered (as earlier shown and discussed elegantly by Vinokur, 1974) that the axisymmetric scenario is an example of a degenerate case in which a strong conservation-law form cannot be obtained. As shown by Vinokur (1974) when considering the equations of gasdynamics (Euler equations) transformed from cartesian to cylindrical coordinates, the radial momentum equation cannot be cast into strong conservation-law form, because of the pressure gradient term (∇P) which gives rise to a source term, P . (Vinokur considered a flow with zero swirl; else the resulting source term would contain both the static pressure and a centrifugal force term.) The transformation of the full Navier-Stokes equations (with a swirl component) into an axisymmetric coordinate system was found to give rise to the source terms: static pressure, P ; a centrifugal force term, ρv^2 ; and a shear stress term, $\tau_{\theta\theta}$, which all serve as pseudo-source terms of radial momentum. (It is also noted that, even had the full divergence form of the body force term in Equation 2-22 been facilitated by use of the Maxwell stress tensor, under the same transformation discussed above, a pseudo-source term of

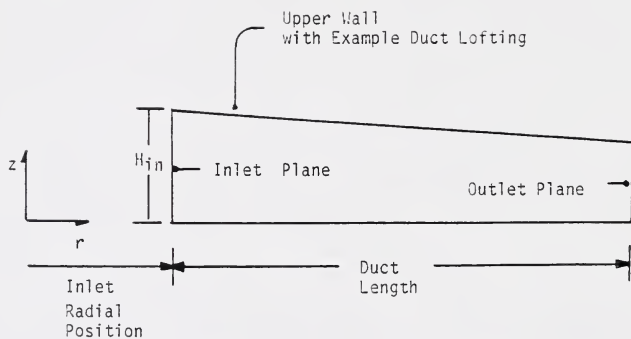


Figure 2.2 Side-View Schematic Diagram of Outflow Disk MHD Generator showing a Typical Generator Duct Lofting.

momentum would also arise from the body force term.) Stated in other words, the divergence of a second order tensor necessarily results in source terms under a transformation from the cartesian-to-cylindrical coordinate system to an axisymmetric coordinate system.

In developing the governing equations, the Navier-Stokes equations (Equations 2-21 to 2-23) are expressed in the cylindrical coordinate system (obtained either by performing a coordinate transformation or by using available equations, for example, from Bird et al., 1960) and tangential-symmetry is imposed ($\partial/\partial\theta = 0$). The equations posed in cylindrical coordinates may be written in the weak conservation-law form

$$\frac{\partial Q}{\partial t} + \frac{\partial E}{\partial r} + \frac{\partial F}{\partial z} = \frac{\partial E_r}{\partial r} + \frac{\partial F_z}{\partial z} + \underline{S} \quad (2-24)$$

as shown in Table 2.2. Note that the source vector, \underline{S} , contains the source terms ($\underline{J} \times \underline{B}$) and ($\underline{J} \cdot \underline{E}$), the fission power density term (\dot{q}_N), as well as the pseudo-source terms arising from the transformation from the cartesian to the cylindrical coordinates.

2.2.1 Generalized Coordinate Transformation

Having imposed tangential-symmetry, the governing equations (Equations 2-24) are transformed (see Figure 2.3) into the generalized curvilinear (ξ, η) boundary-fitted coordinate system, after Pullium and Steger (1980) and earlier Vinokur (1974), or by using the technique of Thompson, Warsi, and Mastin (1985). The transformed equations are

Table 2.2 Governing Equations of Magnetohydrodynamics with Fission Density Terms in Cylindrical Coordinates with Tangential-Symmetry

$$\frac{\partial Q}{\partial t} + \frac{\partial \underline{E}}{\partial r} + \frac{\partial F}{\partial z} = \frac{\partial \underline{E}_r}{\partial r} + \frac{\partial \underline{F}_r}{\partial z} + \underline{S}$$

$$Q = r \begin{bmatrix} \rho \\ \rho u \\ \rho v r \\ \rho w \\ \rho \bar{e} \end{bmatrix}$$

$$\underline{E} = r \begin{bmatrix} \rho u \\ \rho u^2 + P \\ \rho u v r \\ \rho u w \\ \rho \bar{h} u \end{bmatrix}$$

$$\underline{E}_r = r \begin{bmatrix} 0 \\ \tau_{rr} \\ r \tau_{r\theta} \\ \tau_{rz} \\ \beta_r \end{bmatrix}$$

$$\underline{F} = r \begin{bmatrix} \rho w \\ \rho u w \\ \rho v w r \\ \rho w^2 + P \\ \rho \bar{h} w \end{bmatrix}$$

$$\underline{F}_r = r \begin{bmatrix} 0 \\ \tau_{rz} \\ r \tau_{\theta z} \\ r \tau_{zz} \\ \beta_z \end{bmatrix}$$

$$\underline{S} = r \begin{bmatrix} 0 \\ \frac{1}{r}(\rho v^2 + P) + J_\theta B_z - \tau_{\theta\theta} \\ -r J_r B_z \\ 0 \\ J_r E_r + J_z E_z + \dot{q}_N \end{bmatrix}$$

where

$$\beta_r = \tau_{rr} u + \tau_{r\theta} v + \tau_{rz} w - q_r''$$

$$\beta_z = \tau_{rz} u + \tau_{\theta z} v + \tau_{zz} w - q_z''$$

Table 2.2--Continued

$$\tau_{rr} = \mu \left(2 \frac{\partial u}{\partial r} \right) + \lambda \left(\frac{1}{r} \frac{\partial ru}{\partial r} + \frac{\partial w}{\partial z} \right)$$

$$\tau_{\theta\theta} = 2\mu \frac{u}{r} + \lambda \left(\frac{1}{r} \frac{\partial ru}{\partial r} + \frac{\partial w}{\partial z} \right)$$

$$\tau_{zz} = 2\mu \frac{\partial w}{\partial z} + \lambda \left(\frac{1}{r} \frac{\partial ru}{\partial r} + \frac{\partial w}{\partial z} \right)$$

$$\tau_{r\theta} = \mu r \frac{\partial(v/r)}{\partial r}$$

$$\tau_{rz} = \mu \left(\frac{\partial w}{\partial r} + \frac{\partial u}{\partial z} \right)$$

$$\tau_{\theta z} = \mu \frac{\partial v}{\partial z}$$

$$q_r'' = -k \frac{\partial T}{\partial r}$$

$$q_z'' = -k \frac{\partial T}{\partial z}$$

$$\dot{q}_N = \rho \int_E \alpha(E) \Phi(r, E) dE$$

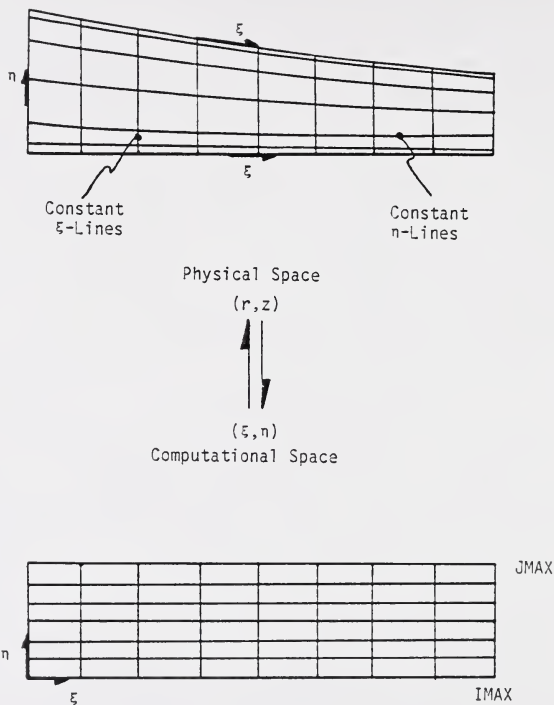


Figure 2.3 Cylindrical (r, z) Coordinate System to Boundary-Fitted (ξ, η) Coordinate System Transformation.

$$\frac{\partial \hat{Q}}{\partial \tau} + \frac{\partial \hat{E}}{\partial \xi} + \frac{\partial \hat{F}}{\partial \eta} = \frac{\partial \hat{E}_r}{\partial \xi} + \frac{\partial \hat{F}_r}{\partial \eta} + \hat{S} \quad (2-25)$$

where

$$\begin{aligned} \hat{Q} &= \sqrt{g} Q \\ \hat{E} &= \sqrt{g} (\xi_r \underline{E} + \xi_z \underline{F}) \\ \hat{F} &= \sqrt{g} (\eta_r \underline{E} + \eta_z \underline{F}) \\ \hat{E}_r &= \sqrt{g} (\xi_r \underline{E}_r + \xi_z \underline{F}_r) \\ \hat{F}_r &= \sqrt{g} (\eta_r \underline{E}_r + \eta_z \underline{F}_r) \\ \hat{S} &= \sqrt{g} \underline{S} \end{aligned}$$

and where $\sqrt{g} = (\xi_r \eta_z - \xi_z \eta_r)^{-1}$ is the Jacobian of the transformation of $(r, z) \rightarrow (\xi, \eta)$.

Thin-layer approximation. The "thin-layer" approximation neglects the diffusion processes parallel to body surfaces (i.e., generator walls in the case studied here) by assuming that viscous terms with derivatives parallel to the body surface are negligible. The thin-layer approximation is similar to the classical boundary-layer approximation in that it neglects diffusion terms parallel to the body surface; however, the momentum equations normal to body surfaces are maintained in the thin-layer approximation whereas in classical boundary layer theory, the momentum equations normal to the body surface are replaced by assumptions of zero normal static pressure gradients through the boundary layer. By maintaining the normal momentum equations, separated and reverse flow regions can be computed with no concern for singularities at the flow separation points. Baldwin and Lomax (1978) provide a detailed discussion of the thin-layer

approximation and indicate that although the viscous terms normal to the wall can generally be resolved, even for high Reynolds number flows, by use of a fine grid structure near the wall, the viscous terms parallel to the body surface--in the stream-wise direction--are generally not resolvable. Degani and Steger (1983) compared full Navier-Stokes and thin-layer approximation computations for separated supersonic flow (through a compression corner) using stream-wise space steps equal to 4.5% of the inlet boundary layer thickness (δ_{in}) in the full Navier-Stokes calculations. They detected only small differences between the thin-layer approximation solution and the full Navier-Stokes results, and these differences were confined to the separation bubble region only. Using courser stream-wise space steps for the Navier-Stokes calculations resulted in no difference between the Navier-Stokes and thin-layer approximation calculation results.

The thin-layer approximation is imposed here by allowing $\partial \hat{\underline{E}} / \partial \xi \rightarrow 0$ and by neglecting all derivatives with respect to the curvilinear coordinate ξ in the $\hat{\underline{F}}$, vector and in the source vector $\hat{\underline{S}}$. Under the thin-layer approximation, the governing equations of fluid mechanics may be rewritten as

$$\frac{\partial \underline{A}}{\partial \tau} + \frac{\partial \underline{B}}{\partial \xi} + \frac{\partial \underline{C}}{\partial \eta} = \underline{D} \quad (2-26)$$

where the vectors \underline{A} , \underline{B} , \underline{C} , and \underline{D} are described in Table 2.3.

2.2.2 Turbulence Modeling

To include the effects of turbulence in the generator model, the instantaneous local primitive variables ($\rho, \underline{u}, \bar{\epsilon}$) of Equations 2-21 to 2-23 are

Table 2.3 Transformed Governing Equations of MHD with Thin-Layer Approximation in Boundary-Fitted Cuvilinear Coordinate System (ξ, η)

$$\frac{\partial \underline{A}}{\partial \tau} + \frac{\partial \underline{B}}{\partial \xi} + \frac{\partial \underline{C}}{\partial \eta} = \underline{D}$$

$$\underline{A} = \sqrt{g} r \begin{bmatrix} \rho \\ \rho u \\ \rho v r \\ \rho w \\ \rho \tilde{e} \end{bmatrix}$$

$$\underline{B} = \sqrt{g} r \left[\xi_r \begin{bmatrix} \rho u \\ \rho u^2 + P \\ \rho u v r \\ \rho u w \\ \rho \tilde{h} u \end{bmatrix} + \xi_z \begin{bmatrix} \rho w \\ \rho u w \\ \rho v w r \\ \rho w^2 + P \\ \rho \tilde{h} w \end{bmatrix} \right]$$

$$\underline{C} = \sqrt{g} r \left[\eta_r \begin{bmatrix} \rho u \\ \rho u^2 + P - \tau_{rr} \\ \rho u v r - r \tau_{r\theta} \\ \rho u w - \tau_{rz} \\ \rho \tilde{h} u - \beta_r \end{bmatrix} + \eta_z \begin{bmatrix} \rho w \\ \rho u w - \tau_{rz} \\ \rho v w r - \tau_{\theta z} \\ \rho w^2 + P - \tau_{zz} \\ \rho \tilde{h} w - \beta_z \end{bmatrix} \right]$$

$$\underline{D} = \sqrt{g} r \begin{bmatrix} 0 \\ \frac{1}{r} (\rho v^2 + P - \tau_{\theta\theta}) + J_\theta B_z \\ -r J_r B_z \\ 0 \\ J_r E_r + J_z E_z + \dot{q}_N \end{bmatrix}$$

Table 2.3--Continued

$$\beta_r = \tau_{rr}u + \tau_{r\theta}v + \tau_{rz}w - q_r''$$

$$\beta_z = \tau_{rz}u + \tau_{\theta z}v + \tau_{zz}w - q_z''$$

$$\tau_{rr} = \frac{1}{\sqrt{g}} \left[2\mu(\sqrt{g}\eta_r u)_\eta + \frac{\lambda}{r}(\sqrt{g}\eta_r r u)_\eta + \lambda(\sqrt{g}\eta_z w)_\eta \right]$$

$$\tau_{\theta\theta} = 2\mu \frac{u}{r} + \frac{1}{\sqrt{g}} \left\{ \frac{\lambda}{r}(\sqrt{g}\eta_r r u)_\eta + \lambda(\sqrt{g}\eta_z w)_\eta \right\}$$

$$\tau_{zz} = \frac{1}{\sqrt{g}} \left\{ (2\mu + \lambda)(\sqrt{g}\eta_z w)_\eta + \frac{\lambda}{r}(\sqrt{g}\eta_r r u)_\eta \right\}$$

$$\tau_{r\theta} = \frac{\mu r}{\sqrt{g}} (\sqrt{g}\eta_r \frac{v}{r})_\eta$$

$$\tau_{rz} = \frac{1}{\sqrt{g}} \left[\mu(\sqrt{g}\eta_r w)_\eta + \mu(\sqrt{g}\eta_z u)_\eta \right]$$

$$\tau_{\theta z} = \frac{\mu}{\sqrt{g}} (\sqrt{g}\eta_z v)_\eta$$

$$q_r'' = -\frac{k}{\sqrt{g}} (\sqrt{g}\eta_r T)_\eta$$

$$q_z'' = -\frac{k}{\sqrt{g}} (\sqrt{g}\eta_z T)_\eta$$

replaced by their mean and fluctuating quantities obtained by conventional mass-weighted, time-averaging procedures (see, for example, Cebeci and Smith, 1974, Schlichting, 1955, or Anderson et al., 1984). The "apparent" or "Reynolds stresses" ($\rho u_i' u_j'$ and $\rho u_i' \bar{h}'$ terms) arising from the time averaging of the governing equations are treated following the Boussinesq assumption (originally by Boussinesq, 1877--referred to by Schlichting, 1955 and Anderson et al., 1984, for example): The apparent turbulent shearing stresses are related to the mean strain through an apparent "eddy" or turbulent viscosity; that is

$$-\overline{\rho u_i' u_j'} = \mu_r \left(\frac{\partial u_i}{\partial x_j} + \frac{\partial u_j}{\partial x_i} \right) - \frac{2}{3} \delta_{ij} \left(\mu_r \frac{\partial u_k}{\partial x_k} + \rho \hat{\kappa} \right) \quad (2-27)$$

where μ_r is the turbulent viscosity and κ is the kinetic energy of turbulence ($u_i' u_i' / 2$). The second coefficient of viscosity (λ) has been related to the first coefficient of viscosity (μ) through the Stokes Hypothesis: $\lambda = -2\mu/3$ (G.G. Stokes, 1845 as referred to by Schlichting, 1955).

Non-vanishing prime terms arise from the time-averaging of the electromagnetics terms $\underline{J} \times \underline{B}$ and $\underline{J} \cdot \underline{E}$ (given that \underline{J} is related to the local velocity \underline{u} and the electric field \underline{E} through the generalized Ohm's law). In general, the degree of turbulence in the flow field is reduced by the presence of the magnetic field. The effect, turbulence damping, arises as some of the energy of turbulence is converted to electrical energy which is dissipated as Joule heating (Rankin, 1978). Rankin indicates that turbulence damping was not an important factor in the supersonic generator flow he studied, due to the high mean velocities. The

non-vanishing electromagnetic terms are neglected in this study; realistically, modeling these terms is beyond the scope of this thesis.

The governing equations of turbulent MHD flow maintain the same form as those given in Equation 2-21 to 2-23 where now the shear stress tensor ($\underline{\tau}$) components are given by

$$\tau_{ij} = \tau_{i_v} + \tau_{i_\tau} = (\mu_l + \mu_\tau) \left[\left(\frac{\partial u_i}{\partial x_j} + \frac{\partial u_j}{\partial x_i} \right) - \frac{2}{3} \delta_{ij} \left(\frac{\partial u_k}{\partial x_k} \right) \right] \quad (2-28)$$

Here, the subscript "l" represents laminar and "τ" represents turbulent properties.

The kinetic energy of turbulence, κ , has been neglected, consistent with the algebraic model for μ_τ employed. In an analogous manner, the components of the heat flux vector, \underline{q}'' , are

$$q_j'' = -(k_l + k_\tau) \frac{\partial T}{\partial x_j} = -c_p \left[\frac{\mu_l}{Pr} + \frac{\mu_\tau}{Pr_\tau} \right] \frac{\partial T}{\partial x_j} \quad (2-29)$$

where Pr is the fluid Prandtl number (e.g., 0.7 for air), Pr_τ is the turbulent Prandtl number. Typically Pr_τ has a value near unity at a wall and decreases through the boundary layer to near 0.5 away from the wall. The manner in which the turbulent Prandtl number varies across a boundary layer is open to question (Schlichting, 1955). In this work, a value of $Pr_\tau = 0.9$ is used, uniform through the flow field, consistent with common algebraic turbulence modeling for wall boundary layers (Anderson et al., 1984).

Algebraic turbulence model. The algebraic model for determining μ_τ developed by Baldwin and Lomax is used in this work to predict the local value of

the apparent or turbulent viscosity, μ_r (Baldwin and Lomax, 1978). Baldwin and Lomax patterned their model, developed to facilitate the analysis of separated flows where there exists question as to the location of the edge of the boundary layer--as is the case encountered in the Hartmann flow discussed in Chapter 1--after that of Cebeci and Smith (1974). The Cebeci-Smith turbulence model divides the near-wall flow region into an inner and outer region. In the inner region

$$\mu_{r,i} = \rho l^2 \left| \frac{\partial V_T}{\partial \hat{z}} \right| \quad (2-30)$$

where V_T is the total velocity $(\underline{u} \cdot \underline{u})^{1/2}$ and where l is the Prandtl mixing length, here modeled using the expression of van Driest (van Driest, 1956)

$$l = \kappa \hat{z} (1 - e^{-\hat{z}^*/A^*}) \quad (2-31)$$

where the von Karman factor, κ , typically has a value of 0.4 to 0.41, $A^* = 26$ typically, and where \hat{z}^* is the local distance from the wall, \hat{z} , measured normal to the wall, and normalized by

$$\hat{z}^* = \hat{z} \frac{u_r}{\nu} \quad (2-32)$$

The friction velocity (or characteristic velocity of turbulence) u_r is

$$u_r = \left(\frac{\tau_w}{\rho_w} \right)^{1/2} \quad (2-33)$$

where τ_w is the shear stress at the wall, ρ_w is the fluid density at the wall and ν is the local (laminar) absolute viscosity (μ/ρ) . The outer region model uses the

Clauser formulation, given by

$$\mu_{\tau,o} = \alpha \rho u_e \delta^* \gamma(\hat{z}) \quad (2-34)$$

where α is the Clauser constant (typically 0.0168), u_e is the value of $(\underline{u} \cdot \underline{u})^{1/2}$ at the edge of the boundary layer, δ^* is the local (incompressible flow) displacement thickness $(\equiv \int_0^{\infty} (1 - \frac{u}{u_e}) dz)$, and γ is the Klebanoff intermittency factor given by

$$\gamma(\hat{z}) = \left[1 + 5.5 \left[\frac{\hat{z}}{\delta} \right]^6 \right]^{-1} \quad (2-35)$$

where δ is the boundary layer thickness. The local turbulent viscosity is then given by

$$\mu_{\tau} = \begin{cases} \mu_{\tau,i} & \text{for } \hat{z} \leq \hat{z}_c \\ \mu_{\tau,o} & \text{for } \hat{z} > \hat{z}_c \end{cases} \quad (2-36)$$

where \hat{z}_c is the minimum value of \hat{z} where $(\mu_{\tau})_i = (\mu_{\tau})_o$. Note that the boundary layer thickness, δ , must be known to implement the Cebeci-Smith model; this is the impetus for Baldwin and Lomax's work. They circumvent this requirement by changing the outer region of Cebeci-Smith model. In the inner region of the Baldwin-Lomax model

$$\mu_{\tau,i} = \rho l^2 |\underline{\omega}| \quad (2-37)$$

where $\underline{\omega}$ is the local vorticity vector ($\underline{\omega} = \nabla \times \underline{u}$), l is the Prandtl mixing length modeled using the van Driest formulation given above. It is noted that under the

thin-layer approximation, $|\underline{\omega}| = |\partial V_T / \partial z|$, and the Cebeci-Smith inner region model is recovered. The local wall shear stress is calculated in this work using

$$\tau_w = \mu_l |\underline{\omega}| \quad (2-38)$$

(Shih, 1990) where μ_l is the laminar viscosity--for indeed at the wall, $\mu_r \rightarrow 0$).

In the outer region the turbulent viscosity is predicted by

$$\mu_{r,o} = \alpha \rho C_{cp} F_{WAKE} \gamma(\hat{z}) \quad (2-39)$$

(using the notation of Baldwin and Lomax). Again, α is the Clauser constant (we use 0.0168), C_{cp} is a constant (typically set to 1.6; however, note P.S. Granville's work on Baldwin-Lomax factors for turbulent boundary layers in pressure gradients (Granville, 1987)), $\gamma(z)$ is the Klebanoff intermittency factor provided by Equation 2-35 of the C-S model; however, note that in the Baldwin-Lomax turbulence model, the boundary layer thickness, δ , in Equation 2-35, is replaced by the ratio \hat{z}_{MAX}/C_{Kleb} where C_{Kleb} is a constant (typically 0.3) and where \hat{z}_{MAX} is the position corresponding to the location of F_{MAX} given by

$$F_{MAX} = \max \{ F(\hat{z}) \} = \max \left\{ \frac{l}{\kappa} |\underline{\omega}| \right\} \quad (2-40)$$

F_{WAKE} (of Equation 2-39) is given by

$$F_{WAKE} = \min \{ \hat{z}_{max} F_{max}, C_{WK} \hat{z}_{max} V_{DIFF}^2 / F_{MAX} \} \quad (2-41)$$

and C_{WK} is a constant (0.25 typically) and

$$V_{DIFF} = (\underline{u} \cdot \underline{u})_{MAX}^{\frac{1}{2}} - (\underline{u} \cdot \underline{u})_{MIN}^{\frac{1}{2}} \quad (2-42)$$

locally; $(\underline{u} \cdot \underline{u})_{MIN}^{\frac{1}{2}}$ is zero in the case of a stationary wall. The constants provided above were calculated by Baldwin and Lomax to match predictions using the Cebeci-Smith model for equilibrium boundary layers (Baldwin and Lomax, 1978). Again, the turbulent viscosity from the inner region model is used near the wall up to that distance (z_c) where the inner region viscosity is first larger than that predicted by the outer region model.

The Baldwin-Lomax turbulence model may, fortuitously, prove ideal for the modeling of MHD flows where the frequently encountered boundary layer region velocity overshoots (Hartmann flow) obscure an accurate determination of the boundary layer thickness, and in fact call into question the meaningfulness of definition of the boundary layer thickness. It should be noted that work by Shirazi and Truman, in which they compared the Cebeci-Smith and Baldwin-Lomax models for supersonic flow past a sphere-cone, suggested that effectively, knowledge of the boundary layer thickness is required when implementing the Baldwin-Lomax turbulence model due to ambiguity in determining the maximum in the vorticity function $F(z)$, which requires that the search for the maximum F be restricted to the boundary layer (Shirazi and Truman, 1989). One objective of this thesis is to determine whether or not this proves true for the Hartmann flow of the type found in the outflow disk MHD generator.

2.2.3 Fluid Properties

Recall that in Section 2.1.1 it was assumed that the MHD generator working fluid may be modeled as a perfect gas and that the single-component fluid mixture does not dissociate. For the analysis of interest in this work it matters little what particular working fluid is employed; however the working fluid must contain a significant fraction of a fissionable isotope (to insure adequate fission densities) and the ratio of specific heat (γ) of the mixture must be relatively high (e.g., $\gamma \geq 1.3$, to facilitate reasonable MHD generator (turbine) operation). Indeed, to avoid controversy over the questions of working fluid dissociation and condensation with the MHD generator, it would seem preferable to restrict attention to a fictitious working fluid with a given molecular weight (25 kg/kg mole), a γ near 1.4 and an atom fraction of 5 to 6% ^{235}U (or other fissionable isotope). Based on work at the University of Florida, however, impetus exists to consider a uranium-tetrafluoride (UF_4) and helium (He) working fluid mixture. It has been asserted the UF_4 gas is expected to be relatively stable at high (2000-4000 K) temperature (cf. Dugan et al., 1988). In this work, then, a UF_4 -He generator working fluid is analyzed; dissociation and condensation in the MHD duct are neglected, and a single-phase, single-component (UF_4 -He) gas is assumed throughout the generator. Further, the gas is treated as a thermally and calorically perfect gas.

Constituent properties. The properties of the pure UF_4 and He constituents of the fluid mixture are presented in Table 2.4 along with the properties of the fluid mixture: 94 mole-percent He ($X_{\text{He}} = 0.94$) and 6 mole-

Table 2.4 Pure UF₄ and He Gas Properties and UF₄-(94%)He Working Fluid Mixture Properties*

UF₄ Properties

M _w	(kg/kg · mole)	311.15
R	(J/kg · K)	26.72
γ		1.09
c _p	(J/kg · K)	323.61
μ _t	(kg/m · s)	8.67 x 10 ⁻⁵
k _t	(W/m · K)	0.031
Pr		0.901

He Properties

M _w	(kg/kg · mole)	4.0
R	(J/kg · K)	2078.5
γ		1.666
c _p	(J/kg · K)	5190.0
μ _t	(kg/m · s)	7.55 x 10 ⁻⁵
k _t	(W/m · K)	0.589
Pr		0.665

UF₄-(94%)He Mixture Properties

M _w	(kg/kg · mole)	22.43
R	(J/kg · K)	370.68
γ		1.482
c _p	(J/kg · K)	1139.4
μ _t	(kg/m · s)	1.0 x 10 ⁻⁴
k _t	(W/m · K)	0.4609
Pr		0.247

* All properties tabulated at 2000 K.

percent UF_4 ($X_{UF_4} = 0.06$). The γ_{UF_4} is taken from data that has been compiled from a number of sources (e.g., Hassan and Deese, 1974) by E.T. Dugan at the University of Florida. Note that the $\gamma_{UF_4} = 1.09$ is slightly higher than that suggested for pure UF_6 by Oliver and Dugan of $\gamma_{UF_6} = 1.056$ (Oliver and Dugan, 1985). The viscosity of pure UF_4 is assumed to be the same as that of UF_6 (reported by Oliver and Dugan, 1985); a reference temperature of 2000 K is chosen. Using the assumed viscosity for UF_4 with Eucken's formula (Chapman and Cowling, 1939),

$$Pr = \frac{4\gamma}{9\gamma - 5} \quad (2-43)$$

a Prandtl number (laminar) for UF_4 is found, from which the UF_4 thermal conductivity (laminar) may be obtained. The uranium component of the UF_4 is assumed to be 95% enriched in ^{235}U , providing a fissionable atom fraction of 0.057. The neutron temperature (assumed to be established in the moderator region external to the MHD duct) used to determine the average thermal microscopic is taken as 1200 K, providing a fission cross section of 230 barns.

The helium properties provided in Table 2.4 are obtained from Oliver and Dugan's paper. Eucken's formula, used above, was verified using both the pure helium properties and the pure UF_6 properties provided in their paper.

Mixture properties. The mixture properties are calculated using

$$M_w = \sum_i X_i M_{wi} \quad (2-44)$$

$$C_p = \frac{1}{M_w} \sum_i X_i M_w C_{p,i} \quad (2-45)$$

and

$$\gamma = \frac{\sum_i \Gamma_i X_i}{\sum_i \Gamma_i X_i - 1} \quad (2-46)$$

where $\Gamma_i = \gamma_i / (\gamma_i - 1)$. The mixture laminar viscosity is calculated using the Wilke formula (after Oliver and Dugan, 1985)

$$\mu_{MIX} = \frac{\mu_1}{1 + \frac{X_2}{X_1} \phi_{12}} + \frac{\mu_2}{1 + \frac{X_1}{X_2} \phi_{21}} \quad (2-47)$$

where

$$\phi_{ij} = \frac{1}{\sqrt{8}} \left[1 + \frac{M_w}{M_{w_j}} \right]^{-\frac{1}{2}} \left[1 + \left[\frac{\mu_i}{\mu_j} \right]^{\frac{1}{2}} \left[\frac{M_w}{M_{w_j}} \right]^{\frac{1}{2}} \right]^2 \quad (2-48)$$

The laminar thermal conductivity of the mixture is calculated using the Mason-Saxina/Lindsay-Bromley formula for a two-constituent mixture (again, discussed by Oliver and Dugan, 1985)

$$k_{MIX} = \frac{k_1}{1 + \frac{X_2}{X_1} G_{12}} + \frac{k_2}{1 + \frac{X_1}{X_2} G_{21}} \quad (2-49)$$

where, it is assumed, after Oliver and Dugan, that $G_{12} = \Phi_{12}$ and $G_{21} = \Phi_{21}$. The above forms allow the viscosity and thermal conductivity to be obtained at a

reference temperature (T_0) of 2000 K. At any temperature other than T_0 it is assumed that

$$\mu_l = (\mu_l)_o \left[\frac{T}{T_o} \right]^\omega \quad (2-50)$$

where $(\mu_l)_o$ is the mixture reference laminar viscosity at T_0 and ω is taken to be 0.5 for the high temperatures in question (Pai, 1981). The laminar Prandtl number is calculated at the reference temperature (T_0) and is assumed constant with temperature. Given that the gas is calorically perfect (c_p is constant) then given $\mu_l(T)$, $k_l(T)$ may be calculated.

2.2.4 Fluid Boundary Conditions

In the disk MHD generator configurations studied in this thesis, the working fluid is assumed to enter the active generator region from a supersonic nozzle region. In the nozzle region, the flow is expanded to an exit radial Mach number above unity, and turning vanes impart tangential momentum to the fluid so that a significant swirl ($s = v/u$) is imparted into the flow. The flows analyzed in this work are supersonic throughout the generator--inlet to outlet--except in the thin regions, very near the wall in the boundary layers, where the flow is subsonic as a consequence of no-slip at the boundaries. The working fluid exits the generator with a supersonic radial velocity and is exhausted, for example, into a supersonic diffuser.

It is noted, for the sake of clarity, that when the term supersonic is used in this work to characterize the flow it refers to the flow condition in which the core flow--that outside of the boundary layer region--has a local radial Mach number,

given by

$$M_R = \left[\frac{u^2}{\gamma R T} \right]^{\frac{1}{2}} \quad (2-51)$$

that is greater than unity, rather than the condition where the total Mach number (in the same core flow region), given by

$$M_T = \left[\frac{u^2 + v^2 + w^2}{\gamma R T} \right]^{\frac{1}{2}} = M_R \sqrt{1 + S^2 + p^2} \quad (2-52)$$

is greater than one. The total Mach number is necessarily greater than one when the flow is supersonic (as defined above); however, the flow is considered subsonic if $M_R < 1$, even if $M_T \geq 1$, due to a large swirl, for example. The flow is characterized in this manner, with reference to the radial Mach number, M_R , because a.) information cannot travel radially upstream (say from the middle of the MHD generator duct to the inlet of the generator duct) if the radial component, u , is greater than the speed of sound (except through the boundary layers themselves, and one presumes that due to the high degree of diffusion in the boundary layers information would not travel far upstream in the boundary layer before it was diffused to the wall or free stream); and b.) the generator mass flow rate depends only on the radial component of the velocity through

$$\dot{m} \equiv \int_{A_s} \rho \underline{u} \cdot \underline{n} dA = \int_{A_s} \rho u dA \quad (2-53)$$

where \underline{n} is the unit normal vector on the generator cross-sectional flow area, A_s . The second reason provided here indicates that choked flow conditions depend on the radial Mach number, M_R , and not the total Mach number, M_T .

Although the flow is characterized by the radial Mach number as explained above, it is the total Mach number that dictates the local static or thermodynamic properties because the local kinetic energy density ($\underline{u} \cdot \underline{u}/2$) is distributed among all the velocity components. The local stagnation temperature, \bar{T} , is given by

$$\bar{T} = T + \frac{\underline{u} \cdot \underline{u}}{2c_p} = T \left(1 + \frac{\gamma-1}{2} M_T^2 \right) \quad (2-54)$$

and the local stagnation pressure, \bar{P} , is given by

$$\bar{P} \equiv P \left[\frac{\bar{T}}{T} \right]^\Gamma = P \left[1 + \frac{\gamma-1}{2} M_T^2 \right]^\Gamma \quad (2-55)$$

(where $\Gamma = \gamma/(\gamma-1)$); i.e., the local stagnation temperature, \bar{T} , is reduced to the local static temperature, T , based on the total Mach number, M_T , rather than the radial Mach number, M_R .

The explicit method of MacCormack, to be discussed in Section 2.2.5, is viable for both subsonic and supersonic flows; therefore, the integration scheme does not require that the generator flow be supersonic, as for example would be the case had a stream-wise marching solution been used to solve the "parabolized" Navier-Stokes (PNS) equations (Anderson et al., 1984); however, the inlet and outlet boundary conditions do depend on the characteristics of the local flow field, and therefore, it is stated here that in this thesis, attention is restricted to flow fields in which the flow is supersonic from inlet to outlet, in the core region of the flow, outside of the boundary layers. The inlet and outlet conditions imposed on the supersonic, thin-layer, Navier-Stokes flows are synthesized from a number of

sources addressing computational fluid dynamics and papers dealing with supersonic fluid mechanics (Pullium, 1986; Pullium and Steger, 1980; Hasen, 1982; Roache, 1972; Peyret and Taylor, 1983; Anderson, 1970; Knight, 1981; Shih, 1990; and MacCormack, 1989). In the course of this work, experience was also gleaned by the author on proper inlet and outlet boundary conditions for both supersonic and subsonic flow fields by experimenting with a time-dependent marching quasi-one-dimensional (Q1D) flow solver developed, by the author, separate from this work. The time-dependent solver, which also uses the explicit method of MacCormack (1969), is used to obtain asymptotically approached steady-state solutions, of the time-dependent, Q1D MHD flow of a fissioning gas in both cylindrical (disk) and cartesian geometries. The overriding philosophy behind the supersonic flow inlet and outlet boundary conditions is based on the fact that in a supersonic flow field, information, traveling as nearly isentropic compression (sound) waves, cannot propagate upstream; therefore, downstream conditions do not influence upstream conditions. The inflow can therefore be fully specified with out regard to the downstream and the outflow conditions may be obtained through extrapolation of the neighboring upstream conditions.

Inflow boundary conditions. The characteristics of the supersonic flow at the entrance of the generator are such that the flow may be fully specified; this is accomplished by specifying the stagnation temperature (\bar{T}), stagnation pressure (\bar{P}), inlet radial Mach number ($M_{R,in}$) and swirl factor (S_m), a normalized inlet radial velocity profile ($f(z)$), profile of the tangent of the axial flow angle ($p = w/u$) of the inlet flow, and the inlet boundary layer thicknesses (δ_{in}). From these

specified values (\bar{T} , \bar{P} , $f(z)$, $M_{R,in}$, S_{in} , p_{in} , δ_{in}), all the primitive variables (ρ , u , v , w , $\bar{\epsilon}$) are calculated at the inlet; the inlet flow, therefore, is fully specified.

It is noted that for the case when the inlet flow is subsonic, the total temperature (\bar{T}), total pressure (\bar{P}), and the flow direction (determined by setting S and p) may be specified, however, the inlet velocity and static properties (or the mass flow rate) may not be specified. Instead, the entrance velocity (or system mass flow rate) must evolve as part of the overall fluid solution since it depends on the downstream conditions.

The flow is assumed to be either laminar or turbulent throughout the generator; either the turbulence modeling, discussed in Section 2.2.2, is employed or only the laminar properties are used. The choice of turbulent or laminar flow dictates the normalized velocity profile, $f(z)$, within the boundary layer region. If u_{in} is the inlet radial velocity corresponding to $M_{R,in}$, then the entrance velocity profiles are calculated using $u(z) = u_{in} f(z)$, $v(z) = S_{in} u(z)$, and $w(z) = p(z) u(z)$, where here the inlet swirl factor, S_{in} , has been assumed to be a constant (independent of the height, z) and where $p(z)$ is obtained by a linear interpolation between the tangents (Z_t/r_t) of the top and bottom walls. The normalized velocity profile, $f(z)$, has a value of one outside the boundary layer; within the boundary layer $f(z)$ depends on whether the flow is taken to be laminar or turbulent. In the core flow region, the static temperature distribution, $T(z)$, is calculated using the relationship given by Equation 2-54, where the stagnation temperature is assumed to be uniform in the core flow ($\bar{T}(z) = \bar{T}_{in}$), and given that the local total Mach number is specified by Equation 2-52. The static temperature distribution, $T(z)$, is

calculated in the upper and lower wall boundary layer regions using a formulation valid for both laminar and turbulent boundary layers in compressible flow (Schlichting, 1955)

$$T(z) = T_e \left\{ 1 + r \frac{\gamma - 1}{2} M_{T_e}^2 \left[1 - \frac{U(z)}{U_e} \right]^2 + \frac{T_w - T_{ad}}{T_e} \left[1 - \frac{U(z)}{U_e} \right] \right\} \quad (2-56)$$

where $U_e = (\underline{u} \cdot \underline{u})_e^{\frac{1}{2}}$ and

$$T_e = \frac{\bar{T}_{in}}{1 + \frac{\gamma - 1}{2} M_{T_e}^2} \quad (2-57)$$

The subscript "e" denotes conditions at the edge of boundary layer. T_{ad} is the adiabatic wall temperature defined by

$$T_{ad} \equiv T_e \left(1 + r \frac{\gamma - 1}{2} M_{T_e}^2 \right) \quad (2-58)$$

the r here is the recovery factor: for turbulent flows we let $r = Pr^{1/3}$ and for laminar flows, $r = Pr^{1/2}$ (see Schlichting, 1955; also Shapiro, 1953; and the summary by Kaye, 1954) where Pr is the laminar Prandtl number. Within the boundary layer region, the local stagnation temperature is calculated using Equation 2-54. The static pressure distribution, $P(z)$, is calculated outside the boundary layer by rearranging Equation 2-55, and assuming that the stagnation pressure is uniform ($\bar{P}(z) = \bar{P}_{in}$) in the core flow region; i.e.,

$$P(z) = \bar{P}_{in} \left(\frac{T(z)}{\bar{T}_{in}} \right)^{\Gamma} . \quad (2-59)$$

As mentioned, the normalized inlet radial velocity, $f(z)$, typically has a value of one outside of the boundary layer region. Within the boundary layer regions--that is adjacent to the upper and lower walls--the $f(z)$ depends on whether the flow is turbulent or laminar. For the case of laminar flow, within the boundary layer region the parabolic approximation--the incompressible, laminar, Couette flow solution--given by,

$$f(z) = \frac{2}{\delta} \left(z - \frac{z^2}{2\delta} \right) \quad (2-60)$$

is used; this approximation provides excellent agreement with the exact Blasius solution to equilibrium laminar incompressible flow over a flat plate at all "running" Reynolds numbers ($Re_t = \rho U l / \mu$) (White, 1979). As a point of interest, the effects of compressibility on the laminar flow velocity profile of flow over a flat plate have been shown to be significant by the analytical work of Chapman and Rubesin (1949). They showed that at low Mach numbers, the Blasius solution for incompressible flow provides an excellent prediction of the compressible flow solution; however, as the local Mach number increases--Chapman and Rubesin provided results for a Mach 3 flow--the boundary layer thickness increases significantly. The large increase in the boundary layer thickness with Mach number is attributed to the increase in the specific volume of the fluid due to the increase in temperature near the wall for the high Mach number flows (Schlichting, 1955). This effect may be expected to be less dramatic in this work

because the wall is cool relative to the flow field so that the increase in temperature due to viscous heating near the wall is less pronounced than say for an adiabatic wall. The inlet boundary layer thickness is set to what is expected to be a reasonable value. The parabolic velocity profile, given by Equation 2-60, with the specified inlet boundary layer height is used to start the laminar flow problem, rather than resorting to the detailed analytical solution of Chapman and Rubesin (1949).

For the case of turbulent flow, following the discussion by Shapiro (1954), the entrance boundary layer regions (next to the upper and lower walls) are each divided into a laminar sublayer (adjacent to the wall) and a turbulent layer (between the laminar sublayer and the edge of the boundary layer). Figure 2.4 illustrates an example inlet velocity profile for the lower wall.

The universal velocity profile for the laminar sublayer

$$u^+ = z^+ \quad (2-61)$$

is assumed throughout the sublayer ($0 \leq z^+ \leq z_i^+$), where z_i^+ is the location of the laminar sublayer/turbulent layer interface in law-of-the-wall coordinates.

Here, $u^+ = u/u_r$, and $z^+ = z u_r \rho_w / \mu_w$, where u_r is the characteristic velocity of turbulence ($= \tau_w / \rho_w$)^{1/2}, ρ_w is the fluid density at the wall, and μ_w is the laminar viscosity at the wall. Equation 2-61 is equivalent to the statement that the shear stress, τ , is constant throughout the laminar sublayer, and is equal to the wall shear stress, τ_w .

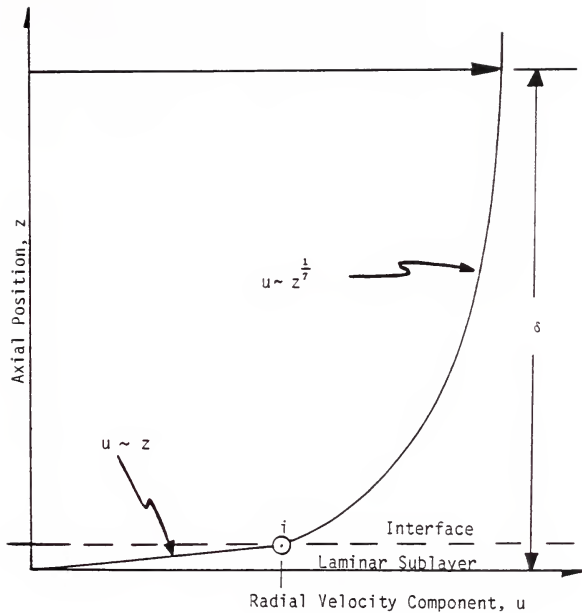


Figure 2.4 Radial Velocity Profile in Turbulent Boundary Layer showing the Laminar Sublayer and Turbulent Regions (after Shapiro, 1954).

In the turbulent region of the boundary layer, the radial velocity is predicted using the seventh-root power law, given in the law-of-the-wall coordinates as

$$\frac{u^+}{u_e^+} = \left[\frac{z^+}{\delta^+} \right]^{\frac{1}{7}} \quad (2-62)$$

where δ^+ is the boundary layer thickness ($= \delta u_r \rho_w / \mu_w$) and u_e^+ is the magnitude of the radial velocity at the edge of the boundary layer, normalized by the friction velocity, u_r . The interface position z_i^+ is found by equating the magnitude u^+ in Equations 2-61 and 2-62:

$$\frac{z_i^+}{\delta^+} = \left[\frac{u_e^+}{\delta^+} \right]^{\frac{7}{2}} = \left[\frac{u_e \mu_w}{\delta u_r^2 \rho_w} \right]^{\frac{7}{2}} \quad (2-63)$$

(Note that the slope of $u^+(z)$ is discontinuous across the interface at z_i^+ .)

The friction velocity, u_r , is related to the wall shear stress, τ_w , and the skin-friction coefficient, c_f by

$$u_r = \left[\frac{\tau_w}{\rho_w} \right]^{\frac{1}{2}} = \left[\frac{1}{2} \left(\frac{\rho_e}{\rho_w} \right) U_e^2 c_f \right]^{\frac{1}{2}} \quad (2-64)$$

where ρ_e is the density and U_e is the speed of the fluid at the edge of the boundary layer. For a given flow condition, then, $u_r \sim c_f^{1/2}$; τ_w (or c_f) may be calculated if the velocity profile is known in advance by the definition of the wall shear stress (cf. the turbulence modeling in Section 2.2.2); however, here the purpose is to predict (specify) the velocity profile. Therefore, in this work, a

correlation is used to obtain the skin-friction coefficient, c_f , and therefore the friction velocity, u_* , avoiding a sophisticated iterative solution for the inlet velocity profile. (As encountered in the laminar inlet conditions above, the philosophy in setting the inlet profiles is simply to start the flow problem in a realistic, yet simply implemented manner.)

Classical correlations for compressible turbulent flow are based on modifications, accounting for the compressibility of the fluid due to high Mach numbers, to von Karman's skin-friction correlation for incompressible turbulent boundary layer flow along a flat plate; these correlations--see Schlichting's (1955) discussion on correlations for compressible turbulent flow developed by von Karman, Van Driest, and Wilson--have the form

$$\frac{a_1}{\sqrt{c_f}} = \log_{10}(a_2 c_f l) \quad (2-65)$$

where a_1 and a_2 are functions dependent on the local fluid properties and Mach number at the boundary layer edge and the recovery factor, and where l is the distance traveled along the flat plate (i.e., the distance in the running Reynolds number, $Re_l = \rho_e U_e l / \mu_e$). In this study, the boundary layer length, l , is a backward extrapolated distance obtained by rearranging the estimate that comes out of von Karman's analysis of turbulent incompressible boundary layer flows ($\delta/l \approx 0.16 / Re_l^{1/7}$) (White, 1979). Noting that the classical correlations of the form of Equation 2-65 are transcendental, this study uses instead the correlation, developed originally for low speed flows by Falkner and extended to high speed (compressible) flows by Tucker (see Shapiro, 1954), given by

$$\frac{1}{2} c_{f,am} = \frac{\tau_w}{\rho_{am} U_e^2} = \frac{0.0131}{Re_{l,am}^{\frac{1}{4}}} \quad (2-66)$$

where "am" refers to fluid properties corresponding to the arithmetic mean (am) temperature between the wall temperature (T_w) and the temperature at the edge of the boundary layer ($T(z = \delta)$). Predictions from the Falkner/Tucker correlation, which provides an explicit expression for the friction velocity (by using Equation 2-64) were compared by the author against results from the theory developed by Wilson (a correlation of the form of Equation 2-65) based on theoretical and experimental investigations of turbulent flows over insulated flat plates at supersonic speeds (Wilson, 1950). For the inlet flow conditions encountered in this thesis work, the predicted friction velocities from the Falkner/Tucker correlation (Equation 2-66) and the Wilson correlation (Wilson, 1950) agree within 13% over the wide range of examined boundary layer lengths ($0.01 \text{ m} \leq l \leq 5 \text{ m}$). Rearranging the von Karman estimate of the boundary layer thickness (see White, 1979) provides

$$l = \left[\frac{\delta}{0.16} \right]^{\frac{7}{4}} \left[\frac{\rho_e U_e}{\mu_e} \right]^{\frac{1}{4}} \quad (2-67)$$

In the spirit of the Falkner/Tucker correlation, one might let $\rho_e \rightarrow \rho_{am}$ and $\mu_e \rightarrow \mu_{am}$ in the estimate for the boundary length corresponding to the specified boundary layer thickness, δ , provided by Equation 2-67 above. For the inlet conditions in this thesis, using the arithmetic mean properties rather than the properties at the edge of the boundary layer had little affect on the estimated

boundary length, l , and ultimately in the laminar sublayer/turbulent region interface, z_i^+ .

Given an inlet flow scenario, typical of the flows analyzed in the thesis, it was found that: a.) the estimated boundary layer length, l , is on the order of a few centimeters; b.) the friction velocity from the Falkner/Tucker correlation (Equation 2.66) is near 80 - 90 m/s (compared to 90 - 95 m/s predicted by the Wilson correlation (Wilson, 1950)); c.) the laminar sublayer constitutes 5-6% of the total boundary layer region; and d.) the interface of the sublayer and the turbulent layer occurs at $z^+ = u^+(z_i) \approx 10-12$. Note that experimental data for turbulent incompressible flow over a flat plate indicates that $z^+ = u^+(z_i) \approx 11.5$ (Shapiro, 1954, referring to von Karman, 1931).

In summary then, for the case of turbulent flow, the normalized inlet radial velocity, $f(z)$, is set to unity outside of the upper and lower wall boundary layers, and, within the boundary layer regions,

$$f(\hat{z}) = \begin{cases} \frac{u}{u_e} = \frac{\hat{z} u_r^2 \rho_w}{u_e \mu_w} & \text{for } 0 \leq \hat{z} \leq z_i \\ \frac{u}{u_e} = \left(\frac{\hat{z}}{\delta} \right)^{1/7} & \text{for } z_i \leq \hat{z} \leq \delta \end{cases} \quad (2-68)$$

where \hat{z} is the appropriate distance for the upper or lower wall, and z_i is the position of the laminar sublayer/turbulent region interface given by Equation 2-63.

The static pressure is assumed uniform throughout the inlet boundary layers (i.e., the boundary layer approximation that $\partial P / \partial z = 0$ in the boundary

layer is applied); i.e., $P(z) = P_e$ within the boundary layer, where P_e is the static pressure at the edge of the boundary layer.

Finally, at each point in the inlet plane, the specific total energy, \bar{e} , and the specific stagnation enthalpy, \bar{h} , are calculated using Equations 2-15 and 2-16 (see Table 2.1 of Section 2.1), respectively.

Outflow boundary conditions. The characteristics of the supersonic flow at the exit of the generator allow the generator outflow conditions to be extrapolated from the upstream conditions, as discussed earlier. Information cannot travel upstream in a supersonic flow, and thus the flow at some arbitrary radial position cannot be affected by the downstream exit conditions; therefore, to close the fluid problem, the exit conditions are simply extrapolated from conditions immediately upstream of the exit plane. If "g" represents any of the primitive fluid variables (ρ , u , v , w , \bar{e}) then, for any line of constant- η (indicated here by the index j)

$$g_{IMAX,j}^n = 3 g_{IMAX-1,j}^n - 3 g_{IMAX-2,j}^n + g_{IMAX-3,j}^n \quad (2-69)$$

A four point (second-order accurate) backward interpolation (after Hasen, 1982), where IMAX corresponds to the total number of grid lines (of constant- ξ) is used to resolve the radial direction, as shown in Figure 2.3.

Wall boundary conditions. The no-slip condition requires that $\underline{u} = \underline{u}_{WALL}$ at any solid boundary, where \underline{u}_{WALL} is the velocity of that solid boundary. In this study, the upper and lower generator walls are stationary, so that $u = v = w = 0$ at any wall. The wall temperature is a specified, arbitrary function (Dirichlet condition); for the calculations presented in this thesis, the wall temperatures are

uniform along the length of the wall. Alternatively, a distribution of the local heat transfer rates along the walls could have been specified leading to a Neumann boundary condition. The static pressure at the wall is calculated by requiring that the derivative of the static pressure normal to the wall be zero (as discussed by Peyret and Taylor (1983) and used by others (Hasen, 1982; Knight, 1981; and MacCormack, 1989): i.e.,

$$P_n = \frac{\partial P}{\partial n} = 0 \quad (2-70)$$

where "n" dictates that the derivative is taken with respect to distance normal to the wall. Using the techniques provided by Thompson et al. (1985), it is found that the derivative of the pressure with respect to the normal along a line of constant- η is given by

$$\left(\frac{\partial P}{\partial n} \right)^\eta = \frac{\{ (\xi_r \eta_r + \xi_z \eta_z) P_\xi + (\eta_r^2 + \eta_z^2) P_\eta \}}{(\eta_r^2 + \eta_z^2)} \quad (2-71)$$

so that the boundary condition of the static pressure (2-70) requires that

$$P_\eta^{n+1} = - \left[\frac{\xi_r \eta_r + \xi_z \eta_z}{\eta_r^2 + \eta_z^2} \right] P_\xi^n = - \zeta P_\xi^n \quad (2-72)$$

Given that the metrics are known, the pressure at the wall is calculated using the first-order approximation

$$P_{i,1}^{n+1} = P_{i,2}^n + \Delta\eta \left[\zeta_{i,1} \frac{P_{i+1,1}^n - P_{i-1,1}^n}{2\Delta\xi} \right] \quad (2-73)$$

Equation 2-73 is solved simultaneously (for $i = 2, 3, \dots, \text{IMAX}-1$) using the

Thomas Algorithm at each time step using the most recently available values of $P_{i,2}^n$; i.e., the boundary condition is explicit in time. It is noted here that a two-point, first-order estimate to P_n is employed rather than a more accurate (e.g., three or four-point) approximation; by experience gleaned in this work, and in the CFD community (e.g., MacCormack, 1989), and by discussion (Shih, 1990), it was decided to use the two-point approximation above. Indeed, it is not beyond convention to simply allow $P_{i,1}^{n+1} = P_{i,2}^n$, assuming that the line of constant- ξ intersecting the point (i,1) is nearly orthogonal to the wall. The justification for using the low (first) order finite-difference representation is that, since the boundary condition is explicit in time, the pressure at the wall is always back calculated based on the current pressure at the nearest neighbors; if a higher order one-sided difference formula is used, essentially what is being required is that information travel, in one time-step, from deeper (farther from the wall) within the flow field to the wall (or vice-versa, i.e., from the wall to the flow field) than is physically possible; this is analogous to not satisfying the Courant-Friedrich-Lewy (CFL) condition. The higher order formulations therefore lead to instabilities in the overall solution method, as indeed rediscovered in this work.

The fluid density, ρ , is calculated given the wall temperature and pressure by using the thermal equation-of-state (Equation 2-10 of Table 2.1 of Section 2.1). The specific total energy (\bar{e}) at the wall is equal to the specific internal energy (e) at the wall, which is related to the local wall temperature (T_w) through the caloric equation-of-state (Equation 2-11).

2.2.5 Fluid Finite-Difference Method

The governing equations of fluid mechanics discussed in Section 2.2.1 may be written as

$$\frac{\partial \underline{A}}{\partial \tau} + \frac{\partial \underline{B}}{\partial \xi} + \frac{\partial \underline{C}}{\partial \eta} = \underline{D} \quad (2-74)$$

where the \underline{A} , \underline{B} , \underline{C} , and \underline{D} vectors are expanded in Table 2.3 of Section 2.2.1. The time-dependent governing equations are integrated using MacCormack's explicit method (MacCormack, 1969), here extended to account for the source vector, \underline{D} . The explicit method of MacCormack is a widely used, well recognized method for solving the Navier-Stokes equations; the method is discussed in detail in many textbooks on computational fluid mechanics (see for example, the excellent CFD reference, Anderson et al., 1984). The MacCormack explicit method is an explicit, predictor-corrector, Lax-Wendroff-type scheme. The method is second-order accurate in both space and time ($O(\Delta x^2, \Delta t^2)$) and is therefore suitable for accurately predicting the time-dependent behavior of the fluid field. It is noted that the MacCormack's method is used in this thesis because it is a well established and widely accepted method in the CFD community and because, as an explicit method, implementation of the method (in a computer code) is a straight-forward process.

The predictor and corrector steps of the MacCormack method applied to Equation 2-74 are

Predictor:

$$\underline{A}_{ij}^* = \underline{A}_{ij}^n - \Delta\tau \left[\underline{B}_{i+1,j}^n - \underline{B}_{ij}^n + \underline{C}_{i,j+1}^n - \underline{C}_{ij}^n - \underline{D}_{ij}^n \right] \quad (2-75)$$

Corrector:

$$\underline{A}_{ij}^{n+1} = \frac{1}{2} \left(\underline{A}_{ij}^n + \underline{A}_{ij}^* - \Delta\tau \left[\underline{B}_{ij}^* - \underline{B}_{i-1,j}^* + \underline{C}_{ij}^* - \underline{C}_{i,j-1}^* - \underline{D}_{ij}^* \right] \right) \quad (2-76)$$

where the finite-difference space step sizes ($\Delta\xi$ and $\Delta\eta$) are set to unity and where "n" indicates the current time step values (at time τ), "*" indicates intermediate step values, and "n+1" indicates a value at the new time step (at time $\tau + \Delta\tau$). As each time step (predictor and corrector) is completed, the vector \underline{A} is decomposed into the primitive fluid variables ρ , u , v , w , and $\bar{\epsilon}$, and the new vectors \underline{B} , \underline{C} , and \underline{D} are calculated. As in the case of Equations 2-75 and 2-76, both space derivatives ($\partial/\partial\xi$ and $\partial/\partial\eta$) may be calculated with a forward differencing in the predictor step and then with backward differencing in the corrector step; however, the second-order accuracy is maintained regardless of the order of direction of the differencing, as long as in the corrector step the space derivatives are differenced in the direction opposite to that used in the predictor step. It is customary to sequentially alternate the forward and backward differencing between the predictor and corrector steps as well as between the spatial derivatives to avoid introducing any bias in the solution due to one-sided differencing (Anderson et al., 1984). The sequentially alternating differencing scheme is accommodated in the following generalized form of Equations 2-75 and 2-76:

Predictor:

$$\underline{A}_{ij}^* = \underline{A}_{ij}^n - \Delta\tau \left[\underline{B}_{i+a,j}^n - \underline{B}_{i-b,j}^n + \underline{C}_{i,j+c}^n - \underline{C}_{i,j-d}^n - \underline{D}_{ij}^n \right] \quad (2-77)$$

Corrector:

$$\underline{A}_{ij}^{n+1} = \frac{1}{2} \left(\underline{A}_{ij}^n + \underline{A}_{ij}^* - \Delta\tau \left[\underline{B}_{i+b,j}^* - \underline{B}_{i-a,j}^* + \underline{C}_{i,j+d}^* - \underline{C}_{i,j-c}^* - \underline{D}_{ij}^* \right] \right) \quad (2-78)$$

where a, b, c, and d are indices that have values of either 0 or 1--depending on which of the four possible difference combinations (variants) in the sequence--as delineated in Table 2.5--is currently being employed. The sequence is realized by successively integrating the governing equations according to the differencing schemes 1, 2, 3, and 4 shown in Table 2.5., in that order.

In order to maintain second-order accuracy, the viscous derivatives--here, under the thin-layer approximation found only in the η -derivatives--must be differenced correctly. For example, on a forward difference of the η -derivative, of the vector \underline{C} , the η -derivatives within the vector \underline{C} (see Table 2.3) must be backward differenced, thus effecting a three-point central difference, second-order accurate representation. If the \underline{C} -vector contained ξ -derivatives (not found here under the thin-layer approximation), the ξ -derivatives would be central differenced in ξ . Note that the divergence-form into which the governing equations are cast avoids ambiguity as to where the fluid transport properties (μ and k) are calculated: the transport properties are calculated at the finite-difference points (as opposed to halfway between the points as, for example, in the Lax-Wendroff method), for example, at $i,j+1$ and i,j on a forward difference of $\partial/\partial\eta$. The correct differencing methodology is provided by MacCormack in a

Table 2.5 Explicit Method of MacCormack with Generalized Finite-Differencing Sequence

Fluid Equations

$$\frac{\partial A}{\partial \tau} + \frac{\partial B}{\partial \xi} + \frac{\partial C}{\partial \eta} = D$$

Predictor Step

$$\underline{A}^*_{ij} = \underline{A}^n_{ij} - \Delta\tau_{ij} \left[\underline{B}^n_{i+a,j} - \underline{B}^n_{i-b,j} + \underline{C}^n_{i,j+c} - \underline{C}^n_{i,j-d} - \underline{D}^n_{ij} \right]$$

Corrector Step

$$\underline{A}^{n+1}_{ij} = \frac{1}{2} \left(\underline{A}^n_{ij} + \underline{A}^*_{ij} - \Delta\tau_{ij} \left[\underline{B}^*_{i+b,j} - \underline{B}^*_{i-a,j} + \underline{C}^*_{i,j+d} - \underline{C}^*_{i,j-c} - \underline{D}^*_{ij} \right] \right)$$

Finite-Difference Index Sequence

Variant	INDICES				PREDICTOR		CORRECTOR	
	a	b	c	d	$\partial/\partial\xi$	$\partial/\partial\eta$	$\partial/\partial\xi$	$\partial/\partial\eta$
1	1	0	1	0	F*	F	B	B
2	0	1	0	1	B	B	F	F
3	1	0	0	1	F	B	B	F
4	0	1	1	0	B	F	F	B

* F - indicates a forward difference

B - indicates a backward difference

later paper (MacCormack, 1985) and is different than that provided in his early paper (MacCormack, 1969). Central differences are used to represent the viscous derivatives (first-order) in the source vector \underline{D} .

Time-step criterion. The stability of the explicit MacCormack method restricts the time-step size, $\Delta\tau$, according to the Courant-Friedrichs-Lewy (CFL) stability criteria. MacCormack (1985) suggests that the maximum allowable time-step be calculated locally using (here in our geometry)

$$\Delta\tau = \sigma \Delta\tau^{CFL} = \sigma \left\{ \frac{|u|}{\Delta r} + \frac{|w|}{\Delta z} + a \left[\frac{1}{\Delta r^2} + \frac{1}{\Delta z^2} \right]^{\frac{1}{2}} + 2\nu \left[\frac{1}{\Delta r^2} + \frac{1}{\Delta z^2} \right] \right\}^{-1} \quad (2-79)$$

where $\nu = (1/\rho) \max\{\mu, (\lambda + 2\mu), k/c, \}$, a is the local speed of sound, and σ is a safety factor. Note that Equation 2-79 simply requires (conservatively) that, locally, information does not travel further than from one grid point to another, within one time-step, either by convection (terms 1 and 2), diffusion (e.g., conduction, term 4), or by compression waves (at the speed of sound, term 2). Because Equation 2-79 provides a conservative estimate of the local maximum time step (MacCormack, 1985), the safety factor, σ , may be set to one for the calculations, and stability will be insured. The high degree of grid refinement necessary to resolve the turbulent boundary layer near the walls in the high Reynolds number flows encountered in this thesis--typically Δz_{\min} near the wall is $O 1 \times 10^{-5}$ m--leads to CFL time-steps, $\Delta\tau^{CFL} \approx \Delta z_{\min}/a = O 10^{-8} - 10^{-9}$ s, where a is the local speed of sound evaluated at a temperature near that of the wall. If

this minimum time step criteria were used throughout the flow, then clearly the overall computation time to a converged solution might prove prohibitive; e.g., using the numbers here, $O 10^5$ to 10^6 time-steps are required to simulate one millisecond of real-time which is near the fluid passage time through the duct.

Li suggested that, for the case where the asymptotically approached steady-state solution is the object of the calculation (and not a time-dependent simulation), local time-stepping be used (Li, 1973 and see brief discussion about local time-stepping by MacCormack, 1984). In this scenario, the time-step is determined locally ($\Delta\tau \rightarrow \Delta\tau_{i,j} = \sigma \Delta\tau_{i,j}^{CFL}$) using the same philosophy described above, and the solution evolves on a warped time-surface into the asymptotic steady-state solution. In this work, the local maximum $\Delta\tau_{i,j}^{CFL}$ is calculated using Equation 2-79 with the added restriction that the $\Delta r_{i,j}$ and $\Delta z_{i,j}$ employed are the local minima; i.e., at some arbitrary position (i,j), $\Delta r_{i,j} = \min\{ |R_{i+1,j} - R_{i,j}|, |R_{i-1,j} - R_{i,j}| \}$, for example. The overall approach results in a conservative estimate of $\Delta\tau_{i,j}^{CFL}$ so that the safety factor, σ , may be set to unity while maintaining stability. It is noted that in the case where variable $\Delta\tau_{i,j}$ are used, the time-dependent part of the solution--from the initial conditions to the final steady-state--is not meaningful; however, if the steady-state solution is desired, then the local time-stepping is suggested.

The residuals (e.g., $|A_1^{n+1} - A_1^n| / |A_1^1 - A_1^0|$) of predictor-corrector methods, in which the difference operators are alternated within a total time-step (e.g., the MacCormack method), converge to limit cycles about their truncation

error rather than to a machine zero as in the case of methods that use the same difference operator at each time step (e.g., Beam and Warming method) (MacCormack, 1989). The limit cycle was indeed encountered in this thesis work; the magnitudes of the residuals (or the average least-squared (L2-norm) errors from iteration to iteration) of the primitive variables were found to be dependent on σ ; although the method is stable and does converge to solution with $\sigma = 1$, the average least-squared error was typically on the order of 10^{-5} rather than the 10^{-6} that is the desired convergence level in this work. The desired convergence levels ($O10^{-6}$) are achieved in the calculations for this thesis by using a safety factor, $\sigma = 0.5$.

2.3 Electromagnetics

Under the modeling assumptions discussed in Section 2.1.1, the governing equations of electromagnetics--presented in full form in Equations 2-4 to 2-6 of Table 2.1--may be written as

$$\nabla \cdot \underline{J} = 0 \quad (2-80)$$

$$\nabla \times \underline{E} = 0 \quad (2-81)$$

and

$$\underline{J} + \mu_e \underline{J} \times \underline{B} = \sigma_e (\underline{u} \times \underline{B} + \underline{E}) \quad (2-82)$$

The notation $\underline{J} = (J_r, J_\theta, J_z)$, $\underline{E} = (E_r, E_\theta, E_z)$, $\underline{u} = (u, v, w)$, and $\underline{B} = (0, 0, B_z)$ is used in this development; the electron transport properties σ_e and μ_e are discussed in Section 2.4.

After Roseman (1982), the stream function, φ , is defined such that

$$J_r = \frac{1}{r} \frac{\partial \varphi}{\partial z} \quad (2-83)$$

and

$$J_z = -\frac{1}{r} \frac{\partial \varphi}{\partial r} . \quad (2-84)$$

Relating the radial (J_r) and axial (J_z) current density components to the stream function, φ , in this manner assures that current continuity expressed in Equation 2-80, viz.

$$\frac{\partial}{\partial r}(rJ_r) + \frac{\partial}{\partial \theta}(J_\theta) + \frac{\partial}{\partial z}(rJ_z) = 0 \quad (2-85)$$

is satisfied, given the tangential-symmetry imposed earlier (see Section 2.1.1).

With tangential-symmetry, Equation 2-81 requires that

$$E_\theta(\underline{r}) = E_\theta(r) = \frac{\text{Constant}}{r} . \quad (2-86)$$

At both the anode and the cathode E_θ is necessarily zero--that is the electrodes are treated as perfect conductors ($\sigma_e \rightarrow \infty$)--by design. Therefore, it may be concluded that $E_\theta(\underline{r}) = E_\theta(r) = 0$ within the MHD generator active volume. The electric field strength, \underline{E} , is therefore expressible as $\underline{E} = (E_r, 0, E_z)$, where the radial (E_r) and the axial (E_z) components are related, again through Equation 2-81, by

$$\frac{\partial E_r}{\partial z} = \frac{\partial E_z}{\partial r} \quad (2-87)$$

Resolving the generalized Ohm's law, Equation 2-82, into electric field strength components provides

$$E_r = \eta_e (1 + \beta_e^2) J_r - (\beta_e u + v) B_z \quad (2-88)$$

and

$$E_z = \eta_e J_z \quad (2-89)$$

where $\beta_e (\equiv \mu_e B_z)$ is the electron Hall Parameter and $\eta_e (\equiv 1/\sigma_e)$ is the electrical resistivity. Using Equations 2-83 and 2-84 with Equations 2-88 and 2-89, and substituting into Equation 2-87, it is found that

$$\frac{\partial}{\partial r} \left(\alpha_1 \frac{\partial \varphi}{\partial r} \right) + \frac{\partial}{\partial z} \left(\alpha_2 \frac{\partial \varphi}{\partial z} \right) = \frac{\partial S}{\partial z} \quad (2-90)$$

where $\alpha_1 = \eta_e$, $\alpha_2 = \alpha_1 (1 + \beta_e^2)$, and $S = (\beta_e u + v) B_z$. The governing equations of electromagnetics are written, therefore, as a single Poisson-type equation with stream function, φ , as the dependent variable; α_1 and α_2 depend only on the local plasma properties and the applied magnetic induction; the source term, S , is a function of the local velocity components, the electron mobility, and the applied magnetic induction. (Equation 2-90 is analogous to the General Heat Conduction equation for a medium with anisotropic (directionally dependent) thermal conductivity in which internal heat is generated.)

2.3.1 Transformed Equations

Equation 2-90 is transformed into the same generalized curvilinear boundary-fitted coordinate system (ξ, η) discussed in Section 2.2.1. The transformed equation may be written as

$$\frac{\partial \hat{A}}{\partial \xi} + \frac{\partial \hat{B}}{\partial \eta} = \frac{\partial C'}{\partial \xi} + \frac{\partial D'}{\partial \eta} \quad (2-91)$$

as shown in Table 2.6. Note that Equation 2-91 is simply a compact form of a Poisson-type equation as \hat{A} and \hat{B} each contain terms containing derivatives with respect to both ξ and η ; C' and D' ; are source terms. Equation 2-91 is elliptic, so that conditions on the dependent variable, φ , must be specified on all boundaries.

2.3.2 Electromagnetics Boundary Conditions

The electromagnetic solution is obtained for the problem space shown in the schematic diagram of the MHD generator in Figure 2.5. The inlet (upstream) and outlet (downstream) boundaries are artificial surfaces, taken to coincide with the inlet and outlet boundaries of the fluid problem. The inlet surface is set, therefore, at some arbitrary distance upstream of the anode; similarly, the outlet surface is placed at some arbitrary distance downstream of the cathode. The generator lofting is determined by the top insulated duct wall. The bottom wall is composed of the anode and cathode surfaces and the insulated wall surfaces as shown in Figure 2.5. Therefore, the active region of the MHD generator is bounded by the upper and lower walls and the imaginary inlet and outlet boundary surfaces.

Table 2.6 Transformed MHD Electromagnetics Equations in Boundary-Fitted Curvilinear Coordinate System (ξ, η)

$$\frac{\partial \hat{A}}{\partial \xi} + \frac{\partial \hat{B}}{\partial \eta} = \frac{\partial C'}{\partial \xi} + \frac{\partial D'}{\partial \eta}$$

where

$$\hat{A} = \alpha_1 \xi_r A' + \alpha_2 \xi_z B'$$

$$\hat{B} = \alpha_1 \eta_r A' + \alpha_2 \eta_z B'$$

with

$$A' = \frac{\partial}{\partial \xi}(\sqrt{g} \xi_r \varphi) + \frac{\partial}{\partial \eta}(\sqrt{g} \eta_r \varphi)$$

$$B' = \frac{\partial}{\partial \xi}(\sqrt{g} \xi_z \varphi) + \frac{\partial}{\partial \eta}(\sqrt{g} \eta_z \varphi)$$

$$C' = \sqrt{g} \xi_z S$$

$$D' = \sqrt{g} \eta_z S$$

and

$$\alpha_1 = \eta_e = \frac{1}{\sigma_e}$$

$$\alpha_2 = \frac{1}{\sigma_1} = \frac{(1 + \beta_e^2)}{\sigma_e}$$

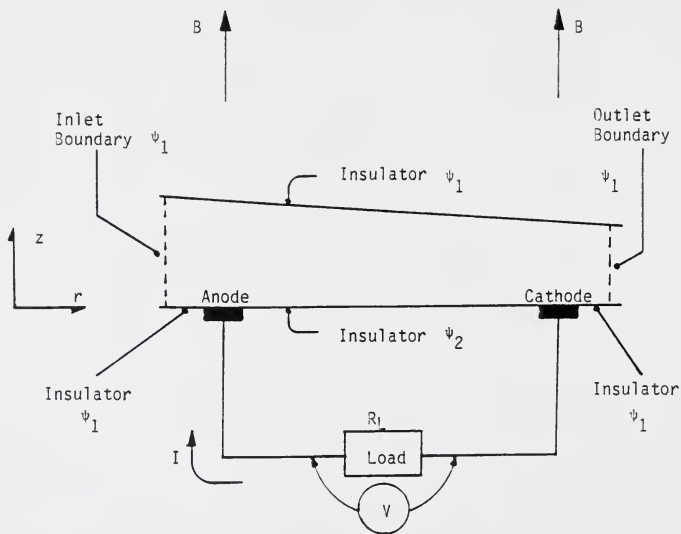


Figure 2.5 Schematic Diagram of Electromagnetics Solver Problem Space.

Insulator surfaces. Along any insulator surface, current continuity requires that $\underline{J} \cdot \underline{n} = 0$, or that the current density component normal to the wall be zero. This condition is satisfied by requiring that stream function, φ , remain constant ($\varphi_{\xi} = 0$) along the insulator wall surfaces (i.e., the lines of constant- η). For example, on the top insulator wall the stream function is set to some arbitrary value, φ_1 , uniform along the wall. Similarly, on the insulated surface between the two electrodes, the stream function is set to the value φ_2 , again requiring that $\underline{J} \cdot \underline{n} = 0$.

Electrode surfaces. The lower wall, composed of both the electrode surfaces and the insulator surfaces upstream, downstream, and between the electrode is required to be flat (i.e., $r_r = 0$ and $z_{\xi} = 0$ along the lower wall). The electrodes are assumed to be perfect conductors ($\sigma_e \rightarrow \infty$) and therefore can sustain no electric field along the surface: i.e., at the electrode surfaces $E_r = 0$. Because of the no-slip fluid condition at the wall, it is apparent considering Equation 2-101 that the radial current density $J_r = 0$ at the electrode surfaces. This condition is enforced by setting $\partial\varphi/\partial\eta = 0$ along the electrode surface.

Inlet and outlet boundary surfaces. The inlet and outlet boundary surfaces coincide with the inlet and outlet surfaces of the fluid problem discussed earlier. The position of the inlet surfaces is arbitrary except that, in this work the surfaces are at least one electrode width away from the electrodes; this gives the stream lines a chance to relax up and downstream from the electrodes. It is assumed that current does not enter (or leave) the active MHD generator region in a manner other than through the electrode surfaces. Therefore, at the inlet and

outlet surfaces, $J_r = 0$ is enforced by requiring that the stream function, φ , remain constant ($\varphi = \varphi_1$) along both the imaginary inlet and outlet surface.

Note therefore that the active region of the MHD generator is bounded by surfaces on which the stream function is a constant $\varphi = \varphi_1$, except for the electrode surfaces where $\partial\varphi/\partial\eta = 0$ is required, and the insulator region between the electrodes in which the stream function has a constant value of $\varphi = \varphi_2$. φ_1 is related to φ_2 through current continuity across the electrodes. For example, if current continuity (Equation 2-80) is applied at the anode surface (see Figure 2.5), then

$$I = \int_{A_E} \underline{J} \cdot \underline{n} dA = \int_{A_E} J_z dA = 2\pi(\varphi_1 - \varphi_2) \quad (2-92)$$

where Equation 2-84, relating the stream function, φ , to the axial current density component, J_z , has been used; A_E is the anode area and I is the generator load current that enters the generator through the anode. The load current is held constant during the solution, that is, in effect the load current is a boundary condition for the solution for $\varphi(\underline{r})$. Typically, φ_2 is set to zero, so that $\varphi_1 = I/2\pi$. Therefore, given that the load current is set for a given solution for the stream function distribution, φ_1 and φ_2 are determined and the boundary conditions for Equation 2-91 are set.

2.3.3 Electromagnetics Finite-Difference Method

The governing equation of the electromagnetics, Equation 2-91 (expanded in Table 2.6) is solved using an alternating-direction-implicit (ADI) finite-difference method. As explained in the historical perspective on computational

fluid mechanics and heat transfer presented in the text by Anderson et al. (1984), the ADI schemes are a family of finite-difference methods developed by Peaceman and Rachford (1955) and Douglas and Rachford (1956), for solving elliptic and parabolic equations. The ADI method is accomplished by marching (or sweeping) in alternating direction (e.g., in the ξ direction, then in η direction) through the computational space. In a certain sweep direction (e.g., ξ -sweep), the finite-difference representation of the governing equation is solved through simultaneous solution for the stream function, along one coordinate line (e.g., a line of constant- η); all dependent variable values off that line are assumed known--that is the latest available values are used--during the simultaneous solution. The ADI scheme is shown schematically in Figure 2.6.

Second-order accurate central difference approximations to the partial derivatives shown in Table 2.6 are employed. Note that Equation 2-91 (see Table 2.6) has been cast into strong conservation-law form. The transport property-like terms (e.g., $\alpha_1 \xi_r$ or $\alpha_2 \xi_z$) are determined at mid-points (e.g., at $i + \frac{1}{2}, j$ or $i, j - \frac{1}{2}$). For example,

$$(\xi_r \alpha_1)_{i+\frac{1}{2},j} \equiv \frac{1}{2} \{ (\xi_r \alpha_1)_{i+1,j} + (\xi_r \alpha_1)_{i,j} \} \quad (2-93)$$

Column sweep. During a column sweep (ξ -sweep), or a marching in the radial direction, the governing equation is solved subsequently at lines of constant- ξ , i.e., at $i = 2, 3, \dots, \text{IMAX}-1$. At each position, i ,

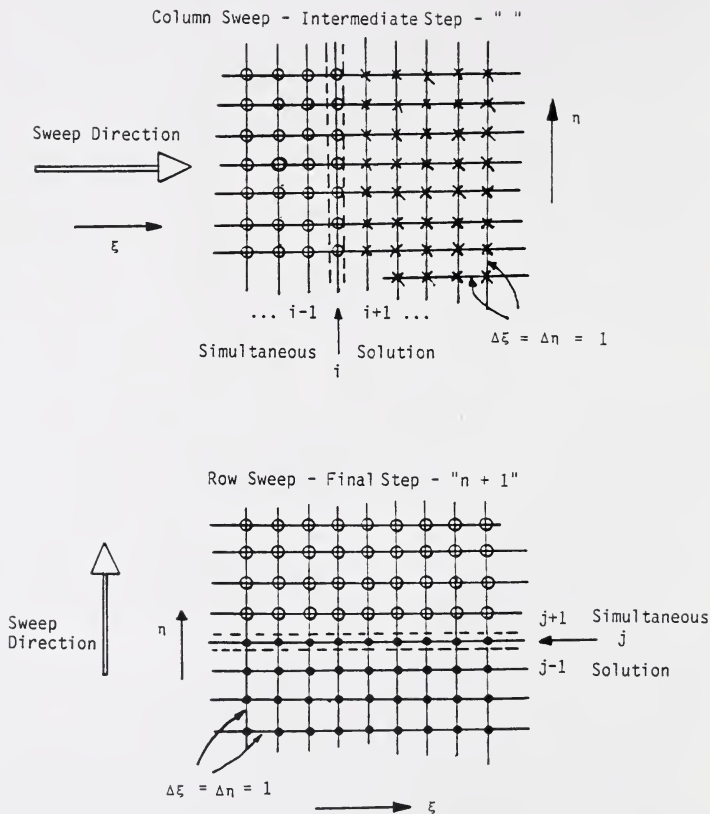


Figure 2.6 Schematic Diagram showing the Alternating-Direction-Implicit (ADI) Solution Scheme.

$$C_1 \varphi_{i,j+1}^* + C_2 \varphi_{i,j}^* + C_3 \varphi_{i,j-1}^* = R.H.S_{i,j}^n \quad (2-94)$$

for $j = 2, 3, \dots, JMAX-1$ is solved using the Thomas Algorithm for tridiagonal matrices (given in many numerical method books) with successive over relaxation (S.O.R.). The C-coefficients are composed of appropriate local transport property and metric terms (e.g., Equation 2-93) and correspond to the stream function variables implicitly involved in the column sweep (intermediate) solution step. The R.H.S.ⁿ term contains all terms (C-coefficients and corresponding values of the current stream function) that are explicitly known at the current solution step. The boundary condition (discussed in Section 2.3.2) are imposed for the simultaneous solution at each row by setting $\varphi_{1,j} = \varphi_{IMAX,j} = \varphi_1 (\equiv I/2\pi)$.

Row sweep. During a row sweep (η -sweep)--marching in the axial direction--the finite-differenced form of Equation 2-91 is solved subsequently at lines of constant- η ; that is at $j=2,3,\dots,JMAX-1$. At each position, j ,

$$D_1 \varphi_{i,j+1}^{n+1} + D_2 \varphi_{i,j}^{n+1} + D_3 \varphi_{i,j-1}^{n+1} = R.H.S_{i,j}^* \quad (2-95)$$

for $i=2,3,\dots,IMAX-1$. The D-coefficients are related to the C-coefficients, and are composed of the appropriate local transport properties and metric terms, and correspond to the stream function variables implicitly involved in the "n+1" step. The R.H.S.* term contains all terms of the finite-difference scheme (D-coefficients and stream function variables) that are explicitly known during the row-sweep (final step).

The boundary condition on the upper generator wall is enforced for each simultaneous column solution by setting $\varphi_{i,JMAX} = \varphi_1$. On the lower generator

wall, the boundary condition for simultaneous column solutions involving the insulated surfaces are set by requiring that $\varphi_{i,1} = \varphi_1$ for the insulated walls outside of the electrodes and by letting $\varphi_{i,1} = \varphi_2 (= 0)$ in the insulated wall region between the electrodes. For the simultaneous column solutions involving either electrode (anode or cathode), the Neumann condition of zero derivative normal to the electrode surface ($\partial\varphi/\partial\eta = 0$) is enforced using a second-order accurate finite-difference formula (i.e., $-3\varphi_{i,1} + 4\varphi_{i,2} - \varphi_{i,3} = 0$). The system of equations (Equation 2-95) is solved using the Thomas Algorithm with S.O.R.

2.3.4 Overall Electrical Solution Algorithm

The overall electrical solution (for a given set of fluid conditions and for a specified load resistance, R_L) is obtained by solving the governing equations using the ADI-solution at the subsequent generator load currents achieved during an iterative search for the true (converged) generator load current. The ADI solution is considered converged for given a load current I^n (and, therefore, for the corresponding stream function φ_1) when the L2-norm of $\varphi_{i,j}$ (over all i and all j) is less than a specified error (typically, 1×10^{-6}). Recall that the boundary conditions (see Section 2.3.2) are determined in part by the current value--the value at the current iteration (represented by "n")--of the load current, I^n , through the relationship between φ_1 and I ; i.e., through $\varphi_1 = I^0/2\pi$. Once the ADI solution is effected, new current densities J_r and J_z are calculated using Equations 2-83 and 2-84. Electric field components (E_r and E_z) and plasma transport properties (σ_e and μ_e), consistent with the new current density values are

then obtained from Equation 2-88 and 2-89 and through the plasma physics modeling (see Section 2.4).

The new value of the load current (I^{n+1}) is next determined by

$$I^{n+1} = (1 - \omega_1)I^n + \omega_1 \left(\frac{V^n}{R_L} \right) \quad (2-96)$$

where ω_1 is a relaxation factor ($0 \leq \omega_1 \leq 1$), and V is the voltage drop across the load resistor, R_L . The load voltage is calculated using

$$V^n \equiv - \int_{L_{A \rightarrow C}} \underline{E} \cdot d\underline{l} = \int_{L_{A \rightarrow C}} \nabla \phi \cdot d\underline{l} = \phi_C - \phi_A = - \int_{R_A}^{R_C} E_r dr \quad (2-97)$$

where ϕ_C and ϕ_A are the electric potentials at the cathode and anode, respectively, R_A is the anode outer radius, R_C is the cathode inner radius; and $L_{A \rightarrow C}$ is the radial distance between the electrodes. The load voltage is obtained by a finite-difference integration; i.e.,

$$V^n = \phi_C - \phi_A = - \int_{R_A}^{R_C} E_r dr = - \sum_{i=I_A}^{I_C-1} \left\{ \frac{(E_r r_\xi)_{i,1}^n + (E_r r_\xi)_{i+1,1}^n}{2} \right\} \quad (2-98)$$

I_A is the radial finite-difference index value at the anode outer radius and I_C is the radial finite-difference index value at the cathode inner radius. Once the new load current, I^{n+1} , is obtained, the current boundary stream function value φ_1 may be determined, and therefore the boundary conditions are specified.

The plasma physics properties, consistent with the newly calculated current density and electric field strength, are used to establish new values for α_1 , α_2 , and S of the governing equation (Equation 2-91). The plasma physics modeling,

presented in Section 2.4, is treated then as an inner-solution, within the overall electrical solution. The outlined iteration procedure discussed here is continued until convergence on the generator load current, I , is obtained. (Typically, a relative error, between the load currents of two subsequent iterations, of 1×10^{-6} is required.) Again, this procedure provides a converged, consistent electrical solution for the specified fluid conditions and generator load.

2.3.5 Generator Electric Power Output

The electric power generated by the MHD generator during steady-state is given by (Sutton and Sherman, 1965)

$$\int_{V_M} \underline{J} \cdot \underline{E} dV = - \int_{V_M} \underline{J} \cdot \nabla \phi dV = - \int_{V_M} \nabla \cdot (\phi \underline{J}) dV = - \int_{A_M} \phi \underline{J} \cdot \underline{n} dA \quad (2-99)$$

where ϕ is a scalar potential, as earlier defined ($\underline{E} = -\nabla\phi$), and V_M and A_M are the MHD generator active volume and surface area, respectively. Because the electric field is uniform over the electrode surfaces and because the current density normal to the insulator surfaces ($\underline{J} \cdot \underline{n}$) is zero, then the electric power produced by the generator is

$$P_e = \int_{V_M} \underline{J} \cdot \underline{E} dV = I(\phi_A - \phi_C) = -IV \quad (2-100)$$

where ϕ_A and ϕ_C are the potentials (voltages) at the anode and cathode, respectively. The load current, I , is given by Equation 2-96 and the voltage, V , is given by Equation 2-98.

2.4 Plasma Physics Modeling and Transport Properties

The full form of the generalized Ohm's law relationship used in this work, (Equation 2-6 of Table 2.1)

$$\underline{J} + \mu_e \underline{J} \times \underline{B} = \sigma_e (\underline{u} \times \underline{B} + \underline{E}) \quad (2-101)$$

indicates the necessity for equation-of-state modeling for the plasma transport properties (e.g., σ_e and μ_e) in order to relate the current density \underline{J} to the electric field strength, \underline{E} . Models for the electrical conductivity and the electron mobility, applicable to the anticipated operating regimes of the MHD generators of interest to this work are developed in this section. The plasma physics modeling provided here is consistent with the continuum description of the MHD generator used throughout this thesis. The models are commensurate with, and influenced by, other engineering MHD work (cf. Sutton and Sherman, 1965 and Rosa, 1968).

2.4.1 Plasma Description

The plasma of primary concern in this work is a collision-dominated, weakly ionized plasma in which fission-fragment induced ionization provides the predominant source of free electrons that effect electrical conductivity. The hypothetical model of a two-temperature plasma is employed here; the plasma is treated as an electron fluid in a Maxwellian distribution about the electron temperature, T_e , superimposed on a background ("heavy"--ions and neutrals) fluid in a Maxwellian distribution about the fluid static temperature, T (cf., Rosa, 1968 after Kerrebrock, 1965). A generous discussion of the two-temperature model is given by Kerrebrock (1965) as he treats nonequilibrium ionization in MHD generators (see Kerrebrock, 1962, referenced by Kerrebrock, 1965 and

Kerrebrock, 1960, referenced by Hale and Kerrebrock, 1964); in studies of the characteristics of gas discharges, Kerrebrock verified the two-fluid theory, which states that the ionization (thermal) is in equilibrium with the electron temperature and that the electron temperature is given locally by the balance between the gain in energy from the electric field and the collisional losses (i.e., by an energy balance between Joule heating and electron-heavy collision losses (Sutton and Sherman, 1965)).

To the extent that the two-temperature model is valid, the modes (or mechanisms) of energy input, causing the ionization in the fluid, are equivalent in effect (Rosa, 1968). In the present work, the energy input terms include the recombination energy, energy input to the electron fluid by fissioning and the Joule heating of the electrons. One of the key assumptions in the plasma physics modeling is that the electron fluid, receiving high energy input from fission-fragment induced ionization, relaxes into a Maxwellian distribution about T_e , as the individual electrons slow down through collisions with the background gas. The electron birth and slowing down processes are not addressed here; however, the assumptions of electrons distributed in a Maxwellian distribution about T_e is based in the theoretical work of Appelbaum at the University of Florida (private communication with J.G. Appelbaum at the University of Florida in 1989; cf. Maya et al., 1991).

The background gas is treated as a single-component fluid with the mixture properties discussed in Section 2.2.3. The transport properties due to ion movement in the plasma are neglected since they are insignificant relative to

those of the electrons. Because the mobility, $\mu \sim (1/m)^{1/2}$, of the ions is very much less than that of the electrons, $\mu_i \ll \mu_e$, both the ion Hall parameter (β_i) and the ion conductivity (σ_i) are negligible. As mentioned earlier in the modeling assumptions, Section 2.1.1, the ion slip $\zeta = \beta_i \beta_e (= \mu_i \mu_e |\underline{B}|^2)$ is negligible.

Therefore, only the electron plasma transport properties are modeled in this work.

2.4.2 Electrical Conductivity and Electron Mobility

The electrical conductivity of the plasma, σ_e , is predicted using (Sutton and Sherman, 1965 and Rosa, 1968)

$$\sigma_e = \frac{n_e e^2}{m_e \bar{\nu}_{eH}} = n_e e \mu_e \quad (2-102)$$

where n_e is the electron number density, μ_e is the electron mobility,

$$\mu_e = \frac{e \bar{\tau}_{eH}}{m_e} = \frac{e}{m_e \bar{\nu}_{eH}} = \frac{\omega_e \bar{\tau}_{eH}}{|\underline{B}|} = \frac{\beta_e}{|\underline{B}|} \quad (2-103)$$

and where $\bar{\tau}_{eH}$ is the mean free time between collisions of an electron and a heavy (ion or neutral) particle. $\beta_e (= \mu_e |\underline{B}|)$ is the electron Hall parameter, $\omega_e = e|\underline{B}|/m_e$, is the electron cyclotron frequency, and $\bar{\nu}_{eH} (= 1/\bar{\tau}_{eH})$ is the "average" electron-heavy collision frequency given by

$$\bar{\nu}_{eH} = n_o \bar{Q}_{eH} \bar{u}_e = n_o \bar{Q}_{eH} \left(\frac{8kT_e}{\pi m_e} \right)^{1/2} \quad (2-104)$$

where n_o is the background fluid number density ($n_o = P/kT$), \bar{Q}_{eH} is the averaged electron-heavy momentum transfer cross section, and \bar{u}_e is the mean speed of the electrons in the electron fluid.

Equations 2-102 and 2-103 are equations-of-state for the electrical conductivity and electron mobility of the plasma in the sense that, given the plasma property data (e.g., \bar{Q}_{eff}) and the thermodynamic state of the plasma, the equations provide σ_e and μ_e .

2.4.3 Electron Number Density and Energy Balance

The following assumptions are imposed on the predictions of the electron number density, n_e and electron temperature, T_e : The effect of gradients are neglected ($\partial/\partial \underline{x} \rightarrow 0$) so that point models are developed; locally, steady-state conditions are reached ($\partial/\partial t \rightarrow 0$); the significant electron source terms are fission-fragment induced ionization (S_{ff}) and thermal ionization of a seed constituent (S_{Saha}); the only significant electron species loss mechanism, at the temperatures and pressures considered here, is the three-body (electron stabilized) recombination ($A^+ + e + e \rightleftharpoons A + e$). It is noted that two-body recombination and electron attachment may be competing loss mechanisms in an actual UF_4 -He fluid mixture (with associated dissociation products). Based on discussions with J.G. Appelbaum at the University of Florida in 1991, the relative importance of the recombination and attachment loss mechanisms in UF_4 -He mixtures is not known at this time (cf. Maya et al., 1991). As a simplifying assumption that allows an explicit expression for the electron number density to be developed (see Equation 2-115, for example), in a manner consistent with typical engineering MHD studies, and after the suggestion of Appelbaum (1991), three-body recombination is the only electron number density loss mechanism considered in the plasma physics modeling presented in this work.

Number density balances. Under these assumptions, the electron number density balance is given by

$$0 = \gamma_i n_e n_s - \alpha_i n_e^2 n_+ + S_{ff} \quad (2-105)$$

where γ_i is the ionization coefficient for the electron-neutral (seed) ionization, α_i is the three-body recombination coefficient, and S_{ff} is the electron source due to fission-fragment induced ionization. Recognizing that, in the absence of the fission source, S_{ff} , the forward and backward mechanisms of the reaction (i.e., $A_s^+ + e \rightleftharpoons A_s + e + e$) are in equilibrium, then, $\gamma_i/\alpha_i = (n_e n_+/n_s)_{eq}$ where this ratio is given by the Saha equation.

Imposing local charge neutrality ($n_+ = n_e$), can be rearranged to yield

$$\alpha_i n_e^3 = S_{Saha} + S_{ff} \quad (2-106)$$

where the thermal ionization electron source is given by

$$\begin{aligned} S_{Saha} &= \alpha_i n_e n_s \left[\frac{n_e n_+}{n_s} \right]_{eq} \\ &= \alpha_i n_e n_s \frac{2g_i}{g_s} \left[\frac{2\pi m_e kT_e}{h^2} \right]^{\frac{3}{2}} \exp \left[-\frac{\epsilon_i}{kT_e} \right] \end{aligned} \quad (2-107)$$

(Rosa, 1968 and Sutton and Sherman, 1965) where g_i and g_s are the internal partition functions of the ions (A_s^+) and the neutral seed (A_s), respectively (typically $2g_i/g_s \approx 1$ for alkali metal seeds used in MHD generators) and ϵ_i is the first ionization potential of the seed (e.g., 3.87 eV for Cesium (Sutton and Sherman, 1965)). It is noted here that if a seed constituent is not added to the

neutral background gas then $n_i \rightarrow n_o$ and all the properties (e.g., ϵ_1 and g_o) of the neutral gas are used in the equations developed above.

The recombination coefficient, α_i , used in this work is given by

$$\alpha_i(T_e) = C_1 T_e^{-1} \quad (2-108)$$

where C_1 is a constant ($7.8 \times 10^{-21} \text{ m}^6/\text{s} \leq C_1 \leq 1.8 \times 10^{-20} \text{ m}^6/\text{s}$, typically [Appelbaum, private communication, 1989]).

The fission source of electrons is given by

$$S_{ff} = \frac{\dot{q}_N}{w_{ff}} = \frac{G_f \beta_f \bar{\sigma}_f n_o \Phi}{w_{ff}} \quad (2-109)$$

where \dot{q}_N is the fission volumetric fission heat generation rate (formally given by Equation 2-14 of Table 2.1), G_f is the energy given to the media per fission event, β_f is the atom-fraction of fissionable isotopes to atoms of background gas, and $\bar{\sigma}_f$ is the average neutron fission cross section; w_{ff} is the average energy required to produce one ion-pair by fission-fragment induced ionization. Typically, w_{ff} varies in differing media ($20 \leq w_{ff} \leq 50 \text{ eV/ion-pair}$); however, in a given medium, w_{ff} is relatively constant (Knoll, 1979).

Energy balance. Considering the modeling above, the number density, n_e , is typically a strong function of the electron temperature, T_e ; T_e is predicted by the energy balance on the electron fluid. Under the assumptions mentioned above--i.e., local steady-state, negligible spatial gradient effects, and significant electron number density losses by three-body electron stabilized recombination only--the energy balance on the electron fluid is given by

$$0 = w_i \gamma_i n_e n_s + w_r \alpha_i n_e^2 n_+ - \dot{E}_C + \dot{q}_N + \dot{q}_{Other} \quad (2-110)$$

where w_i ($= -C_2 \epsilon_i$) is the power loss per ionization event and w_r ($= C_3 \epsilon_i$) is the power gain per recombination event (where C_2 and C_3 are both on the order of unity); \dot{E}_C is the power lost by electron-heavy collisions (i.e., lost from the electron fluid)

$$\dot{E}_C = n_e \bar{\nu}_{eH} \epsilon^i = n_e \bar{\nu}_{eH} \delta \epsilon^\epsilon = n_e \bar{\nu}_{eH} \delta \left[\frac{2m_e}{m_H} \right] \frac{3}{2} k (T_e - T) \quad (2-111)$$

where $\bar{\nu}_{eH}$ is the average electron-heavy collision frequency (Equation 2-104), ϵ^i is the average energy lost per inelastic collision between an electron and a heavy atom ($\epsilon^i = \delta \epsilon^\epsilon$), δ is the inelastic scatter energy-loss factor, and ϵ^ϵ is the average energy-loss per elastic collision event ($(2m_e/m_H) 3k(T_e - T)/2$); \dot{q}_{Other} is the local power density added to the electron fluid from all other sources (e.g., Joule heating). Note that any radiation losses from the electron fluid are neglected in this work. Again, using the fact that $\gamma_i/\alpha_i = (n_e n_+/n_s)_{eq}$ at equilibrium, Equation 2-109 for the fission power density (\dot{q}_N), and making use of the number density balance (Equation 2-106), it is found that

$$\dot{E}_C = (w_i + w_r) S_{Saha} + (w_r + w_{ff}) S_{ff} + \underline{J} \cdot \underline{E}' \quad (2-112)$$

where \dot{q}_{Other} has been set to the Ohmic heating $\underline{J} \cdot \underline{E}'$ ($= \underline{J} \cdot \underline{J} / \sigma_e$). It is expected that $|w_i| \approx |w_r| \approx \epsilon_i$ and, therefore, because w_i is negative while w_r is positive, the first term on the RHS of Equation 2-112 is negligible. Using Equation 2-111 for \dot{E}_C and rearranging, the electron temperature may be

predicted by

$$T_e = T + T_{NON} = \frac{m_H}{3m_e \delta \nu_{eH} n_e} \left\{ (w_r + w_{ff}) S_{ff} + \underline{J} \cdot \underline{E}' \right\} . \quad (2-113)$$

The electron temperature is therefore equal to the background (heavy) gas temperature plus a nonequilibrium enhancement, T_{NON} . Iterating between the electron number density balance (Equation 2-106) and the energy equation above (Equation 2-113) provides the local number density and electron temperature.

As mentioned in Chapter 1, of primary interest to this study are conditions under which the fission fragment induced ionization is the dominant mechanism giving rise to the free electrons effecting the generator electrical conductivity. The working fluid is envisioned as a UF₄-He mixture (discussed in Section 2.2.3), without any seed component; in this case $S_{ff} \gg S_{Saha}$. For purposes of comparison, also considered in this work is the separate and classic MHD generator problem in which $S_{Saha} \gg S_{ff}$; here, the working fluid may be imagined to have no fissionable isotope--or indeed, the neutron flux may be taken as zero--but instead be laden with an alkali metal seed (e.g., Cs) which, due to its low first ionization potential, experiences thermal ionization, as mentioned earlier, in equilibrium at the electron temperature. In the following two sections the "Fission Model" ($S_{ff} \gg S_{Saha}$) and the "Saha Model" ($S_{Saha} \gg S_{ff}$) are addressed separately. The intermediate regime in which S_{Saha} and S_{ff} are comparable in magnitude is effectively modeled using the equations developed above, provided that the physical data (e.g., cross sections) are known; however, this intermediate regime is not analyzed in this thesis.

2.4.4 Fission Model ($S_{ff} \gg S_{Saha}$)

Treating the background gas as having a relatively high (e.g., 10 eV) first ionization potential and having no low ionization potential seed constituent, then the electron number density is predicted by

$$n_e = \left[\frac{S_{ff}}{\alpha_i} \right]^{\frac{1}{3}}. \quad (2-114)$$

This cube root dependence of the electron number density on the (fission) interaction rate was used by Braun to predict the number density of ${}^3\text{He}^+$ in the case of ionization during an expansion of ${}^4\text{He}$ gas, seeded with ${}^3\text{He}$, in a nozzle in the presence of a constant neutron flux (Braun, 1965). Note that the ${}^3\text{He}$ "seed" (experiencing (n,p) interactions) plays an analogous role to the fissionable isotope in the current study. Expanding 2-114 with Equations 2-108 and 2-109 yields

$$n_e = a_1 n_o^{\frac{1}{3}} \Phi^{\frac{1}{3}} T_e^{\frac{1}{3}} = a_1 \left[\frac{P}{kT} \right]^{\frac{1}{3}} \Phi^{\frac{1}{3}} T_e^{\frac{1}{3}} \quad (2-115)$$

which shows the functional dependence of n_e on the fluid thermodynamic conditions (P and T), the neutron flux (Φ), and the electron temperature (T_e); a_1 is a constant given in Table 2.7.

The electron temperature for this case where $S_{ff} \gg S_{Saha}$ is given by Equation 2-113. Therefore, Equation 2-115 and Equation 2-113 can be used to obtain n_e and T_e at which point the electrical conductivity and electron mobility may be calculated.

In the limiting case where $T_{NON} \rightarrow 0$, for example, in the case of a fluid in which the inelastic scatter energy loss factor, δ , is large, then $T_e \approx T$. This

Table 2.7 Constants of Plasma Physics Transport Property Models

Plasma Transport Property Constants

$$a_1 = \left[\frac{G_f \sigma_f \beta_f}{w_{ff} C_1} \right]^{\frac{1}{3}}$$

$$a_2 = \left[\frac{e}{m_e} \right] \left[\frac{\pi m_e}{8k} \right]^{\frac{1}{2}}$$

$$a_3 = \left[\frac{2g_i}{g_s} \left[\frac{2\pi m_e k}{h^2} \right]^{\frac{3}{2}} \right]^{\frac{1}{2}}$$

Property Data

G_f	=	Energy Release per Fission (MeV)	190
β_f	=	Atom Fraction of Fissionable Isotope (e.g., ^{235}U) in Working Fluid (e.g., UF_4 -He mixture)	0.05704
σ_f	=	^{235}U Neutron Fission Cross-Section (with $T_N \approx 1200$ K) (cm^2)	2.3×10^{-22}
w_{ff}	=	Energy Consumed per Ion-Pair Produced (eV/I.P.)	35
C_1	=	Recombination Rate Coefficient (m^6/s)	1.2×10^{-20}
g_i	=	Internal Partition Function of Ion	
g_s	=	Internal Partition Function of Seed Constituent ($2 g_i / g_s$)	(≈ 1)

Constants

e	=	Electronic Charge (C)	1.602×10^{-19}
m_e	=	Electron Mass (kg)	9.110×10^{-31}
k	=	Boltzmann Constant (J/K)	1.381×10^{-23}
h	=	Planck Constant ($\text{J} \cdot \text{s}$)	6.626×10^{-34}

condition is referred to as the "equilibrium" condition in this study. Under equilibrium ($T_e \approx T$) conditions the electron number density is a function of only the local fluid thermodynamic conditions and the neutron flux level. The electrical conductivity is predicted explicitly by

$$\sigma_e = \frac{a_1 a_2 e}{Q_{eH}} \left(\frac{kT}{P} \right)^{\frac{1}{2}} \Phi^{\frac{1}{2}} T \sim \frac{T^{\frac{3}{2}}}{P^{\frac{1}{2}}} \Phi^{\frac{1}{2}} \quad (2-116)$$

and the electron mobility is given by

$$\mu_e = \frac{a_2}{Q_{eH}} \left(\frac{kT}{P} \right) \frac{1}{\sqrt{T}} \sim \frac{\sqrt{T}}{P} \quad (2-117)$$

where a_1 and a_2 are constants (see Table 2.7). Under the equilibrium condition, Equations 2-116 and 2-117 can be written as

$$\sigma_e = \sigma_{e,r} \left[\frac{\Phi}{\Phi_r} \right]^{\frac{1}{2}} \left[\frac{T}{T_r} \right]^{\frac{1}{2}} \left[\frac{P_r}{P} \right]^{\frac{1}{2}} \quad (2-118)$$

and

$$\mu_e = \mu_{e,r} \left[\frac{T}{T_r} \right]^{\frac{1}{2}} \left[\frac{P_r}{P} \right] \quad (2-119)$$

where the subscript "r" represents values at a reference condition.

The models provided in this section for $S_{ff} \gg S_{Saha}$ are applicable then for nonequilibrium conditions (Equations 2-113 and 2-115) or equilibrium ($T_e = T$) conditions. Under equilibrium conditions, the conductivity and mobility, and their dependence on the neutron flux and fluid thermodynamic conditions, are provided

by Equations 2-116 and 2-117. Equations 2-118 and 2-119 provide convenient forms for the transport properties, where σ_e and μ_e are calculated using Equations 2-116 and 2-117 at reference conditions (T_r, P_r, Φ_r). Alternatively, the functional forms developed are convenient for cases in which all the physical data are not accurately known for a given plasma; in this case the reference electrical conductivity may be specified at some reference temperature, pressure, and neutron flux level and the corresponding reference electron mobility (and certain property data) may be back calculated. Then Equations 2-118 and 2-119 may be used to predict the plasma transport properties spatially as a function of the local thermodynamic conditions and neutron flux levels.

2.4.5 Saha Model ($S_{\text{Saha}} \gg S_{\text{ff}}$)

The background gas in this scenario is seeded with a small fraction (≤ 0.01) of a low first ionization potential seed constituent (e.g., an alkali metal). The seed constituent is ionized to an equilibrium ionization at the electron temperature, T_e as discussed earlier; the background gas (other than the seed constituent) makes no contribution to the ionization in this scenario. In the limit when $S_{\text{Saha}} \gg S_{\text{ff}}$, the electron number density may be expressed as

$$n_e = a_3 \left(\frac{P}{kT} \right)^{\frac{1}{2}} T_e^{\frac{3}{2}} \exp\left(-\frac{\epsilon_I}{2kT_e} \right) \quad (2-120)$$

where the constant a_3 is given in Table 2.7. The electron temperature is again given by Equation 2-113. Using Equation 2-120 for the number density, n_e , with Equation 2-113 for the electron temperature, T_e , the electrical conductivity and electron mobility may be calculated.

As before, in the "equilibrium" condition, the electron temperature, T_e , is equal to the background gas temperature, T ; again, this is likely in the case of a molecular gas in which inelastic scattering energy losses preclude significant nonequilibrium ionization. In this case ($T_e \approx T$), the electron conductivity may be expressed explicitly as

$$\sigma_e = \frac{a_2 a_3 e}{Q_{eH}} \left[\frac{kT}{P} \right]^{\frac{1}{2}} T^{\frac{1}{2}} \exp\left(-\frac{\epsilon_I}{2kT}\right) \sim \frac{T^{\frac{1}{2}}}{P^{\frac{1}{2}}} \exp\left(-\frac{\epsilon_I}{2kT}\right) \quad (2-121)$$

exhibiting the classical functional form of the electrical conductivity arising from thermal ionization. The electron mobility for this case is the same as that for the case of the equilibrium fission model; i.e., the electron mobility is given by Equation 2-117. If Equation 2-121 is used to determine a reference electrical conductivity $\sigma_{e,r}$ at reference thermodynamic conditions (T_r and P_r), then σ_e can be written as

$$\sigma_e = \sigma_{e,r} \left[\frac{T}{T_r} \right]^{\frac{1}{2}} \left[\frac{P_r}{P} \right]^{\frac{1}{2}} \exp\left(\frac{\epsilon_I}{2kT_r} \left[1 - \frac{T_r}{T}\right]\right) \quad (2-122)$$

which is the same expression used earlier by Kerrebrock (1961). (It is interesting to compare the functional forms of the electrical conductivity arising from the equilibrium case where $S_{ff} \gg S_{Saha}$ (Equation 2-116) and the equilibrium case in which $S_{Saha} \gg S_{ff}$ (Equation 2-121); in the fission model $\sigma_{e,r} \sim T^{5/3}$, a power-law temperature dependence, while in the Saha model $\sigma_{e,r} \sim T^{3/4} \exp(-\epsilon_I/2kT)$, indicating a strong exponential temperature dependence.) The functional form of the electron mobility is given by Equation 2-117.

The nonequilibrium case where $S_{\text{Saha}} \gg S_{\text{ff}}$ is modeled using Equation 2-120 for the electron number density with Equation 2-113 for the electron temperature. In the limit where $T_e \rightarrow T$ ("equilibrium") the Saha ionization model predicts an electrical conductivity and electron mobility given by Equation 2-122 and Equation 2-119 where $\sigma_{e,r}$ and $\mu_{e,r}$ are calculated at a reference background gas temperature and pressure (T_r and P_r). In the case when physical data (e.g., \bar{Q}_{eH} or ϵ_1) are not accurately known, Equation 2-122 may be used by specifying the reference conductivity (at T_r and P_r) and back calculating either an unknown \bar{Q}_{eH} (assuming a known ϵ_1) or an unknown ϵ_1 (assuming a known \bar{Q}_{eH}).

2.5 Overall MHD Solution

The steady-state 2-D MHD solution is obtained by iteration between a fluid solver (FLUID) and an electromagnetics solver (ELEMAG).

Fluid solver. The thin-layer Navier-Stokes equations with turbulence modeling and MHD and fission source terms (developed in Section 2.2) are integrated in time to an asymptotic steady-state, using the explicit method of MacCormack, in the fluid solver (FLUID). Within a given fluid calculation, the electromagnetic variables (the MHD terms) that influence the fluid solution--i.e., the current density and electric field strength components--are held constant; the electromagnetic variables are known "boundary functions" calculated in the electromagnetics solver (ELEMAG).

Electromagnetics solver. The electromagnetics equations (developed in Section 2.3) with variable plasma properties (developed in Section 2.4) are

integrated, using the ADI method, in the electromagnetic solver (ELEMAG).

Within a given electromagnetics solution, the fluid dynamic variables profiles that influence the electromagnetics solution (e.g., fluid density, velocity components, etc.) are held constant; the fluid dynamic variable profiles are, therefore, specified boundary functions, calculated in the fluid solver.

The fluid and electromagnetics calculations are performed on the same numerical grid. The structure of the numerical grid--the number of grid lines and the location of the grid lines--is dictated by the resolution requirements of the fluid solution; the numerical grid generation is described in Appendix B.

An overall consistent MHD solution is obtained by a series of outer iterations between the fluid solver and the electromagnetics solver until the generator load current (see Section 2.3) is converged upon; at this point all fluid mechanic, electromagnetic, and plasma physics field variables are necessarily consistent and are converged upon.

CHAPTER 3

ANALYSIS

3.0 Introduction

The MHD flow of a fissioning gas in the outflow disk MHD generator geometry is analyzed in this chapter using the solution methodology developed in Chapter 2. The influence of duct geometry and the effects of variable neutron flux levels (fission power densities), applied B-fields, and generator load resistances on the spatial profiles of important generator variables are studied here. Comparisons are made between the predictions of the 2-D MHD solver developed in this thesis and a quasi-one-dimensional (Q1D) Euler solver (with MHD and fission source terms), that was developed by the author, separate from this work; the Q1D solver is described in Appendix A.

Modifications that evolved in the course of implementing the solution methodology provided in Chapter 2 are presented in Section 3.1 of this chapter. Section 3.2 provides an examination of the influence of the duct geometry and neutron flux (or fission power density) level on internal, supersonic flow, without MHD effects. The 2-D turbulent flow predictions of the thin-layer Navier-Stokes fluid solver, developed in this work, are compared with Q1D flow predictions for flow with and without fissioning, in the absence of MHD effects, in Section 3.3.

Section 3.4 provides a study of fissioning MHD flow with uniform plasma properties. Sections 3.5 and 3.6 provide analysis of disk MHD generator flows with variable plasma properties; the plasma properties are analyzed in Section 3.5 and a study of the nonuniform plasma property MHD flows, similar to that presented in Section 3.4 for uniform plasma property MHD flows, is carried out in Section 3.6. To conclude the chapter, nonuniform plasma property MHD flow predictions of the 2-D Navier-Stokes MHD solver and the Q1D MHD solver are compared.

3.1 Solution Method Modifications for MHD Calculations

The theoretical modeling of the MHD flow of a fissioning gas is developed in Chapter 2. The actual process of obtaining convergence to overall MHD solutions has required four additions, or modifications, to the modeling presented in Chapter 2. The modifications arose in addressing the following concerns: a.) physically incorrect oblique shock waves that were found to develop at the interface of the upper and lower duct walls with the inlet boundary plane, and propagate downstream through the duct; the oblique shock waves appeared in all of the obtained flow solutions, for the duct geometries analyzed; b.) the fact that in early generator calculations the flow field was prematurely becoming subsonic, given the MHD interaction levels and duct lengths analyzed; and c.) in some cases where the calculations were not ending due to subsonic conditions, it was found that the developed fluid solver (see Section 2.2), with the MHD source terms from the electrical solver (see Section 2.3), was ending on calculational errors--

instabilities in the solution flow field. These instabilities were first made manifest in the local stagnation temperature rapidly increasing in some regions (near the exit plane), indicating a local power generation source term. An examination of these concerns led to the following observations. First, the oblique shock waves that originate at the inlet plane are due to a mismatch between the specified inlet plane velocity axial flow angle and the calculated flow solutions immediately downstream of the exit plane. Second, at significant MHD interaction levels (e.g., $\sigma_e = 70 \text{ S/m}$ and $B [= B_z] = 4 \text{ T}$) the generator flow is decelerated towards a radial Mach number of one and the boundary layer thicknesses are larger than those for a purely expanded flow. Under these conditions, a significant portion (e.g., 10%) of the exit plane flow is subsonic (in a radial sense); this calls into question the validity of the full-extrapolation used to set the outlet boundary conditions. Third, the strength of compression or rarefaction waves (e.g., oblique shock waves originating at the boundary) is apparently increased by the MHD effects, thus complicating the flow field; this raises the question as to whether non-physical oscillations are introduced by the capture of physically correct compression and rarefaction wave structure in the generator. Finally, the oscillations in stagnation temperature call into question whether the turbulence modeling (developed in Section 2.2.2) is introducing numerical oscillations. These issues led to the modifications and additions to the overall MHD solution methodology presented in this section.

3.1.1 Inlet Boundary Axial Flow Angle

In the development of the inflow boundary conditions in Section 2.2.4, the axial component of velocity was specified as

$$w(z) = p(z) u(z) \quad (3-1)$$

where $u(z)$ is the inlet radial velocity component profile and $p(z)$ is the axial profile of the tangent of the local (inlet) axial flow angle. It was stated in Section 2.2.4 that $p(z)$ is obtained using a linear interpolation between the tangent of the upper wall and the tangent of the lower wall; however, it was found in the course of this work that the $p(z)$ profile obtained from the linear interpolation is not appropriate, especially for the Mach 2 or 3 inlet flow analyzed in this work.

Figure 3.1 provides a diagram of the generator inlet lower duct wall boundary layer region. The boundary layer (δ) and displacement thickness (δ^*) are shown in the figure. The displacement thickness is defined as

$$\delta^* \equiv \int_0^{\delta} \left(1 - \frac{\rho U(z)}{\rho_e U_e} \right) dz \quad (3-2)$$

and is a measure of the mass flow deficiency in the boundary layer due to no-slip at the wall (Shapiro, 1954); the displacement thickness is bounded by a stream line through which, by definition, no mass flow can pass, and is the thickness by which the stream lines near the edge of the boundary layer would be lifted in an external flow. The slope of the displacement thickness ($d\delta^*/dl$) provides an accurate measurement of the tangent of the angle at which the flow travels, relative to the tangent of the wall, at the edge of the boundary layer.

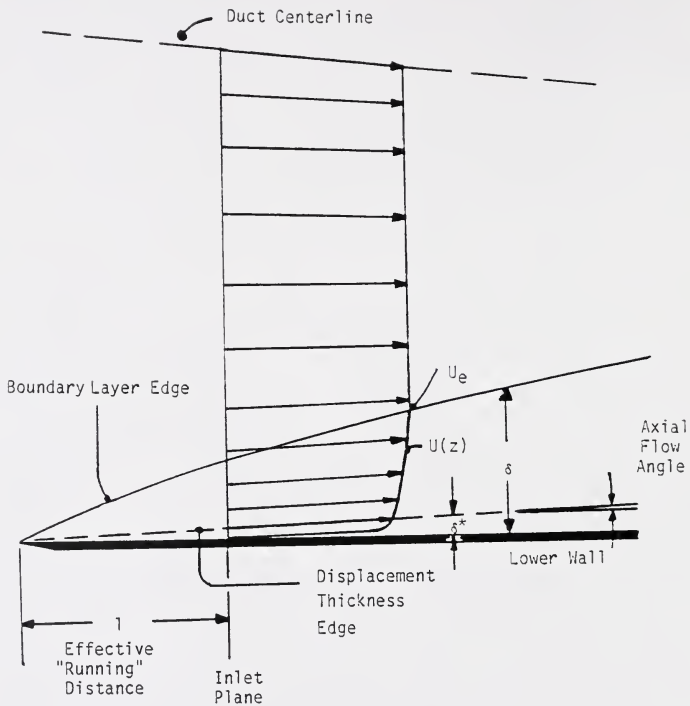


Figure 3.1 Schematic Diagram of Lower Wall Corner of Inlet Plane Showing Exaggerated Boundary Layer and Displacement Thicknesses.

If the bottom wall is flat ($\partial z/\partial r = 0$), the flow at the edge of the boundary layer travels tangent to the displacement thickness streamline; i.e., the flow has a positive axial component. The original boundary condition proposed in Section 2.2.4 requires that the flow have zero axial velocity component if the top wall and the bottom wall are flat (parallel), but it requires that the axial velocity component in the lower boundary layer be negative if the top wall is sloped downward; i.e., not only does the original boundary condition not provide the physically correct positive displacement thickness slope at the lower wall but errantly requires a negative displacement thickness slope. Although the flow angles of discussion here are extremely small, a problem arises in the transition from the incorrect inlet $w(z)$ profile to the correct $w(z)$ profiles immediately downstream of the inlet plane; the transition from the negative (or zero) axial flow angles to the correct positive flow angles (at the lower wall boundary layer region) obtained in the solution at the downstream locations is accomplished through a supersonic "compression corner" change, with the corresponding generation of an oblique shock wave. Figure 3.2 provides the static pressure contour plot ($P(r,z)$) of a fissioning flow with inlet conditions, in an example duct geometry, used in the MHD flow solutions of Section 3.4 and 3.6. Oblique shock waves originating from the boundary layer regions of the inlet plane, and propagating downstream, are clearly evident in Figure 3.2. It is again emphasized that the waves are artificial in that they show up due to this mismatch in the inlet flow angles as discussed above. It is also noted that mismatch is probably a negligible effect in the case of subsonic flows; it is apparent from Figure 3.2 that

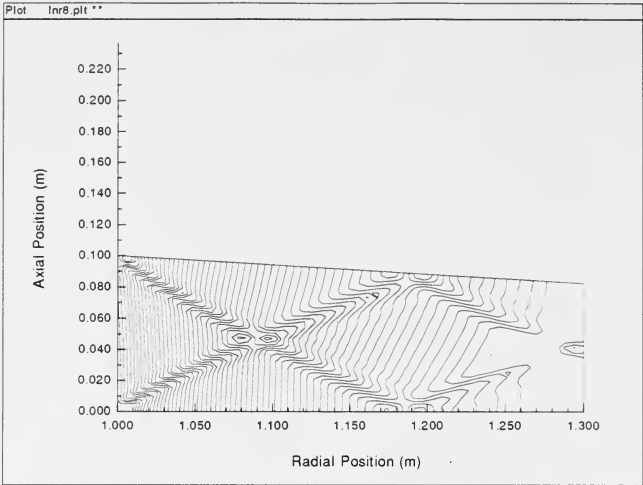


Figure 3.2 Static Pressure Contour Plot of Fissioning Flow in Example Duct Geometry of MHD Calculations of Section 3.4.

care must be taken when starting an internal supersonic flow calculation at some arbitrary position.

In the course of this work it was found that the oblique shock waves proved detrimental to both the performance of the examined MHD generators, because the shock wave contributed to decelerating the flow towards Mach one, and to the analysis of the MHD solutions; the effects of the oblique shocks waves on the flow field, especially the boundary layer regions, in many cases obscured the MHD effects that are of interest to this work.

von Karman integral analysis. Expressions for the correct axial flow directions (w/u) are developed in this section using the integral boundary layer theory of von Karman, as applied by Wilson (1950) to supersonic, compressible, turbulent flows, as reported by Shapiro (1954). Using von Karman's integral analysis, the u-momentum equation of the boundary layer equations may be rewritten as (Shapiro, 1954)

$$\frac{d\Theta}{dl} = \frac{\tau_w}{\rho_e U_e^2} - g(l)\Theta \quad (3-3)$$

where

$$g(l) = \frac{(2 + M_e^2) + H}{M_e \left(1 + \frac{\gamma - 1}{2} M_e^2\right)} \frac{dM_e}{dl} \quad (3-4)$$

and where the momentum thickness, Θ , is defined as

$$\Theta \equiv \int_0^{\delta} \frac{\rho U(z)}{\rho_e U_e} \left(1 - \frac{U(z)}{U_e}\right) dz \quad . \quad (3-5)$$

H ($\equiv \delta^*/\Theta$) is the ratio of the displacement thickness to the momentum thickness; for convenience a second ratio is defined as, $I \equiv \delta/\Theta$.

Wilson used Equation 3-3 with the skin-friction correlation he proposed (Wilson, 1950) (see also discussion in Section 2.2.4 on the inlet boundary conditions) to numerically calculate H and I ratios as functions of free stream Mach number, for flows with favorable pressure gradients ($dM/dl \geq 0$); Shapiro (1954) reports that supersonic wind tunnel data on boundary layer growth shows Wilson's method to be adequately accurate for most applications. Given the H and I factors from Wilson's work (1950, or see table of H and I values in Shapiro, 1954), the slope of the displacement thickness ($d\delta^*/dl$) may be obtained using Equations 3-3 and 3-4. Recall from Section 2.2.4 that Wilson's skin-friction coefficient correlation is transcendental--as is von Karman's for incompressible flows, from which Wilson's is extended--and is therefore not used in the inlet flow boundary condition formulation in Section 2.2.4, simply to avoid iteration on the inlet boundary conditions. Instead, the skin friction coefficient (or wall shear stress) is obtained using the Falkner/Tucker relationship (see Equation 2-66 and associated discussion) given by

$$\frac{\tau_w}{\rho_{am} U_e^2} = \frac{0.0131}{Re_{l,am}^{1/2}} \quad (3-6)$$

Using Equations 3-2 and 3-6, an approach for obtaining the slope $d\delta^*/dl$ that avoids iteration (at least within the 2-D Navier-Stokes solver, FLUID) is developed in the following.

Equation 3-3 is integrated by assuming that the terms $g(l)$, H , and I , are constant (uniform) over the short effective boundary layer development ("running") length, l , shown to be on the order of a centimeter in Section 2.2.4. It is found that

$$\delta(l) = \alpha l e^{-sl} \int_0^l l^{-1/2} e^{sl} dl \quad (3-7)$$

where α is specified by the local flow and thermodynamic conditions. The effective "running" length, l , is therefore determined as that distance that satisfies Equation 3-7, for which $\delta(l) = \delta_{in}$ is the specified (inlet) boundary layer thickness. With l determined, the running Reynolds number, $Re_{l,am}$, is known; using Equation 3-3 the slope of the displacement thickness may be determined using

$$\frac{d\delta^*}{dl} = \frac{0.0131}{Re_{l,am}^{1/2}} - g(l) \frac{H}{I} \delta \quad (3-8)$$

The shape factors, H and I , are dependent on the velocity and temperature axial profiles within the boundary layer region.

A program (TEMPDIS) was developed to solve Equations 3-2 through 3-8 for a fixed (e.g., inlet) position. It is assumed in the program that the velocity

boundary layer profile is divided into a laminar sublayer region and a one-seventh power law region as discussed in Section 2.2.4 (on the inlet boundary conditions). The static temperature is assumed to vary through the boundary layer according to the temperature profile provided by Equation 2-56 of Section 2.2.4; heat transfer occurs to, or from, the wall in this case. The fluid mechanics calculations performed in TEMPDIS are consistent with those used to set the inlet boundary conditions in the thin-layer Navier-Stokes fluid solver (FLUID) of this work.

As a modification to the fluid solver, FLUID, the axial component of velocity is calculated using Equation 3-1 where, now, the distribution of the ratio $p(z) = w(z)/u(z)$ --within the boundary layer region-- is given by

$$p(z) = \begin{cases} \left(\frac{z_\xi}{r_\xi} + \frac{d\delta^*}{dl} f(z) \right) & \text{for } Z_{\min} \leq z \leq Z_{\min} + \delta \\ \left(\frac{z_\xi}{r_\xi} - \frac{d\delta^*}{dl} f(z) \right) & \text{for } Z_{\max} - \delta \leq z \leq Z_{\max} \end{cases} \quad (3-9)$$

where recall z_ξ/r_ξ is the tangent of the wall and $d\delta^*/dl$ is given by Equation 3-8, and $f(z)$ is the shape of the radial velocity component, given by Equation 2-68 of Section 2.2.4. Outside of the boundary layer, $p(z)$ is set by linear interpolation between $p(Z_{\min} + \delta_{in})$ and $p(Z_{\max} - \delta_{in})$.

For completeness, it is noted that the actual manner in which the displacement thickness slope, $d\delta^*/dl$, is implemented in the fluid solver (FLUID) is

$$\frac{d\delta^*}{dl} = CF \left(\frac{d\delta^*}{dl} \right)_{FLUID} = CF \left[\frac{0.0131 H_0}{Re_{l,am}^{1/7}} \right] \quad (3-10)$$

where H_0 is the shape factor for incompressible flow (assuming the one-seventh law velocity profile throughout the boundary layer region); $H_0 = 9/7$ (see Shapiro, 1954, or obtain using Equations 3-2 and 3-5). The "code factor" (effectively a compressibility factor), CF , is defined by Equation 3-10 as the ratio of the actual slope calculated by TEMPDIS, $d\delta^*/dl$, and $(d\delta^*/dl)_{FLUID}$ calculated internal to the program FLUID; $(d\delta^*/dl)_{FLUID} \equiv 0.0131 H_0 / (Re_{l,am})^{1/7}$ is the slope of an incompressible turbulent boundary layer, modified by $Re_l \rightarrow Re_{l,am}$.

Again, the code factor, CF , is provided by the program TEMPDIS; however, a good approximation of the code factor is obtained by neglecting the term $g(l)$ of Equation 3-8. In this case

$$\frac{d\delta^*}{dl} \approx \frac{0.0131 H}{Re_{l,am}^{1/7}} \quad (3-11)$$

and it is found that

$$CF_{th} = \frac{H}{H_0} \left[\frac{I}{I_0} \right]^{1/2} \quad (3-12)$$

where CF_{th} is a theoretical estimate of the code factor, and $H_0 (= 9/7)$ and $I_0 (= 72/7)$ are the shape factors for incompressible turbulent (one-seventh power law profile) flow. Therefore, as an alternative to obtaining CF from the TEMPDIS program, Equation 3-12 may be used, along with the H and I factors available in the literature--e.g., from Wilson (1950), reported in Shapiro (1954).

Application. For inlet conditions considered in Sections 3.4 and 3.6 of this work, the following were observed: A comparison between the H and I factors of TEMPDIS--for a case in which the one-seventh power law profile is used throughout the boundary layer region and in which the stagnation temperature is uniform through the boundary layer--and the H and I factors of Wilson (reported in Shapiro, 1954) show good agreement between the two approaches; when the laminar sublayer region is included, and heat transfer is allowed in the TEMPDIS calculation, the H from TEMPDIS is generally lower than that predicted by Wilson, and the I from TEMPDIS is also lower than that predicted by Wilson. The code factors from TEMPDIS are, therefore, lower than those calculated when Wilson's results are used in Equation 3-12. When the H and I values predicted by TEMPDIS are used in Equation 3-12, it is found that CF_{b} is an excellent approximation to CF, especially in the limit that $dM_T/dl \rightarrow 0$; i.e., given the correct values of H and I, Equation 3-12 will do a good job in providing the necessary code factor for the FLUID solver. A favorable pressure gradient, when $dM_T/dl \geq 0$, increases the CF (i.e., it increases the compressibility effects, and therefore the relative slope of the displacement thickness, $d\delta^*/dl$) at the conditions of interest here. The code factor (or $d\delta^*/dl$) is found to increase with increasing wall temperature (decreasing wall fluid density) and with total Mach number (M_T), but is found to be independent of the way in which M_T is distributed in radial Mach number, M_R , and swirl factor, S.

Effect of CF on FLUID predictions. For the example inlet conditions of the MHD generator calculations provided in Section 3.4 and 3.6--i.e., $M_R = 2.0$, S

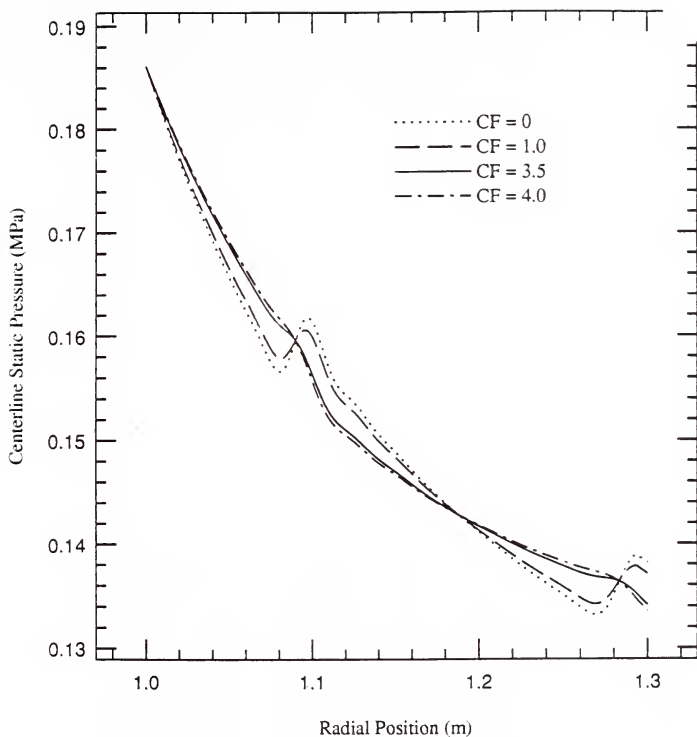


Figure 3.3 Comparison of Centerline Static Pressure as a function of Radial Position for Code Factors CF = 0, 1, 3.5, and 4.0.

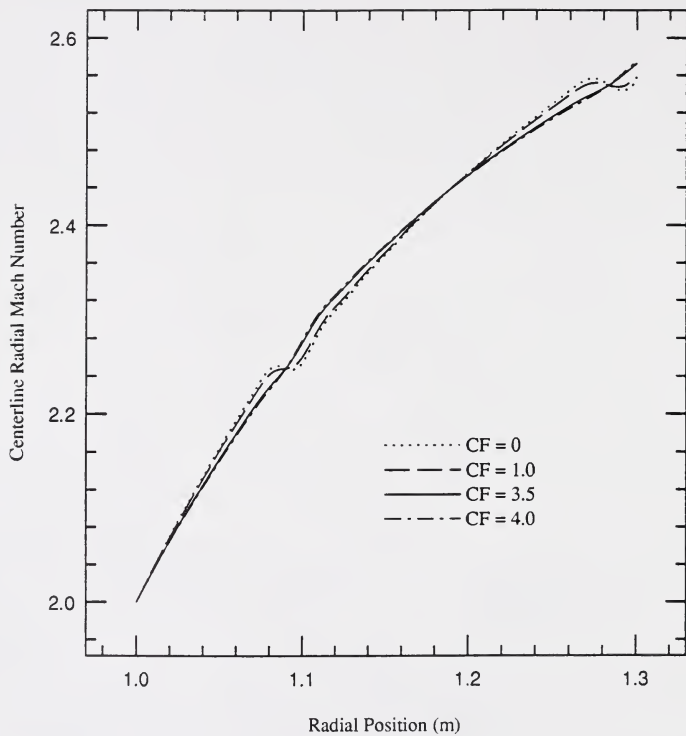


Figure 3.4 Comparison of Centerline Radial Mach Number as a function of Radial Position for Code Factors $CF = 0, 1, 3.5,$ and 4.0 .

$= 1$, $M_T \approx 2.83$, $\bar{T} = 3000$ K, $\bar{P} = 50$ atm, $T_w = 2000$ K, and $dM_T/dl \approx 4.4/m$ - it is found that the code factor varies between $CF = 3.3$, (value predicted by TEMPDIS), and $CF_{th} = 4.0$ (value obtained when Wilson's results (Shapiro, 1954) used in Equation 3-12).

Figures 3.3 and 3.4 provide a comparison of the centerline static pressure and radial Mach number radial profiles for the solutions in which $CF = 0$ (original modeling provided in Section 2.2.4), $CF = 1$ (nearly incompressible flow), $CF = 3.5$ (used in the MHD generator calculations of Sections 3.4 and 3.6), and $CF = 4.0$ (Wilson's H and I ratios (see Shapiro, 1954) and Equation 3-12). It is evident in Figures 3.3 and 3.4 that the fluid experiences an increase in pressure and decrease in Mach number as it passes through the oblique shock. The pressure gain and radial Mach number loss are relatively large at the low CF values; as the code factor and, therefore, the slope of the specified inlet displacement thickness is increased to account for compressibility effects, the changes in Mach number and static pressure across the shock are significantly reduced, indicating that the inlet boundary conditions more correctly match the solution calculated immediately downstream of the inlet plane.

Figure 3.5 provides the static pressure contour plot, $P(r,z)$, for a calculation of a fissioning flow, with $CF = 3.5$, in the same duct geometry and for the same flow conditions as that shown in Figure 3.2 (for which $CF = 0$). It is clear from comparison of Figures 3.5 and 3.2 that the modifications provided in this section serve to more correctly specify the inlet boundary conditions and, therefore,

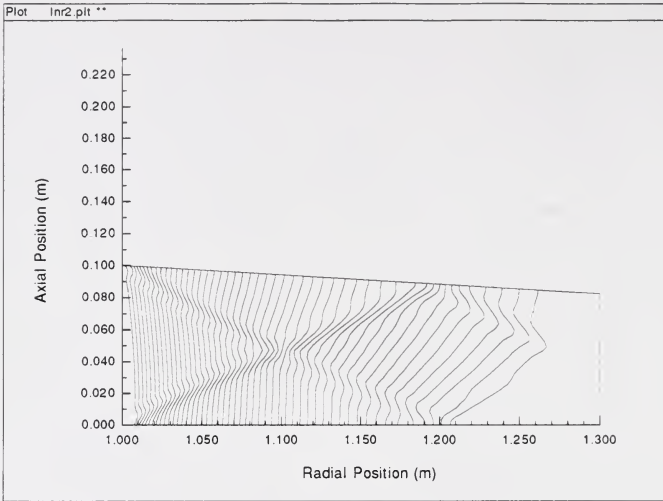


Figure 3.5 Static Pressure Contour Plot of Fissioning Flow in Example Duct Geometry Considered in Figure 3.2, with Code Factor $CF = 3.5$.

significantly reduce the strength of the oblique shocks that originate at the inlet plane.

3.1.2 Outflow Fluid Boundary Condition

The fluid boundary conditions are developed in Section 2.2.4. Recall that because in the supersonic flow fields information cannot travel upstream, against the flow, it was stated that simple extrapolation, from interior points immediately adjacent to and upstream of the exit boundary plane, was adequate to set the outflow boundary condition. It is conventional to use extrapolation at the exit boundary as a means to set the exit boundary conditions for supersonic, as well as subsonic, compressible flows (Roache, 1972 and Peyret and Taylor, 1983). Typically in supersonic flow calculations, full extrapolation of all fluid primitive variables is used to set the exit boundary conditions. In subsonic flows, all but one primitive variable (e.g., ρ or T) are extrapolated, and a "back pressure", or static pressure at the exit plane, is specified, and the remaining primitive variable is back calculated. The boundary condition approaches are consistent with the characteristics of the supersonic and subsonic flow fields (MacCormack, 1989). The appropriate choice of exit conditions is complicated by the viscous effects in the Navier-Stokes flow in that the core of the flow may indeed be supersonic (or subsonic) but the flow in the boundary layer, at some point near the wall, is necessarily subsonic. (It is the experience of the author in looking at the literature that typically if the core flow is supersonic, full extrapolation is used at the exit boundary, in spite of the typically thin subsonic region near the wall.)

As mentioned, in the early MHD calculations (e.g., similar to those reported in Section 3.4), it was found that a significant (e.g., 10%) portion of the duct exit plane was subsonic, in contrast to a very thin boundary layer region in the expanded flows with no MHD effects. In the subsonic boundary layer adjacent to the duct walls, the full extrapolation approach to setting the exit plane boundary conditions (physically incorrectly) inhibits information from traveling upstream in the subsonic boundary layer region; as the boundary layer then thickens, the full extrapolation boundary condition approach is increasingly in error. A number of alternative methods for setting the outlet plane boundary conditions were examined. A method for both specifying a back pressure in the subsonic region while being consistent with extrapolation in the supersonic flow region was developed and is summarized below.

Outflow plenum. It is assumed that a plenum exists adjacent to and downstream of the MHD generator duct (or problem space) in which a plenum "back" pressure axial profile $P_b(z)$ is specified as shown in Figure 3.6. For a given fluid calculation, having specified $P_b(z)$, the static pressure at the outflow (exit) plane is then obtained using the second-order accurate interpolation

$$P_{IMAX,j} = \frac{1}{3} (P_b(z_j) + 3P_{IMAX-1,j} - P_{IMAX-2,j}) \quad (3-13)$$

($j = 1, 2, \dots, JMAX$). Given the static pressure profile at the exit plane, in the subsonic portions of the exit plane, all the fluid primitive variables, except the fluid density, are extrapolated from the interior solution space to the boundary (see Section 2.2.4.); the fluid density is back calculated at each time step using the

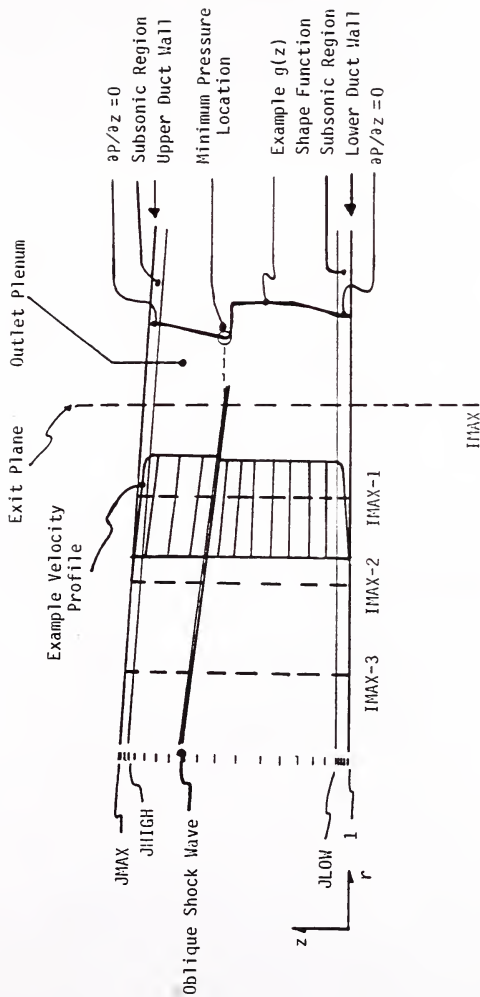


Figure 3.6 Modified Outflow Pressure Boundary Condition Diagram.

current local static pressure and temperature. In the supersonic portion of the exit plane, all the fluid primitive variables are extrapolated from the interior onto the exit plane; at each time step the static pressure in this region is reset to the pressure calculated in Equation 3-13.

A number of schemes have been developed for setting the plenum back pressure distribution $P_b(z)$. In general, the distribution is set using

$$P_b^{n+1}(z_j) = P_{back} g^n(z_j) \quad (3-14)$$

where $g(z)$ is a shape function. The shape function may be specified (e.g., as $g(z) = 1$ to set a uniform outlet plenum back pressure) or calculated. Currently the shape $g(z)$ in the exit plenum is set using

$$g^n(z_j) = \begin{cases} \frac{P_{IMAX,j}^n}{P_{MIN}^n} & \text{in supersonic core flow region} \\ \frac{\partial g(z)}{\partial z} = 0 & \text{in subsonic regions adjacent to walls} \end{cases} \quad (3-15)$$

where

$$P_{min}^n = \min \{ (P^n(IMAX, j)), j = JLOW, JHIGH \}; \quad (3-16)$$

i.e., $g^n(z)$ in the outlet plenum is set so that the shape of the pressure distribution within the supersonic portion (bounded by $j = JLOW$ and $j = JHIGH$) of the outlet plenum flow is the same as the shape of the pressure distribution at the exit plane, and so that the static pressure in the outlet plenum is ($\partial P / \partial z = 0$) through the subsonic layers adjacent to the walls (see also Figure 3.6). The minimum plenum back pressure, P_{back} , can be a specified value (e.g., 0.1 MPa).

Alternatively, to recapture the spirit of the original extrapolation boundary

condition in the supersonic region, P_{back} can be extrapolated using the interpolation Equation 3.14, rearranged with $P_b(z)$, applied at the location of minimum pressure at the exit plane; this approach effects a prediction of the minimum pressure (P_{back}) in the outlet plenum that is consistent with upstream conditions in lieu of the specification of P_{back} .

What is accomplished in the above boundary condition approach is the following: a.) full extrapolation, from the interior solution to the exit plenum, is carried out only in the supersonic region of the flow; b.) the static pressure in the subsonic regions--within the boundary layers--is completely specified through a boundary layer approximation assumption that the static pressure is uniform through the boundary layer; and c.) using the shape function $g(z)$ approach--rather than specifying uniform back pressure in the outlet plenum--accommodates non-uniform exit plane pressure profiles as caused, for example, in the case where an oblique shock wave is propagating out of the exit of the generator, or by asymmetries due to the duct geometry.

3.1.3 Artificial Damping

The third modification to the methodology propounded in Chapter 2 is developed to address (physically incorrect) numerical oscillations that were seen to arise near shock waves captured in the flow solutions obtained, and high frequency oscillations in the free stream total temperature radial distribution upstream of the duct exit in the case where the flow at the duct exit was very close to Mach one. (It should be noted here that the high frequency oscillations were seen in cases in which either a normal shock had entered the exit of the

generator--a case beyond the scope of the supersonic flow solver--or cases in which it can be expected that a normal shock would exist had the duct been a little longer--i.e., cases in which a normal shock was about to enter the duct. Peyret and Taylor (1983) indicate that numerical oscillations can arise in solution schemes based on stable (in the von Neumann sense of linear stability, unaffected by boundary conditions) numerical methods due to nonlinear effects, large spatial gradients (e.g., shock waves or separating flows), large adverse pressure gradients, and the effects of boundary conditions; to this list we can suggest, in the category of adverse pressure gradients, that oscillations may be induced or amplified by strong MHD body forces. The conventional approach to damping these non-physical oscillations is to introduce artificial damping, based on von Neumann and Richtmeyer's proposed introduction of artificial diffusion (artificial viscosity) terms in the Euler equations (see treatment by Roache, 1972). The artificial damping implemented in this thesis is influenced by the work reported by Li and Kroll (1989) and the texts by Anderson et al. (1984), Peyret and Taylor (1983), and Roache (1972).

Approaches to artificial damping typically include adding second-order diffusion terms ($\sim \Delta x^2 |\partial^2 Q / \partial x^2|$) to reduce potentially large-scale oscillations in the neighborhood of shock waves, arising from (odd-even) decoupling of the finite-difference points when central differences (effected by MacCormack's scheme) are employed, and adding fourth-order diffusion terms ($\sim \Delta x^4 |\partial^4 Q / \partial x^4|$) to reduce high frequency oscillations that remain undamped in the central-differenced schemes. The second and fourth-order damping terms can be explicitly added to the

governing equation--i.e., outside of the flux vector derivative terms--or they can be implicitly included as part of the flux vectors; the latter approach is employed here. (See Pullium and Steger, 1981 for discussion and example of fourth-order explicit terms and second-order implicit damping terms; see Li and Kroll, 1989 for insightful discussion on the implicit second and fourth-order damping approach proposed by Jameson et al., 1981.) In the present work, the implicit second-order damping developed by MacCormack and Baldwin (1975) (recorded both in Anderson et al., 1984 and Peyret and Taylor, 1983) and the implicit fourth-order damping term of Jameson et al. (1981) (reported in Li and Kroll, 1989) are employed.

The artificial damping is included in the developed fluid solver in both the r and z directions. For brevity, the philosophy behind the methods is presented below by considering only the radial damping terms. Considering Equation 2-24 (the vector form of the governing fluid equations in cylindrical coordinates) and neglecting for the sake of simplifying the discussion the z -dependence and the viscous, fission, and MHD source terms, the resulting Euler equations are

$$\frac{\partial Q}{\partial t} + \frac{\partial \underline{E}}{\partial r} = 0 \quad (3-17)$$

where \underline{E} is the flux vector. Introducing the damping, Equation 3-17 is modified to

$$\frac{\partial Q}{\partial t} + \frac{\partial (\underline{E} - \underline{S} + \underline{T})}{\partial r} = 0 \quad (3-18)$$

\underline{S} is the second-order damping term of MacCormack and Baldwin and \underline{T} is the fourth-order term, after, Jameson. In this work we use

$$\underline{S}_{ij}^* \equiv \epsilon_1 \left((|u| + a)_{ij}^n \nu_{ij}^n [Q_{ij}^n - Q_{i-1,j}^n] \right) \quad (3-19)$$

where "*" indicates the predictor step of the MacCormack scheme; the backward difference approximation used in Equation 3-19 is appropriate for a forward difference predictor step (see alternating order delineated in Table 2.5). ϵ_1 is a specified constant, and u and a are the local radial component of velocity and the speed of sound, respectively; the pressure "sensor", ν_{ij}^n , is given by

$$\nu_{ij}^n \equiv \frac{|P_{i+1,j}^n - 2P_{ij}^n - P_{i-1,j}^n|}{P_{i+1,j}^n + 2P_{ij}^n + P_{i-1,j}^n} . \quad (3-20)$$

Using the damping term of Equation 3-19 in Equation 3-18 effects an implicit second order damping term of the form

$$\frac{\partial \underline{S}}{\partial r} = \epsilon_1 \Delta r^4 \frac{\partial}{\partial r} \left\{ \frac{|u| + a}{4P} \left| \frac{\partial^2 P}{\partial r^2} \right| \frac{\partial Q}{\partial r} \right\} \sim \frac{\partial}{\partial r} \left(\mu_a \frac{\partial Q}{\partial r} \right) \quad (3-21)$$

where μ_a is an artificial viscosity given by

$$\mu_a = \epsilon_1 \left[\frac{|u| + a}{4P} \left| \frac{\partial^2 P}{\partial r^2} \right| \right] \Delta r^4 . \quad (3-22)$$

Note that this viscosity is very small in locations away from rapid spatial gradients in the static pressure (e.g., around shock waves) and increases with the speed of the flow.

The fourth-order damping for the high frequency oscillations is added through

$$\underline{T}_{ij}^* = \epsilon_2 (|u| + a)_{ij}^n \nu_{ij}^n (Q_{i+1,j}^n - 3Q_{ij}^n + 3Q_{i-1,j}^n - Q_{i-2,j}^n) \quad (3-23)$$

(here for a forward-difference in the predictor-step of the MacCormack scheme).

The pressure sensor, $\nu_{i,j}^n$ is given by Equation 3-20 and ϵ_2 is given by $\epsilon_2 = \max \{ 0, k_4 - \epsilon_1 \nu_{\max} \}$ where k_4 is a constant within a specified range and where ν_{\max} is the maximum of pressure sensors at the finite-difference points involved in the third-order derivative of Equation 3-23. (Note, in this work we let $\nu_{\max} = \nu_{i,j}$.)

Therefore, an artificial damping term of the form

$$\frac{\partial T}{\partial r} = \epsilon_2 \frac{\partial}{\partial r} \left[\frac{|u| + a}{4P} \left| \frac{\partial^2 P}{\partial r^2} \right| \frac{\partial^3 Q}{\partial r^3} \right] \Delta r^4 \quad (3-24)$$

is added to the governing equations.

By the author's interpretation of the literature, MacCormack and Baldwin (1975) suggest that $0 \leq \epsilon_1 \leq 0.5$, Li and Kroll (1989) after Jameson et al., (1981) suggest $3 \leq \epsilon_1 \leq 5$ and Knight (1981) suggests for high speed flows $\epsilon_1 = 5$; Jameson et al. (1981) suggest that $1/32 \leq k_4 \leq 1/16$; Li and Kroll (1989) suggest $1/128 \leq k_4 \leq 1/32$. Typically for the calculations performed in this work, $\epsilon_1 = 1$ and $k_4 = 3 \times 10^{-2}$ are used; i.e., the damping is kept relatively small compared to the values suggested in the literature for high speed flows.

The effect of damping was found to be small in terms of the change in the larger oscillations (which take place over several grid points) encountered in the immediate neighborhood of a captured shock (with the ϵ_1 value used); however, the damping was added primarily to control the high frequency oscillations evidenced before stronger normal shocks encountered at the larger MHD

interaction levels. The damping was found to be successful in damping the higher frequency oscillations; this was seen by the smoothing-out of high frequency spatial oscillations--for example, in the total temperature--and in the enhanced rate of convergence in the fluid solver due to the damping of nonlinear induced effects.

3.1.4 Turbulence Model Restriction

The final modification to the developed solution methodology is a restriction placed on the Baldwin-Lomax model (discussed in Section 2.2.2) which is used in the turbulent flow calculations of this thesis to obtain the turbulent (eddy viscosity) component of the fluid viscosity. Recall that the Baldwin-Lomax (B-L) model is used, rather than the more conventional Cebeci-Smith (C-S) turbulence model, specifically because the B-L model does not require determination of the boundary layer thickness (needed in the Klebanoff Intermittency Factor, $\gamma(z)$, used in the C-S model); however, the B-L model requires that the position z_{\max} (measured normal to and away from the wall) corresponding to the maximum (F_{\max}) in the $F(z)$ vorticity function distribution be accurately determined. F_{\max} is given by

$$F_{\max} = \max\{F(z)\} = \max\left\{\frac{l}{\kappa} |\underline{\omega}(z)|\right\} \quad (3-25)$$

where l is the Prandtl mixing length, for which the van Driest mixing length model is used (see Equation 2-31), κ is the von Karman factor (typically 0.41), and $\underline{\omega}$ is the local vorticity. F_{\max} is determined by searching from the wall outward toward the centerline.

As noted in Section 2.2.2, Shirazi and Truman (1989) discovered ambiguity in determining the location of F_{\max} for the case of supersonic flow past a sphere-cone: They found it necessary to restrict the search for F_{\max} to the boundary layer region, and they developed criteria to determine the boundary layer edge for their problem. One of the objectives of this work stated in Section 2.2.2 is to determine whether there are multiple local-maxima in the $F(z)$ distribution for the case of the Hartmann flow profiles expected in the MHD flow, leading to ambiguity in determining F_{\max} . In the course of this work, it was found that for the MHD flows there is indeed ambiguity introduced into the search for F_{\max} .

Example $F(z)$ distributions are provided in Figure 3.7 (showing $F(z)$ as a function of the axial grid number index, plotted from the wall ($j = 1$) the center grid line ($j = 51$)) for generator flows in ducts with linearly decreasing duct height (described in Section 3.1.4) with applied magnetic inductions of 0 T, 3.5 T, and 4.0 T; these example cases are discussed in detail in Section 3.4. Recall that the axial grid distribution is highly stretched: Grid lines 10, 20, and 50 correspond to distances from the lower wall of 9×10^{-5} m, 1.52×10^{-3} m, and 4.79×10^{-2} m, respectively. Note that both the $B = 3.5$ T and the $B = 4.0$ T cases exhibit two large peaks; the correct F_{\max} is located near grid line 25 or $z = 4.98 \times 10^{-3}$ m. In the $F(z)$ distributions shown in Figure 3.7, the second large peak away from the lower wall is lower in magnitude than the first (F_{\max}) large peak, located closer to the wall; this is not always the case. The $F(z)$ distribution for the $B = 4.0$ T case exhibits a local maxima (near grid line $j = 10$, located at $z = 9 \times 10^{-5}$ m) which is

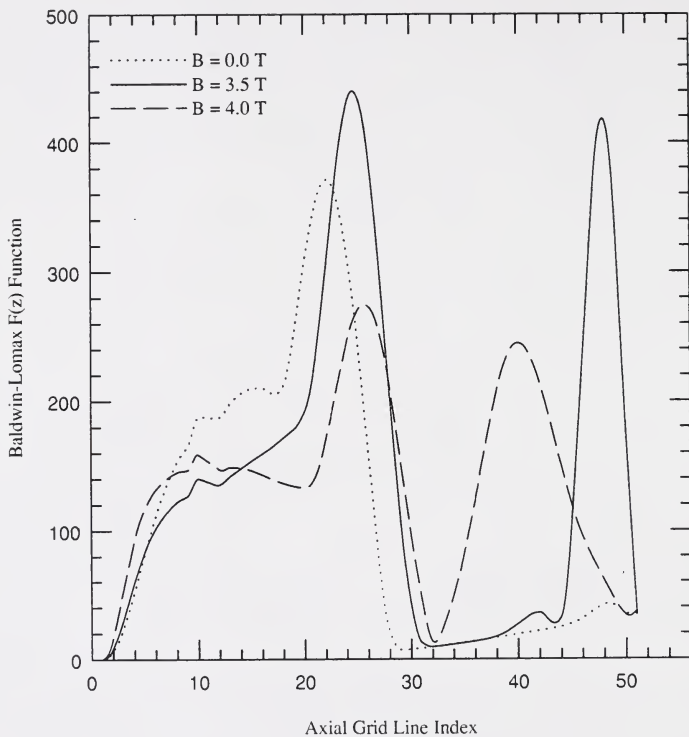


Figure 3.7 Comparison of the Baldwin-Lomax $F(z)$ Distribution for Various Applied B-Fields; $F(z)$ is Plotted as a function of Axial Grid Line Index, from Wall to Center Grid Line.

not the F_{\max} . It is not advisable that the search for F_{\max} consist of simply searching from the wall outward toward the centerline for the first local maxima.

The turbulence modeling is modified in the calculations in this work by restricting the search to a restricted range between the wall and some specified point (grid line), determined to be closer to the wall than the position of the second peak. For example, in the calculations for the results presented in the following section, F_{\max} is determined as the maximum value in the $F(z)$ distribution in the range $j = 1$ ($z = 0$ m) and $j = 35$ (corresponding to $z = 1.89 \times 10^{-2}$ m).

Similar to the findings of Shirazi and Truman (1989), it is concluded that the search for F_{\max} should be restricted to a specified region to avoid ambiguity. It is not the intention of the author here to suggest that the multiple local-maxima in $F(z)$ arise because of the Hartmann-type profiles--i.e., flows that may exhibit velocity overshoot--but rather to record that ambiguity arose in the MHD flows and to note the restriction placed on the general Baldwin-Lomax model. With the approach taken here of specifying a maximum grid line (or distance from the lower wall) in which the search for F_{\max} takes place, the Baldwin-Lomax model still maintains the flexibility of not necessitating determination of the actual boundary layer thickness.

3.2 Duct Geometry Selection

The disk MHD generator duct geometry is found to profoundly affect the spatial profiles of generator fluid mechanic and electromagnetic variables, and

therefore generator performance levels. As discussed in Section 1.2, the supersonic disk MHD generator internal flows tend to decelerate towards Mach one. The generator duct height (or cross-sectional flow area) can be designed to overcome, to an extent, the diffusing and decelerating influences in the generator. Indeed the outflow cylindrical geometry facilitates rapid expansion of the working fluid; for example, in ducts of constant height--those which introduce no axial turning to the fluid--the flow area increases linearly with radius. On the other hand, according to analysis using the quasi-one-dimensional MHD solver described in Appendix A, over-expanding the generator flow may prove detrimental to desired generator performance levels.

An evolution of generator duct geometries is examined in this section. The constant (cross-sectional flow) area and constant height duct geometries are first considered first; the duct geometry used in the MHD generator calculations in the remainder of the work is then considered. The effects of varying the level of the spatially uniform neutron flux level on the supersonic flow field, in the absence of MHD effects, are studied in these geometries.

Lower wall. As noted in Section 2.3.2, the lower wall of the ducts analyzed in this work is flat; i.e., the lower wall has no curvature and is everywhere perpendicular to the z -axis of the cylindrical coordinate system. This dictates that the metrics r_n and z_t are each uniformly zero along the lower wall of the generator ducts. Although this necessarily produces geometry induced axially asymmetric flow fields (except in the special case of the constant height duct), this

restriction is imposed (see Section 2.3.2) to simplify the electromagnetic boundary condition application along the lower wall.

3.2.1 Constant Area Duct

Figure 3.8 provides a schematic diagram of the constant area duct geometry. The duct inlet is located at $r = 1.0$ m and the inlet duct height is 0.1 m. The inlet conditions considered here include stagnation temperature, $\bar{T} = 3000$ K, stagnation pressure, $\bar{P} = 5.066$ MPa (50 atm), radial Mach number, $M_r = 1.5$, and swirl factor, $S = 0.5$ (the last two combine to provide a total Mach number, $M_T = 1.68$). The inlet boundary layer thickness, δ , at both the upper and lower walls, is assumed to be 1×10^{-3} m (1 mm). The upper and lower wall temperatures are uniformly 2000 K.

The radial profiles of the radial Mach number along the duct centerline (grid line 51 of 101) for flow with neutron flux levels of 0, 10^{16} n/cm²s (the nominal level for the MHD calculations in Sections 3.4 and 3.6), and 10^{17} n/cm²s are compared in Figure 3.9. It is seen that: a.) the fission energy deposition in the fluid works to decelerate (or inhibit acceleration of) the flow toward Mach one (see earlier discussion in Section 1.2); and b.) the radial Mach number does not vary smoothly (monotonically) with radial position but rather exhibits significant inflections.

Wave structure. The inflections in the radial Mach number curves of Figure 3.9 arise as a result of compression and rarefaction waves. The wave structure is evident in the static pressure contour plot of the constant area flow

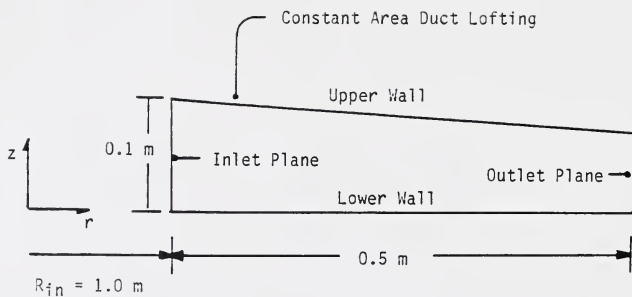


Figure 3.8 Schematic Diagram of Constant Area Duct Geometry.

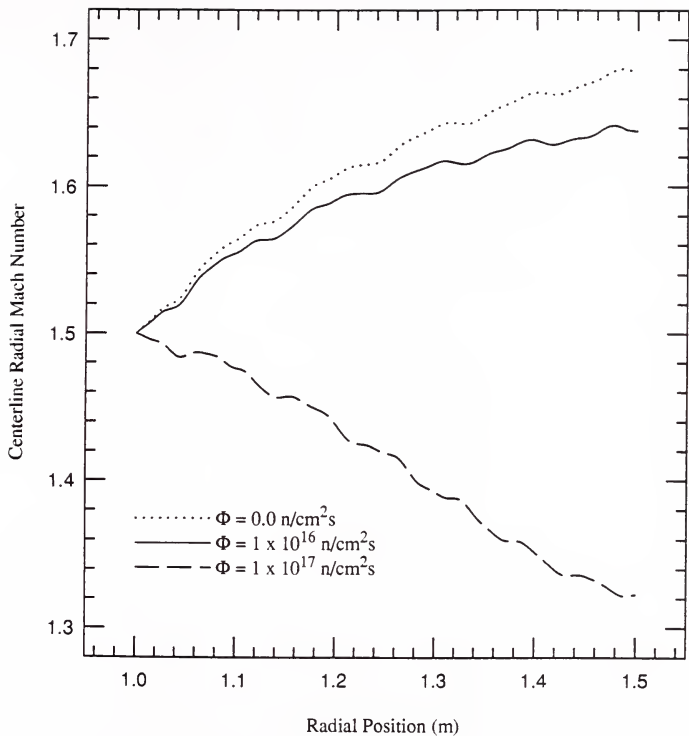


Figure 3.9 Comparison of Centerline Radial Mach Number as a function of Radial Position and Neutron Flux Level for Constant Area Duct Geometry.

without fissioning provided in Figure 3.10. The highly complicated wave structure is thought to arise in the interaction of the rarefaction (Prandtl-Meyer) waves, continuously generated in the expansion along the curved upper wall, compression waves formed in the apparent converging (impinging) of the flow near the lower wall with the flow near the upper wall, and compression waves generated by the specified boundary conditions (see the discussion in Section 3.1.1); numerical oscillations introduced by the numerical method (MacCormack's method) in the vicinity of compression waves may further complicate the flow field (cf. discussion regarding the compression corner calculations in Appendix C).

Neutron flux level. As indicated in Figure 3.9, increasing the neutron flux level, increasingly serves to decelerate (diffuse) the duct flow. Figure 3.11 reflects this in a comparison of the axial profiles of the predicted radial component of velocity for the same three neutron flux levels of 0, 10^{16} n/cm²s, and 10^{17} n/cm²s, near the lower wall, at a radial position of 1.4 m. The axial profiles at the three neutron flux levels are qualitatively the same, but the flow is decelerated as the neutron flux level increases. Figure 3.12 provides a comparison of the axial static temperature profiles, at the same position, for the three neutron flux levels. Again, the effect of increasing neutron flux levels (and fission density) is exhibited: static temperature in the core flow region increases with increasing neutron flux level; i.e., considering the decrease in velocity (Figure 3.11) and the increase in temperature (Figure 3.12) in the core flow region, the working fluid is clearly diffused as the neutron flux increases. Interestingly, as the increase in flux level and the fission power diffuses the flow, the increase in static temperature

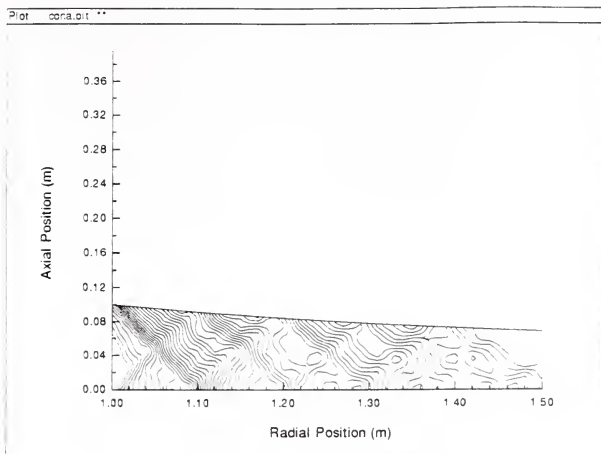


Figure 3.10 Static Pressure Contour Plot of Fissioning Flow ($\Phi = 10^{16}$ n/cm²s) in Constant Area Duct Geometry.

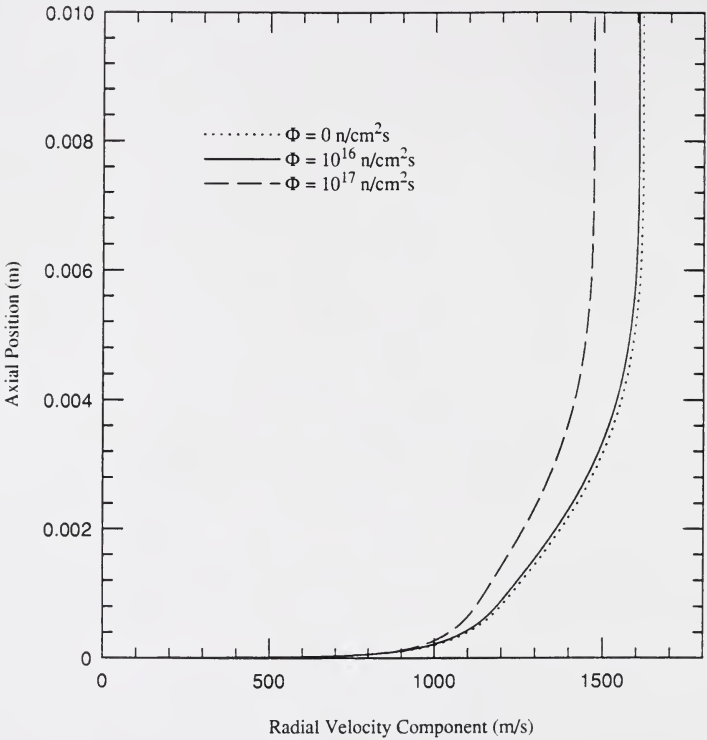


Figure 3.11 Comparison of Radial Velocity Component Axial Profile at the Lower Wall and Radial Position $r = 1.4 \text{ m}$ as a function of Neutron Flux Level for Constant Area Duct Geometry.

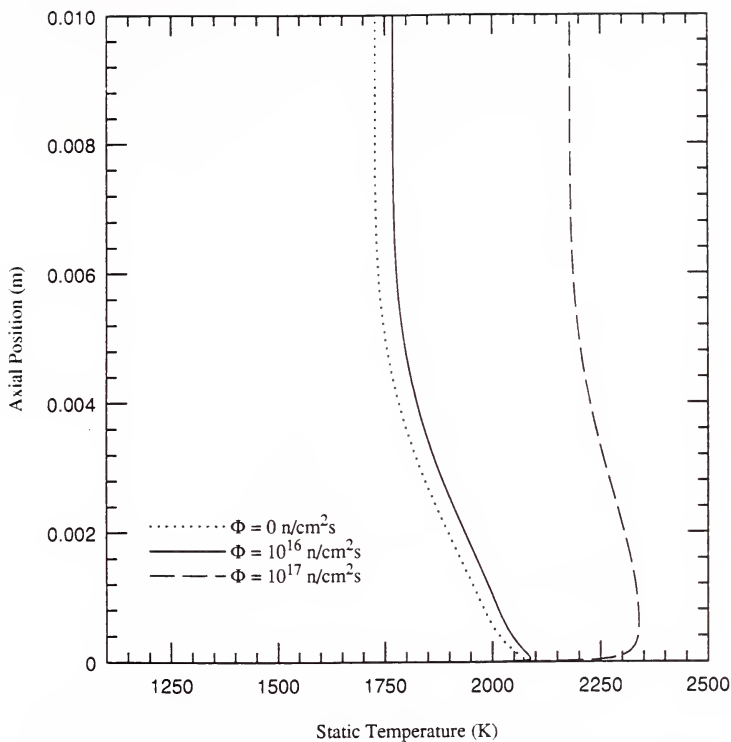


Figure 3.12 Comparison of Static Temperature Axial Profiles at the Lower Wall and Radial Position $r = 1.4 \text{ m}$ as a function of Neutron Flux Level for Constant Area Duct Geometry.

and static pressure yield an increase in the local fluid density, further increasing the fission power density at the given flux level.

Figure 3.12 further illustrates the behavior of the static temperature near the lower duct wall. The temperature increases through the boundary layer due to viscous heating and decreasing convective heat transfer (due to the boundary layer velocity defect). Temperature overshoots are evident at each of the neutron flux levels considered. The heat transfer rate (to the wall) increases with increasing neutron flux level; clearly at a neutron flux level of 10^{17} n/cm²s, the heat transfer rate to the wall (with a temperature of 2000 K) is dramatically increased over that with zero fissioning ($\Phi = 0$ n/cm²s).

It is noted that the constant area duct geometry serves to insure that $\partial A/\partial r \approx 0$; recall from Figure 3.8 that the constant area geometry actually provides for a slight increase in the flow area to account for estimated boundary layer growth. The radial Mach number increases, in the case of zero fissioning flow, and the swirl factor decreases so that the total Mach number remains nearly uniform throughout the duct. In this example, the inlet total Mach number is purposely set relatively low ($M_T \approx 1.68$)--that is relative to the inlet Mach number used in the constant height duct of the next subsection and for the linearly decreasing duct height MHD generator calculations of Section 3.2.3, 3.4, 3.6, and 3.7 ($M_T \approx 2.83$)--so that the fluid density is (relatively) high; i.e., the constant area duct geometry and the specified inlet conditions of the example case considered provide for high fission power density levels, for the given neutron flux levels.

The effects of fissioning seen in the figures in this subsection are, in general, more profound, more marked, than those seen in the remainder of this work.

3.2.2 Constant Height Duct

The constant height duct geometry examined here is identical to that of the constant area duct shown in Figure 3.8 save that the upper wall is parallel to, and is located at a constant distance (0.1 m) from, the lower wall; $\partial A/\partial r \sim r$ in this geometry. The inlet conditions considered here are $\bar{T} = 3000$ K, $\bar{P} = 5.066$ MPa (50 atm), $M_R = 2.0$ and $S = 1.0$ ($\Rightarrow M_T \approx 2.83$); the inlet boundary layer thickness (δ) at the lower and upper wall is set at 1×10^{-3} m; the upper and lower wall temperatures are uniformly 2000 K.

The radial profiles of the centerline radial Mach number for neutron flux levels of 0 , 10^{16} n/cm²s, and 10^{17} n/cm²s in the constant height duct are compared in Figure 3.13.

Wave structure. The radial Mach number profiles (in contrast to those of the constant area duct in Figure 3.9) exhibit smooth increases with radial position; slight inflections in the profiles do exist near $r = 1.1$ m and $r = 1.3$ m. Figure 3.14 provides a static pressure contour plot of the flow field without fissioning ($\Phi = 0$ n/cm²s). It is evident that the small inflections seen in Figure 3.13 correspond to the positions in which the weak oblique waves that originate at the inlet plane interact with each other, first at $r \approx 1.1$ m and again, further downstream at $r \approx 1.3$ m, after having reflected off the walls near $r \approx 1.2$ m. The oblique waves are artifacts of the inlet boundary conditions (see discussion in Section 3.1.1). It is seen by comparing the pressure contour plot of Figure 3.14

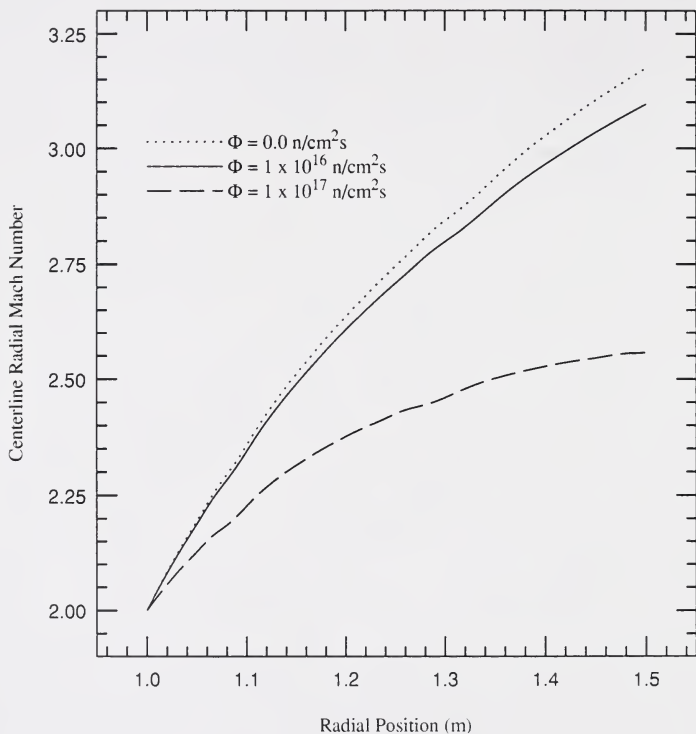


Figure 3.13 Comparison of Centerline Radial Mach Number as a function of Radial Position and Neutron Flux Level for Constant Height Duct Geometry.

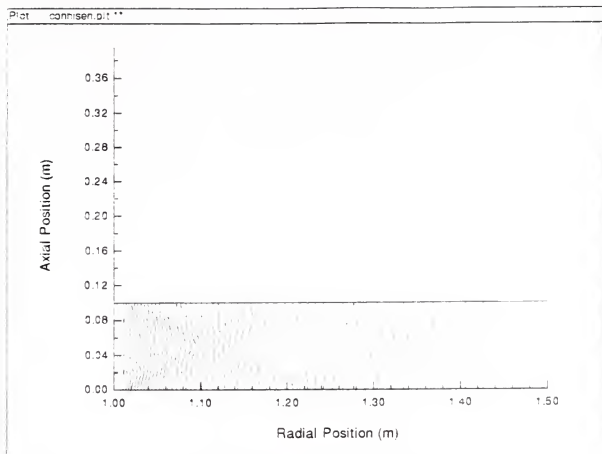


Figure 3.14 Static Pressure Contour Plot for flow in Constant Height Duct Geometry.

with that in Figure 3.10 for the constant area duct that the flow in the constant height duct is much less complicated in terms of the wave structure due to the lack of the Prandtl-Meyer expansion waves and impinging flow compression effects. Further, the "clean" wave structure of Figure 3.14 lends confidence to the theory modifications developed in Section 3.1.1 to avoid strong inlet plane-generated oblique shock waves and also suggests that the MacCormack method itself is not alone responsible for the complicated structure in Figure 3.10.

Neutron flux levels. The effect of fissioning seen in Figure 3.13 is to reduce the rate at which the working fluid is expanded in the duct of increasing area; i.e., the fissioning again tends to diffuse the flow. Because the area increases linearly with radial position in this case, in contrast to the constant area duct examined in the previous section, the flow is accelerated to a greater extent. Further, the higher inlet total Mach number considered in this example, and the increasing radial Mach number through the duct, assure that the fluid density is significantly lower in the constant height duct as compared to that in the constant area duct; e.g., the ratio of centerline fluid density corresponding to $M_{T,in} \approx 2.83$ of the constant height case to that, corresponding to $M_{T,in} \approx 2.83$, of the constant area case is ≈ 0.3 . For a given neutron flux level, therefore, the fission power density levels encountered in the constant area duct example are three times higher than those experienced in the constant height duct example.

3.2.3 Linearly Decreasing Duct Height

The disk MHD generator solutions presented in the remainder of this chapter are for duct geometries with linearly decreasing upper wall duct heights;

the duct cross-sectional flow area is given by

$$A(r) = A_{in} \left[\frac{r}{R_{in}} \right] \left[1 + \left(\frac{H_{ex} + \Delta}{H_{in}} - 1 \right) \left(\frac{r - R_{in}}{R_{ex} - R_{in}} \right) \right] \quad (3-26)$$

where H_{ex} is set to

$$H_{ex} = H_{in} \left(1 - \frac{R_{ex} - R_{in}}{2R_{ex} - R_{in}} \right) \quad (3-27)$$

to assure that $\partial A/\partial r \geq 0$ and that $\partial A/\partial r \approx 0$ at the exit; $\partial A/\partial r = 0$ at the duct exit if $\Delta = 0$. Δ is typically set to 1×10^{-3} , and is simply a factor that allows for the expected boundary layer growth (i.e., increase in the displacement thickness) through the generator. (If $H_{ex} = H_{in}$ then a constant height duct is specified.)

Figure 3.5 (of Section 3.1.1) provides a static pressure contour plot for the linearly decreasing duct height geometry considered here and in Sections 3.3 and 3.4. The inlet conditions are $\bar{T} = 3000$ K, $\bar{P} = 5.066$ MPa (50 atm), $M_R = 2.0$ and $S = 1.0$ ($\Rightarrow M_T \approx 2.83$); the inlet boundary layer thickness (at both the upper and lower walls) is assumed to be 1×10^{-3} m; the upper and lower wall temperatures are uniformly 2000 K.

As a point of documentation, the effect of neutron flux levels on the radial velocity component and the static temperature axial profiles, in the linearly decreasing duct height geometry, at $r = 1.25$ m (corresponding to the cathode in the MHD generator calculations of Section 3.4), are presented in Figure 3.15 and 3.16, respectively. The effects of fissioning on the axial profiles, in this geometry and with the inlet conditions considered, are small. The flow is diffused slightly at

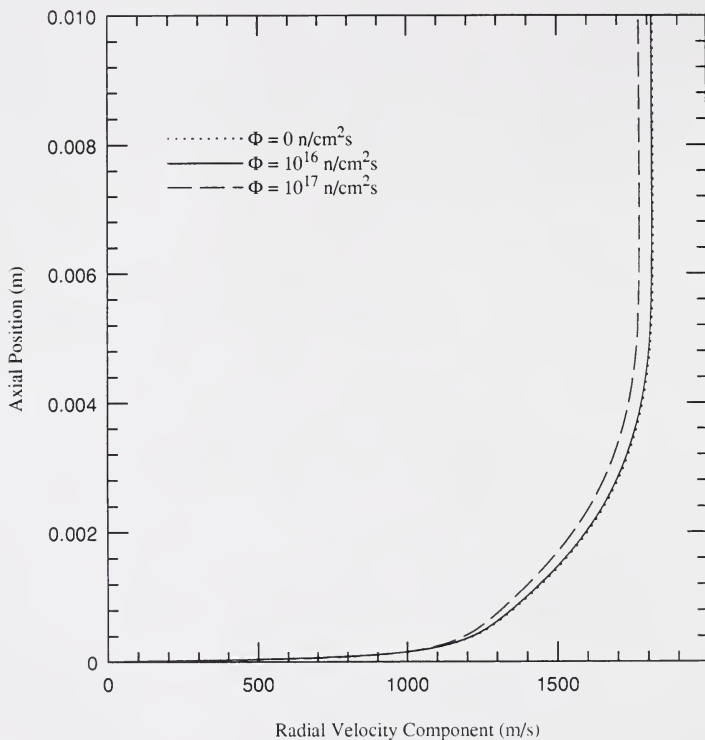


Figure 3.15 Comparison of Radial Velocity Component Axial Profile at Lower Wall and Radial Position $r = 1.25 \text{ m}$ as a function of Neutron Flux Level for Linearly Decreasing Duct Height Geometry.

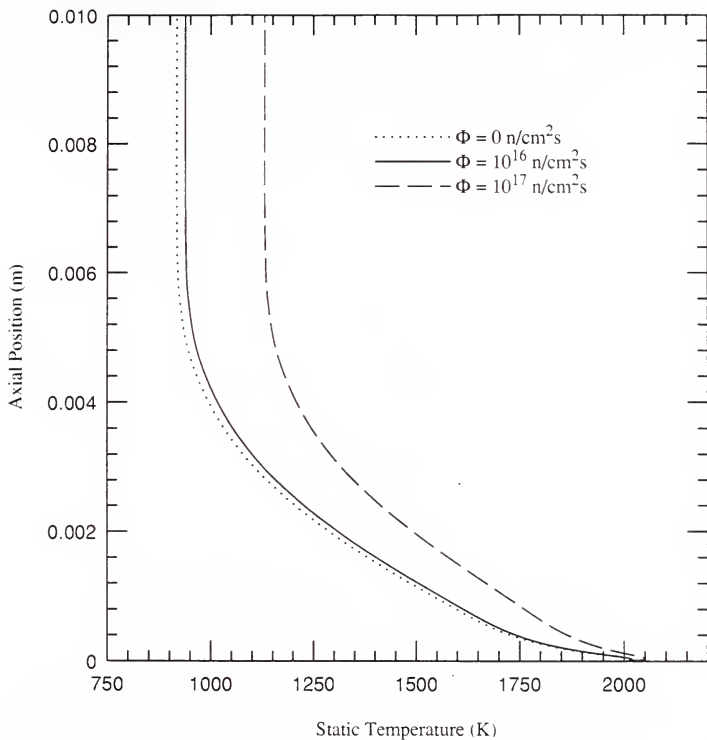


Figure 3.16 Comparison of Static Temperature Axial Profile at Lower Wall and Radial Position $r = 1.25 \text{ m}$ as a function of Neutron Flux Level for Linearly Decreasing Duct Height Geometry.

the flux levels of 10^{17} n/cm²s; however, at $\Phi = 1 \times 10^{16}$ n/cm²s, the radial velocity and static temperature profiles are virtually indistinguishable from those for flow without fissioning ($\Phi = 0$ n/cm²s).

The effects of fissioning on the radial flow variable profiles are consistent with the diffusing action of the fission energy deposition in the fluid as seen in the following section and as seen in the previous two subsections, especially in Section 3.2.1.

3.3 Comparisons with Quasi-One-Dimensional Flow Solver

A quasi-one-dimensional (Q1D) Euler (inviscid) solver with MHD and fission source terms was developed by the author separate from this work; the Q1D solver is described in Appendix A. In this section, radial profile solutions for selected flow variables from the Q1D Euler solver for the linearly decreasing duct height geometry shown in Figure 3.17 are compared with centerline (grid line 51 of 101) radial profiles for the corresponding flow variables as predicted by the thin-layer Navier-Stokes (N-S) solver developed in this work. The inlet conditions, identical to those used in the MHD calculations of Section 3.4 (and also earlier for the constant height duct examined in the last section), are $\bar{T} = 3000$ K, $\bar{P} = 5.066$ MPa (50 atm), $M_R = 2.0$, $S = 1.0$; $\delta = 1 \times 10^{-3}$ m is assumed; and the lower and upper wall are uniformly 2000 K. The spatially uniform neutron flux level values examined are 0, 1×10^{16} n/cm²s, and 1×10^{17} n/cm²s.

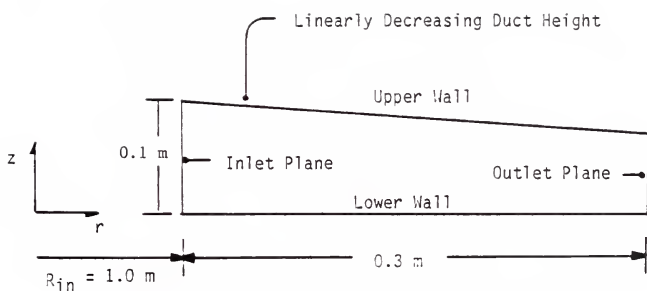


Figure 3.17 Schematic Diagram of Linearly Decreasing Duct Height Geometry Typical of Ducts considered in the Remainder of Chapter 3.

3.3.1 2-D Zero Viscosity/Q1D Euler Flow Comparison

Fortuitously, in an early calculation involving the 2-D N-S solver, the laminar and turbulent viscosity and thermal conductivity were accidentally set to zero, effecting what was essentially a 2-D Euler solution by the 2-D N-S code; the flow variable centerline values of this solution were found to agree nearly exactly with the corresponding values from the Q1D solution, providing, to an extent, a check on the consistency of the two codes.

Continuing in the same vein, Figure 3.18 provides a comparison of the 2-D N-S solution centerline radial Mach number radial profile, in which the laminar viscosity and thermal conductivity are set near zero and the turbulent eddy viscosity and conductivity are set to zero, and the Q1D solution radial Mach number radial profile for flow in the linearly decreasing duct geometry; both flow without fissioning ($\Phi = 0 \text{ n/cm}^2\text{s}$) and flow with fissioning ($\Phi = 1 \times 10^{16} \text{ n/cm}^2\text{s}$, the flux level used in the MHD generator calculations of this work) are shown in the same figure. Further, for the case of the flow without fissioning, an analytical solution of the quasi-one-dimensional flow equations in the outflow disk geometry (see equations in Appendix A, setting MHD and fission source terms to zero) can be formulated; analytical solution points are included in the zero fissioning case on the same Figure 3.18. Evidently, the 2-D N-S flow with (near) zero viscosity solution agrees exactly with the Q1D Euler solutions--numerical and analytical--for flow without fissioning. The 2-D N-S flow with (near) zero viscosity solution for the case of fissioning flow also agrees exactly with the Q1D numerical solution. Although not shown here, it is found that the agreement in the total

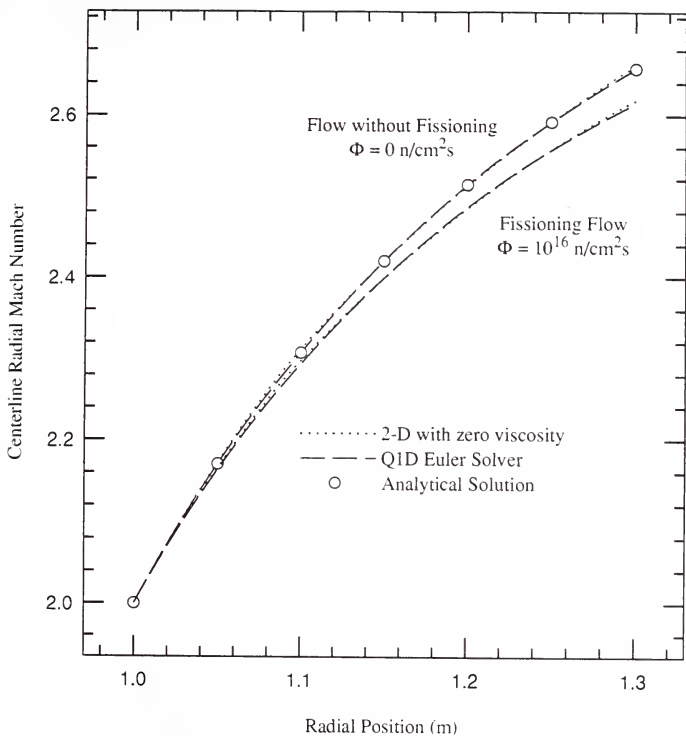


Figure 3.18 Comparison of 2-D Navier-Stokes and Q1D Euler Numerical and Analytical Predictions of the Centerline Radial Mach Number as a function of Radial Position for Linearly Decreasing Duct Height Geometry.

temperature and total pressure--key to calculating MHD generator system power levels and efficiency--between the 2-D and Q1D solutions is also exact. The agreement seen in Figure 3.18 helps give confidence that the governing equations are integrated correctly by the 2-D code and also that the thin-layer Navier-Stokes equations solved in the developed code properly become the Euler equations in the limit that viscosity goes to zero.

3.3.2 2-D Turbulent/Q1D Euler Comparison

Figures 3.19 through 3.22 provide comparisons of the centerline radial Mach number (M_R), swirl factor (S), total temperature (\bar{T}), and total pressure (\bar{P}) predictions of the developed 2-D N-S solver with those of the Q1D Euler Solver (Appendix A) for neutron flux levels of 0, 10^{16} n/cm²s, and 10^{17} n/cm²s, in the linearly decreasing duct height geometry. The neutron flux level of 1×10^{16} n/cm²s is the nominal, or baseline, neutron flux level considered in the remainder of the thesis. The solid curves of Figure 3.19 through 3.22 provide, therefore, the behavior of the radial Mach number, swirl factor, total temperature and total pressure, respectively, for linearly decreasing duct height geometry for flow with fissioning and without MHD effects.

Figure 3.19 again indicates that the effect of fissioning is to decelerate (or inhibit the acceleration of) the flow; as the neutron flux increases, the flow is more decelerated. The viscous effects of the turbulent flow are evident in the same figure. As expected (see discussion of Section 1.2), the radial Mach numbers predicted by the 2-D N-S solver are lower, for a given flux level, than those predicted by the Q1D (inviscid) solver. Recall that Figure 3.18 shows that

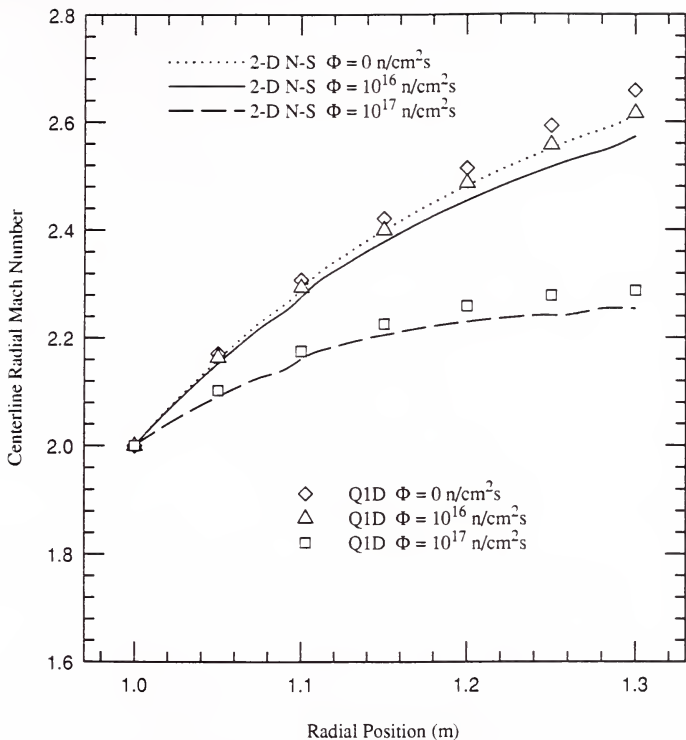


Figure 3.19 Comparison of 2-D Navier-Stokes and Q1D Predictions of Centerline Radial Mach Number as a function of Radial Position and Neutron Flux Level in Linear Decreasing Duct Height Geometry.

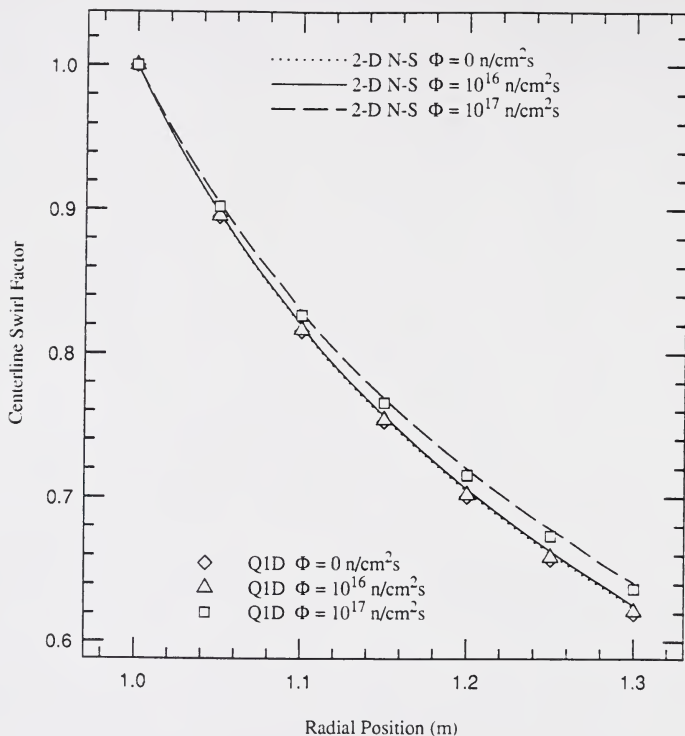


Figure 3.20 Comparison of 2-D Navier-Stokes and Q1D Predictions of Centerline Swirl Factor as a function of Radial Position and Neutron Flux Level in Linear Decreasing Duct Height Geometry.

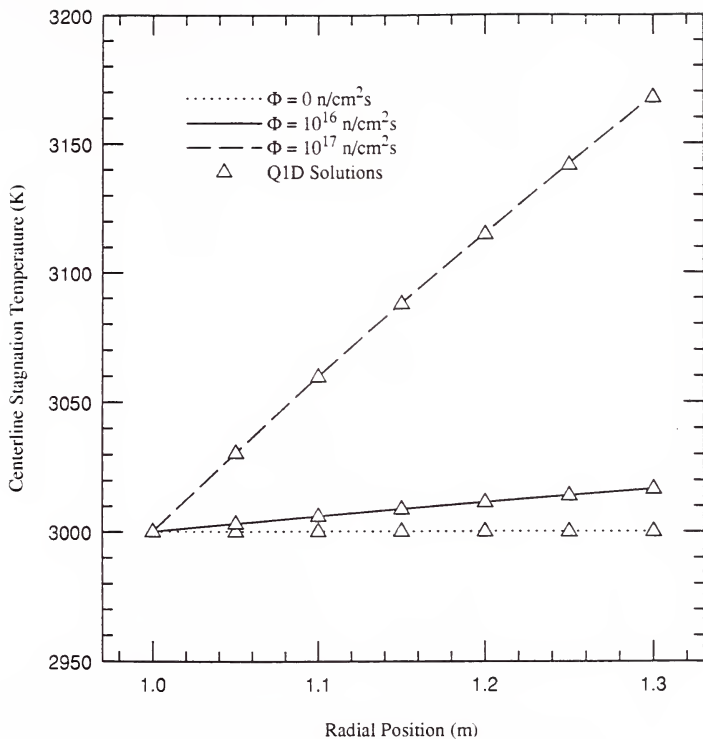


Figure 3.21 Comparison of 2-D Navier-Stokes and Q1D Predictions of Centerline Stagnation Temperature as a function of Radial Position and Neutron Flux Level in Linear Decreasing Duct Height Geometry.

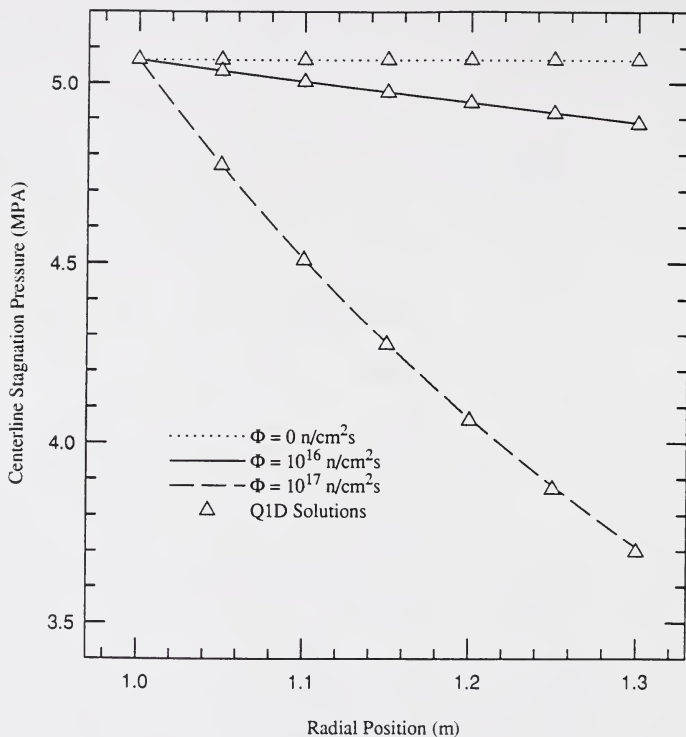


Figure 3.22 Comparison of 2-D Navier-Stokes and Q1D Predictions of Centerline Stagnation Pressure as a function of Radial Position and Neutron Flux Level in Linear Decreasing Duct Height Geometry.

in the absence of viscosity, the 2-D (centerline) and Q1D solutions agree exactly; therefore, the discrepancy between the Q1D points and 2-D N-S curves in Figure 3.19 is attributable to the turbulent flow viscous effects, including friction and the decrease in the apparent cross-sectional flow area due to the developing boundary layer.

The 2-D centerline and Q1D swirl factor radial profile predictions shown in Figure 3.20, again illustrate remarkable agreement between the 2-D N-S solution to the turbulent flow field and the inviscid Q1D solution. The effect of fissioning in the duct is to decrease the radial velocity component (u) while having negligible effect on the tangential velocity component (v). The swirl factor, S ($= v/u$), therefore decreases in the duct less rapidly as the neutron flux level is increased.

Figures 3.21 and 3.22 provide a comparison of the 2-D N-S (centerline) and Q1D predictions of the total temperature and total pressure radial profiles, respectively, as functions of neutron flux level. The 2-D and Q1D predictions of duct total properties are seen to agree nearly exactly. The stagnation temperature rise through the duct increases with increasing neutron flux level (and fission density). Increasing the neutron flux level, or fission density, serves to decrease the stagnation pressure (as expected for Rayleigh flow).

The comparisons presented above provide not only confidence in the 2-D thin-layer N-S solver developed in this thesis but also indicate that the Q1D Euler solver described in Appendix A does an excellent job of predicting the behavior of

the high Reynolds number, turbulent, fissioning gas flows in ducts that are relatively free of oblique wave structure.

3.4 Uniform Plasma Property MHD Solutions

Prior to analyzing the full problem of the MHD flow of a fissioning gas with locally varying plasma properties, the flow of a fissioning gas with (artificially) uniform plasma properties (σ_e and μ_e) is studied. The uniform plasma properties allow for an initial study of basic MHD interaction effects without the added effects of the spatial variation (radially or axially) of the plasma properties. In this section, the electrical conductivity and electron mobility are set at 70 S/m and 2 T^{-1} , respectively, uniformly throughout the duct. The duct geometry studied in the section is described in Figure 3.23. With the generator parameters specified in Table 3.1, the MHD interaction (which scales as $\sigma_e B^2$) is significant. In the comparison provided here, effects of varying the applied magnetic induction, at a fixed load resistance, are first discussed; this is followed by a discussion on the effects of varying load resistance at a specific magnetic induction.

3.4.1 Varying Applied Magnetic Induction

Radial profiles. The stagnation temperature radial profiles at the mid-gridline--axial grid 51 of 101--are compared in Figure 3.24 for the cases of 0 T, 3.0 T, 3.5 T, and 4.0 T applied magnetic induction. The generator load resistance in each case is 0.25Ω which corresponds to the case where the effective generator resistance nearly equals the generator load resistance. Outside (upstream or

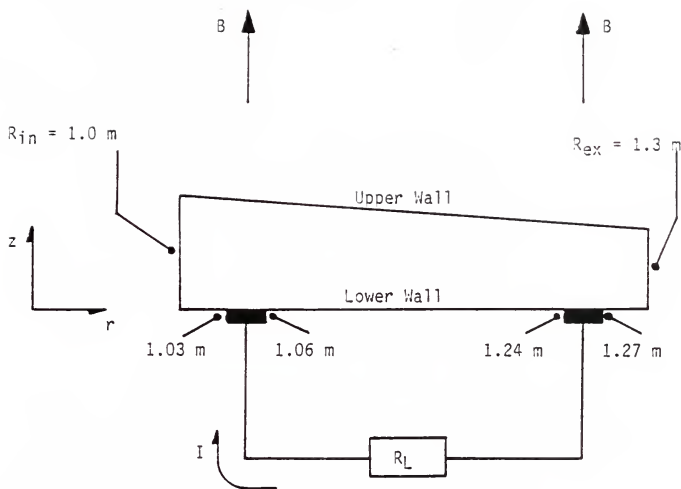


Figure 3.23 Schematic Diagram of MHD Generator with Linearly Decreasing Duct Height used for Uniform Plasma Transport Property MHD Calculations.

Table 3.1 Uniform Plasma Property MHD Generator Parameters

Plasma Transport Properties

Scalar Electrical Conductivity (S/m)	70
Electron Mobility (T^{-1})	2

Inlet Flow Free Stream Parameters

Stagnation Temperature (K)	3000
Stagnation Pressure (MPa,atm)	5.066,50
Radial Mach Number	2.0
Swirl Factor	1.0
Static Temperature (K)	1025 K
Static Pressure (MPa,atm)	0.186,1.84

<u>Wall Temperature (K)</u>	2000
-----------------------------	------

<u>Neutron Flux Level ($n/cm^2 s$)</u>	1×10^{16}
---	--------------------

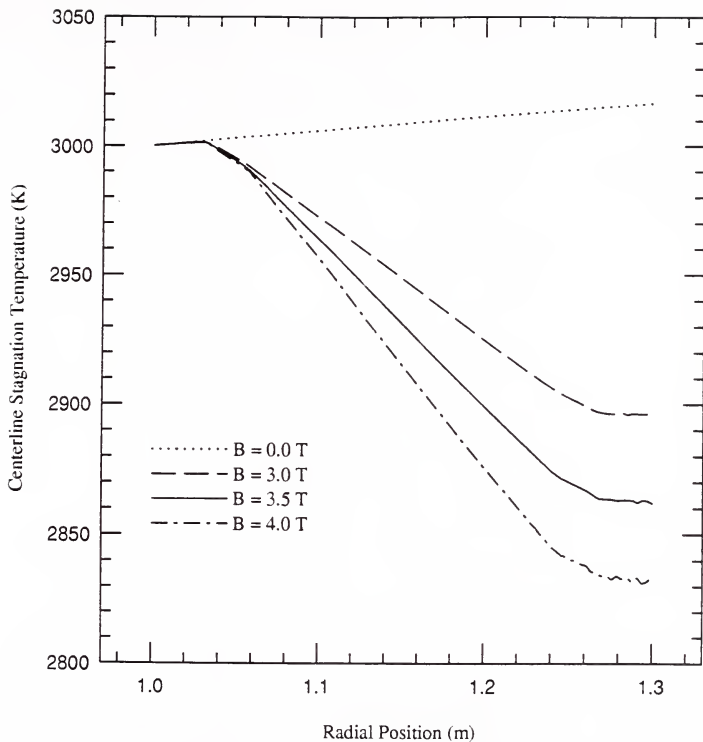


Figure 3.24 Comparison of Centerline Stagnation Temperature as a function of Radial Position for $B = 0$ T, 3.0 T, 3.5 T and 4 T Generators with Uniform Plasma Transport Properties.

downstream) of the electrodes, no temperature change occurs; no enthalpy (or power) extraction occurs outside of the inter-electrode region. The four curves coincide in the region upstream of the anode (or first electrode). In the case of no applied B-field it is seen that the fission heating causes an increase in the total temperature. The total temperature increase appears to be linear, indicating that the fluid density (and therefore the fission density) is very nearly uniform in this generator. The enthalpy extractions of the three generators with 3.0 T, 3.5 T, and 4.0 T applied B-fields are estimated to be 3.5%, 4.6%, and 5.6%, respectively; the corresponding electric power densities are $263 \text{ MW}_e/\text{m}^3$, $347 \text{ MW}_e/\text{m}^3$, and $424 \text{ MW}_e/\text{m}^3$. It is emphasized here that the energy extraction occurs only in the region including, and between, the electrodes. The region between and including the electrodes is referred to in the remaining parts of this thesis as the "active generator region".

Figure 3.25 provides a comparison of the stagnation pressure radial profiles along the center grid line (51 of 101) for the same variation in applied B-fields, for the 0.25 ohm load resistance. For the $B = 0 \text{ T}$ case, as seen earlier, the stagnation pressure drops due to the fission heating and friction effects. A striking feature of the 3.0 T, 3.5 T, 4.0 T curves is that a large fraction (e.g., 37% at $B = 3 \text{ T}$ and 48% at $B = 4 \text{ T}$) of the total pressure loss occurs outside of the active generator region (upstream of the anode and downstream of the cathode). Figure 3.26 provides a plot of the current stream function, $\varphi(r,z)$, spatial distribution (see Section 2.3 where the stream function is introduced). It can be noted in this figure that immediately upstream of the anode (and also

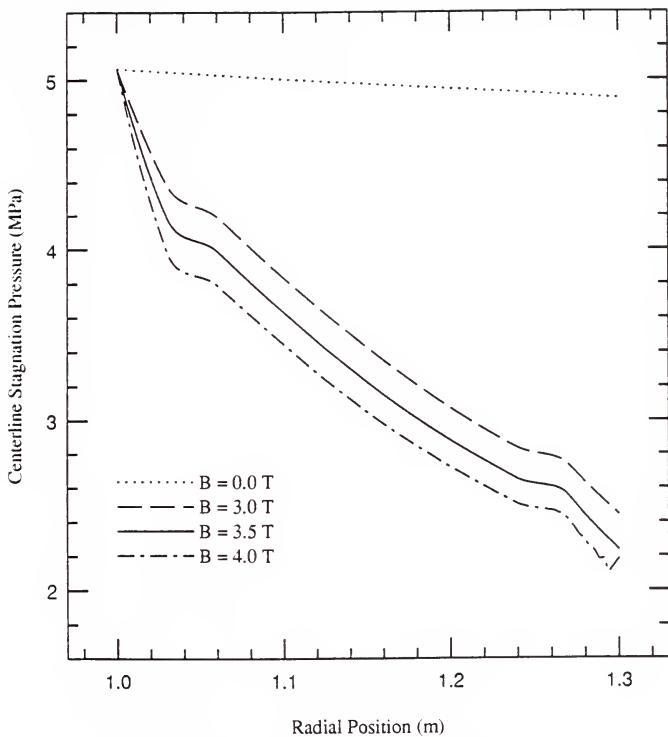


Figure 3.25 Comparison of Centerline Stagnation Pressure as a function of Radial Position for $B = 0$ T, 3.0 T, 3.5 T and 4 T Generators with Uniform Plasma Transport Properties.

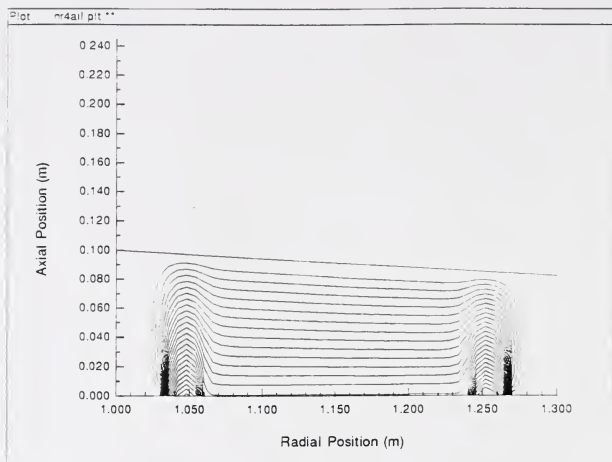


Figure 3.26 Current Density Stream Function Contour Plot for Generator with $B = 3.5 \text{ T}$, $R_L = 0.25 \Omega$, and Uniform Plasma Transport Properties.

immediately downstream of the cathode) $\partial\varphi/\partial z \approx 0$, or $J_r \approx 0$; i.e., outside of the active generator region the Hall current density component is zero and the generator operates as if in open-circuit. Using the generalized Ohm's law

$$J_r = \sigma_{\perp} ((u\beta_e + v)B + E_r) = \frac{1}{r} \frac{\partial\varphi}{\partial z} \quad (3-28)$$

and

$$J_{\theta} = \beta_e J_r - \sigma_e u B \quad (3-29)$$

indicating that without the effect of the Hall current, J_r , a large (open-circuit) $J_{\theta}B$ body force works against the flow in these regions (outside of the active generator region); further, with $J_r \approx 0$, no electric power ($J_r E_r$) is extracted in these same regions. The large body force against the flow, $J_{\theta}B$, works to decelerate the flow and causes the large total pressure losses indicated in Figure 3.25.

In the active generator region, the $J_{\theta}B$ body force is reduced by the Hall effect by the amount $J_r\beta_e B$ (see discussion in Section 1.1.2). The energy extraction serves as a form of "cooling" (in a Rayleigh flow sense) further reducing the extent of stagnation pressure losses. Note that in the regions axially above the electrodes (e.g., above the anode in $1.03 \leq r \leq 1.06$ m) the total pressure loss rate with radial position is reduced relative to the loss rate either between the electrodes or upstream of the anode and downstream of the anode. The curves for 3.0 T, 3.5 T, and 4.0 T are qualitatively the same and the pressure loss is evidently proportional to the applied B-field.

Having noted the large pressure drop occurring outside of the active generator region it is evident that design of the size and position of the electrodes

in relation to the applied magnetic field radial distribution, greatly affects generator performance. From an isentropic efficiency standpoint, the applied field should be designed to be zero outside of the active generator region; in this way the large $J_{\theta}B$ body forces that cause the large pressure drops outside of the active generator region in the cases examined here will not be made manifest. (In this thesis, recall, it is assumed that the applied magnetic induction is uniform throughout the MHD generator duct geometries.) For example, it may be suggested, in light of Figure 3.25, that the anode begin in the nozzle region--e.g., be part of the nozzle lower wall--rather than downstream of the nozzle, as is the case in this analysis.

Neglecting the fission energy deposition in the fluid, the isentropic efficiency, η^I of the generator can be expressed as

$$\eta^I = \frac{\epsilon}{1 - r_T^{-\frac{1}{\Gamma}}} \quad (3-30)$$

where ϵ is the generator enthalpy extraction ($\equiv ((\bar{T}_{in} - \bar{T}_{ex}) / \bar{T}_{in})$), r_T ($\equiv \bar{P}_{in} / \bar{P}_{ex}$) is the generator (or turbine) total pressure ratio, and Γ is the ratio, $\gamma/(\gamma-1)$. Using the results presented in Figure 3.24 and 3.25, the isentropic efficiencies of are estimated, using Equation 3-30, to be 16.3%, 19.6%, and 22.5%, for the $B = 3$ T, 3.5 T, and 4.0 T cases, respectively. The generators analyzed are extremely inefficient; this is due in large part to the pressure losses before and after the electrodes. Note, if the $J_{\theta}B$ losses did not exist--if $B = 0$ T in the regions upstream of the anode and downstream of the cathode--the generator efficiencies

are expected to be near (using the same two figures) 24%, 31%, and 37%. It is emphasized that it is beyond the scope of the thesis to optimize generator performance, either for the generator geometry analyzed here or by varying generator geometry; however, it is noted that the example generators studied in the thesis, considering the above cited efficiencies, are not optimally designed.

The radial profiles of the radial Mach number along the center gridline (51 of 101) predicted for the $B = 0$ T, 3.0 T, 3.5 T, and 4.0 T cases are shown in Figure 3.27. Consistent with the pressure loss already discussed, outside of the active generator region the flow is decelerated by the large $J_\theta B$ forces; the radial Mach number drops in these regions for the case where the applied magnetic induction is not zero. It is interesting that, for this particular geometry, the radial Mach number is approximately constant between the electrodes. Over the electrodes themselves--i.e., over the anode ($1.03 \text{ m} \leq r \leq 1.06 \text{ m}$) and over the cathode ($1.24 \text{ m} \leq r \leq 1.27 \text{ m}$), the core flow accelerates, or decelerates at a reduced rate relative to that experienced between the electrodes. Considering the current density stream function profile presented in Figure 3.26, it is apparent that the Hall current density J_r ($= 1/r \partial\varphi/\partial z$) is largest over the electrodes where the current is comprised of both the load current and the recirculation current loops; therefore, the Hall effect significantly, by the amount $J_r \beta_c B$, reduces the $J_\theta B$ body forces in these regions.

Electrode generated shock waves. Figure 3.28 provides a contour plot of the static pressure, $P(r, z)$, for the case where $B = 3.5$ T. Figure 3.28 shows that oblique shock waves are formed at the upstream edge of the anode ($r = 1.03 \text{ m}$)

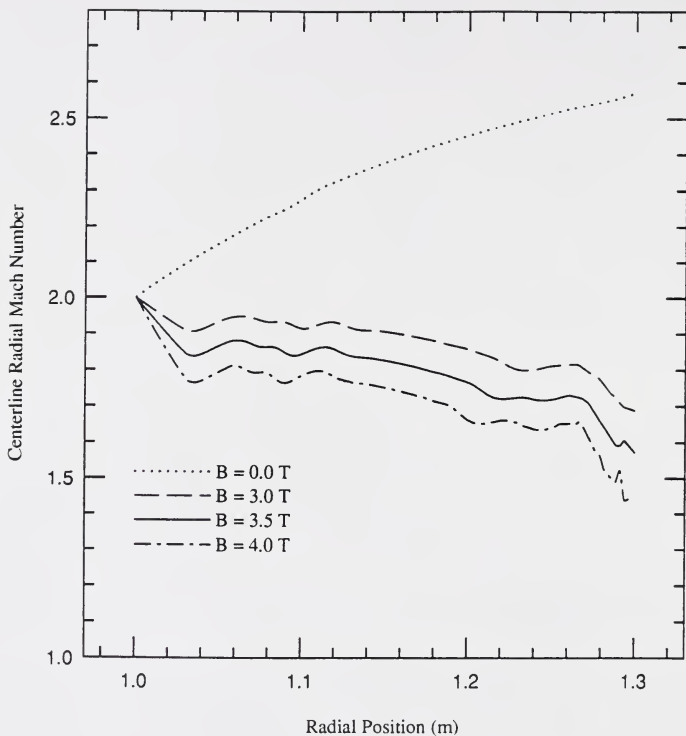


Figure 3.27 Comparison of Centerline Radial Mach Number as a function of Radial Position for $B = 0$ T, 3.0 T, 3.5 T and 4 T Generators with Uniform Plasma Transport Properties.

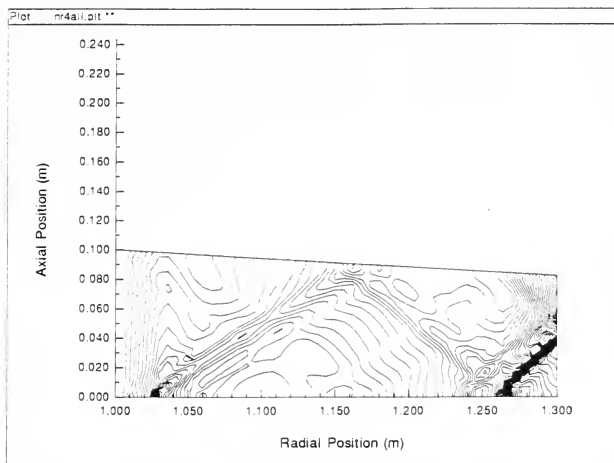


Figure 3.28 Static Pressure Contour Plot for Generator with $B = 3.5 \text{ T}$, $R_L = 0.25 \Omega$, and Uniform Plasma Transport Properties.

and the downstream edge of the cathode ($r = 1.27$ m). Considering the current stream function distribution of Figure 3.26, it is apparent that these electrode positions correspond to regions of high current density; as discussed later in Section 3.5.2, the load current leaves the anode (and enters the cathode) through a small fraction (e.g., 10 or 20 %) of the electrode area. The upstream edge of the anode and the downstream edge of the cathode are therefore the regions of the highest (by an order-of-magnitude) Joule heating in the generator. The result of the localized high Joule heating density is to locally increase the fluid static temperature (and fluid specific volume). The localized increase in fluid specific volume results in a sudden (i.e., step-like) increase in the boundary layer thickness in these locations. The increase causes the flow to turn, away from the wall. The turning of the flow at the anode and cathode is accomplished through the generation of the oblique shock waves evident in Figure 3.28.

Axial profiles. The axial profiles of the radial velocity component ($u(z)$) predicated for the three non-zero B-fields, over the cathode (at $r = 1.25$ m) are compared in Figure 3.29. The effects of varying the magnitude of the applied magnetic induction are evident. For a given load resistance, the fluid is increasingly diffused as the magnetic field increases; both the radial and tangential body force components increase as the applied magnetic induction is increased. The $J_{\theta}B$ body force (radial) component can be expressed as

$$J_{\theta} = \sigma_e u B \left(\zeta \beta_e \left[\frac{\beta_e + S}{1 + \beta_e^2} \right] - 1 \right) \quad (3-31)$$

where ζ is the local load factor ($J_r / (J_r)_{\text{SHORT}}$). In the limit that the Hall

parameter (β_e) is much greater than the swirl factor and also much greater than unity, $J_\theta B \sim \sigma_e u B$; in this limit, the body force against the radial component of the flow is proportional to the square of the magnetic induction.

If it is assumed that $E_r(r, z) \approx E_r(r)$ (i.e., that E_r is uniform in z)--valid away from the electrodes--then the ratio of the body forces at the duct wall and in the core flow (free stream) can be expressed as

$$\begin{aligned} \frac{J_{\theta, w}}{J_{\theta, \infty}} &= \frac{(\zeta - 1)(\beta_e + S)\beta_e}{(S - \beta_e) + (\zeta - 1)\beta_e(\beta_e + S)} \\ &\approx \frac{\beta_e(\zeta - 1)}{\beta_e(\zeta - 1) - 1} \quad \text{in} \quad \lim_{\beta_e \rightarrow \beta_e \gg S} \end{aligned} \quad (3-32)$$

where S is the local swirl factor and properties are uniform. At the swirl numbers encountered in these calculations ($0.5 \leq S \leq 1.0$), the above ratio indicates that the $J_\theta B$ body force near the wall is 75% to 80% of that in the free stream, and it has the same direction, against the flow, as the that in the free stream.

Considering for a moment an equilibrium condition in which effectively $\partial(\rho u^2 r)/\partial r = 0$ in the core flow and $\partial P/\partial z = 0$ through the boundary layer, it is feasible that $\partial(\rho u^2 r)/\partial r \geq 0$ near the wall; i.e., it is possible that the radial velocity component will be more squared off than a nominal turbulent equilibrium axial profile due to reduced deceleration near the wall. Indeed, in this Hartmann flow (see Section 1.2), the velocity may overshoot near the wall. Considering Figure 3.29, even at the rather low (though significant) MHD interaction levels encountered and the short duct lengths (0.3 m) analyzed in these runs, the profiles in Figure 3.29

exhibit definite MHD effects (and slight velocity overshoots in the $B = 3.0 \text{ T}$ and 3.5 T cases).

Figure 3.30 provides a comparison of the axial profiles of the tangential velocity component ($v(z)$) for the same B-field comparisons. The tangential component of the MHD body forces is $-J_r B$, oriented against the flow, which can be expressed as

$$J_r B = \sigma_e \mu B^2 \zeta \left[\frac{\beta_e + S}{1 + \beta_e^2} \right] \left[\begin{array}{l} \lim \\ \beta_e \rightarrow \beta_e \gg S \\ \beta_e \rightarrow \beta_e \gg 1 \end{array} \right] \approx \frac{\sigma_e \mu B^2 \zeta}{\beta_e} \quad (3-33)$$

The effect of the B-field on the current density component, J_r , in the limit of large Hall Parameter (recalling that $\beta_e = \mu_e B$) is negligible. Under this condition, the body force against the tangential component of the flow is nearly proportional to the applied B-field. Using the tangential momentum equation, one can infer that, to a good approximation, the tangential velocity in the core flow will vary with radial position as

$$v(r) = v_{in} \frac{R_{in}}{r} \left(1 - \frac{I (r^2 - R_{in}^2) B}{2 \dot{m} v_{in} R_{in}} \right) = v_{in} \frac{R_{in}}{r} (1 - \Delta) \quad (3-34)$$

where I is the generator load current and \dot{m} is the generator mass flow rate.

In the cases examined, Δ is nearly 2 to 3% so that, although the tangential profile, $v(r)$, is influenced by the MHD interaction (the Δ -term), the influence is small at these MHD interaction ($\sim \sigma B^2 L$) levels. The curves in Figure 3.30 reflect the small MHD perturbation of the $v(z)$ profile away from the $v(z)$ profile corresponding to $B = 0 \text{ T}$ (zero MHD interaction).

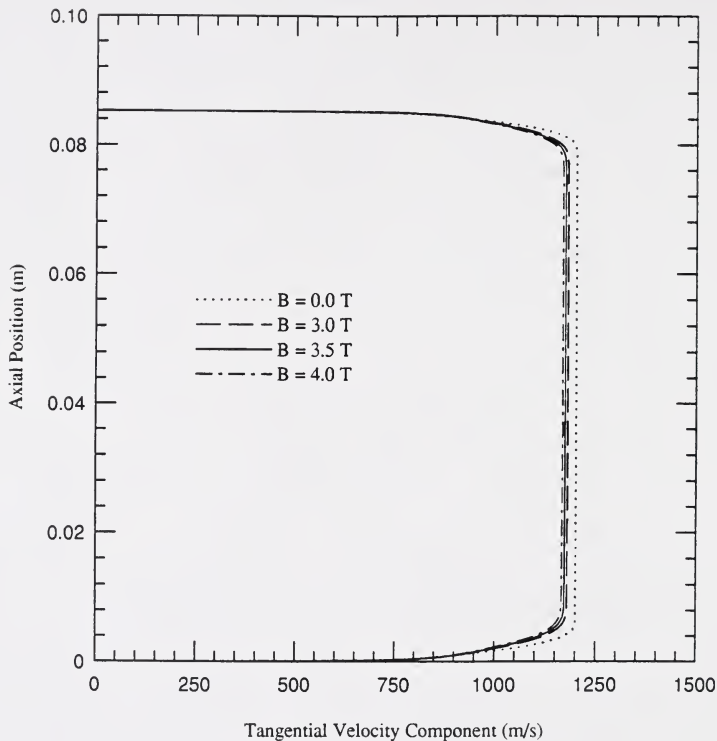


Figure 3.30 Comparison of Tangential Component of Velocity as a function of Axial Position at Cathode ($r = 1.25$ m) for $B = 0$ T, 3.0 T, 3.5 T, and 4.0 T Generators with Uniform Plasma Transport Properties.

It is interesting that although the tangential component axial profile does not exhibit MHD modifications to Hartmann-type profiles, it is this component that has potential for marked MHD effects. Following the same line-of-argument as in the discussion above, it is found that the ratio of the tangential components of the MHD body forces at the wall and in the free stream is

$$\frac{J_{r,w}}{J_{r,\infty}} = \frac{\zeta - 1}{\zeta} = -\frac{R_L}{R_{MHD}} \quad (3-35)$$

where ζ is the load factor in the free stream, R_L is the generator load resistance, and R_{MHD} is the effective generator resistance. It is apparent that the magnitude of the ratio varies greatly with the load factor (or, with the load resistance) and is negative, so that the body force component reverses direction from against the flow in the free stream to with the flow near the wall. For the high Reynolds number, thin boundary layer thickness, turbulent boundary layers investigated here the fluid is accelerated only in a region very near the wall, most likely within the laminar sublayer, and thus should not be expected to greatly influence the $v(z)$ profile; however, considering the comparison of the axial component of tangential velocity near the lower wall (at the cathode) in Figure 3.30, the acceleration effect of the applied B-field on the fluid velocity near the wall is evidently small. As the generator length, MHD interaction levels, and boundary layers thicknesses increase, the effect of the variable axial profile of the tangential body force component should be expected to effect increased MHD-induced modification of the velocity profiles, axially and radially. It is emphasized here that spatially

variable plasma properties will further complicate the $J_r B$ body force profile through the boundary layer.

Figure 3.31 provides a comparison of the static temperature axial profiles at the cathode ($r = 1.25$ m) for the same applied B-field cases. The static temperatures in the core flow region vary as expected for the degree to which each flow is diffused by the MHD interaction (see the radial Mach number profiles in Figure 3.27). The temperature increases through the boundary layer, which is estimated in these case (from Figure 3.29) to be approximately 8 mm thick in the cathode region. Near the laminar sublayer region, a small temperature overshoot occurs (over the 2000 K wall temperature); the overshoot is most evident at the highest B-field, indicating higher shear stress, thus viscous heating, as the B-field increases. The temperature overshoots are small for this low Prandtl number (near 0.24) flow.

3.4.2 Varying Load Resistance

In the preceding subsection, the generator load resistance is fixed at $R_L = 0.25 \Omega$. In this section the results of calculations for generators with load resistances of 0.1 Ω , 0.25 Ω , and 1.0 Ω are compared. These resistances correspond to estimated load parameters, ζ , of approximately 0.2 ($R_L = 1.0 \Omega$), 0.5 ($R_L = 0.25 \Omega$), and 0.8 ($R_L = 0.1 \Omega$). The load parameter, ζ , is estimated using

$$\zeta \equiv \frac{J_r}{J_{r,SHORT}} \approx \frac{1}{\Psi + 1} = \frac{R_{MHD}}{R_L + R_{MHD}} \quad (3-36)$$

where $\Psi \equiv R_L/R_{MHD}$ and R_{MHD} , the generator effective resistance, is estimated

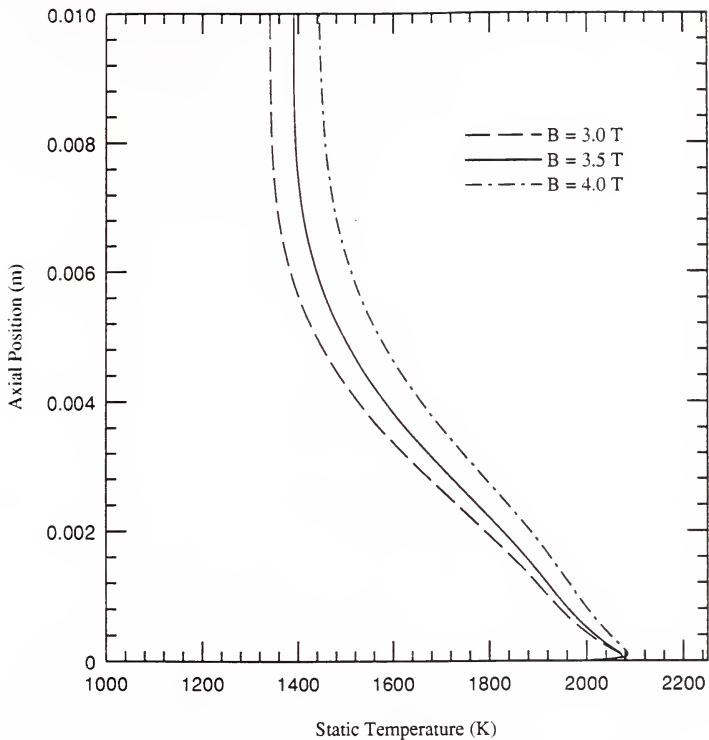


Figure 3.31 Comparison of Static Temperature as a function of Axial Position at Cathode ($r = 1.25$ m) for $B = 3.0$ T, 3.5 T, and 4.0 T Generators with Uniform Plasma Transport Properties.

using

$$R_{MHD} \equiv \frac{\Delta R_E}{A_c \sigma_{\perp}} = \frac{\Delta R_E (1 + \beta_e^2)}{A_c \sigma_e} \quad (3-37)$$

where ΔR_E is the length of the active generator region, and A_c is the duct cross-sectional flow area. (Equations 3-36 and 3-37 are used only to estimate a global or average generator load parameter (or load resistance) in order to facilitate varying the load resistance through a realistic load range and to estimate the load resistance corresponding to the maximum generator power extraction mode.) The condition of $\zeta = 1/2$ corresponds to a load resistance which maximizes power extraction for a given set of generator operating conditions and design; $R_L = R_{MHD}$ at this condition. In the Hall generator, the isentropic efficiency is maximized as $\zeta \rightarrow 1$ ($\zeta = 1$ being short circuit); $\zeta = 0.8$ is examined to include the high efficiency regime (while still producing power). The $\zeta = 0.2$ case is examined as an off-design condition in which the generator is approaching open circuit ($\zeta = 0$). In the following, the three load parameter cases are examined for a generator with applied magnetic induction of 3.5 T.

Radial profiles. Figure 3.32 provides a comparison of the stagnation temperature radial profiles at the mid-gridline (51 of 101) for the three load resistances $R_L = 0.1 \Omega$, 0.25Ω , and 1.0Ω . (The $R_L = 0.25 \Omega$ case is included in the variable B-field work in Section 3.4.1.) The profiles follow the trends already noted in Section 3.3.1: no power is extracted outside of the active generator region; the power extraction between the electrodes (exclusive) is nearly constant (i.e., the $\Delta \tilde{T}$ is linear); and the power extraction over the electrodes is decreased

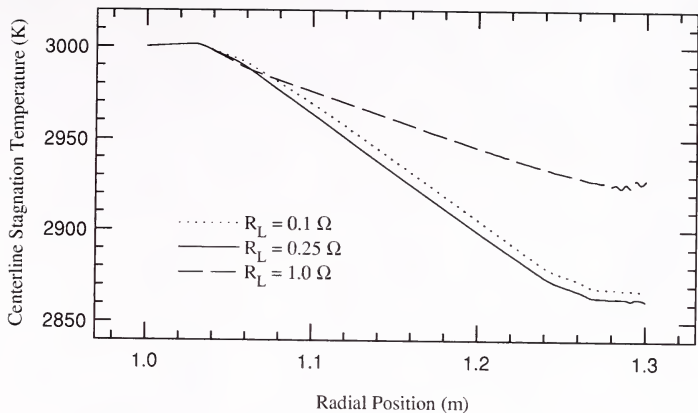


Figure 3.32 Comparison of Centerline Stagnation Temperature as a function of Radial Position for $R_L = 0.1 \Omega$, 0.25Ω , and 1.0Ω Generators with Uniform Plasma Properties.

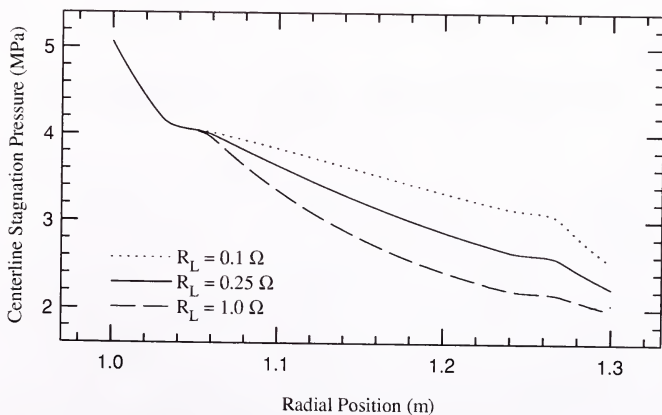


Figure 3.33 Comparison of Centerline Stagnation Pressure as a function of Radial Position for $R_L = 0.1 \Omega$, 0.25Ω , and 1.0Ω Generators with Uniform Plasma Properties.

from that between the electrodes, except in the case of $R_L = 1.0 \Omega$ (closest to open circuit) case. The enthalpy extractions for the 0.1Ω , 0.25Ω and 1.0Ω cases are 4.4%, 4.6%, and 2.5%, respectively; the corresponding power densities are $339 \text{ MW}_e/\text{m}^3$, $424 \text{ MW}_e/\text{m}^3$, and $169 \text{ MW}_e/\text{m}^3$.

The stagnation pressure radial profiles along the mid-gridline (51 of 101) are compared in Figure 3.33 for the same variation in load parameters. Consistent with comments in Section 3.4.1, the pressure drop in the regions outside of the "active generator region"--both upstream of the anode and downstream of the cathode--are large. In contrast to Figure 3.25 (variable B-fields compared), and consistent with the argument that the $J_\theta B$ forces--those acting radially against the flow--are maximized (to $\sigma_c u B^2$) upstream of the anode ($1.0 \text{ m} \leq r \leq 1.03 \text{ m}$), the three curves in Figure 3.33 coincide in the region upstream of the anode; i.e., the $J_\theta B$ body force upstream of the anode (and downstream of the cathode) is maximized to the open circuit value corresponding to the applied B-field, and is independent of generator loading. Again, in the regions above the electrodes (e.g., in the cylinder bounded axially by the upper and lower duct walls and radially by the cathode [$1.24 \leq r \leq 1.27 \text{ m}$]) the pressure loss is reduced to less than that outside of the electrodes or between the electrodes. The largest stagnation pressure loss occurs in the $R_L = 1.0 \Omega$ ($\zeta = 0.2$) generator due to the larger $J_\theta B$ body forces. The 0.1Ω experiences the least overall pressure loss. The isentropic efficiencies for the $R_L = 0.1 \Omega$, 0.25Ω , and 1.0Ω generator loads are 21.8%, 19.4%, and 9.6%, respectively.

The radial Mach number radial distributions for the three load resistances are shown in Figure 3.34. The effect of the wave structure in the duct (due to entrance boundary condition artifacts) is apparent in the tortuous $M_R(r)$ profile. In general the oblique shock waves contract (move upstream) as the load resistance (R_L) is increased, which increases the $J_\theta B$ body force. The flows are clearly increasingly diffused as the load resistance is increased from 0.1Ω to 1.0Ω . Again, the large diffusing action, outside the active generator region, is evidenced by the rapid decrease in Mach number in these regions. In general the flow appears accelerated--is actually less decelerated--axially above the electrodes; the apparent acceleration is greater for the smaller load resistances, until at $\zeta = 1$ there is no $J_\theta B$ body force and the flow approaches $B = 0$ T (nozzle) flow (see Figure 3.27 for the $B = 0$ T case).

Axial profiles. The radial velocity component axial profiles at radial position $r = 1.25$ m (at the cathode) for the generator with $B = 3.5$ T applied field and variable load resistors are compared in Figure 3.35. As the load resistance is increased from 0.1Ω to 1.0Ω ($\zeta = 0.8$ to 0.2), the MHD body force against the radial flow increases, the flow is increasingly diffused, and the boundary layer thickens. The Hartmann flow profiles exhibit velocity overshoots, especially clear in the $R_L = 1.0 \Omega$ curve. Using Equation 3.32 the ratio $(J_{\theta,w}/J_{\theta,\infty})$ suggests that at $R_L = 1.0 \Omega$ the body force at the wall is reduced to about 88% of the free stream value while at $R_L = 0.1 \Omega$ the body force near the wall is reduced to 66% of the free stream value.

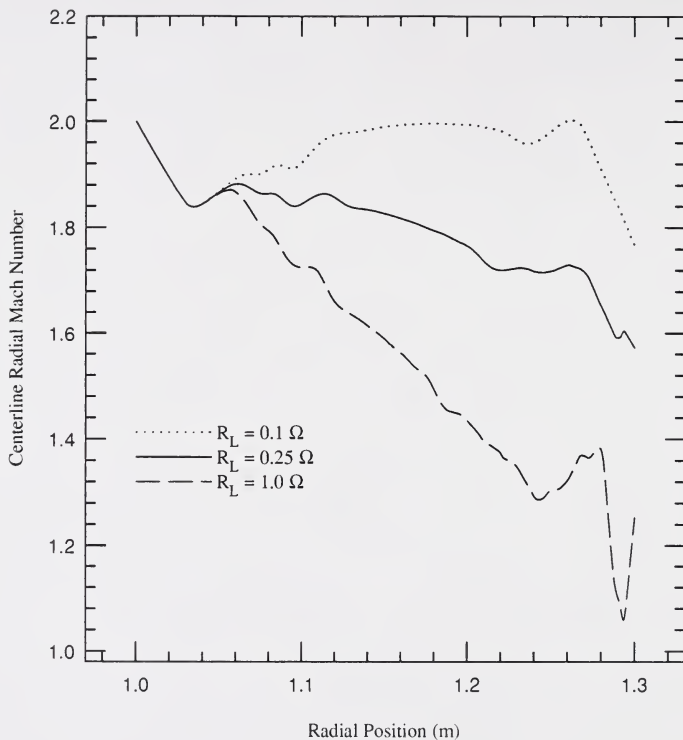


Figure 3.34 Comparison of Centerline Radial Mach Number as a function of Radial Position for $R_L = 0.1 \Omega$, 0.25Ω , and 1.0Ω Generators with Uniform Plasma Properties.

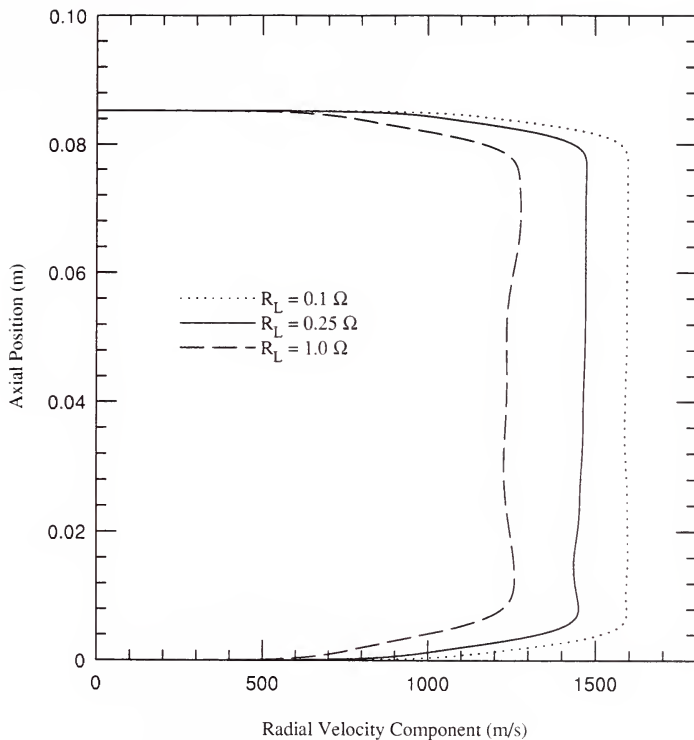


Figure 3.35 Comparison of Radial Component of Velocity as a function of Axial Position at Cathode ($r = 1.25$ m) for $R_L = 0.1 \Omega$, 0.25Ω , and 1.0Ω Generators with Uniform Plasma Properties.

Figure 3.36 compares the axial profiles of the tangential velocity component at the cathode ($r = 1.25$ m) for the same variation in load resistances. As mentioned in Section 3.4.1, the MHD effects on the flow profile at the MHD interaction levels in these examples are small as suggested by Equation 3-34. The Hall current (J_r) is proportional to the load parameter (Ψ) so that as the load resistance (R_L) increases the MHD body force against the tangential flow direction--or the term Δ in Equation 3.34--decreases.

Recall that the ratio $J_{r,w}/J_{r,\infty} = -\Psi = -R_L/R_{MHD}$ so that as the load resistance is increased, the ratio of the body force near the wall (with the flow) to that in the free stream (which is against the flow) also increases; at $R_L = 1.0 \Omega$ the magnitudes of the ratio of body forces is 4.0 while at $R_L = 0.25 \Omega$ and $R_L = 0.1 \Omega$ it is 1.0 and 0.25, respectively.

Figure 3.37 compares the static temperature axial profiles for the three load resistance cases, again at the cathode (at $r = 1.25$ m). Because the flow is more and more diffused as the load resistance (and the $J_\theta B$ force) is increased, the static temperature near the free stream is higher at the higher load resistances. The temperature overshoot in the boundary layer region increases dramatically as the load resistance (load parameter) is increased (decreased).

3.5 Nonuniform Plasma Transport Properties

The plasma physics property models for scalar electrical conductivity (σ_e) and electron mobility (μ_e) are developed in Section 2.4. In Section 2.4, electron "fluid" number density and energy balances are provided for weakly ionized

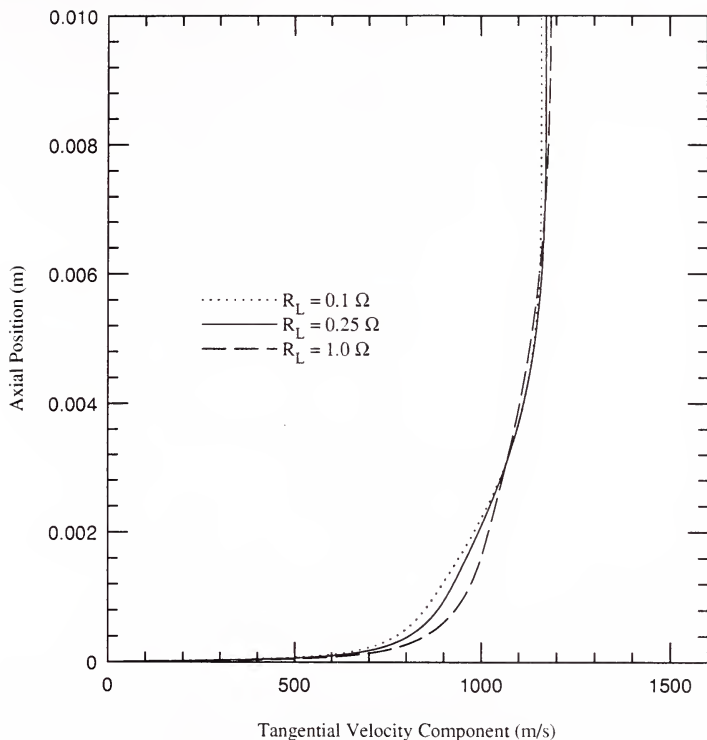


Figure 3.36 Comparison of Tangential Component of Velocity as a function of Axial Position at Cathode ($r = 1.25$ m) for $R_L = 0.1 \Omega$, 0.25Ω , and 1.0Ω Generators with Uniform Plasma Properties.

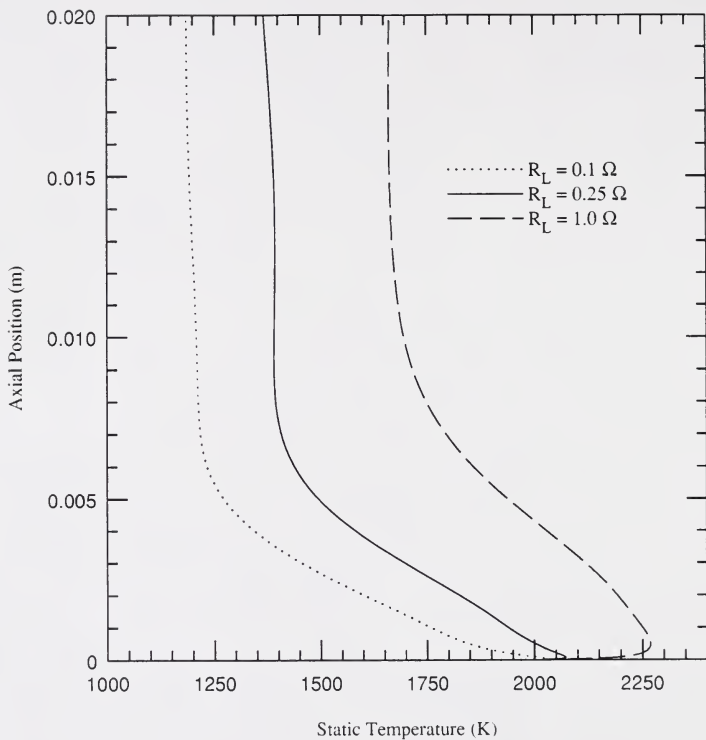


Figure 3.37 Comparison of Static Temperature as a function of Axial Position at Cathode ($r = 1.25$ m) for $R_L = 0.1 \Omega$, 0.25Ω , and 1.0Ω Generators with Uniform Plasma Properties.

plasmas with electron sources from thermal ionization (S_{Saha}) and fission-fragment induced ionization (S_{ff}); three-body electron stabilized recombination is considered to be the dominant loss term. Predictions of nonequilibrium electron temperatures are available from the modeling.

Expression for the electron number density as a function of the electron temperature in the limiting cases of: 1.) a dominant thermal ionization source of electrons (Saha-limit, $S_{\text{Saha}} \gg S_{\text{ff}}$); and 2.) dominant fission-fragment induced ionization source term (Fission-limit, $S_{\text{ff}} \gg S_{\text{Saha}}$) are provided in Sections 2.4.5 and 2.4.4, respectively. In each section, the further limiting case of "equilibrium" electron temperatures (i.e., $T_e \approx T$) is examined, and explicit formulas for the electrical conductivity and electron mobility are provided. Further, for both the Saha-limit and the Fission-limit, functional forms for the electrical conductivity and electron mobility are provided in that same section.

In this section, the nonequilibrium conditions are first addressed. Attention is then restricted to plasmas with equilibrium electron temperatures; equilibrium electron temperatures are expected for the molecular gases considered. In the equilibrium condition, the $S_{\text{Saha}} \gg S_{\text{ff}}$ (Saha-limit) and the $S_{\text{ff}} \gg S_{\text{Saha}}$ (Fission-limit) models are both employed to study the spatial variation of predicted plasma properties.

3.5.1 Nonequilibrium Electron Temperatures

Recall from Section 2.4.3 that the local electron temperature is given by (see Equation 2-113) the local fluid temperature plus a nonequilibrium component that is sustained by fission heating, the energy release of

recombination and Joule heating; i.e.,

$$T_e = T + T_{NON} = T + \frac{m_H}{3m_e \delta \nu_{eH} n_e} ((w_r + w_{ff}) S_{ff} + \underline{J} \cdot \underline{E}') \quad (3-38)$$

(see Section 2.4 for nomenclature). Using the modeling already presented in Section 2.4--specifically Equations 2-102 and 2-103 for the electrical conductivity and electron mobility, respectively, and Equations 2-114 and 2-113 for the electron number density and the electron temperature, respectively--estimates are made of the effects of the nonequilibrium temperature on the plasma transport properties in the disk MHD generator for the Fission-limit in which $S_{ff} \gg S_{Saha}$. The calculations are performed using a computer program, DISKCON (developed by the author), which predicts the local disk MHD generator operating conditions (e.g., thermodynamic conditions, Joule heating, etc.) for specified stagnation properties (\tilde{T} and \tilde{P}) and local radial Mach numbers (M_R) and swirl factors (S).

$S_{ff} \gg S_{Saha}$ / nonequilibrium. In the limit where the dominant mechanism for production of conduction electrons is fission-fragment induced ionization, recall (from Section 2.4) that

$$\sigma_e = \frac{a_1 a_2 e}{Q_{eH}} \left(\frac{kT}{P} \right)^{\frac{1}{2}} \Phi^{\frac{1}{2}} T_e \quad (3-39)$$

and

$$\mu_e = \frac{a_2}{Q_{eH}} \left(\frac{kT}{P} \right) \frac{1}{\sqrt{T_e}} \quad (3-40)$$

where the plasma physics model constants a_1 , a_2 , and a_3 are provided in Table 2.7

and where \bar{Q}_{eH} is the electron-heavy (ions and neutrals) momentum transfer cross-section. The electron temperature, T_e , is given by Equation 3-38, where the non-elastic scatter factor, δ ($= 1$ for elastic scattering), determines to a large extent the magnitude of the local nonequilibrium, T_{NON} .

Table 3.2 provides "best estimate" fluid and plasma property data for an example working fluid mixture (85 mole% He and 15 mole% UF_4). Consider operating conditions of $M_R = 1.5$ and $S = 1.5$ (providing a total Mach number, $M_T = 2.7$), stagnation temperature, $\bar{T} = 4000$ K, stagnation pressure, $\bar{P} = 50$ atm, applied magnetic induction, $B = 4$ T, and local neutron flux level, $\Phi = 1 \times 10^{16}$ n/cm²s. Figures 3.38 and 3.39 present the calculated electron conductivity and electron mobility, respectively, plotted against the electron-heavy momentum transfer cross-section and parametrically as a function of the non-elastic scatter factor, δ . It is interesting that the electrical conductivity and the electron mobility both vary linearly (on log-log scales) with \bar{Q}_{eH} , indicating a power law relationship, $\sigma_e \sim \bar{Q}_{eH}^\alpha$ where α varies with δ . Considering an example range of \bar{Q}_{eH} values (available from engineering MHD texts, e.g., Rosa, 1968) from that of argon at 3.5×10^{-21} m², to that of helium at 5.4×10^{-20} m², to that of air at 8×10^{-20} m², and that of water vapor at 7.5×10^{-19} m², it is expected that \bar{Q}_{eH} for the UF_4 -He molecular gas mixture used as the example working fluid in this work will certainly be greater 5×10^{-20} m²; i.e., the momentum transfer cross-section of the UF_4 -He mixture will certainly not be less than that of helium (5.4×10^{-20} m² [Rosa,

Table 3.2 Fluid Property Data for a UF_4 -(85%)He Working Fluid Mixture for Example Fissioning Plasma Transport Property Calculations

Working Fluid Mixture Property Data

Molecular Weight, M_w (kg/kg · mole)	50.05
Ratio of Specific Heats, γ	1.353
Energy Release per Fission, G_f (MeV)	190
Atom Fraction of Fissionable Isotope (e.g., ^{235}U) in Working Fluid (e.g., UF_4 -He mixture), β_f	0.05112
^{235}U Neutron Fission Cross-Section, σ_f (at $T_N \approx 1200$ K) (cm^2)	2.3×10^{-22}
Energy Consumed per Ion-Pair Produced (eV/I.P.), w_{if}	35
Energy Released per Recombination Event, $w_r = C_2 \epsilon_1$	
C_2	1
First Ionization Potential, ϵ_1 (eV)	10
Recombination Rate Coefficient (m^6/s), C_1	1.2×10^{-20}
Ratio of Internal Partition Function of Ions ($2 g_i / g_a$)	≈ 1

Conditions Fixed for Nonequilibrium Fissioning Plasma Property Calculations

Stagnation Temperature, \tilde{T} (K)	4000
Stagnation Pressure, \tilde{P} (MPa, atm)	5.066, 50
Neutron Flux Level, Φ (n/cm^2s)	1×10^{16}
Applied Magnetic Induction, $ \underline{B} $ (T)	4.0

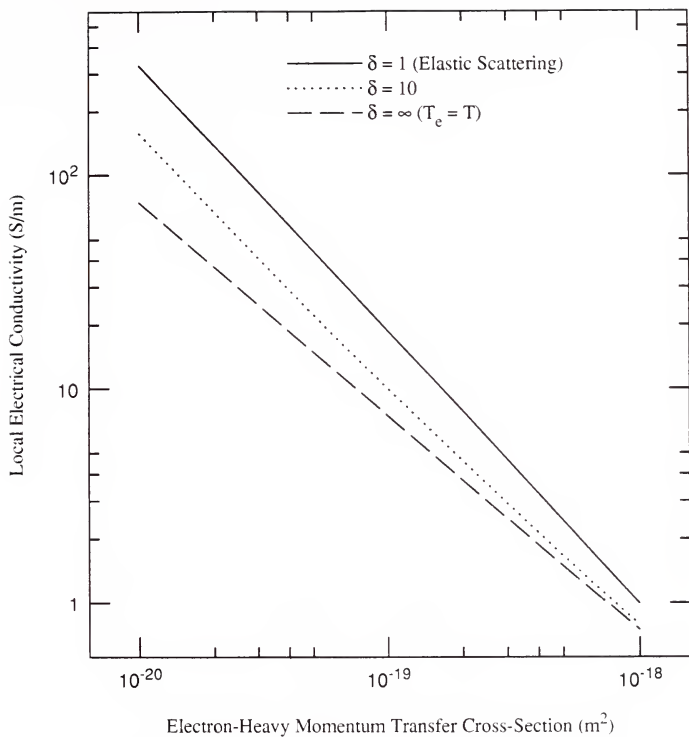


Figure 3.38 Scalar Electrical Conductivity of Fissioning Plasma as a function of Electron-Heavy Momentum Transfer Cross-Section, \bar{Q}_{eH} , and Nonelastic Scatter Factor, δ .

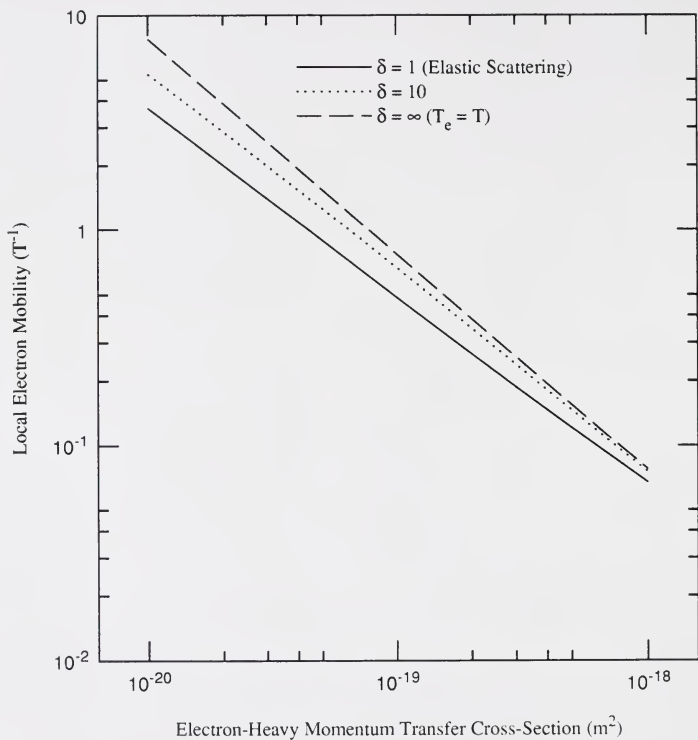


Figure 3.39 Electron Mobility in Fissioning Plasma as a function of Electron-Heavy Momentum Transfer Cross-Section, \bar{Q}_{eH} , and Nonelastic Scatter Factor, δ .

1968]). Figures 3.38 and 3.39 indicate that nonequilibrium electron temperatures can greatly enhance the electrical conductivity while reducing the electron mobility (Hall Parameter) of the fissioning plasma. The nonequilibrium temperatures, therefore, increase both the scalar electrical conductivity (σ_e) and the Hall conductivity ($\sigma_{\perp} \equiv \sigma_e / (1 + (\mu_e B)^2)$). Figures 3.38 and 3.39 also indicate that if $\delta \gg 010$, the equilibrium limit is effectively approached. Note that the non-elastic scatter factor, δ , for molecular gases is typically $0100-1000$, indicating that little useful nonequilibrium effects are expected in molecular gases (Rosa, 1968).

For the same physical data provided in Table 3.2, and for generator local conditions of $\bar{T} = 4000$ K (or 1000 K higher than the 3000 K value used in the generator calculations throughout this thesis), $\bar{P} = 50$ atm, $B = 4$ T, $\Phi = 1 \times 10^{16}$ n/cm²s, and for values of $\bar{Q}_{eH} = 5 \times 10^{-20}$ (which is the value used throughout this thesis) and $\delta = 10$, Figures 3.40 and 3.41 provide the local electrical conductivity and the electron mobility plotted against the swirl factor, S , and parametrically as a function of the local radial Mach number (M_R). In general, an increase in the total Mach number ($M_T = M_R (1 + S^2)^{1/2}$) serves to increase the electrical conductivity and the electron mobility. Figures 3.40 and 3.41 are included to indicate the behavior of σ_e and μ_e as functions of M_R and S ; the values of $\bar{Q}_{eH} = 5 \times 10^{-20}$ and $\delta = 10$ are likely both small--i.e., best-estimates for the UF₄-He working fluid mixture are more like $\bar{Q}_{eH} = 010^{-19}$ m² and $\delta = 0100-1000$;

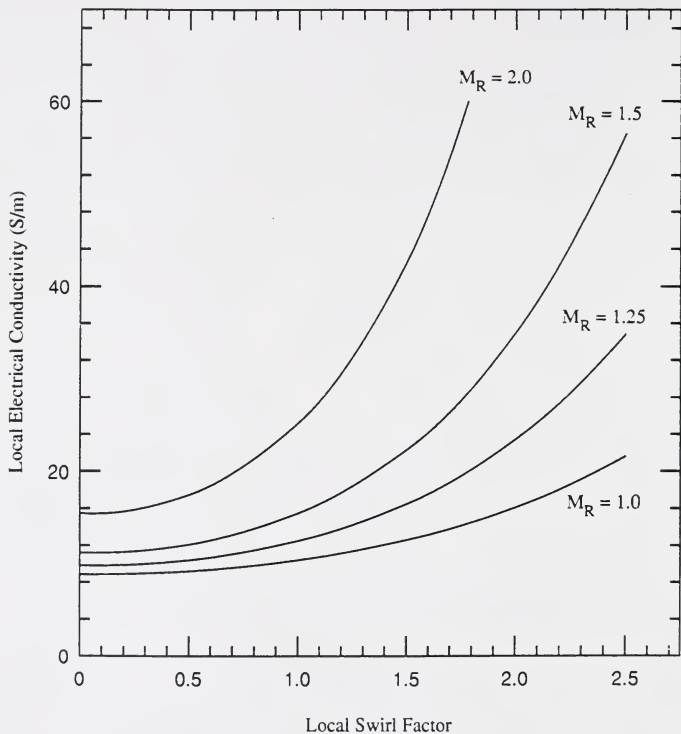


Figure 3.40 Nonequilibrium Enhanced Scalar Electrical Conductivity of Fissioning Plasma as a Function of Local Swirl Factor and Radial Mach Number.

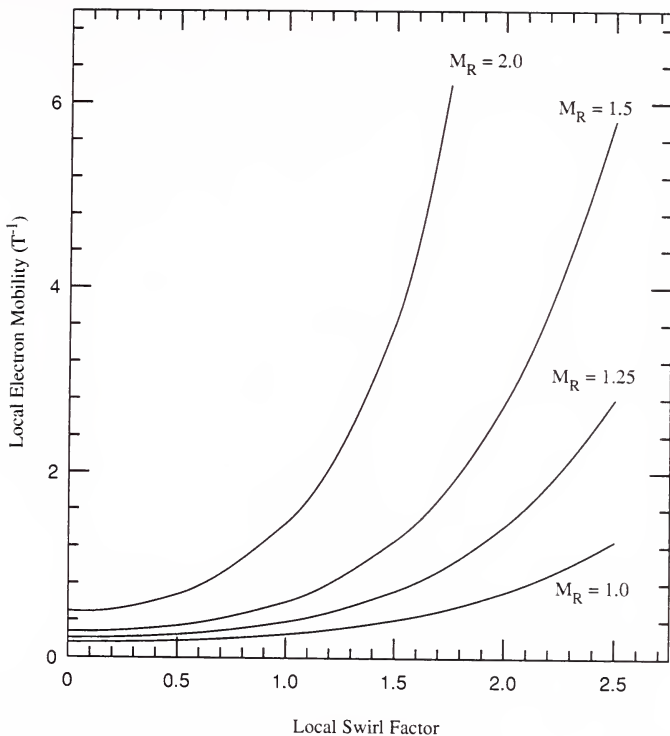


Figure 3.41 Electron Mobility in Fissioning Plasma, with Nonequilibrium Electron Temperatures, as a function of Local Swirl Factor and Radial Mach Number.

the magnitudes of the electrical conductivity and electron mobility provided in this section should be considered optimistic. Further, the simplicity of the point models developed in Section 2.4 suggests that the predicted electrical conductivity values will differ quantitatively from reality; however, it is hopeful that the developed functional forms provide a qualitative sense (functional dependence) of the behavior of the plasma transport properties.

3.5.2 Equilibrium Restriction

The nonequilibrium enhancement of the electrical conductivity is documented above for completeness; however, in addition to, and independent of the fact that nonequilibrium temperatures are indeed unlikely in molecular gas mixtures, it was found necessary in the course of this thesis work to restrict the plasma physics property models used for full MHD generator solutions to the equilibrium condition. This is due to the coupling described below.

Electrical conductivity/Joule heating feedback. As the electron temperature (T_e) locally is enhanced by nonequilibrium effects, the electrical conductivity increases (linearly with T_e , see Equation 3-39). But as the electrical conductivity increases, so does the local Joule heating, and therefore, in turn, the nonequilibrium temperature enhancement, T_{NON} (see Equation 3-38). As can be seen in the contour plots of the current stream function, φ (see Figure 3.26, for example), at both the electrodes (anode and the cathode), the current leaves or enters preferentially from one end of the electrode, leading to high local current densities, and then, high Joule heating. The result of the conductivity/Joule

heating positive feedback is a localized spatial spike in the electrical conductivity at the high current density end of each electrode.

The acute increase in the local Joule heating, due to the increase in electrical conductivity, potentially exacerbates the tendency for the load current to leave (or enter) the electrode through the upstream (downstream) end of the anode (cathode); this is so because as the local Joule heating is increased, not only is the electron temperature increased, but also the local fluid temperature. The increase in the electron temperature results in increased electron-heavy momentum exchange rate--tending to lower the electron mobility, but the increase in the fluid temperature leads to lower fluid number densities, serving to decrease the electron-heavy momentum exchange rate, which in turn tends to increase the electron mobility. Because the electron mobility is proportional to the fluid temperature, while inversely proportional to the square-root of the electron temperature, it is possible that the electron mobility will increase with the Joule heating. An increase in the electron mobility (and the Hall Parameter) at the electrode is expected to lead to a further decrease in the "active area" of the electrodes through which the load current flows (cf. Sutton and Sherman, 1968 for reference to Hurwitz et al., 1961 and their work on the effects of tensor conductivity; also see James (1980) who refers to work [Crown, 1961; and Celinski and Fischer, 1966] on 2-D solutions that show current concentrations due to the Hall effect); it is suggested by the author, based on conservation of current arguments, that the magnitude of the "active area" of the electrode through which the load current flows varies inversely with $(1 + (\mu_e B)^2)$. An increase in the

electron mobility in the vicinity of the electrodes is expected to lead to higher local current densities; the increase in the current density further increases the Joule heating.

As a result of the phenomena discussed here, extremely high electrical conductivity values are obtained at the "active areas" of the electrodes in the nonequilibrium MHD solutions predicted by the ELEMAG (electromagnetics) solver. The peak electrical conductivity values are believed to be greater in magnitude than what would be encountered in an actual generator. Nature, it seems likely, would try to diffuse the electrical conductivity through transport of electrons (density and energy); the gradient-driven transport mechanisms do not exist in either the plasma physics or generalized Ohm's law point models used in this work.

In the calculations presented in the remainder of this work, the plasma physics properties are calculated assuming that the electrons are locally in thermal equilibrium with the background fluid ($T_e = T$). This equilibrium restriction suggests that effectively $\delta \geq 0100$. The plasma physics property models for the equilibrium condition in both the Fission-limit and the Saha-limit, used in the remainder of this work, are developed in Sections 2.4.4 and 2.4.5.

3.5.3 Saha-Limit ($S_{\text{saha}} \gg S_{\text{fl}}$)

The plasma transport property models for the limiting case of a plasma in which thermal ionization is the dominant source of conduction electrons is presented in Section 2.4.5. In the course of this work it has been found by applying the Saha-model developed in Section 2.4.5 that the generator operating

conditions (i.e., local Mach numbers and stagnation conditions [cf. Table 3.1]) are not consistent with conditions in which thermal ionization is a practicable mechanism for inducing significant electrical conductivity; this becomes evident in the discussion below.

The functional form of the scalar electrical conductivity, σ_e , in the equilibrium electron temperature and Saha-limit is (see Equation 2-122)

$$\frac{\sigma_e}{\sigma_{e,r}} = \left(\frac{T}{T_r} \right)^{\frac{1}{2}} \left(\frac{P_r}{P} \right)^{\frac{1}{2}} \exp \left[\frac{\epsilon_I}{2kT_r} \left[1 - \frac{T_r}{T} \right] \right] . \quad (3-41)$$

Recall that "r" designates a reference electrical conductivity ($\sigma_{e,r}$) at reference thermodynamic conditions (T_r and P_r) while ϵ_I is the first ionization potential of the seed constituent (e.g., Cs).

Consider an example generator operating with the local conditions described in Table 3.1; i.e., $M_R = 2$, $S = 1$, $\bar{T} = 3000$ K, and $\bar{P} = 50$ atm. The first ionization potentials (ϵ_I) of typical seed constituents are on the order of 3.8 eV (e.g. Cs) to 4.3 eV (for K). If it is assumed that for the hypothetical working fluid the reference electrical conductivity is (generously) 20 S/m at $T_r = 2000$ K and $P_r = 1$ atm, and given that the static conditions at the free stream total Mach number of 2.83 are $T = 1025$ K and $P = 1.85$ atm, the ratio of the free stream electrical conductivity ($\sigma_{e,\infty}$) to the reference conductivity ($\sigma_{e,r} = 20$ S/m) is $\sigma_{e,\infty}/\sigma_{e,r} \approx 0.10^{-5}$; i.e., the electrical conductivity in the free stream is effectively zero.

It is evident, therefore, that to have significant (0.10 S/m) electrical conductivity levels, the generator must operate at low (≤ 1 atm) static pressures, with high static temperatures (i.e., greater than 2000 K for the above example). To obtain 10 to 20 S/m in typical dissociated combustion gases (with 3% Potassium seed) at 1 atm pressure--and under equilibrium conditions--requires fluid static temperatures of 2300 to 2400 K (Sutton and Sherman, 1965, referencing Moffat, 1961). These conditions are much different than those dictated by the high Mach number, high pressure (to maintain high fluid density for fission density-sake) flows analyzed in this work. For the high Mach number fissioning plasmas analyzed in the next section, the free stream (core flow) static temperature is typically lower than 2000 K--usually nearly 1000 K--with static pressures in the range of 2 to 15 atm. This contrast is pointed out to indicate that the "Saha-limit" generators operate in a subsonic regime, or slightly supersonic regime ($M_T \leq 1.4$) of low pressure, high static temperature while the "Fission-limit" (fissioning plasma) generators operate at higher Mach numbers ($M_T \geq 1.4$) and at high pressures and fluid densities and at lower static temperatures, as will be shown desirable in the following section.

3.5.4 Fission-Limit ($S_{ff} \gg S_{Saha}$)

The plasma physics model employed for the transport properties in the remainder of this chapter is presented in Section 2.4.4; the "fission-model" pertains to the equilibrium electron temperature, fission-limit ($S_{ff} \gg S_{Saha}$) in which fission-fragment induced ionization of the working fluid is the dominant source of conduction electrons, and in which the thermal ionization of the working fluid--

which contains no seed constituent--is negligible. In this fissioning plasma, the functional forms of the scalar electrical conductivity and electron mobility are (see Equations 2-118 and 2-119)

$$\frac{\sigma_{\epsilon}}{\sigma_{\epsilon,r}} = \left(\frac{\Phi}{\Phi_r} \right)^{\frac{1}{2}} \left(\frac{T}{T_r} \right)^{\frac{1}{2}} \left(\frac{P_r}{P} \right)^{\frac{1}{2}} \quad (3-42)$$

and

$$\frac{\mu_{\epsilon}}{\mu_{\epsilon,r}} = \left(\frac{T}{T_r} \right)^{\frac{1}{2}} \left(\frac{P_r}{P} \right) \quad (3-43)$$

where, again, "r" denotes reference neutron flux (Φ_r), static temperature (T_r), and static pressure (P_r) conditions which provide the reference scalar electrical conductivity ($\sigma_{\epsilon,r}$); the reference electron mobility ($\mu_{\epsilon,r}$) is back calculated.

To an extremely good approximation--which is verified using the developed fluid code--the fluid static pressure is uniform through the boundary layer (a boundary-layer theory approximation)--from the free stream (or core flow) to the wall. Recalling that little axial neutron flux depression ($\partial\Phi/\partial z$) is expected through the boundary layer because the gas is relatively transparent to neutrons at the fissionable-isotope partial pressures existing in the generator, then to a good approximation, the wall-to-free stream scalar electrical conductivity ratio is

$$\frac{\sigma_{\epsilon,w}}{\sigma_{\epsilon,\infty}} \approx \left(\frac{T_w}{T_{\infty}} \right)^{\frac{1}{2}} \quad (3-44)$$

Similarly, the wall-to-free stream electron mobility ratio is

$$\frac{\mu_{e,w}}{\mu_{e,\infty}} = \left[\frac{T_w}{T_\infty} \right]^{\frac{1}{2}} \quad (3-45)$$

In the limit that the electron Hall parameter, β_e , both near the wall and in the free stream, is much greater than unity, then the Hall conductivity component (σ_{\perp}) wall-to-free stream ratio is

$$\frac{\sigma_{\perp,w}}{\sigma_{\perp,\infty}} \approx \left[\frac{T_w}{T_\infty} \right]^{\frac{1}{2}} \left[\text{in } \lim_{\beta_e \rightarrow \beta_e \gg 1} \right] \quad (3-46)$$

Table 3.3 provides example values for the above wall-to-free stream plasma transport property ratios for generators with both "hot" (2000 K) and "cold" (800 K) walls; the local operating conditions are assumed to be those provided in Table 3.1; i.e., $T_\infty = 1025$ K, corresponding to $T = 3000$ K and $M_T = 2.83$. Note that, although in this example the temperature varies by as much as a factor of 2 (in the case of the "hot" wall generator) through the boundary layer, the scalar electrical conductivity varies only by a factor of 3 and the Hall conductivity varies by a factor of 1.6. This is to be contrasted with large ($O10^5$) electrical conductivity variation in the Saha-limit example generator, operating under the same conditions, examined in the previous section.

Influence of \bar{Q}_{eh} . As an aside note, it has already been mentioned (see Section 3.5.1) that the electron-heavy momentum cross-section ($\bar{Q}_{eh} = 5 \times 10^{-20}$ m²) used in the example calculations throughout this thesis is assumed to be a low estimate--perhaps an order-of-magnitude low--relative to what might actually be

Table 3.3 Wall-to-Free Stream Plasma Property Ratios for Hot and Cold Generator Walls with Example Generator Free Stream Flow Conditions (see Table 3.1)

Plasma Property Ratio	Functional Form	Hot Walls (2000 K)	Cold Walls (800 K)
$\frac{\sigma_{e,W}}{\sigma_{e,\infty}}$	$\left[\frac{T_W}{T_\infty} \right]^{\frac{5}{3}}$	3.0	0.66
$\frac{\sigma_{i,W}}{\sigma_{i,\infty}}$	$\left[\frac{T_W}{T_\infty} \right]^{\frac{2}{3}}$	1.6	0.85
$\frac{\mu_{e,W}}{\mu_{e,\infty}}$	$\left[\frac{T_W}{T_\infty} \right]^{\frac{1}{2}}$	1.4	0.63

expected for the electron-heavy momentum cross-section of the UF₄-He mixture. Note for comparison that the total electron-heavy momentum transfer cross-section of example seeded combustion gases is reported (by Rosa, 1968, referencing Brogan, 1963) to be $\bar{Q}_{eH} \approx 5.3 \times 10^{-19} \text{ m}^2$ at 2000 K, which, if assumed to vary as $1/v_e$, suggests that the cross-sections for combustion gases is as high as $8 \times 10^{-19} \text{ m}^2$ in the range of electron temperatures of interest to this work (i.e., 800-2250 K). The low \bar{Q}_{eH} value is used specifically so that the calculated electrical conductivities at the generator operating conditions, nominal to this work, are of sufficient magnitude ($\geq 01 \text{ S/m}$) to create MHD interaction levels that modify the generator flow field to an extent that permits analysis. It should be noted that, having assumed a low \bar{Q}_{eH} value, the electron mobility ($\mu_e \sim 1/\bar{Q}_{eH}$) is large, and therefore so are the Hall parameters in this analysis.

An alternative approach to obtaining the desired electrical conductivity levels (again, $\geq 01 \text{ S/m}$), at higher \bar{Q}_{eH} values (i.e., at relatively lower electron mobilities for the same conditions), is to increase the local electron number density. The electron number density of the fissioning plasma, for fixed thermodynamic conditions (T and P) scales as the cube root of the local specific fission density; i.e. $n_e \sim (\beta_f \sigma_f \Phi)^{1/3}$. To increase the number density, the atom fraction of the fissionable atom β_f can be increased, and/or the fissionable isotope itself can be changed to an isotope with a higher fission cross-section (σ_f) at the system neutron temperature, and/or the local neutron flux (Φ) can be increased.

An order-of-magnitude increase in any one of these mentioned variables (assuming the other remain fixed) increases the number density by a factor of 2.15. For a specified fluid mixture (β_f and σ_f specified), the neutron flux level can be changed to effect a change in the number density. A factor of 2.15 increase in the electron number density--and a corresponding increase in electrical conductivity for a given electron mobility--results in an order-of-magnitude increase in the fission energy deposition rate in the fluid. However, as has already been discussed (see Section 1.2), the fission energy addition to the fluid contributes to diffusing the generator flow, and therefore to reducing the generator length in which supersonic flow can be maintained. Therefore, it might be anticipated that for a given generator duct design and inlet conditions there exists a maximum desirable neutron flux level. In the calculations performed in this work, the neutron flux level is set uniformly through the MHD duct to be 1×10^{16} n/cm²s, leading to electron number densities of typically 2 to 6×10^{19} /m³. These number density levels are low compared with those of typical (equilibrium electron temperature, seeded Saha-ionization) MHD generators. For example, again using the numbers provided by Rosa (1968), referring to Brogan's report on seeded combustion gas electrical properties (Brogan, 1963), suggests that at static pressures of 1 atm and local static temperatures of 2500 K, the electrical conductivity and electron mobility are $\sigma_e \approx 6$ S/m (reported) and $\mu_e \approx 0.4$ T⁻¹ (calculated by the author using the reported \bar{Q}_{eff} value); at T = 3000 K, the same data suggests that $\sigma_e \approx 75$ S/m and $\mu_e \approx 0.6$ T⁻¹. Using Equation 2-102 of Section 2.4.2, the electron number densities in these seeded combustion gases are

estimated to be in the range of $9 \times 10^{19} / \text{m}^3$ (at 2500 K) to $8 \times 10^{20} / \text{m}^3$ (at 3000 K). Therefore, the electron number densities arising from fission-fragment induced ionization at the $1 \times 10^{16} \text{ n/cm}^2\text{s}$ flux level may be as much as an order-of-magnitude lower than that typically encountered in the seeded thermal-ionization generators. Hence the necessity for assuming a low \bar{Q}_{eff} is to assure an electron mobility that is high enough to provide the electrical conductivity levels required for significant MHD interaction.

Although the electron number densities of the fissioning plasma are low, a positive aspect of the fission plasma is that the (albeit low) electron number densities can be obtained at significantly lower static temperatures than those that can be accommodated in thermal-ionization generators.

3.6 Nonuniform Fission-Model Plasma Property MHD Solutions

Section 3.4 presents analysis of fissioning MHD flows for which uniform plasma transport properties of $\sigma_e = 70 \text{ S/m}$ and $\mu_e = 2 \text{ T}^{-1}$ are assumed. This section provides analysis of MHD generator solutions that include the spatial variation of the plasma physics properties obtained using the equilibrium electron temperature fission-model ($S_{ff} \gg S_{Saha}$) developed in Section 2.4.4, and discussed in Section 3.5.4. The local scalar electrical conductivity, σ_e is calculated using Equation 2-116; the local electron mobility is calculated using Equation 2-117. The working fluid properties used in the fissioning plasma model are presented in Table 3.4.

Table 3.4 Working Fluid Properties for Equilibrium Electron Temperature/Fissioning Plasma ($S_{ff} \gg S_{Saha}$) MHD Generator Calculations

UF₄-He Working Fluid Mixture Property Data

Molecular Weight, M_w (kg/kg · mole)	22.429
Ratio of Specific Heats, γ	1.482
Specific Heat, c_p (J/kg · K)	1139.7
Gas Constant (J/kg · K)	370.68

Fissioning Plasma Model Data

Energy Release per Fission, G_f (MeV)	190
Atom Fraction of Fissionable Isotope (e.g., ²³⁵ U) in Working Fluid (e.g., UF ₄ -He Mixture), β_f	0.05704
²³⁵ U Neutron Fission Cross-Section, σ_f (at $T_N \approx 1200$ K) (cm ²)	2.3×10^{-22}
Energy Consumed per Ion-Pair Produced (eV/I.P.), w_{ff}	35
Energy Released per Recombination Event, $w_r = C_2 \epsilon_1$	
C_2	1
First Ionization Potential, ϵ_1 (eV)	10
Recombination Rate Coefficient (m ⁶ /s), C_1	1.2×10^{-20}

Duct geometry. The generator duct geometry considered in this section is described in Figure 3.42. The duct has a linearly decreasing upper wall that prescribes the cross-sectional flow area, A , given in Equations 3-26 and 3-27 of Section 3.2.3. The duct is designed so that $\partial A/\partial r \geq 0$ throughout the duct and so that $\partial A/\partial r = 0$ at the duct exit (at $r = 1.25$ m). The lower duct wall is flat; i.e., it has no curvature. It is noted that the duct considered in this section is 0.5 m in length, while the duct length considered in Section 3.4--the uniform plasma property solution analysis--is 0.3 m. (The longer duct length used in this section helps compensate for the low MHD interaction per unit length of the equilibrium, non-uniform property fissioning plasma flows.) The generator inlet is located at 0.75 m in this section (as compared to 1.0 m duct inlet used in Section 3.4).

Generator inlet conditions. The generator inlet conditions shared by the example generators considered here are presented in Table 3.5. The neutron flux level is specified as 1×10^{16} n/cm²s, uniform throughout the duct.

The behavior of the generator radial and axial variable profiles are analyzed below, first for generators of different applied magnetic induction and the same load resistance, then for generators of different load resistance and the same applied magnetic induction. The "reference" generator has a 8 Ω load resistance and a 5 T applied magnetic induction.

3.6.1 Reference Generator Plasma Property Profiles

Radial profiles. The radial profiles of the electrical conductivity (σ_e) and the electron mobility μ_e at the duct centerline (grid 51 of 101) and at the lower wall (grid 1 of 101), calculated as part of the overall MHD solution of the

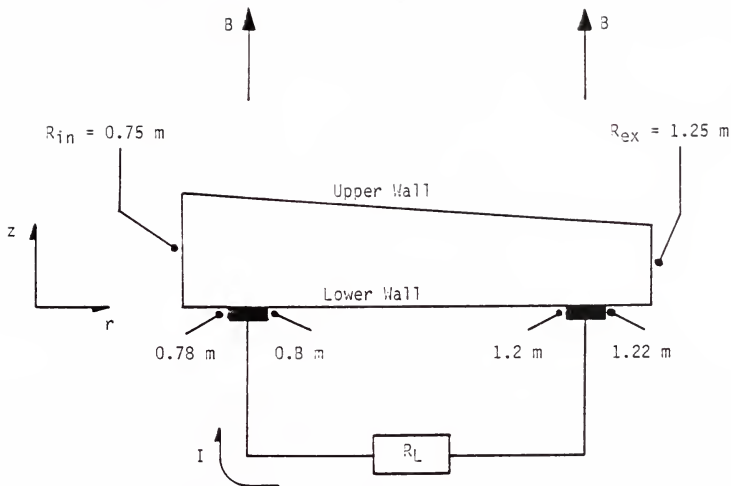


Figure 3.42 Schematic Diagram of MHD Duct with Linear Decreasing Duct Height used for Nonuniform Plasma Property MHD Calculations.

Table 3.5 MHD Generator Inlet Conditions and Specified Global Parameters for Nonuniform Fission-Model Plasma Property MHD Generator Calculations

Inlet Flow Free Stream Parameters

Stagnation Temperature (K)	3000
Stagnation Pressure (MPa,atm)	5.066,50
Radial Mach Number	2.0
Swirl Factor	1.0
Total Mach Number	2.83
Static Temperature (K)	1025 K
Static Pressure (MPa,atm)	0.186,1.84

Inlet Boundary Layer Thickness (m) 1×10^{-3}

Wall Temperature (K) 2000

Neutron Flux Level (n/cm²s) 1×10^{16}

reference generator ($B = 5 \text{ T}$, $R_L = 8 \Omega$) problem, are provided in Figure 3.43 and 3.44; the profiles presented in these figures can be considered typical of the plasma property profiles obtained in the MHD generator solutions of this section.

Both the $\sigma_e(r)$ and $\mu_e(r)$ lower wall distributions exhibit fluctuations (oscillations) in both the anode ($0.78 \text{ m} \leq r \leq 0.8 \text{ m}$) and cathode ($1.2 \text{ m} \leq r \leq 1.22 \text{ m}$) regions; these oscillations are a result of radial-spatial fluctuations in the static pressure and temperature in the vicinity of both anode and cathode. Figure 3.45 provides the static pressure radial distribution along the lower generator wall and Figure 3.46 provides the static temperature radial distribution at grid line 11 of 101--the 10th gridline ($z \leq 1 \times 10^{-4} \text{ m}$) from the lower wall. Recall that the wall temperature is specified as a uniform 2000 K along the lower wall; therefore, to see the temperature oscillations in the vicinity of the electrodes (at the lower wall) the region (grid line 11) $\leq 10^{-4} \text{ m}$ from the wall is examined; the static pressure profile at grid 11 of 101 is the same as the static pressure profile at the wall. Considering the (reference generator) current stream function spatial distribution provided in Figure 3.47 and the static pressure contour provided in Figure 3.48, the following explanation of the fluctuations in the static conditions (T and P)--and therefore the plasma properties (σ_e and μ_e)--near the electrodes is offered.

Electrode generated shock waves. Considering the current stream function distribution in Figure 3.47, it is apparent that the upstream end of the anode and the downstream end of the cathode are both regions of high current because both the load current and the short circuit recirculation currents that are driven by the

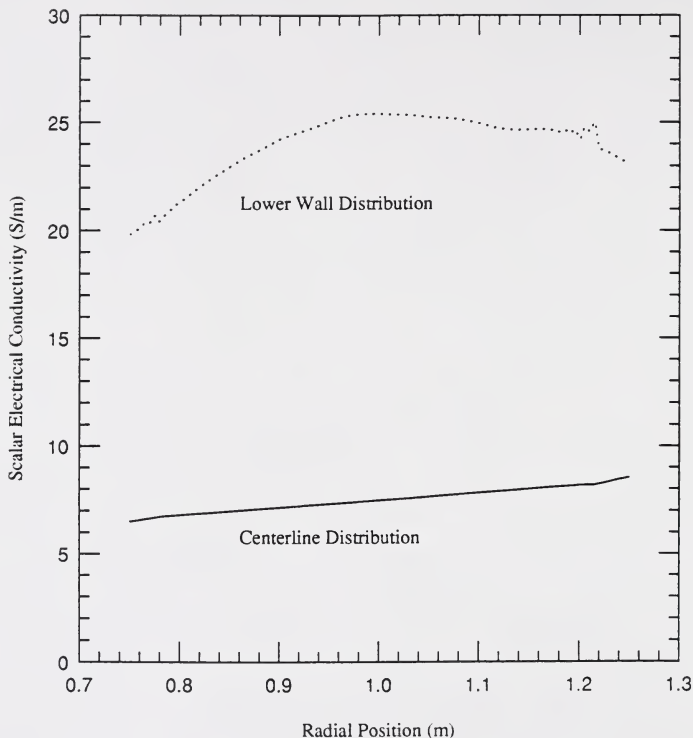


Figure 3.43 Centerline and Lower Wall Radial Profiles of Scalar Electrical Conductivity of Equilibrium Fissioning Plasma in Reference Generator with $B = 5 \text{ T}$ and $R_L = 8 \Omega$.

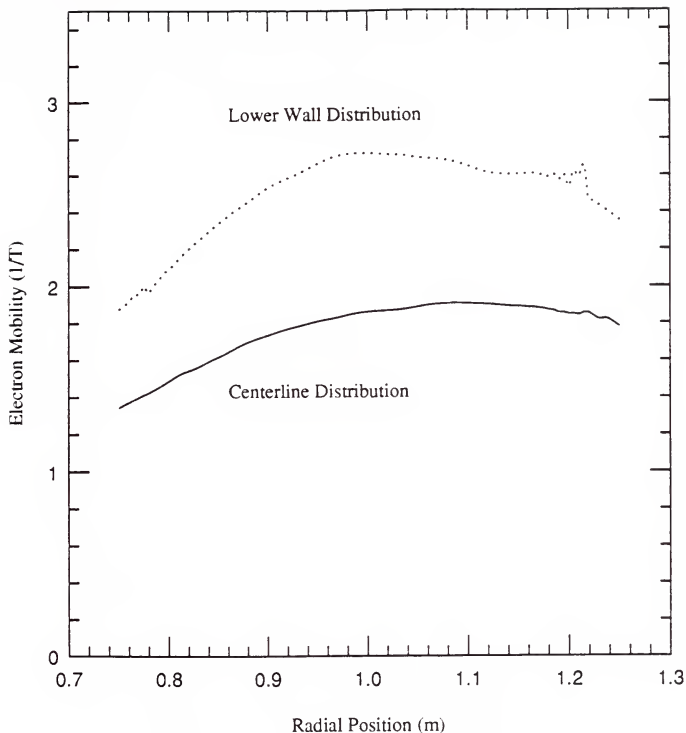


Figure 3.44 Centerline and Lower Wall Radial Profiles of Electron Mobility of Equilibrium Fissioning Plasma in Reference Generator with $B = 5 \text{ T}$ and $R_L = 8 \Omega$.

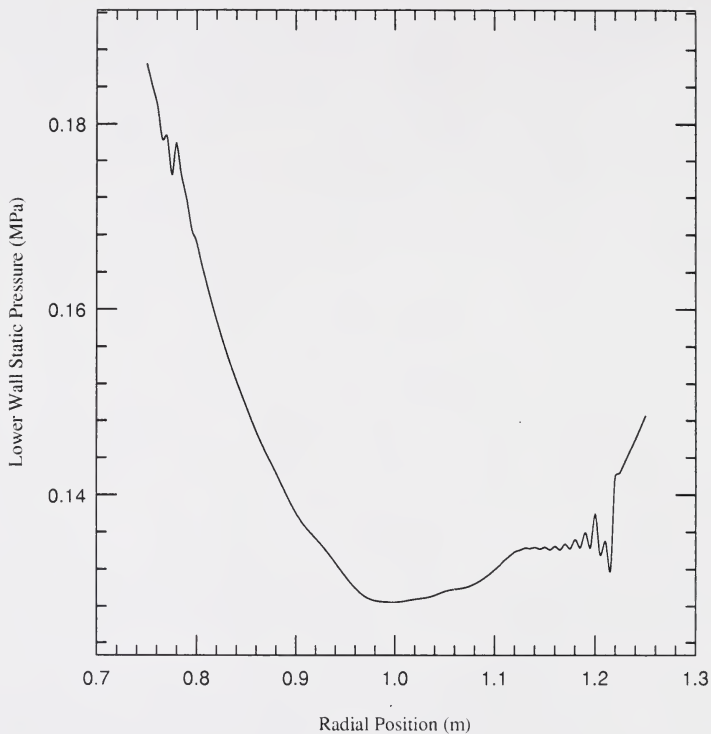


Figure 3.45 Static Pressure as a function of Radial Position at Lower Duct Wall of Reference Generator with Equilibrium Fissioning Plasma.

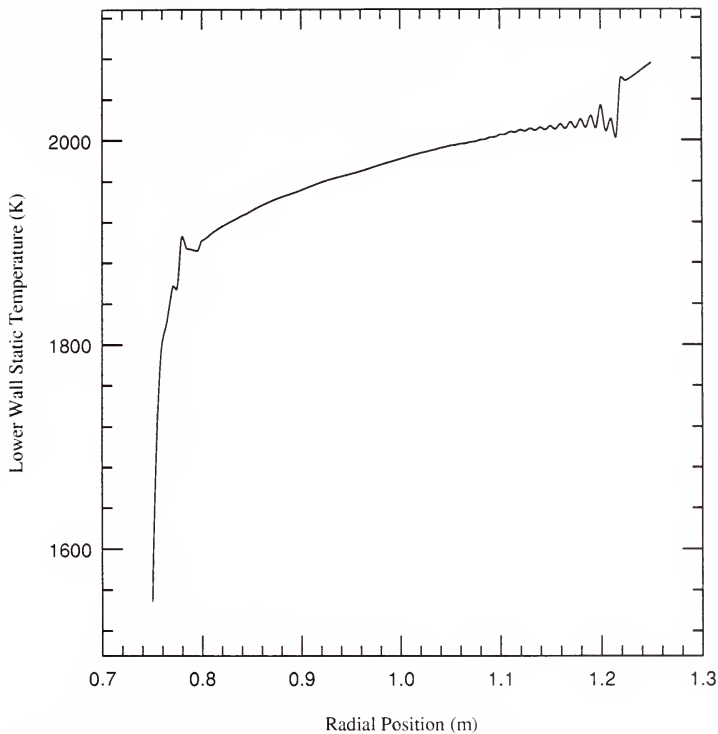


Figure 3.46 Static Temperature as a function of Radial Position at Grid Line 11 (near Lower Wall) of Reference Generator with Equilibrium Fission Plasma.

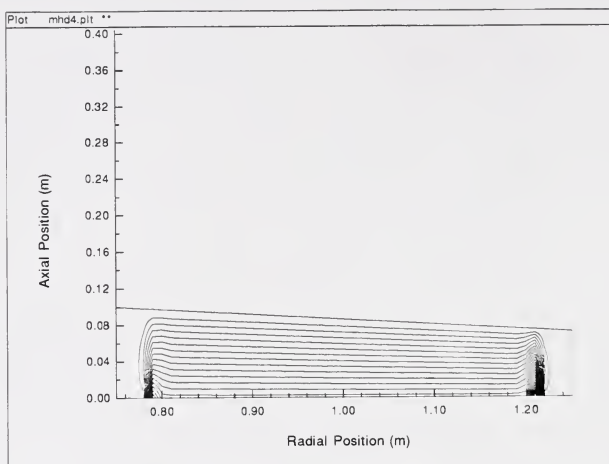


Figure 3.47 Current Density Stream Function Contour Plot of Reference ($B = 5 \text{ T}$ and $R_L = 8 \Omega$) Generator with Nonuniform Plasma Transport Properties.

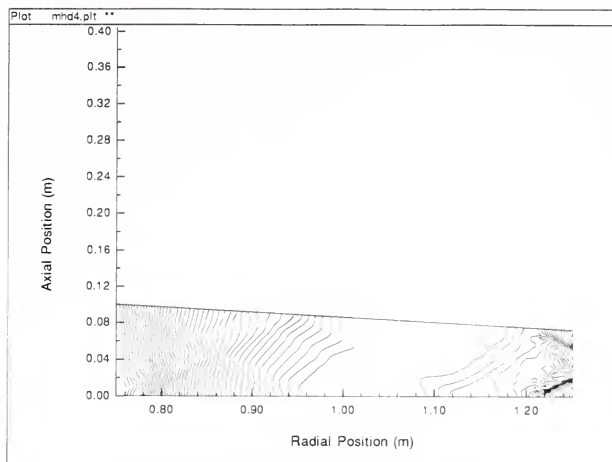


Figure 3.48 Static Pressure Contour Plot of Reference ($B = 5$ T and $R_L = 8 \Omega$) Generator with Nonuniform Plasma Transport Properties.

E-field over the "inactive" part of the electrode (see discussion in Section 3.5.2) combine to leave (enter) the anode (cathode) at these locations. Figure 3.43 shows that the scalar electrical conductivity at the wall is relatively--relative to the free stream--large. Therefore, as mentioned in an earlier discussion (Sections 3.4.1 and 3.5.2) the upstream end of the anode ($r = 0.78$ m) and downstream end of the cathode ($r = 1.22$ m) are the regions of the highest Joule heating ($\underline{J} \cdot \underline{E}'$) in the generator. The highly localized Joule heating density causes local static temperature increases (see locations $r = 0.78$ m and $r = 1.22$ m of Figure 3.46), and the temperature increase causes a localized decrease (increase) in fluid density (specific volume). From the upstream flow point-of-view, a sudden (i.e., step-like) increase in boundary layer displacement thickness is encountered at these locations, and the flow must change directions, to a more positive flow angle relative to the lower wall. The effect is felt throughout the boundary layer; the turning of the supersonic flow away from the wall (e.g., at the boundary layer edge) is accomplished through the generation of an oblique shock wave. The shock wave suggested here is evident in Figure 3.48 at the upstream end of the anode and the downstream end of the cathode. The effect of the generated oblique shock waves are evident, at the same radial positions, in the lower duct wall static pressure radial profile (Figure 3.45). A sudden increase in pressure is noticeable at the locations ($r = 0.78$ m and $r = 1.21$ m) of highest current density and Joule heating.

Finally, the fluctuations in the σ_e and μ_e wall radial distributions--which are particularly pronounced at the cathode ($1.2 \text{ m} \leq r \leq 1.22 \text{ m}$)--clearly coincide

with the oscillations of the fluid static temperature and pressure in that region. The oscillations in temperature and pressure are considered, by the author, to be physically incorrect, possibly examples of the oscillations, discussed in Section 3.1.3 on "Artificial Damping", that can occur near captured shock waves. For documentation-sake, the artificial damping constants ϵ_1 and k_4 are set at 1.0 and 3×10^{-2} , respectively, in the calculational results presented; both values are small, considering the range of damping constants suggested by the literature (see Section 3.1.3). It may be expected that increasing the artificial damping coefficients ϵ_1 to near 5.0 and k_4 to near 6.25×10^{-2} will help damp the oscillations manifested in Figures 3.45 and 3.46. It is noted, however, that the radial profiles of the static temperature at grid line 11 and the wall static pressure in the uniform property calculations of Section 3.4 do not exhibit the oscillations discussed here. Therefore, although the oscillations in the fluid static pressure and temperature may indeed exist because of the oblique shock wave captured at the cathode, the fact that the oscillations persist so that they are manifest in the converged steady-state solution, appears to be influenced by the feedback between the fluid static temperature, the plasma physics properties, the Joule heating, and the MHD interaction (cf. discussion in Section 3.5.2).

Apart from the near-electrode oscillations discussed above, the σ_c and μ_e radial profiles are fairly uniform (e.g., $20 \text{ S/m} \leq \sigma_{c,w} \leq 25 \text{ S/m}$) throughout the duct. To an extent there is a feedback that contributes to plasma property uniformity (away from the electrodes) in the duct. If locally the conductivity increases, then so do the body forces against the flow; the increased body forces

will diffuse the flow more effectively, raise the pressure, decrease the electron mobility, and therefore decrease the local conductivity.

Leakage currents. Using the plasma property values provided in Figures 3.43 and 3.44, it is also interesting to note that the Hall conductivity ($\sigma_{\perp} = \sigma_e / (1 + (\mu_e B)^2)$) at the centerline of the duct experiences an overall decrease (from 0.13 S/m at the inlet to 0.095 S/m at the exit) as the duct is traversed; along the lower wall the Hall conductivity decrease from near 0.2 S/m at the inlet to 0.014 S/m near the cathode. The ratios of the scalar conductivity (σ_e) to the Hall conductivity (σ_{\perp}) at the inlet and the outlet are approximately 100 and 170, respectively. This suggests that the path for leakage currents-- currents flowing between the cathode and anode along the lower wall--are of high resistance relative to the path taken by the load current in entering (exiting) the cathode (anode); therefore, the leakage currents should be small. It was suggested earlier in Section 1.2 that possibly less than a percent of the boundary layer (e.g., along the lower wall) is available for negative Hall current densities, in the high Reynolds number (thin boundary layer) supersonic flows. The small effective path size (thickness on the order of the laminar sublayer) and the low Hall conductivity (relative to the scalar conductivity) along the lower wall combine to minimize leakage currents between the cathode and anode. Recall from Section 3.5.4 that the functional forms of σ_e and μ_e show that the variation in the plasma properties between the free stream and the wall is dictated in large part by the free stream conditions (T and P) and the wall conditions; therefore, the wall temperature dictates to an extent the leakage current level.

Axial profiles. Figures 3.49 and 3.50 provide the axial profiles of the scalar electrical conductivity and electron mobility, respectively, at both the center of the anode ($r = 0.79$ m) and the center of the cathode ($r = 1.21$ m) for the "reference generator ($B = 5$ T and $R_L = 8 \Omega$). As discussed in Section 3.5.4, the static pressure is relatively uniform through the boundary layer so that $\sigma_e(z) \sim T(z)^{5/3}$ and $\mu_e(z) \sim T(z)^{1/2}$. For the "reference" generator conditions, the electron mobility (Figure 3.53) is nearly constant, but increases slightly in passing through the boundary layer, from the free stream to the wall.

3.6.2 Varying Applied Magnetic Induction

Radial profiles. Figures 3.51 and 3.52 provide comparisons of the stagnation temperature and pressure radial profiles along the duct centerline (grid 51 of 101) for generators with applied magnetic inductions of 0 T, 5 T (reference case), and 6 T; the load resistance of each generator is 8Ω . Using Figure 3.51 the enthalpy extractions of the 5 T and 6 T generators are estimated to be 2.3% and 3.6%, respectively. The corresponding electric power densities, for the 5 T and 6 T generators, are $140 \text{ MW}_e/\text{m}^3$ and $190 \text{ MW}_e/\text{m}^3$, respectively. Using Figure 3.52 and Equation 3-30 the isentropic conversion efficiencies for the $B = 5$ T and 6 T generators are estimated to be 14.9% and 20.4%, respectively. The \bar{T} and \bar{P} profiles exhibit features similar to those seen for the generators with uniform plasma properties. The $B = 0$ T generator exhibits a linear increase in total temperature (Figure 3.51) and a linear decrease in stagnation pressure (Figure 3.52), due to the fission heat addition. In the $B = 5$ T and 6 T

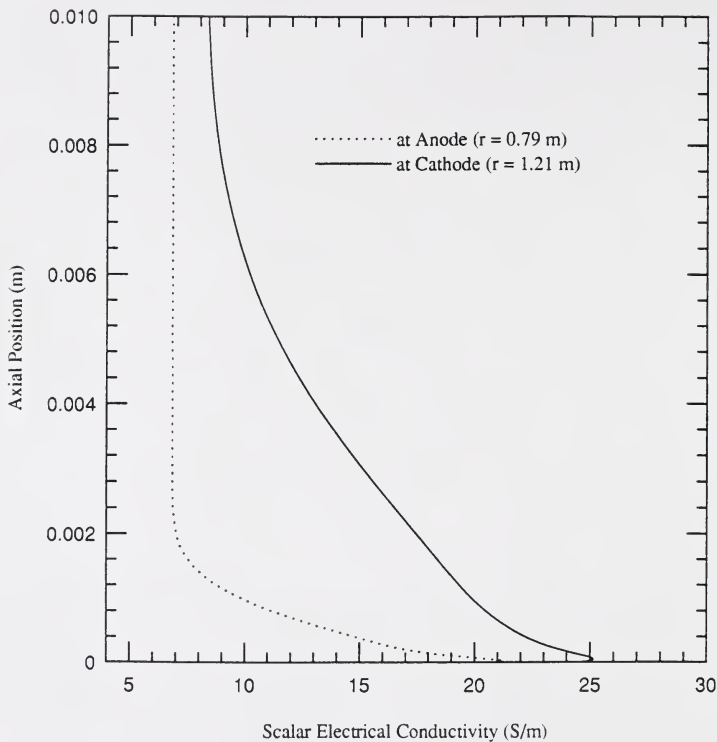


Figure 3.49 Scalar Electrical Conductivity at Anode ($r = 0.79$ m) and Cathode ($r = 1.21$ m) as a function of Axial Position in Reference ($B = 5$ T and $R_L = 8 \Omega$) Generator with Equilibrium Fissioning Plasma.

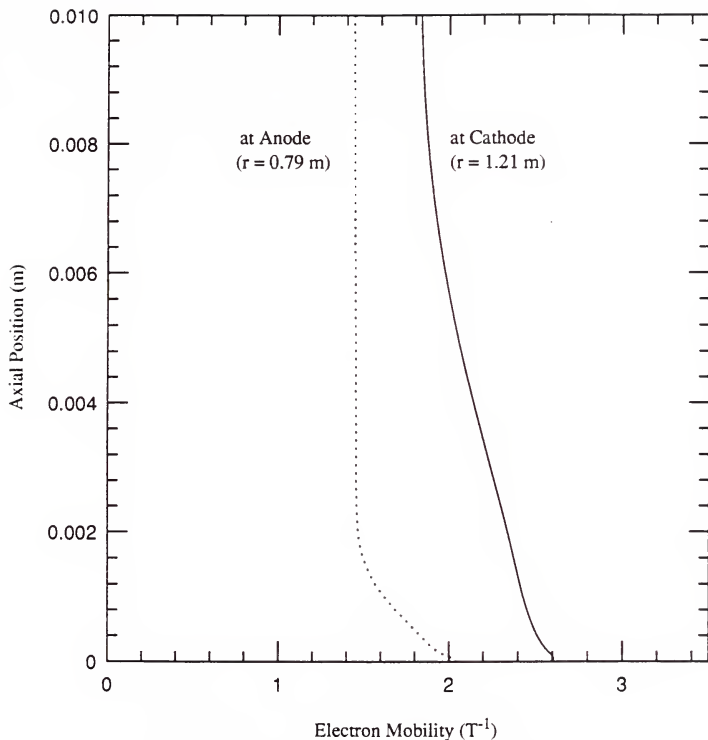


Figure 3.50 Electron Mobility at Anode ($r = 0.79$ m) and Cathode ($r = 1.21$ m) as a function of Axial Position in Reference ($B = 5$ T and $R_L = 8 \Omega$) Generator with Equilibrium Fissioning Plasma.

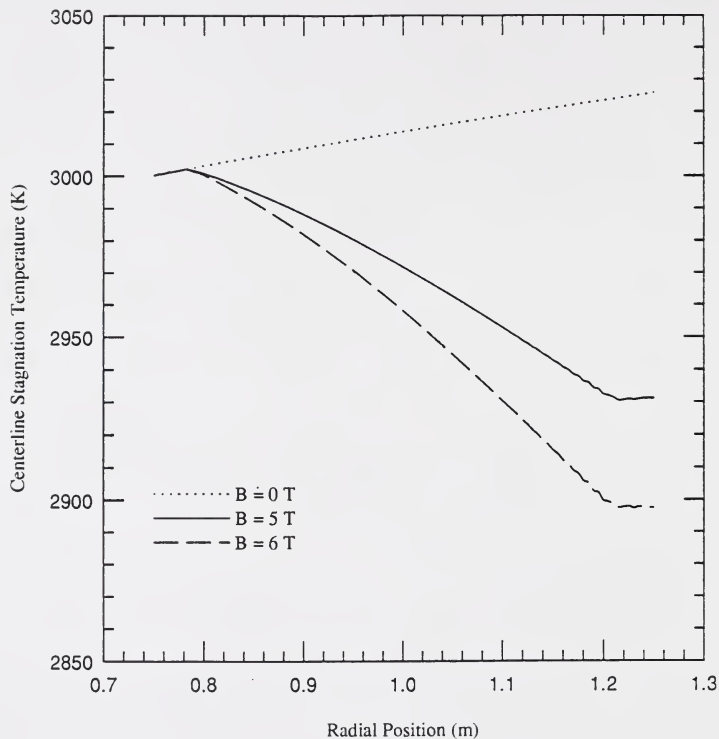


Figure 3.51 Comparison of Centerline Stagnation Temperature as a function of Radial Position for $B = 0$ T, 5 T, and 6 T Generators with Nonuniform Plasma Transport Properties.

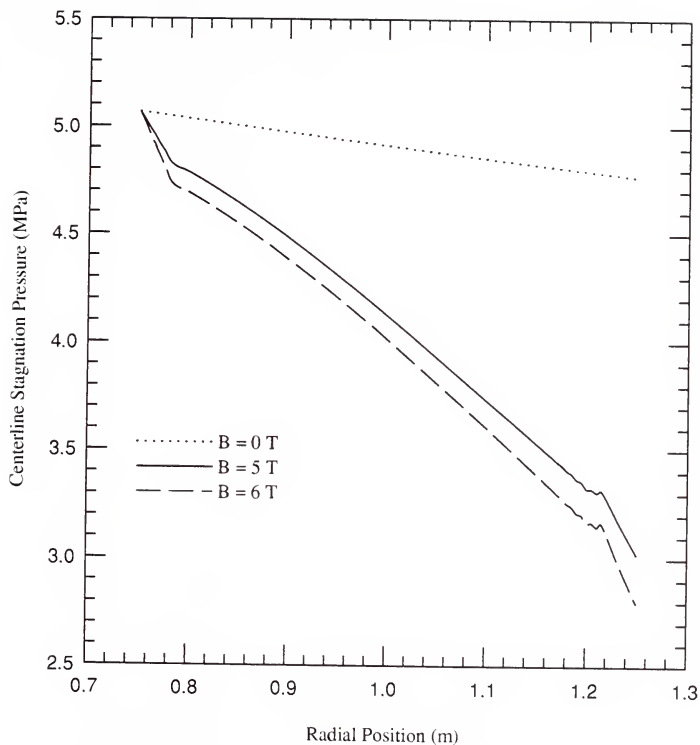


Figure 3.52 Comparison of Centerline Stagnation Pressure as a function of Radial Position for $B = 0$ T, 5 T, and 6 T Generators with Nonuniform Plasma Transport Properties.

generators, outside (upstream and downstream) of the "active generator region"--defined as the region between and including the electrodes ($0.78 \text{ m} \leq r \leq 1.22 \text{ m}$)--negligible electric power extraction occurs because the Hall current is nearly zero (see the discussion in Section 3.4.1); in these regions--outside of the active generator region--the generator operates in effectively an open circuit mode. The $J_r \approx 0$ condition in these regions leads to large $J_\theta B$ body forces (oriented radially against the flow), evidenced by the rapid total pressure losses upstream of the anode and downstream of the cathode (see Figure 3.52).

The tendency of the MHD interaction to decelerate the flow is evident in Figure 3.53 where the radial profiles of the radial Mach number along the center grid line (51 of 101) of the $B = 0 \text{ T}$, 5 T , and 6 T generators are compared. The flow is increasingly decelerated--or inhibited from accelerating--as the applied magnetic induction, and therefore the MHD interaction, is increased. Comparing the profiles provided in Figure 3.53 with the centerline radial Mach numbers provided in the Figure 3.27 of Section 3.4.1 suggests that the MHD interaction levels in the nonuniform property fission-model generators examined here are low. Note that in Figure 3.27, the MHD flow upstream of the anode ($1.0 \text{ m} \leq r \leq 1.03 \text{ m}$)--in the region where $J_r \approx 0$ and the $J_\theta B$ forces are largest--is diffused by the body forces to the extent that, although the duct area is increasing ($\partial A / \partial r \geq 0$) in that region, the radial Mach number decreases. In contrast the ($B = 5 \text{ T}$ and 6 T) flows represented in Figure 3.53, though exhibiting departure from the $B = 0 \text{ T}$ generator, are accelerated in the region upstream of the anode ($0.75 \text{ m} \leq r \leq 0.78 \text{ m}$).

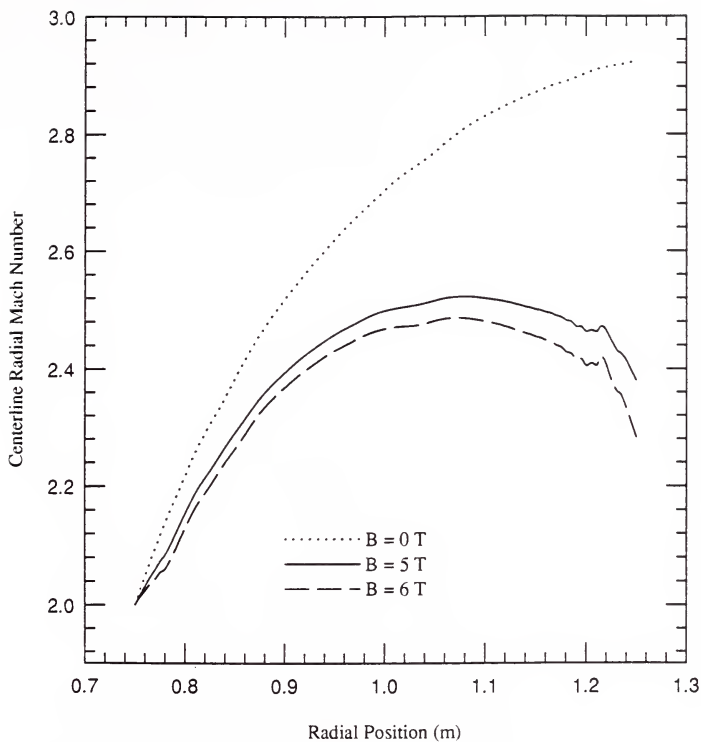


Figure 3.53 Comparison of Centerline Radial Mach Number as a function of Radial Position for $B = 0$ T, 5 T, and 6 T Generators with Nonuniform Plasma Transport Properties.

Utilizing the MHD interaction parameter, Π (discussed by Sutton and Sherman, 1965), defined as the ratio of the MHD body forces to the fluid inertial forces, the relative levels of MHD interaction in the uniform plasma property and nonuniform (fission-model) generators can be compared. For the disk MHD generator, Π can be written as

$$\Pi = \frac{\sigma_e u B^2}{\rho u^2} = \frac{\sigma_e B^2 L}{\rho u} \quad \left[\approx \sigma_e B^2 \left(\frac{V_{MHD}}{\dot{m}} \right) \right] \quad (3-47)$$

where L is a characteristic length--appropriately the generator length. For the purpose of comparison, it is assumed that the inlet inertial forces, as well as the radial velocity components, u , of the two generators are the same so that $\Pi_{\text{Uniform}}/\Pi_{\text{Fission}} \approx (\sigma_e B^2)_{\text{Uniform}}/(\sigma_e B^2)_{\text{Fission}}$. Recalling that for the uniform generator calculations, $\sigma_e = 70 \text{ S/m}$ and considering the "reference" uniform generator, with $B = 3.5 \text{ T}$, the $(\sigma_e B^2)_{\text{Uniform}} \approx 860 \text{ S T}^2/\text{m}$. Using the centerline inlet scalar electrical conductivity, $\sigma_e \approx 6.5 \text{ S/m}$, for the $B = 5 \text{ T}$ nonuniform generator (see Figure 3.43), then the $(\sigma_e B^2)_{\text{Fission}} \approx 163 \text{ S T}^2/\text{m}$. Therefore $\Pi_{\text{Uniform}}/\Pi_{\text{Fission}} \approx 5.25$, or the uniform "reference" generator of Section 3.4.1 experiences over five times the MHD interaction at the inlet of the generator compared to the nonuniform (fission model) generators examined in this section. The interaction parameters of the uniform and nonuniform property generator calculations are compared here to indicate that the fission-model generators examined here experience relatively low MHD interaction levels.

Axial profiles. The axial profiles of the radial velocity component ($u(z)$) predicted for the $B = 0$ T, 5 T, and 6 T applied B-fields over the cathode (at $r = 1.21$ m) are compared in Figure 3.54. At the fixed 8Ω load resistance the flow is increasingly decelerated as the magnetic induction is increased. The ratio of the $J_{\theta}B$ body forces against the flow at the wall to that against the flow in the free stream--again assuming that $E_r(r,z) \approx E_r(r)$ --can be estimated to be

$$\frac{J_{\theta,w}}{J_{\theta,\infty}} = \frac{\sigma_{\perp,w}}{\sigma_{\perp,\infty}} \left[\frac{\beta_{e,w}(\beta_{e,\infty} + S)(\zeta - 1)}{(S - \beta_{e,\infty}) + \beta_{e,\infty}(\zeta - 1)(\beta_{e,\infty} + S)} \right] \quad (3-48)$$

which in the limit that $\beta_c \gg S$ and $\beta_c \gg 1$ approaches $(J_{\theta,w}/J_{\theta,\infty}) \approx (\sigma_{\perp,w}\mu_{e,w})/(\sigma_{\perp,\infty}\mu_{e,\infty})$. Note that this ratio can be estimated, for example sake, using the values provided in Table 3.3. Using the values for "hot walls", in the limit that $\beta_c \gg S$ and $\beta \gg 1$, the ratio of the body forces $(J_{\theta,w}/J_{\theta,\infty}) \approx 2.2$. Taking another approach, considering Figure 3.50 and the axial profiles of the electron mobility (at the cathode for example) it is seen that the mobility is relatively uniform through the boundary layer. If then $\mu_{e,w} \approx \mu_{e,\infty}$, it might be expected, in the limit that $\beta_c \gg S$ and $\beta_c \gg 1$, that $(J_{\theta,w}/J_{\theta,\infty}) \approx (\sigma_{e,w}/\sigma_{e,\infty})$ which is approximately 3 at the cathode. The estimates above indicate that, for the case of 2000 K walls and generator free stream conditions similar to those of the $B = 5$ T, $R_L = 8 \Omega$ reference generator, the $J_{\theta}B$ body force at the wall is 2 to 3 times that in the free stream, and is also directed radially against the flow; this is in contrast to the uniform plasma property generator (see Section 3.4.1 for discussion

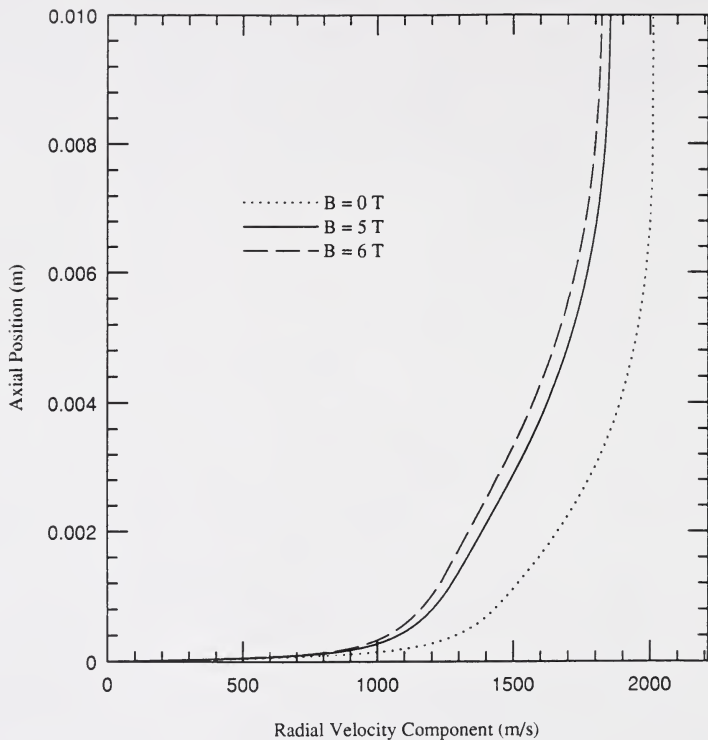


Figure 3.54 Comparison of Radial Component of Velocity as a function of Axial Position at Cathode ($r = 1.21$ m) for $B = 0$ T, 5 T, and 6 T Generators with Nonuniform Plasma Transport Properties.

on axial profiles) in which the same type of estimate suggests that the ratio of $(J_{\theta,w}/J_{\theta,\infty})$ is near unity.

It is reiterated that the dependence of the plasma properties--and therefore the ratio of body forces and the subsequent influence of body forces on the velocity profiles and shear stress--is dictated in large part by the temperature of the wall (or the adiabatic wall temperature in the case of an insulated wall) relative to the free stream temperature. For example, again using Table 3.3, for the case of a "cold wall" temperature of 800 K and the nominal free stream conditions considered in this work, an estimate of $J_{\theta,w}/J_{\theta,\infty} \approx 0.5$ is obtained for the nonuniform generator, in marked contrast to the hot wall case. For the case of an insulated wall, using the same free stream conditions (see Table 3.1) used to generate Table 3.3 and using Equation 2-58 for the adiabatic wall temperature (estimated to be ≈ 2250 K), the estimated ratio $J_{\theta,w}/J_{\theta,\infty} \approx 2.5$, similar to the hot wall (2000 K) case discussed above.

Figure 3.55 presents a comparison of the axial profiles of the tangential velocity component, at the cathode ($r = 1.21$ m) for the $B = 0$ T, 5 T, and 6 T generator cases. As discussed in Section 3.4.1, the tangential velocity component may be estimated using $v(r) \approx v_{in} \cdot (R_{in}/r) \cdot (1 - \Delta)$ where Δ contains the MHD interaction effects. At the interaction levels experienced in Section 3.4.1 (with $\sigma_e = 70$ S/m and $B = 3.5$ T), $\Delta \approx 2$ to 3%. Recall that in the fission-limit generators treated here, the MHD interaction is estimated to be on the order of 20% for that of the generators examined in Section 3.4.1; therefore, the Δ for the cases examined here may be expected to be $\Delta \approx 0.4$ to 0.6%. The body force J,B

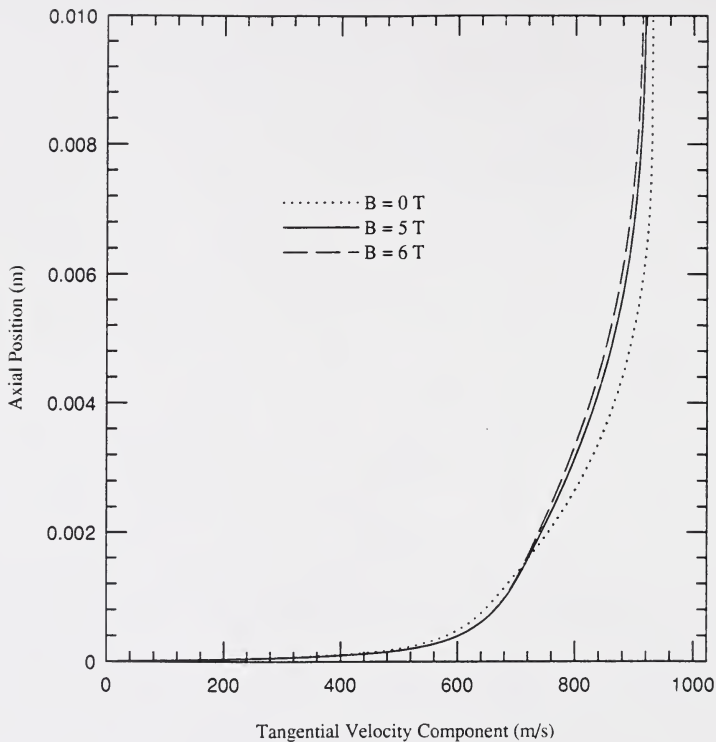


Figure 3.55 Comparison of Tangential Component of Velocity as a function of Axial Position at Cathode ($r = 1.21$ m) for $B = 0$ T, 5 T, and 6 T Generators with Nonuniform Plasma Transport Properties.

against the flow has little influence on the magnitude of the tangential velocity component at these interaction levels. This is evident by noting the agreement in the magnitudes of the tangential velocity component of the $B = 0$ T, 5 T, and 6 T generators in the free stream (e.g., at $z = 0.01$ m).

The difference in the shape of the velocity profiles--the exhibited Hartmann flow profiles--evident in Figure 3.55 is attributed to the variation in the $J_r B$ body force profile through the boundary layer. The ratio of the body forces experienced near the wall compared to those experienced in the free stream--again assuming that some position away from the electrodes is considered so that $E_r(r, z) \approx E_r(r)$ --may be estimated using

$$\frac{J_{r,w}}{J_{r,\infty}} \approx \left(\frac{\zeta - 1}{\zeta} \right) \frac{\sigma_{\perp,w}}{\sigma_{\perp,\infty}} \approx - \left(\frac{R_L}{R_{MHD}} \right) \frac{\sigma_{\perp,w}}{\sigma_{\perp,\infty}} \quad (3-49)$$

That is, the ratio of the body forces is the same as that found in the uniform plasma property case, multiplied by the wall-to-free stream ratio of the Hall conductivities. The generator load parameter ζ ($\equiv J_r/J_{r,short}$) is related to the generator load resistance (R_L) by Equation 3-36; however, in the generators with nonuniform plasma properties, determination of the effective generator resistance, R_{MHD} , is a nontrivial task. The magnitude of the ratio of $J_r B$ body forces through the boundary layer, expressed by Equation 3-49, evidently varies greatly with the load parameter ζ (or load resistance, R_L) so that $-\infty \leq J_{r,w}/J_{r,\infty} \leq 0$. For the particular case of $R_L = R_{MHD}$ ($\zeta = 0.5$) the magnitude of the body force at the wall is a factor of $\sigma_{\perp,w}/\sigma_{\perp,\infty}$ times the magnitude of the body force in the free stream, and is opposite in direction. In the free stream, the body force is against

the flow, tending to decelerate the flow; near the wall (estimated to be within a distance of 1% of the boundary layer thickness next to the wall for turbulent flows), the body force works to accelerate the flow. For the case of the hot (2000 K) wall, the ratio of body forces is estimated to be $J_{\theta,w}/J_{\theta,\infty} \approx -1.6$ (using the values in Table 3.3). The shape of the velocity profiles in Figure 3.55 indicates that indeed for $B > 0$ the flow near the wall is accelerated while the flow in the free stream is decelerated. The amount of acceleration (or deceleration) increases with increasing B-field (and MHD interaction).

Figure 3.56 provides a comparison of the static temperature axial distributions in the boundary layer of the lower wall at the cathode ($r = 1.21$ m) for the $B = 0$ T, 5 T, and 6 T generators. As the magnetic induction (and the MHD interaction) increases, the free stream flow is increasingly diffused so that the free stream static temperature increases. A temperature overshoot occurs very near the wall in all three profiles; the overshoot increases with increasing B-field, as a result of increased Joule heating--here at the cathode--and, in general, increased boundary layer thicknesses at the higher magnetic induction levels. As found in the uniform plasma property calculational results analyzed in Section 3.4.1, the temperature overshoots shown in Figure 3.56 are small in the low Prandtl number fluid.

3.6.3 Varying Load Resistance

In the preceding section, the generator load resistances are all fixed at $R_L = 8 \Omega$. In this section the results of three generators with load resistances of $R_L = 1.8 \Omega$, 8Ω (reference generator), and 32Ω are examined; the applied magnetic

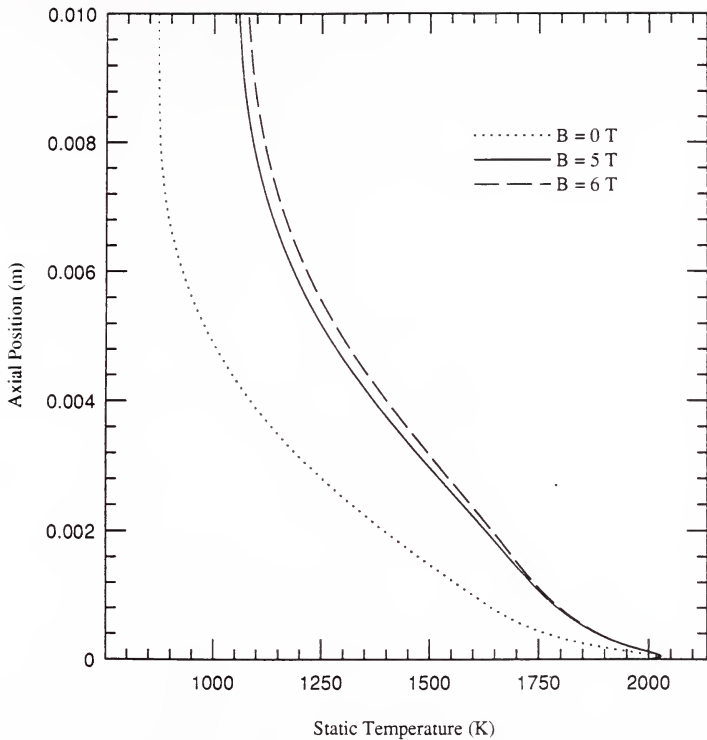


Figure 3.56 Comparison of Static Temperature as a function of Axial Position at Cathode ($r = 1.21$ m) for $B = 0$ T, 5 T, and 6 T Generators with Nonuniform Plasma Transport Properties.

induction is $B = 5 \text{ T}$ in each case. Although an approximation for the generators with variable plasma properties, the load parameters (ζ) corresponding to the specified load resistances are estimated, using Equation 3-36 with the centerline values of electrical conductivity (Figure 3.43) and electron mobility (Figure 3.44) of the reference generator, to be approximately $\zeta = 0.2$ ($R_L = 32 \Omega$), 0.5 ($R_L = 8 \Omega$), and 0.8 ($R_L = 1.8 \Omega$); the effective resistance of the reference generator is estimated to be $R_{\text{MHD}} \approx 8 \Omega$. Assuming these estimates to be correct, the $R_L = 8 \Omega$ ($\zeta = 0.5$) resistance corresponds to the load for maximum generator power output (balanced load) while $R_L = 1.8 \Omega$ ($\zeta = 0.8$) corresponds to a lower power generator operating near short circuit, in the range in which Hall generators operate most efficiently. $R_L = 32 \Omega$ ($\zeta = 0.2$) is examined as an off-design condition, near open circuit.

Radial profiles. Figure 3.57 provides a comparison of the radial profile of the stagnation temperature along the centerline of the duct (on grid 51 of 101) of the $R_L = 1.8 \Omega$, 8Ω , and 32Ω generators. (The $R_L = 8 \Omega$ reference case is included in the variable B-field work presented in the previous section.) The total temperature profiles for the three generators follow the trends discussed in Section 3.4.2. Power extraction occurs in the active generator region; and outside of the active generator region where $J_r \approx 0$ (and $\underline{J} \cdot \underline{E} \approx 0$), the stagnation temperature increases due to the fission heating. At the lower MHD interaction levels of the generators analyzed here (relative to the uniform property generators analyzed in Section 3.4), the total temperature decrease with radial position is nonlinear and the power extraction increases with radial position. As expected,

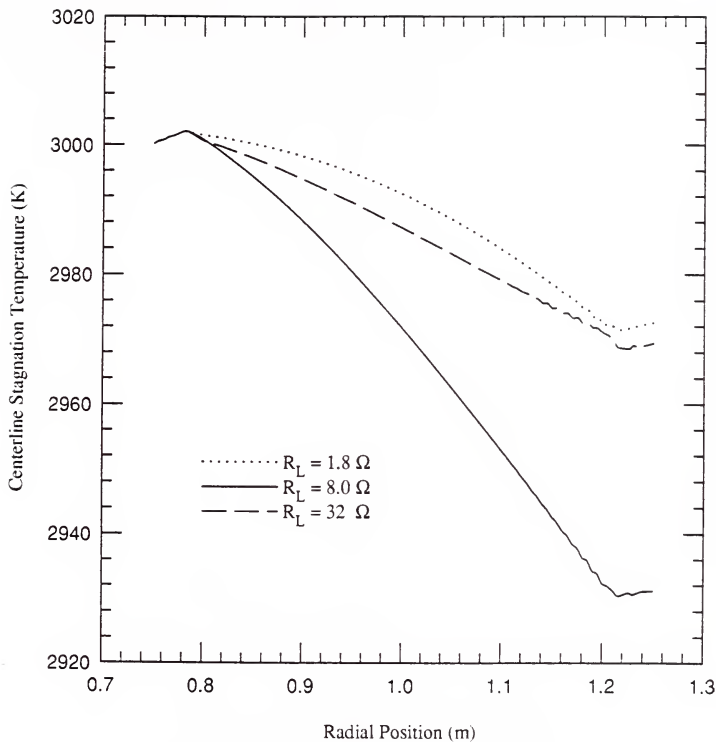


Figure 3.57 Comparison of Centerline Stagnation Temperature as a function of Radial Position for $R_L = 1.8 \Omega$, 8Ω , and 32Ω Generators with Nonuniform Plasma Transport Properties.

the decrease in the stagnation temperature is greatest in the $R_L = 8 \Omega$ (balanced load, $\zeta \approx 0.5$) generator; the lower electric power densities ($\underline{I} \cdot \underline{E}$) of the $R_L = 32 \Omega$ ($\zeta \approx 0.2$) and $R_L = 1.8 \Omega$ ($\zeta \approx 0.8$) generators are reflected in the smaller decrease in stagnation temperature through the generator (i.e., the smaller enthalpy extractions). The enthalpy extractions for the 1.8Ω , 8Ω , and 32Ω generators are estimated (using values from Figure 3.61) to be 0.9%, 2.3%, and 1.0%, respectively. The corresponding generator power densities (from the electrical solver, ELEMAG) are $77.6 \text{ MW}_e/\text{m}^3$, $140 \text{ MW}_e/\text{m}^3$, and $75.4 \text{ MW}_e/\text{m}^3$, for the 1.8Ω , 8Ω , and 32Ω generators, respectively.

The stagnation pressure radial profiles along the duct centerline (grid 51 of 101) for the same three generators are compared in Figure 3.58. Consistent with comments presented in Section 3.4.1, the pressure drop outside the active generator region--both upstream of the anode and downstream of the cathode--are large. Upstream of the anode, the $J_\theta B$ body forces--tending to diffuse all three generator flows--are at the maximum (open circuit) value, $\sigma_e u B^2$. In this region, the open circuit conditions are identical for the three generators and therefore the three pressure curves coincide. The pressure loss rate within the active generator region is nonlinear. The pressure decrease is reduced in the vicinity of both electrodes (e.g., in the cathode region $1.2 \text{ m} \leq r \leq 1.22 \text{ m}$). The Hall current density, J_r , is largest in the free stream region axially away from but above the electrodes because the Hall current density in these regions carries not only the generator load current but also the short-circuit recirculation currents driven over the "inactive" portion of the electrode (see the discussion in Section

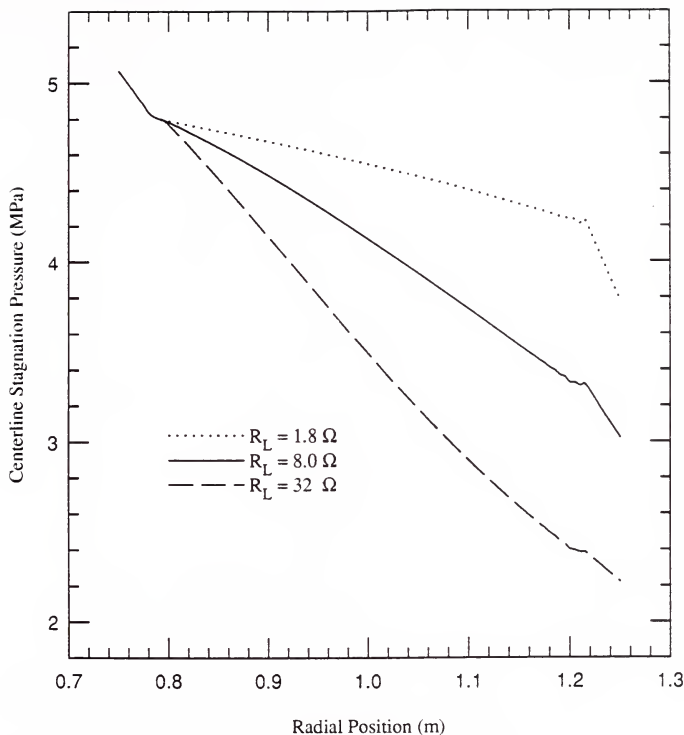


Figure 3.58 Comparison of Centerline Stagnation Pressure as a function of Radial Position for $R_L = 1.8 \Omega$, 8Ω , and 32Ω Generators with Nonuniform Plasma Transport Properties.

3.5.2 and the reference generator current stream function spatial distribution in Figure 3.47). The local increase in the Hall current density (J_θ) results in a reduction in the Faraday current density (J_z) by the Hall effect (see discussion in Section 1.1.2), and therefore the $J_\theta B$ body force against the flow over the electrode region is reduced. The generator overall pressure drops increase as the load parameter, ζ (load resistance, R_L), decreases (increases) towards open circuit, $\zeta \rightarrow 0$ ($R_L \rightarrow \infty$). The overall isentropic efficiencies of the $R_L = 1.8 \Omega$, 8Ω , and 32Ω generators are estimated, using Equation 3-30 and the stagnation temperature and pressure values provided in Figures 3.57 and 3.58, to be 10.1%, 14.9%, and 4.2%, respectively.

Figure 3.59 compares the centerline (grid 51 of 101) radial Mach number radial profiles for the $R_L = 1.8 \Omega$, 8Ω , and 32Ω generators. The effect of varying the $J_\theta B$ force by varying the generator load resistance is evident. At the high load resistances (e.g., 32Ω), the $J_\theta B$ forces are larger than at lower generator load resistances (e.g., 1.8Ω); this is reflected in the degree to which each flow is decelerated (or inhibited from accelerating, at these interaction levels), as shown in Figure 3.59.

Axial profiles. The radial velocity component axial profiles at the cathode ($r = 1.21$ m) for the variable load resistances at the fixed 5 T B-field are compared in Figure 3.60. In agreement with what is found for the uniform plasma property generators of Section 3.4.4, as the load resistance is increased (from 1.8Ω to 32Ω) the MHD body force against the flow increases, the flow is increasingly diffused, and the boundary layer thickens. In contrast to the

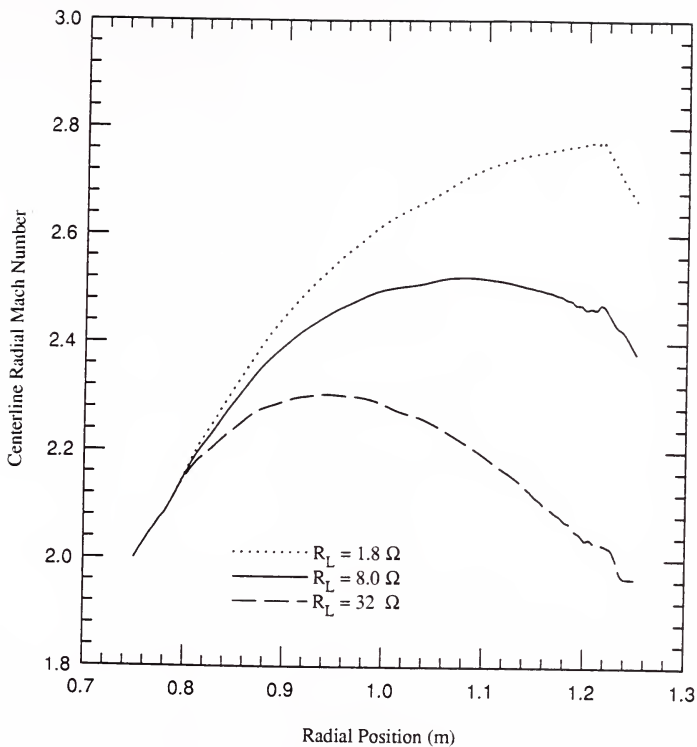


Figure 3.59 Comparison of Centerline Radial Mach Number as a function of Radial Position for $R_L = 1.8 \Omega$, 8Ω , and 32Ω Generators with Nonuniform Plasma Transport Properties.

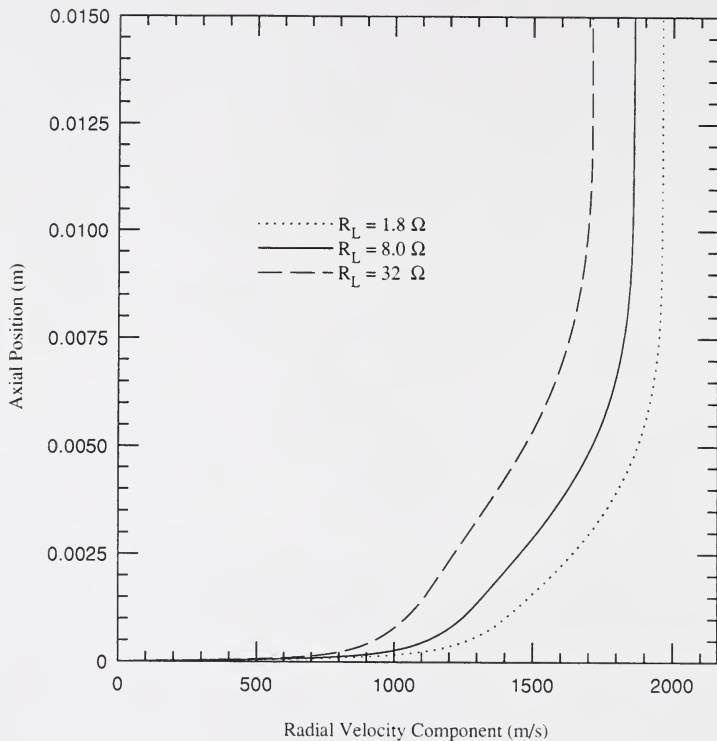


Figure 3.60 Comparison of Radial Component of Velocity as a function of Axial Position at Cathode ($r = 1.21$ m) for $R_L = 1.8 \Omega$, 8Ω , and 32Ω Generators with Nonuniform Plasma Transport Properties.

analogous profiles obtained using the uniform plasma properties (see Figure 3.35) no velocity overshoots occur here; indeed, the flow near the wall experiences larger body forces than those in the core, as discussed in the previous section.

Figure 3.61 provides a comparison of the axial profiles of the tangential velocity component at the cathode (at $r = 1.21$ m) for the same variation in load resistances. Recall from the previous section (3.6.2) that the wall-to-free stream ratio of the tangential body forces against the flow is estimated using $J_{r,w}/J_{r,\infty} \approx -(\sigma_{\perp,w}/\sigma_{\perp,\infty}) \cdot (R_L/R_{MHD})$. The flow near the wall tends to be accelerated, while the free stream is decelerated. The magnitude of this wall-to-free stream ratio of body forces increases with increasing load resistance. The $v(z)$ profiles shown in Figure 3.61 reflect this fact. As the load resistance is increased, the velocity of fluid in the boundary layer becomes higher (is accelerated) while in the free stream the flow is decelerated. Considering Equation 3-49 along with the ratio estimates provided in Table 3.3 suggests that the magnitude of the body force accelerating the flow near the wall, relative to that in the free stream, will decrease as the wall temperature is reduced (cooling is increased); i.e., the effect of lower wall temperature is to reduce the Hartmann flow effects.

Considering the slopes of the velocity profiles in Figure 3.60 and 3.61, it appears that as the load resistance is increased (e.g., from $R_L = 1.8 \Omega$ to 32Ω) the shear stress attributable to $\partial u/\partial z$ is decreased while that attributable to $\partial v/\partial z$ is increased.

Figure 3.62 provides a comparison of the static temperature axial profile at the cathode for the generators of varying load resistances. As the load resistance

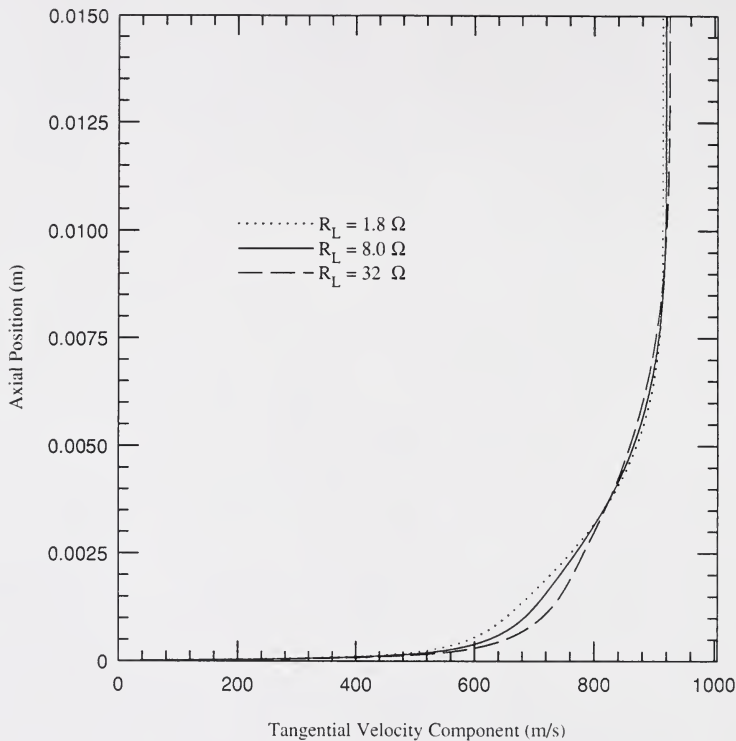


Figure 3.61 Comparison of Tangential Component of Velocity as a function of Axial Position at Cathode ($r = 1.21$ m) for $R_L = 1.8 \Omega$, 8Ω , and 32Ω Generators with Nonuniform Plasma Transport Properties.

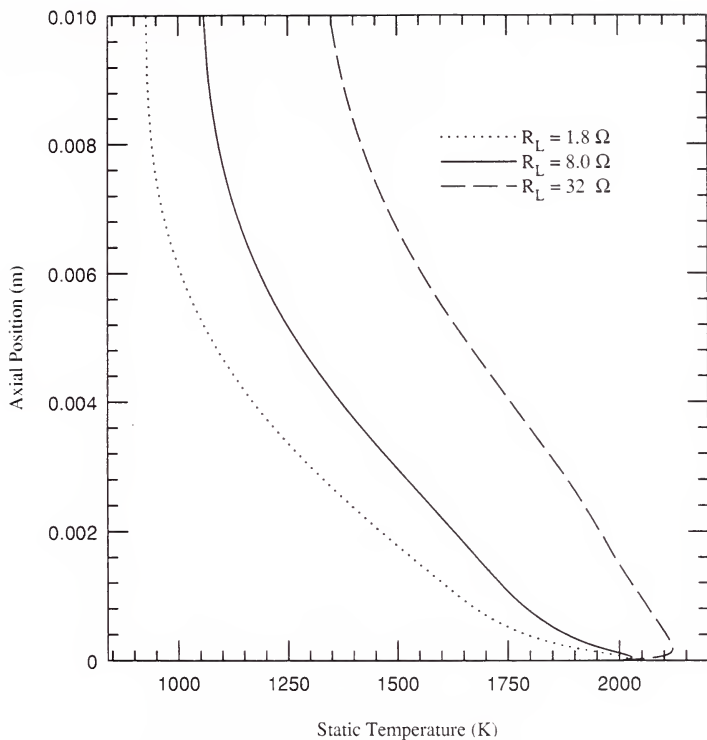


Figure 3.62 Comparison of Static Temperature as a function of Axial Position at Cathode ($r = 1.21$ m) for $R_L = 1.8 \Omega$, 8Ω , and 32Ω Generators with Nonuniform Plasma Transport Properties.

in increased from 1.8Ω to 32Ω , the larger $J_{\theta}B$ body forces increasingly decelerate the flow as indicated by the magnitude of the temperature near the free stream. A temperature overshoot is evident at the wall; the magnitude of the overshoot increases with increasing load resistance.

3.7 Comparison of Two-Dimensional and Quasi-One-Dimensional Predictions for Reference Equilibrium/Fission-Model Generator

In this section, predictions of the behavior of the reference MHD generator ($B = 5 \text{ T}$ and $R_L = 8 \Omega$) variables from the two-dimensional (2-D) thin-layer Navier-Stokes/MHD solver (developed in this work), and the quasi-one-dimensional (Q1D) Euler/MHD solver (described in Appendix A) are compared; the reference MHD generator geometry and inlet conditions are described in Section 3.6.

3.7.1 Q1D/2-D Comparison Description

A meaningful comparison between the Q1D and 2-D MHD solvers is accomplished by analyzing the "active generator region"--defined earlier as the region between and including the electrodes--which, in the reference generator geometry, is located at $0.78 \text{ m} \leq r \leq 1.22 \text{ m}$. The comparison is restricted to this region because the Q1D solver does not currently accommodate the solution of the generator flow and electromagnetic fields upstream of the anode and downstream of the cathode; the code can be modified to account for these open-circuit regions.

The Q1D geometry (e.g., duct lofting) matches that of the 2-D solution (see Figure 3.42 in Section 3.6) except that the Q1D solution begins at $r = 0.78$

m, corresponding to the location of the upstream end of the anode of the 2-D generator geometry and is ended at the downstream end of the cathode. The Q1D solution is accomplished by the step-wise marching through the MHD generator described in Appendix A. The inlet conditions required to begin the Q1D solution--specifically, the stagnation temperature (\bar{T}) and pressure (\bar{P}), and the inlet Radial Mach number (M_R) and swirl factor (S)--are obtained (at $r = 0.78$ m) from the 2-D solver. This matching assures that the local thermodynamic and electromagnetic variables of the two MHD solvers agree at the beginning of the active generator region; further, in the case that equilibrium electron temperatures are assumed (as in the present reference generator comparison), the plasma properties at the beginning of the active generator match also. The inlet conditions for the present Q1D calculations are: $\bar{T}_{in} = 3001.96$ K, $\bar{P}_{in} = 4.8379$ MPa (47.746 atm), $M_{R,in} = 2.085$, and $S_{in} = 0.9256$.

Inlet load parameter. With the duct geometry specified, the load parameter, ζ ($\equiv J_r/J_{r,short}$) varies throughout the generator. A question arises as to what is the most appropriate way, for purposes of comparison and similitude, to determine, or specify, the load parameter. Specifically, should the load parameter be set so that the load current of the Q1D generator is the same as that of the 2-D generator (matched-load current condition) or, alternatively, should the load parameter be set so that the predicted load resistance of the Q1D generator equals that of the 2-D generator (matched-load resistance condition)-- 8Ω in this case? Both approaches are considered in the following.

3.7.2 Q1D/2-D Comparison Results

Table 3.6 provides a comparison of the reference generator predictions from the 2-D solver with those of the Q1D solver for matched-load current and matched-load resistance conditions. The estimated load factor, $\zeta = 0.5$, of the 2-D calculation provides a good first guess for the inlet load parameter of the matched-load current condition, $\zeta = 0.55$, and the inlet load parameter of the matched-load resistance condition, $\zeta = 0.583$.

The distinctive difference between the 2-D and Q1D predictions is the electric power density which is approximately $140 \text{ MW}_e/\text{m}^3$ for the 2-D generator and approximately $177\text{-}178 \text{ MW}_e/\text{m}^3$ in the Q1D cases. The difference in power density leads to the differences in total electric power output levels and enthalpy extractions of the 2-D and Q1D solvers. Figure 3.63 provides a comparison of Q1D stagnation temperature radial profile predictions with the center grid line (51 of 101) stagnation temperature radial profile; the greater enthalpy extraction levels of the Q1D generators are evident in the larger temperature drops of the Q1D generators relative to that of the 2-D generator.

The Q1D and 2-D generator isentropic efficiency predictions are also provided in Table 3.6. For the 2-D generator, efficiencies are provided for the overall generator, including the open-circuit region of large pressure loss, upstream and downstream of the active generator regions (see discussions in Sections 3.6.2 and 3.4.1), and for the active generator region only (i.e., using inlet \bar{T} and \bar{P} values at $r = 0.78 \text{ m}$ and exit \bar{T} and \bar{P} values at $r = 1.22 \text{ m}$).

Table 3.6 Comparison of Two-Dimensional MHD Solver and Quasi-One-Dimensional Euler Solver Predictions for Reference Fissioning Plasma Generator

Parameter	2-D Reference Fission Generator		Q1D Matched Current	Q1D Matched Load
Load Resistance Ω	8.0		8.928	8.0
Load Current (A)	2162.4		2162.4	2292.1
Load Voltage (V)	17,299		19,305	18,339
Power (MW _e)	37.407		41.746	42.034
Average Power Density (MW _e /m ³)	139.98 †		177.19	178.41
Mass Flow Rate (kg/s)	344.27		354.27	354.27
Volume (m ³)	0.2672 †		0.2356	0.2356
$\zeta \left[\equiv \frac{J_r}{J_{r,Short}} \right]$	0.5 †		0.55 *	0.583
	Overall	Active Region		
Enthalpy Extraction (%)	2.30	2.38	2.67	2.69
Isentropic Efficiency (%)	14.9	20.0	20.5	21.9

* Specified inlet value

† Generator average load parameter estimate

‡ The generator volume includes regions upstream and downstream of the active generator region.

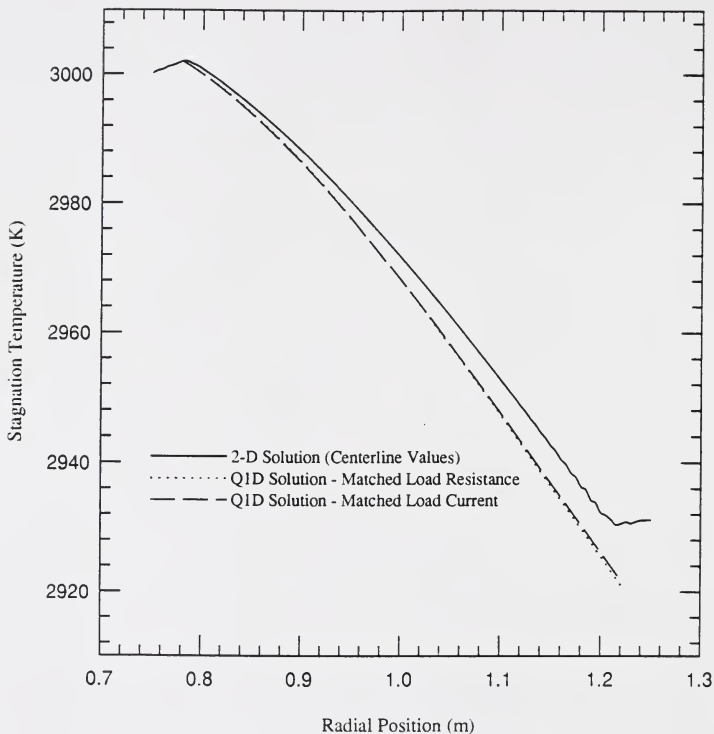


Figure 3.63 Comparison of 2-D Navier-Stokes MHD Solver and Q1D MHD Solver Predictions of the Centerline Radial Profile of Stagnation Temperature in the Reference ($B = 5 \text{ T}$ and $R_L = 8 \Omega$) Generator with Equilibrium Fissioning Plasma.

Figure 3.64 provides a comparison of the stagnation pressure radial profiles of the Q1D solutions with total pressure radial profile along the center grid line (51 of 101) of the 2-D solver. The pressure loss rate in both the Q1D generators is greater than that of the 2-D generator, in spite of the frictional effects of the 2-D generator; however, the higher pressure drops of the Q1D solutions simply correspond to the higher enthalpy extractions.; for the same enthalpy extraction, the 2-D generator would exhibit a larger pressure loss than either of the Q1D generator conditions.

Figures 3.65 and 3.66 compare the radial Mach number and swirl factor profiles of the Q1D generator results with those from the 2-D solver (center grid line values). Interestingly, the results from the Q1D predictions (matched-load current and matched-load resistance) bound the 2-D predictions of the radial Mach number profiles (Figure 3.65). The higher relative resistance (and higher load voltage) conditions of the matched-load current Q1D solution, as compared to the matched-load resistance Q1D solution, lead to larger generator $J_r B$ body forces against the flow. This is reflected in both the radial Mach number profiles in Figure 3.65 and the total pressure profiles in Figure 3.64; in each case the flow is more decelerated (or less accelerated) in the matched-load current operating condition. The swirl factors profiles (Figure 3.66) predicted by the Q1D and 2-D solver are nearly indistinguishable. The agreement between the 2-D and Q1D predictions for the radial Mach number and swirl factor gives confidence in the two solution methods.

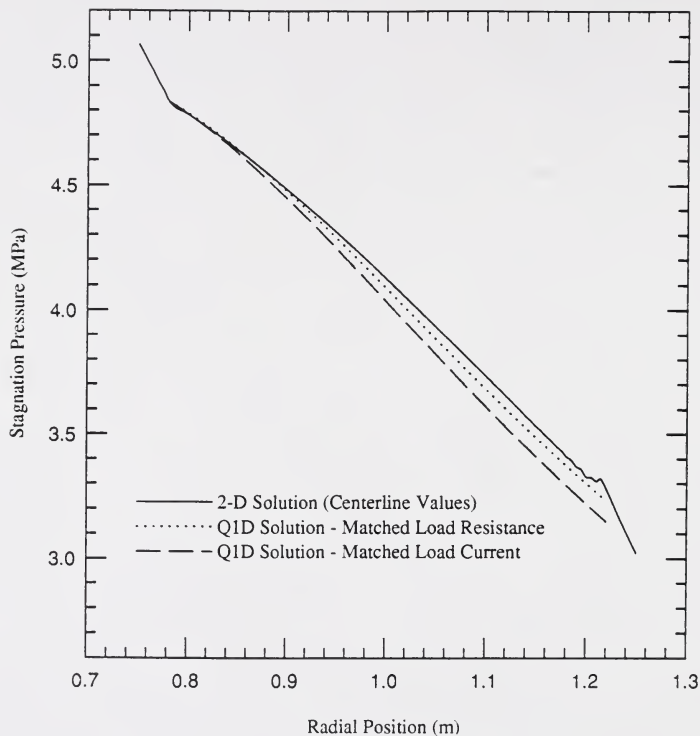


Figure 3.64 Comparison of 2-D Navier-Stokes MHD Solver and Q1D MHD Solver Predictions of the Centerline Radial Profile of Stagnation Pressure in the Reference ($B = 5 \text{ T}$ and $R_L = 8 \Omega$) Generator with Equilibrium Fissioning Plasma.

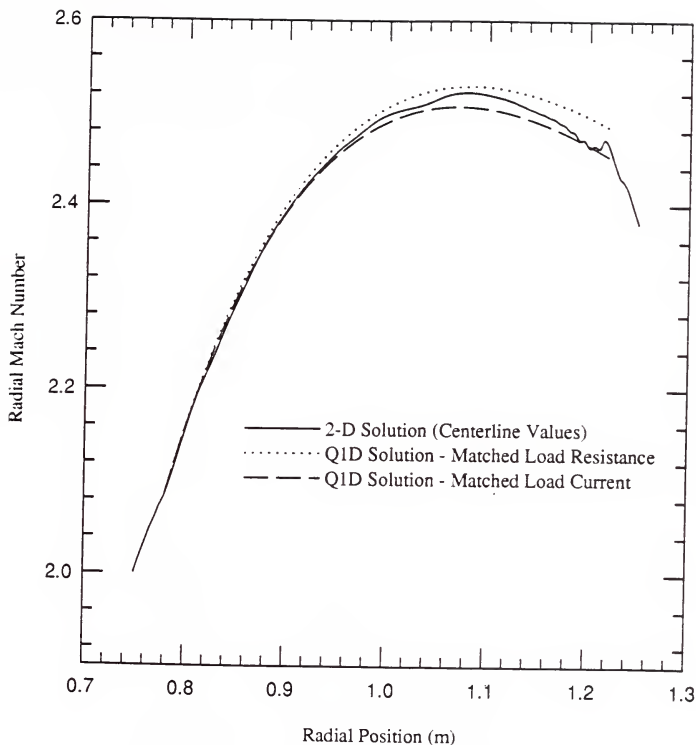


Figure 3.65 Comparison of 2-D Navier-Stokes MHD Solver and Q1D MHD Solver Predictions of the Centerline Radial Profile of the Radial Mach Number in the Reference ($B = 5 \text{ T}$ and $R_L = 8 \Omega$) Generator with Equilibrium Fissioning Plasma.

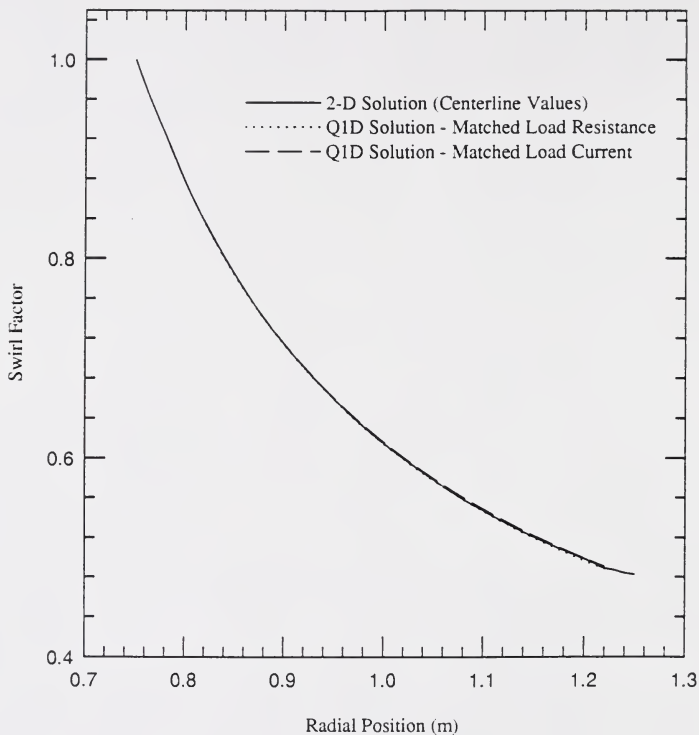


Figure 3.66 Comparison of 2-D Navier-Stokes MHD Solver and Q1D MHD Solver Predictions of the Centerline Radial Profile of the Swirl Factor in the Reference ($B = 5 \text{ T}$ and $R_L = 8 \Omega$) Generator with Equilibrium Fissioning Plasma.

3.7.3 Q1D/2-D Comparison - Comments

The Q1D and 2-D prediction of the reference MHD generator operating conditions agree remarkably well considering the marked difference in the modeling and solution methodologies of the Q1D and 2-D solvers. It is interesting to note that, where an overall 2-D MHD solution may require $O(1/2-1)$ cpu-day for convergence, the Q1D solver runs in $O(1)$ cpu-second (on the same machine).

For the sake of closure, considering the results provided here, it is suggested that the matched-load resistance Q1D solution approach is more compatible with the 2-D solution than the matched-load current Q1D approach. First, in an actual generator, it should be expected that there will exist a load resistance; i.e., there will exist some fixed, known resistance across the electrodes. Second, the Q1D and 2-D free stream short-circuit Hall current densities are (specified to be) identical through the matching of inlet conditions, at the beginning of the active generator region; therefore, requiring the Q1D and 2-D load currents ($\int J, dA$) to be equal--given equal free stream conditions--necessarily requires that the Q1D and 2-D load resistances be different, since the 2-D solution account for the variation in plasma properties through the boundary-layer, the velocity defect of the boundary-layer, and the negative current densities in the boundary-layer.

Assuming that the matched-load resistance approach is followed, it remains for future work to reconcile the Q1D and 2-D local power density differences. A starting point for this problem is the analysis of the effects of the variation in

plasma properties and velocity in the boundary layer region, as well as the non-negligible volume losses occupied by the electrode recirculation loops (see Figure 3.47).

CHAPTER 4

SUMMARY, CONCLUSIONS, AND RECOMMENDATIONS

A summary of the results of the analysis performed in this dissertation, conclusions derived from this work, and recommendations for extensions of this work are provided in this chapter.

4.1 Summary of Results

A summary of the results of the analysis of the MHD flow of a fissioning gas in an outflow disk MHD generator, performed using the two-dimensional MHD solution methodology developed in this thesis, is provided in this section.

4.1.1 Internal, Supersonic, Fissioning, MHD Flow

The inlet and outlet fluid mechanic boundary conditions imposed in this work require that the flow field be supersonic everywhere in the duct except within the thin boundary layer region adjacent to both the upper and lower duct walls. The results obtained in this work a.) provide evidence for the potentially complicated wave structure of internal supersonic flow fields, and b.) show that geometry, fissioning, and MHD effects act to decelerate the flow--making it difficult to maintain supersonic flow throughout the outflow disk MHD generator geometries considered in this work.

Wave structure. The supersonic flow fields analyzed exhibit wave structure arising from several processes including:

- a. Oblique shock waves generated in turning the flow through compression turns caused by abrupt or gradual changes in the duct height (e.g., see the 5-degree compression corner problems of Appendix C) or by sudden changes in the boundary layer thickness caused by local Joule heating (see discussion in Section 3.6.1);
- b. Rarefaction (Prandtl-Meyer) waves generated in turning the flow through expansion turns caused by curvature in the duct walls (e.g., analysis of constant area duct geometry in Section 3.2.1);
- c. Artifacts of the inlet boundary conditions; i.e., oblique wave structure, introduced in the process of starting a Mach two or three flow at some arbitrary inlet plane, due to mismatches between best-estimate boundary conditions and the actual downstream solution (e.g., see the modification to the inlet boundary condition theory presented in Section 3.1.1).

Decelerating effects. As anticipated in Section 1.2, it is indeed found through the calculational results that a number of processes combine to decelerate the working fluid towards (radial) Mach one:

- a. Fission energy addition works to increase (or maintain) the stagnation temperature of the working fluid and decrease the Mach number (Rayleigh flow) (e.g., see comments on the effects of neutron flux level in Sections 3.2.1 and 3.2.3);

- b. The MHD $\underline{J} \times \underline{B}$ body forces act against the flow and work to decelerate the flow. The MHD generator calculational results discussed in Sections 3.4 (dealing with uniform plasma properties) and 3.6 (fission-fragment induced plasma properties) show that: 1.) the body forces against the flow are the principle mechanism by which the flow field is decelerated; 2.) the extent to which the flow field is decelerated is dictated principally by the $J_{\theta}B$ body force which is proportional to the MHD interaction level and is oriented radially against the flow; 3.) the $J_{\theta}B$ force increases with generator load resistance (e.g., see discussions in Sections 3.4.2 and 3.6.3); and 4.) outside (upstream and downstream) of the region between and including the anode and cathode, are regions of particularly large $J_{\theta}B$ body force (e.g., see Sections 3.4.1 and 3.6.2);
- c. The oblique compression wave structure discussed above inhibits acceleration of the flow (e.g., strong oblique waves can significantly decelerate the flow as shown in the compression corner problem of Appendix C);
- d. Viscous effects work to decrease the radial Mach number both through friction, like Fanno flow (e.g., see the discussion in Section 3.3.2 comparing 2-D turbulent flow results with inviscid flow results) and also through the effect of decreasing cross-sectional flow area due to boundary layer growth (see comments in Appendix C).

- e. The tangential velocity component, intentionally introduced at the generator inlet so as to enhance generator performance, decays with radial position in conservation of angular momentum; the loss of kinetic energy contributes to an increase in internal energy, static temperature, and the local speed of sound, thus reducing the radial Mach number.

The extrapolation outlet boundary condition requires that the core flow be supersonic. However, it is found that the very nature of the fissioning, outflow disk MHD generator is to decelerate the flow field below the supersonic range of validity for the developed solution methodology. Considering the efficiency of supersonic diffusers (see the discussion provided by Shapiro, 1953), it is expected that in an actual supersonic generator operating in a closed-cycle system (e.g., the space nuclear power system mentioned in Section 1.0), the generator duct lofting and active length would indeed be dictated by the requirement that the flow be near Mach one at the exit; i.e., the generator modeling and results obtained are realistically constrained by the requirement that the flow be supersonic throughout the duct length. Unfortunately, the transition from supersonic to subsonic flow cannot be studied by the developed MHD solver, in its current form.

Compensating accelerating effects. The decelerating effects delineated above are compensated to an extent by effects that accelerate the flow:

- a. The cross-sectional flow area of the duct can be increased with radial position. This method of radial Mach number control is not exploited in the MHD generator calculations carried out in the this

- thesis. In this study, no attempt is made to design the generator duct lofting to obtain practical enthalpy extraction levels (e.g., 20%); the linearly decreasing duct height geometry (described in Section 3.2.3) is used for all MHD generator calculations. The linearly decreasing duct height geometry provides some cross-sectional flow area increase with radial position; however, it may be expected that in an actual generator design, the cross-sectional flow area increase with radial position will be larger, in order to maintain supersonic flow and increase the generator active length.
- b. The $(\underline{J} \cdot \underline{E})$ power extraction serves as a "cooling" mechanism (in the Rayleigh flow sense) and more than compensates for the fission power density term in flow with both MHD and fissioning effects--at least at fission power densities commensurate with neutron flux levels equal to or less than 1×10^{16} n/cm²s; however, the $\underline{J} \cdot \underline{E}$ "cooling" does not compensate for the $\underline{J} \times \underline{B}$ body forces working to decelerate the flow.
- c. The Hall effect gives rise to the J_r component of current density and effectively reduces the magnitude of the J_θ component (constituting the $J_\theta B$ body force against the flow) by the amount $\beta_e J_r$. The Hall effect increases the magnitude of J_r relative to J_θ as the electron Hall parameter, β_e , is increased and as the generator load resistance approaches zero (short circuit) (e.g., see the discussion in Sections 3.4.1, 3.4.2, and 3.3.6).

- d. Guide vanes are used to introduce an inlet swirl component to the generator flow in order to increase the disk MHD generator performance level (as described in Section 1.1.2). The effect of the positive swirl is to increase the Hall current (J_r) and, similar to the Hall effect, reduce the Faraday (J_θ) current and therefore the $J_\theta B$ body force that works to decelerate the flow.

4.1.2 2-D Navier-Stokes Solver/Q1D Euler Solver Agreement

Calculated results from the two-dimensional thin-layer Navier-Stokes MHD code developed in this thesis are compared with those predicted by the quasi-one-dimensional Euler solver described in Appendix A. Comparisons for flow with and without the effects of fissioning in the absence of MHD effects are provided in Section 3.3 and results for flow with fissioning and MHD effects are provided in Section 3.7. The agreement between the 2-D N-S solutions and the Q1D solutions is remarkable.

For flows with and without fissioning, in the absence of MHD effects, the results essentially agree exactly in predictions of the duct centerline total properties; the differences in predicted flow variable radial profiles are attributable to viscous effects that are not considered in the Q1D formulation.

For flow with MHD effects and plasma properties arising from fission fragment-induced ionization of the working fluid, the Q1D solver overpredicts the generator enthalpy extraction and isentropic efficiency. It may be assumed that primarily two factors contribute to the lower enthalpy extraction levels in the 2-D generator as compared to the Q1D generator: a.) the no-slip velocity boundary

condition and viscous effects result in a velocity defect in the boundary layer region; this defect, though actually existing in the relatively thin boundary layer region results in a decrease in average generator power density; and b.) the current recirculation loops (discussed in the following section and in Sections 3.4.1, 3.5.2, and 3.6.1) are short circuit current loops driven by the free-stream E-field over the inactive part of the electrodes and effectively occupy volume within the active generator region without contributing to the generator electric power output. In a comparison in which only the active region of the generator is considered, the disagreement between the 2-D and Q1D generator efficiency predictions is small (see Table 3.6). The differences in generator efficiency are attributable to viscous effects--both friction and reduction in the geometry induced expansion of the flow due to a decrease in the effective cross-sectional flow area as a result of boundary-layer growth.

4.1.3 Two-Dimensional Electrode Effects

The 2-D N-S solver/Q1D Euler solver comparisons have shown that the Q1D solver does a good job predicting the radial profiles of important fluid mechanic and electromagnetic variables; however, a number of two-dimensional (r,z) "end effects" greatly affect generator performance and are outside of the scope of the Q1D analysis. The 2-D N-S code developed in this work has facilitated analysis of the electrode region of the MHD generator.

Short-circuit recirculation loops. Already mentioned above, it is found from the analysis performed in this thesis that the electric field drives short-circuit current loops over the inactive portion of the cathode and anode; "inactive"

designates that portion of the electrode through which the load current density does not flow. It has already been mentioned that these short-circuit current loops occupy volume without contributing to power production (see Section 3.7). The short circuit loops result in an increase in the Hall current density in the vicinity axially above each electrode so that, in general, the flow is relatively more accelerated in the region immediately above the electrodes.

Active electrode region. It is found in the results, consistent with referenced work (see Section 3.5.2), that at the Hall parameters encountered in this work, the load current typically flows out of a small part (e.g. 10 %) of the electrode surface. The portion of the electrode through which the load current passes is referred to in this work as the "active electrode region." Conservation of current arguments suggest that the required active electrode area scales inversely with $(1 + (\mu_e B)^2)$ (or simply inversely with β_e^2 at large Hall parameters) and inversely with generator load; i.e., as the Hall parameter increases (either due to increased applied magnetic induction or electron mobility), the active electrode region decreases; also, as the generator approaches open circuit, little active area is required for the load current. Recalling that it is over the remainder of the electrode--the inactive region--that the short circuit recirculation loops are driven, then as the load resistance and/or the Hall parameter is increased, the portion of the electrode over which the recirculation currents are driven increases.

The result of the load current passing through the small active surface area is locally high current densities; the highest generator Joule heating occurs at the upstream edge of the anode (through which the load current enters the generator)

and the downstream edge of the cathode (through which the current exits the generator) (e.g., see Section 3.5.2). In the case where nonequilibrium electron temperatures are significant, the Joule heating concentrations raise the electron "fluid" temperature. The local electrical conductivity increases with electron temperature, linearly in the case of the fissioning plasmas considered in this work and exponentially in the case of thermally ionized plasma. The local nonequilibrium enhancement of the electrical conductivity further increases the Joule heating levels. Adequate modeling of this positive feedback loop, and potential plasma instability, was found to be outside of the scope of the developed electrical solution methodology due to limitations in the plasma physics transport property modeling (see comments in Sections 3.5.1 and 3.5.2). In the case where inelastic scattering relaxes the electron temperature to that of the fluid temperature--equilibrium electron temperatures, expected for the molecular gases considered in this work--the local electron mobility and electrical conductivity are increased as the Joule heating heats the working fluid.

Electrode generated compression waves. The enhancement in the Joule heating at the active electrode region leads to abrupt local increases in the static temperature and, therefore, the specific volume of the fluid in the same region. These local increase in the specific volume result in a near-step increase in the boundary layer thickness, requiring a compression turn of the working fluid, resulting, interestingly, in the generation of an oblique shock wave (see Figure 3.28 and related discussion in Section 3.4.1 and Figure 3.48 and related discussion in Section 3.6.1).

4.2 Conclusions

This section provides concluding remarks on the analysis of the MHD flow of a fissioning gas in an outflow disk MHD generator performed in this work.

4.2.1 Solution Methodology

The primary objectives of the thesis are successfully accomplished. A consistent methodology for solving the governing equations of steady-state, two-dimensional (r,z) , viscous, supersonic, MHD flow of a fissioning, compressible, weakly ionized plasma in an outflow disk MHD generator is developed. The spatial profiles of important fluid dynamic, electromagnetic, and plasma physics variables are studied using the developed solution methodology.

4.2.2 Fissioning MHD Flow Characterization

Using the simple models developed for plasma physics transport properties of an equilibrium electron temperature, weakly ionized plasma in which the electrical conductivity is obtained through fission-fragment induced ionization of the working fluid, the following are found.

- a. At a significant flux level of $1 \times 10^{16} \text{ n/cm}^2\text{s}$, and assuming optimistic working fluid property data (e.g., see discussion on the electron-heavy momentum transfer cross-section in Section 3.5), the scalar electrical conductivity levels are relatively low ($\leq 10 \text{ S/m}$); this is because the electron number densities produced are low, even at this high neutron flux level. With the modeling assumption that three-body recombination is the dominant electron number density loss mechanism, the electron number density and therefore the

- electrical conductivity are found to scale as the cube root of the neutron flux level; to increase the scalar electrical conductivity by a factor of two, therefore, requires nearly an order-of-magnitude increase in the neutron flux level.
- b. The scalar electrical conductivity increases with increasing Mach number, due to increasing electron mobility; however, the effective (Hall) electrical conductivity decreases with increasing Mach number due to the Hall effect and increasing electron mobility. In terms of electric power density, the fissioning MHD generators are found to operate more effectively at high total Mach numbers; however, the two-dimensional electrode "end effects" discussed in Section 4.1.3 are exacerbated, or are more pronounced, as the electron mobility (and Hall parameter for a given B-field) increase with increasing total Mach number.
- c. In contrast to plasma transport properties arising from thermal ionization (Saha-ionization) of a seed constituent at the conditions of interest to this study, the fission fragment-induced ionization plasma properties are relatively uniform both radially and axially in the generator.

The three items listed above lead one to deduce that the generator performance level (e.g., electric power density) is not exceptionally high in generators in which the only source of electron number density production is from fission-fragment induced ionization. To obtain the high Hall conductivity required

for effective power production in the disk MHD generator requires a large scalar electrical conductivity relative to the Hall parameters; however, for the fissioning plasmas the opposite is true. Because the electron number densities are relatively low, high scalar electrical conductivity comes only through high electron mobility (and, therefore, large Hall parameters at the applied B-field levels necessary for significant electric power density). The Hall effect, in this case, assures that the Hall electrical conductivity is low, therefore limiting power production.

A positive aspect of the low Hall conductivity is that the load current, upon approaching the cathode, will want to enter the cathode through the high (scalar) conductivity (low resistivity) path parallel to the applied B-field, rather than following the lower (Hall) conductivity (high resistivity) path from the cathode to the anode; i.e., the same Hall effect that limits power production so poignantly in the case where the electrical conductivity is dominated by the electron mobility also serves to minimize leakage currents between the cathode and anode.

4.2.3 Quasi-One-Dimensional Euler Solver Agreement

The agreement between the calculational results from the two-dimensional (2D) MHD solver developed in this work and those from the quasi-one-dimensional (Q1D) MHD Euler solver described in Appendix A is remarkable, considering the difference in the models. The excellent agreement, to an extent, provides confidence in the overall 2-D thin-layer Navier-Stokes/2-D electromagnetic MHD solution; perhaps more importantly, the agreement indicates that the Q1D solver does an excellent job modeling the high Reynolds number, supersonic, fissioning, MHD flows in the outflow disk MHD generator

geometry. Implicit in this statement is that the 2-D flow field is free of significant wave structure (e.g., oblique shock waves).

The Q1D solver typically overpredicts the generator enthalpy extraction. The discrepancy between the 2-D N-S predictions and the Q1D predictions is attributed to the effects of the velocity defect due to viscous effects and to finite-size (non-point) electrode effects. Suggestions are made for reducing the Q1D/2-D discrepancy in Section 4.3.

4.2.4 Supersonic Generator Flows

The enthalpy extraction which occurs over the length that the supersonic flow can be maintained in the outflow disk MHD generators studied in this work is too low for the generators to be considered practical in terms of power generation. As discussed in Section 4.1.1, several effects, including the MHD body forces and fission energy deposition, combine to decelerate the supersonic flow to Mach one. This suggests that perhaps a subsonic outflow disk MHD generator should be investigated; many of the same effects will work in the subsonic generator to accelerate, rather than decelerate the flow.

4.3 Recommendations for Future Study

In this final section, recommendations for work and study that are either extensions of this work, or ideas obtained in this study are provided.

4.3.1 Further Analysis

The development of the 2-D thin-layer Navier-Stokes MHD solver--that is the theory, solution methodology, and back-fit modifications to the theory--

demanded a significant portion of the time dedicated to this thesis. Although representative generator operating conditions are examined in Section 3.4 and 3.6, it is recognized that further characterization of the outflow disk MHD generator is of interest. Beyond parametric study--e.g., varying the inlet swirl parameter or wall temperatures--which is itself of interest, there remain items which are simply not analyzed in the present work:

- a. The details of heat transfer (e.g., the wall thermal loading) and wall shear stress as functions of generating operating conditions, wall temperatures, and radial position;
- b. A detailed examination of the electromagnetic variables; e.g., a comparison of electromagnetic variable profiles at the anode, the cathode, and at the insulated surfaces.

4.3.2 Extensions of Inflow and Outflow Boundary Conditions

It is suggested that effort be dedicated to extending the inflow and outflow boundary conditions, developed in Section 2.2.4 and extended in Sections 3.1.1 and 3.1.2, to allow modeling of subsonic flows; this is a non-trivial task. It is necessary that the boundary conditions correctly treat the characteristics of the flow.

Inlet boundary conditions. It may be appropriate that a number of inlet boundary conditions be developed for different flow conditions; i.e., boundary conditions would be developed that treat the flow as either supersonic or subsonic at the inlet plane (for example). The supersonic or subsonic inlet flow will provide

a more tenable problem than the general case that allows the supersonic flow to transition to subsonic flow.

Outflow boundary condition. It would be of interest (to the author at least) and an extension of this thesis to work through the theory and develop an outflow boundary condition that treats both the supersonic and subsonic flow and rigorously accommodates the transition between the two, as a normal shock enters the generator, for example. This is of interest in studying the problem of how the generator flows pass from supersonic to subsonic flow under the influence of the MHD effects. A subsonic outflow boundary condition would also allow study of an off-design generator condition in which a normal shock is standing in the duct.

4.3.3 Extensions of Quasi-One-Dimensional Solver

The quasi-one-dimensional (Q1D) Euler solver with MHD and fission source terms was developed by the author outside of this present work; however, one of the refreshing, pleasant surprises of this work has been the consistent agreement between predictions of the Q1D solver and the developed 2-D thin-layer Navier-Stokes solver (see comments in the Conclusions, Section 4.2). Recommendations for enhancing the Q1D solver so that the Q1D modeling methodology will incorporate some 2-D effects are listed below:

- a. Implement the "Velocity Effectiveness Theory" of Lear (1984) in order to incorporate into the Q1D solver the boundary layer effects that contribute to the effective loss of electric power production potential due to velocity defect and to account for the axial variation in plasma physics properties.

- b. Include a skin-friction term in the Euler solver in order to include shear stress effects.
- c. Develop the theory for estimating the volume effectively short-circuited by the electrode current recirculation loops discussed in Section 4.1.3.; reconcile this theory with the Q1D modeling philosophy; and, if consistent with the developed theory, incorporate a simple model for effective loss of power-production-volume due to recirculation loops.

4.3.4 Extensions of Solution Methodology

As concluded in Section 4.2, a successful solution methodology is developed that consistently solves the 2-D MHD flow of a fissioning gas in the outflow disk MHD generator geometry. A number of extensions to the solution methodology naturally follow.

Integrated MHD solver. The 2-D MHD solutions are currently obtained through iteration between a 2-D Navier-Stokes solver with MHD and fission source terms (FLUID) and an electromagnetics solver with plasma physics modeling (ELEMAG); as a natural closure to this work, the two codes should be integrated.

Fluid solver numerical method. The MacCormack's explicit method (MacCormack, 1969) is used to integrate the fluid equations. MacCormack has extended his 1969 method to a number of solution methodologies (e.g., incorporation of time-splitting [MacCormack, 1971, reported in Anderson, et al., 1984] and his explicit/implicit hybrid rapid-solver method [MacCormack, 1976]).

Anderson et al., report that the rapid-solver method of MacCormack is one or two orders-of-magnitude faster than MacCormack's time-split method; the time-split method may be assumed to be commensurate (in terms of execution time) with the un-split explicit method with local time-stepping used in this work. Replacing MacCormack's 1969 explicit integration scheme used in this work with MacCormack's hybrid method promises great reduction in the fluid solver execution time requirements, and is recommended.

Parallel processing. The MHD problem appears to be a natural candidate for parallel processing. (Out of ignorance on the author's part, a crude interpretation of parallel processing is assumed here to mean simply the type of calculations that are run independently, simultaneously, on different processors.) For example, the solution methodology is designed such that the electrical solver uses the fluid mechanic variables as specified "boundary" functions in any calculation; similarly, the fluid solver uses the electromagnetic variables as specified functions in any calculation. Therefore, it seems natural that a common block storage be set aside in which the latest fluid mechanic and electromagnetic variable values are stored, and that the fluid and electromagnetic calculations proceed independently, on separate processors, always using the most current values stored in the "common block".

The solution methodology developed to solve the nonlinear MHD problem in this work is by nature a series of iterations towards steady-state. In the same sense as for the example of the fluid and electromagnetic solutions just mentioned, much of the numerical algorithm internal to the fluid and

electromagnetic solvers can be calculated simultaneously on separate processors. This is inherent in the nature of, and is a strong point of, the predominantly explicit numerical methodology employed; i.e., explicit finite-difference methods, or the marching, or sweeping (e.g., ADI) methods, are naturals for parallel processing. It can be imagined that the explicit method of MacCormack, for example, could eventually be set up so that a single processor is dedicated to a single finite-difference node.

APPENDIX A

QUASI-ONE-DIMENSIONAL DISK MHD FLOW SOLVER

Introduction

The quasi-one-dimensional (Q1D) disk MHD Euler solver presented in this appendix was developed by the author for outflow disk MHD studies performed separate from this dissertation (see, for example, Welch et al., 1990). The Q1D Euler solver was developed originally to meet scoping-study needs for estimating the performance levels of the supersonic outflow disk MHD generator components of conceptual nuclear space power systems. The weakly ionized fissioning plasma working fluids analyzed in these systems included UF_6 -He (Welch et al., 1987), UF_4 -He (INSPI, 1988), and UF_4 -metal-fluoride (e.g., KF, NaF, and LiF) (Welch et al., 1990).

The primary purpose of the Q1D MHD solver is to provide radial distributions of important MHD generator fluid, electromagnetic, and plasma physics parameters: To this extent, the purpose of the Q1D solver is similar to that of the two-dimensional Navier-Stokes MHD flow solver developed in this dissertation--i.e., to facilitate study of the MHD flow of a fissioning gas. By virtue of design of the conceptual nuclear space power system to which the generator belongs, it is again assumed that high neutron flux levels exist in the active

generator region, and that fission-induced ionization of the working fluid provides necessary electrical conductivity. In the case of the Q1D solver described in this appendix, only cross-sectional area-averaged radial profiles are calculated; however, the quasi-one-dimensional formulation allows the effects of duct area changes to be accounted for.

The nomenclature used in this appendix is purposely identical, where possible, to that used throughout the dissertation. The general operation of the outflow disk MHD generator is described in Section 1.1; a brief description of the generator is included here for completeness of the text. The Q1D disk MHD solver includes the plasma physics modeling presented in Section 2.4; this modeling is not repeated here.

The appendix presents first a brief description of the outflow disk MHD generator, an overview of the theoretical modeling including the governing equations of the quasi-one-dimensional MHD flow in the outflow disk MHD generator geometry, and finally the marching solution method used to integrate the governing equations through the duct.

Generator Description

A schematic diagram of the disk MHD generator component is provided in Figure A-1. A magnetic field (B) is applied in the positive z (axial) direction. The high temperature gaseous working fluid (e.g., the UF_4 -He mixture described in Section 2.2.3) enters the active region of the MHD generator at some radial Mach number (M_R) greater than one and with some positive swirl factor (S , defined as the ratio of tangential-to-radial velocity components (v/u)), induced by

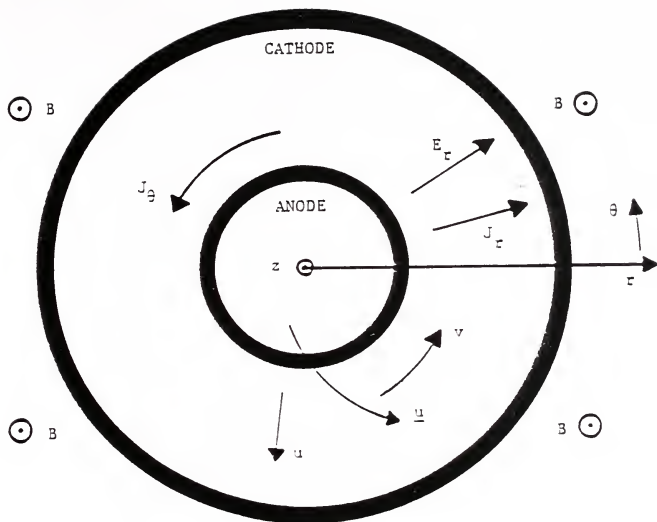


Figure A-1 Outflow Disk MHD Generator Schematic Diagram (Top-View).

turning vanes. The high temperature, weakly ionized fissioning plasma has a finite electrical conductivity, σ_e , and Hall parameter, β_e . The supersonic plasma working fluid interacts with the applied magnetic field and establishes an electric current density with a short circuit tangential (Faraday) component (J_θ) and a radial (Hall) component (J_r), and a radial (Hall) electric field (E_r); the magnitudes of E_r and J_r depend in part on the resistance of the load connected between the anode and cathode. The current density (components) in turn interacts with the applied B-field and gives rise to large radial and tangential body force components $J_\theta B$ and $-J_r B$, respectively; these body force components each act against the direction of the flow and tend to diffuse the flow towards Mach one. The electric power extracted from the MHD generator is given by $\int |\mathbf{J} \cdot \mathbf{E}| dV$. The local electrical conversion efficiency, the local electric power density, and the generator isentropic efficiency are all enhanced by high inlet swirl flows.

Governing Equations and Solution Method

The Q1D governing equations used here are a re-cast form of those used routinely in Q1D generator analyses (e.g., Nakamura, 1983) and are presented by Louis (1968); the fission power density is included in this work as a fluid density-dependent source term. (A formal development of quasi-one-dimensional magnetogasdynamic flow is presented by Pai (1965).)

The disk MHD generator analysis is based on the governing equations of the MHD flow of a fissioning gas under the following assumptions: the flow is a

quasi-one-dimensional, tangentially-symmetric, steady-state, inviscid, perfect gas flow; heat transfer effects are neglected; the effects of induced magnetic fields are neglected and the applied magnetic field is treated as a specified function; and the neutron flux profile is specified. Under these assumptions, the equations governing the MHD flow may be written as follows:

Fluid Equations

$$\frac{d}{dr}(\dot{m}) = 0 \quad (\text{A-1})$$

$$\frac{d}{dr}(\dot{m} u + PA) = \frac{\rho A v^2}{r} + P \frac{dA}{dr} + J_{\theta} A B \quad (\text{A-2})$$

$$\frac{d}{dr}(\dot{m} v r) = -J_r A B r \quad (\text{A-3})$$

$$\frac{d}{dr}(\dot{m} \bar{h}) = J_r E_r A + \dot{q}_N A \quad (\text{A-4})$$

Electromagnetics Equations

$$\frac{d}{dr}(J_r A) = 0 \quad (\text{A-5})$$

$$J_r = \frac{\sigma_e \zeta}{1 + \beta_e^2} (u \beta_e + v) B \quad (\text{A-6})$$

$$J_{\theta} = \beta_e J_r - \sigma_e u B \quad (\text{A-7})$$

The notation used is $\underline{u} = (u, v, 0)$, $\underline{J} = (J_r, J_{\theta}, 0)$, and $\underline{B} = (0, 0, B)$. β_e is the Hall parameter given by $\beta_e = \mu_e B$. The electron mobility, μ_e , and the electrical conductivity, σ_e , are either specified as uniform throughout the generator or are calculated using the equilibrium, nonequilibrium, or equation-of-state-type fission-

fragment induced ionization models developed in Section 2.4. ρ is the fluid density, \bar{h} is the stagnation (or total) specific enthalpy, P is the static pressure (related to T and ρ through the perfect gas law), \dot{m} ($= \rho u A$) is the disk generator mass flow rate, \dot{q}_N is the fission power density (see Equation 2-14), and A is the generator cross-sectional flow area as a function of radial position. The load parameter, ζ , has been defined as the ratio of the local (uniform across the cross-sectional flow area) radial current density to the local short circuit (zero load) radial current density ($0 \leq \zeta \leq 1$). By this definition, the electric field strength may be expressed as

$$E_r = (\zeta - 1)(u\beta_e + v)B \quad (\text{A-8})$$

Using the definition of the load parameter along with the requirement of current continuity (Equation A-5), an expression is obtained for the MHD generator cross-sectional flow area, dictating the generator lofting, as a function of radial position; i.e.,

$$A(r) = A_{in} \frac{\zeta_{in}}{\zeta_{opt}} \frac{(u\beta_e + v)_{in}}{(u\beta_e + v)} \frac{(1 + \beta_e^2)}{(1 + \beta_e^2)_{in}} \frac{\sigma_{e,in}}{\sigma_e} \quad (\text{A-9})$$

where the "in" represents generator inlet values and where ζ_{opt} is a load parameter value selected specifically to enforce a certain mode of generator operation. To everywhere enforce a maximized local electric power density, $\zeta_{opt} = 0.5$ is required. To everywhere maximize the local electrical conversion efficiency, given by

$$\eta_e \equiv \frac{|\underline{J} \cdot \underline{E}|}{|\underline{u} \cdot (\underline{J} \times \underline{B})|} = \frac{(\beta_e + S)^2 \zeta (\zeta - 1)}{\zeta (\beta_e^2 - S^2) - (1 - \beta_e^2)} \quad (\text{A-10})$$

requires that

$$\zeta_{opt} = \begin{cases} \frac{1 + \beta_e^2 - ((1 + \beta_e^2)(1 + S^2))^{\frac{1}{2}}}{\beta_e^2 - S^2} & \text{for } \beta_e \neq S \\ \frac{1}{2} & \text{for } \beta_e = S. \end{cases} \quad (\text{A-11})$$

Alternatively, the duct geometry can be specified (e.g., constant area duct); in this case, an inlet load parameter, ζ_{in} , is specified and the local load parameter, ζ (replacing ζ_{opt} of Equation A-9), is back calculated.

Fluid Solution Method

Equations A-1 through A-4 may be rewritten in the form

$$\frac{d\underline{E}}{dr} = \underline{S} \quad (\text{A-12})$$

where

$$\underline{E} = \begin{bmatrix} \dot{m} \\ \dot{m} u + PA \\ \dot{m} v r \\ \dot{m} \bar{h} \end{bmatrix} \quad (\text{A-13})$$

and

$$\underline{S} = \begin{bmatrix} 0 \\ \frac{\rho A v^2}{r} + P \frac{dA}{dr} + J_{\theta} A B \\ -J_r A B r \\ J_r E_r A + \dot{q}_N A \end{bmatrix} \quad (\text{A-14})$$

In a supersonic flow field—that is provided the radial Mach number, M_R , is greater than one—Equation A-13 may be solved using the marching solution

$$\underline{E}_{i+1} = \underline{E}_i + \frac{\Delta r}{2} (\underline{S}_{i+1} + \underline{S}_i) . \quad (\text{A-15})$$

At each node $i+1$, the vector \underline{E} is decomposed into the primitive variables required to calculate the source vector \underline{S} , and iteration is performed until Equations A-13 through A-15 are satisfied. The maximum allowed generator length is specified; a given generator design (calculation) is ended when the generator length equals the maximum allowed length or when the radial Mach number approaches one and supersonic flow (in the radial sense) can no longer be maintained.

APPENDIX B

GRID GENERATION

In order to resolve both the thin boundary layer regions of the turbulent supersonic flows considered in this work and the much larger, essentially inviscid, core flow regions, in a computationally efficient manner, nonuniformly spaced (stretched) numerical grids are used. The grid spacing is nonuniform in that the (axial) spatial frequency of grid lines adjacent to the duct walls is high relative to the spatial frequency of the grid lines towards the centerline of the core flow region; i.e., the grid lines are clustered in the boundary layer regions, at both the upper and lower duct walls, and the spatial frequency of the grid lines decreases near the duct centerline. A number of algebraic grid stretching algorithms were considered in this work. This appendix provides the algebraic grid generation methodology used to discretize the physical space for all the fluid flow and electromagnetic solutions of this thesis.

Line of Constant- ξ

Figure B-1 provides a schematic diagram of a close-up view of a generic grid near the lower wall ($j = 1$), and at some arbitrary ξ -position (i). Prior to considering the axial stretching algorithms, it is noted that in all the grids generated for this work, the radial spacing (Δr) of grid lines in the physical space

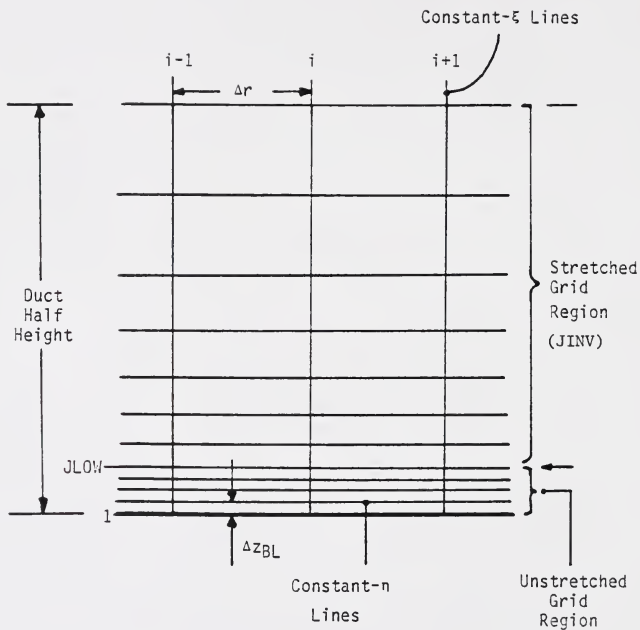


Figure B-1 Schematic Diagram of a Close-up View, Near the Lower Duct Wall, of a Generic Stretched Grid used for MHD Flow Calculations.

(r, z) is uniform ($\Delta r = \text{Constant}$); further, the grid lines of constant- Δ are also grid lines of constant- r ; that is, the lines of constant- ξ are parallel to the unit vector \hat{e}_z of the physical space. By construct, in lieu of the restriction that the lower duct wall ($j = 1, \eta = 0$) is flat ($r_\eta = z_\xi = 0$), as discussed in Section 2.3.2, the grid lines of constant- ξ are everywhere perpendicular to the lower wall. In general, for duct designs in which $\partial H(r)/\partial r \neq 0$ --i.e., in places in which the duct height varies with radial position--the lines of constant- ξ (and lines of constant- r) are not perpendicular to the upper wall ($j = \text{JMAX}, \eta = \eta_{\text{MAX}}$).

Lines of Constant- η

Grid stretching in the axial direction permits high density clustering of finite-difference points in the boundary layer region and, economically, an increasingly lower density of finite-difference points away from the wall, towards the duct centerline. It is common that the grid is stretched throughout the flow physical space, from the wall to the duct centerline; however, in the course of this work, gained experience suggested that the regions immediately adjacent to the duct wall--that region that includes the laminar-sublayer (where $u^+ = z^+$ [see nomenclature in Section 2.2.4]) and high flow field gradients (e.g., $\partial u/\partial z$)--is best discretized using an unstretched grid, as shown in Figure 1: The metrics of the $((r, z) \rightarrow (\xi, \eta))$ physical space-to-computational space coordinate transformation, $\xi_r, \xi_z, \eta_r, \eta_z$, are calculated using second-order finite-difference approximations for the metrics $r_\xi, r_\eta, z_\xi, z_\eta$, in the computational space. At grid line $j = 1$ (or $j = \text{JMAX}$) of the computational space, the metrics are calculated using a three-point second order accurate forward (or backward) difference formula. Early in this work,

before it was recognized by the author that the rate of change of the grid spacing should be restricted to, for example, $|\Delta z_{j+1}/\Delta z_j| \leq 2$, it was found that on a highly stretched grid (e.g. $|\Delta z_{j+1}/\Delta z_j| \geq 10$) the calculated metric values can be wrong in both magnitude and in sign; i.e., the basis of the three point finite-difference formula can not span the highly stretched space. To address this, higher order difference approximations could be employed--those which would span the space--or, to insure the metric has at least the same sign, the lower, two-point forward (or backward) finite-difference approximation could be used, or, more appropriately, the local grid stretching should be controlled as indicated above. In a conservative extreme, a region of unstretched grid is placed adjacent to both the lower and upper duct walls. A second, and more important reason for not stretching the fine grids in this same region, adjacent to the duct walls is suggested in the discussion by Thompson et al. (1985) on the origin of truncation error arising, for example, in the finite-difference representation of a spatial first derivative of an arbitrary function: Thompson et al. show that numerical diffusion is introduced by the finite-difference approximation and that the magnitude of the diffusion term constituent of the truncation error is proportional to the local rate of change (e.g., $z_{\eta\eta}$), or stretching, of the grid. Further, the introduced numerical diffusion can be negative in some conditions, leading to instabilities in the numerical method (Thompson et al, 1985). Recognizing that it is in this same region, adjacent to the wall, that the actual or physical axial gradients (e.g., $\partial u/\partial z$) are high and that the diffusion terms (e.g., $\partial^2 u/\partial z^2$ and $\partial^2 T/\partial z^2$) become relatively important, it was again deemed inadvisable to stretch the grid spacing in this

region. Typical in this work, the first 10 grid spaces near the duct walls are uniform; grid stretching nominally begins following the eleventh grid line ($j = 11$).

As a result of discussions with T. I-P. Shih (1989), who works extensively with algebraic grid generation, it is suggested that the axial grid stretching be restricted to $|\Delta z_{j+1}/\Delta z_j| \leq 2$; i.e., the ratio of the grid spacing ($\partial z/\partial \eta$) should not exceed 2 between immediate neighbors.

Roberts' stretching transformation. Early in this study, the stretching transformation proposed by Roberts (Roberts, 1971, and see discussion in Anderson, et al, 1984) was used to generate the axial distribution of the grid lines in the stretched grid region (see Figure B-1). Roberts' stretching transformation is designed specifically for boundary layer problems; it contains one stretching parameter, and this parameter is conveniently related to the local boundary layer thickness and duct height. It was found--possibly due to the author's inexperience with the Roberts' transformation, but more likely due to the insufficient number of axial grid lines (e.g., 51 as opposed to 101) used in the early phases of this work--that Roberts' transformation led to grids which either had a sufficiently resolved boundary layer region and an insufficiently resolved near-centerline duct core flow region, or, vice-versa. The Roberts' transformation was therefore abandoned early on and the grid generation scheme developed by the author and described below is used.

Axial grid stretching algorithm. The algebraic grid stretching algorithm used for the thesis calculations is presented here. The algorithm, though simple and easily implemented, affords, in certain limits, strict specification of the

$|\Delta z_{j+1}/\Delta z_j|$ ratio, or the rate of grid change between nearest neighbors. In its simplest form the idea, which comes from discussion with T. I-P. Shih, is that one specifies that

$$\frac{\Delta z_{k+1}}{\Delta z_k} = \epsilon \quad (\text{B-1})$$

where ϵ is the stretching factor ($1 \leq \epsilon \leq 2$). (Note that if $\epsilon = 1$ then the grid is uniform.) In this work, at a given line of constant- ξ , the grid stretching algorithm works outward from the outer edge of the unstretched region ($j = \text{JLOW}$ or $k = 1$) at the lower wall to the duct centerline; the grid line distribution in the upper half of the duct is a mirror image, again at a fixed line of constant- ξ , of that in the lower half of the duct. Equation B-1 has the attractive feature that the grid stretching is explicitly set throughout the stretched region of the duct; however, it was found, similar to the experience with Roberts' method, that if the near wall region is resolved with the desired grid resolution (typically $\Delta z \approx 1 \times 10^{-5}$ m as discussed later), in the geometries of interest to this work and with a maximum of 101 axial grid lines, that the corresponding grid in the duct centerline region is too coarse.

To address this issue, the stretching factor, ϵ , is allowed to vary axially, from the outer edge of the unstretched grid region to the duct centerline. We let

$$\epsilon_k = 1 + (\epsilon_{\text{MAX}} - 1) e^{-(k-1)/\text{JRELAX}} \quad (\text{B-2})$$

($k = 1, 2, \dots, \text{JINV}$), where $\epsilon_{\text{MAX}} = \epsilon_{\text{JLOW}+2}$ is the maximum stretch factor, JRELAX is a grid relaxation index (analogous to relaxation length), JLOW is the number of grid spaces in the unstretched (lower wall) region, and JINV is the

number of grid spaces in the stretched region of the lower-duct half-space. This function accomplishes a smooth variation in the stretching factor between the limits

$$\epsilon_k = \begin{cases} \epsilon_{MAX} & \text{as } k \rightarrow 1 \\ 1 & \text{as } \frac{(k-1)}{JRELAX} \gg 0 \end{cases} \quad (\text{B-3})$$

By specifying the relaxation index JRELAX, the rate of stretching and the extent of the flow field in which the grid is stretched is controlled. Note that if JRELAX is set to unity, $\epsilon_k \rightarrow 1$ in the first few grid points; i.e., only the grid lines immediately next to the unstretched region experience stretching. Alternatively, if JRELAX is made large--e.g., if it is set to many times JMAX--then $\epsilon_k \rightarrow \epsilon_{MAX}$ uniformly in the stretched-grid region; Equation B-1 is recovered in this limit.

Using the distribution function in Equation B-2, and specifying the regional grid spacings (JLOW, JHIGH, and JINV), it can be shown that the minimum grid spacing Δz_{BL} (of the unstretched-grid regions) is given by

$$\Delta z_{BL} = \frac{Z_{MAX} - Z_1}{JHIGH + JLOW + 2 \left\{ \sum_{k=1}^{JINV} (\epsilon_k * \epsilon_{k-1} * \dots * \epsilon_1) \right\}} \quad (\text{B-4})$$

where $Z_{MAX} = z(\xi, JMAX)$, $z_1 = z(\xi, 1)$, $\epsilon_1 = \epsilon_{MAX}$, and JMAX (= JHIGH + JLOW + 2 JINV + 1) is the maximum number of axial grid lines.

The numerical grids used in this work are generated using a program (SETGRID) that incorporates the axial grid spacing algorithm discussed above and enforces uniform radial grid spacing.

Sample Grid Specifications

The duct geometries analyzed in this work are all discretized using a 101 (constant- η lines) x 101 (constant- ξ lines) mesh, with the exception of the smooth compression turn problem of Appendix C for which a 121 x 101 mesh is used.

Radial distribution. The duct lengths analyzed in this work range from 0.3 m to 0.5 m; therefore, using 101 equally spaced (in the physical space) grid lines provides finite-difference spatial step sizes of $3 \times 10^{-3} \text{ m} \leq \Delta r \leq 5 \times 10^{-3} \text{ m}$. MacCormack and Lomax, in discussion concerning high Reynolds number flows, indicate that they typically use finite-difference spacing, along the boundary layer, in the principal flow direction (Δr in our case), on the order of the boundary layer thickness itself (MacCormack and Lomax, 1979). The inlet boundary layer thickness in the calculations in this work is set to $1 \times 10^{-3} \text{ m}$ (1 mm), and the boundary layer thickness increases with radial position, through the duct; the 3 mm to 5 mm radial finite-difference step sizes used in this work are on the order of the boundary layer thickness.

Axial distribution. MacCormack and Lomax (1979) indicate that typically 20 mesh points are used to span the boundary layer in their work with high Reynolds number flows. Baldwin and Lomax (1978), in their paper that provides the development of the algebraic turbulence model used in this work (see Section 2.2.2), consider turbulent flow over a flat plate, and require that the axial grid space-size, between the wall and the grid line adjacent to wall, be less than 2 (in law-of-the-wall coordinates); i.e., $\Delta z^+ \leq 2$ along the flat plate. The numbers provided here are typical of the literature; that is, the boundary layer is typically

resolved by 10 to 20 grid points; for turbulent flow, at least a couple of grid points should be in the laminar sublayer if the wall shear stress, τ_w , used in the turbulence model is calculated using a finite-difference approximation.

The extent of the laminar sublayer may be estimated in a number of ways. Cebeci and Smith (1974) divide the turbulent boundary layer-region velocity profile into two principle regions: the inner region (10-20% of the boundary layer) and the outer region (80-90% of the boundary layer). 0.1 to 1 % of the inner region is formally the laminar sublayer (in which $u^+ = z^+$); Cebeci and Smith indicate that typically $z^+ \leq 5$ is the extent of the laminar sublayer. With this interpretation of the laminar sublayer, then Baldwin-Lomax (1978) effectively place two grid points in the sublayer region.

It is noted that for high Reynolds number (thin boundary layer) flow calculations, some investigators (e.g., see Knight's discussion on the "computational sublayer" (Knight, 1981) and Baldwin and Lomax, 1978) recommend using law-of-the-wall boundary conditions, in which the governing equations are solved analytically in the laminar sublayer region (assuming an adiabatic wall, $\tau = \tau_w$, and $\partial P/\partial z = 0$). In these approaches, the laminar sublayer is typically assumed to extend between $0 \leq z^+ \leq 50$ or 60 .

The estimate of the laminar sublayer thickness used to set the grid size in this work is made following the same approach discussed in Section 2.2.4 (after Shapiro, 1954) that is used to set the inlet boundary condition velocity profile. Based on Equations 2-62 through 2-68, with the inlet conditions typical of the MHD generator calculations of Section 3.4 and 3.6, the laminar sublayer portion

is estimated to constitute 5 to 6 % of the boundary layer; in law-of-the-wall coordinates, it occupies $0 \leq z^+ \leq 12$. If this same theory is modified to account for compressibility effects as discussed in Section 3.1.1, then (using the program TEMPDIS discussed in Section 3.1.1) the laminar sublayer is found to constitute $\approx 4\%$ of the boundary layer. For the inlet boundary layer thickness of 1×10^{-3} m considered in this work, the laminar sublayer is therefore calculated to vary between 4×10^{-3} m $\leq z \leq 6 \times 10^{-3}$ m (corresponding to $4\% \leq z^+/\delta^+ \leq 6\%$, where δ^+ is the boundary layer thickness in law-of-the-wall coordinates).

Using the value of 4 % (corresponding to $z^+ = 11.6$ [also from TEMPDIS]), the laminar sublayer includes the region $0 \leq z \leq 4 \times 10^{-5}$ m of the 1×10^{-3} m boundary layer thickness. Assuming that the edge of the laminar sublayer region extends to 4×10^{-5} m at $z^+ = 11.6$, and following the example of Baldwin and Lomax (1978) in requiring that $\Delta z^+ \leq 2$ at the wall, then a minimum axial grid spacing at the wall is $\Delta z_{BL} \leq 6.7 \times 10^{-6}$ m; 6 grid points would bound the laminar sublayer in this case. In this work, the grid spacing is set at $\Delta z_{MIN} = \Delta z_{BL} = 1 \times 10^{-5}$ m = 0.01 mm; 5 grid lines bound the laminar sublayer at the inlet boundary and $\Delta z^+ \approx 3$. Noting that the boundary layer thickness grows with radial position (e.g., $\delta \sim r^{6/7}$ for flat plate flow), the laminar sublayer region is resolved by an increasing number of grid lines; further, in the calculations in this work, the upper wall is usually sloped downwards so that the duct height, $H(r)$, decreases with increasing radial position--this further crowds grid points into, and increasingly resolves, the laminar sublayer region.

To obtain the $\Delta z_{BL} = 1 \times 10^{-5}$ m using 101 grid points, while maintaining the desired resolution (Δz) near the duct centerline, the maximum stretching factor, ϵ_{MAX} , is set to $\epsilon_{MAX} = 1.85325$, and the grid relaxation index JRELAX is set at 7; i.e., the right-hand-most term of Equation B-2 experiences an e-folding decrease every 7 grid lines. JLOW and JHIGH are both set to 10 and JINV is set to 40: This provides the $\Delta z_{BL} = 1 \times 10^{-5}$ and a centerline finite-difference size-step of $\Delta z_C = \Delta z_{MAX} = 2.05 \times 10^{-3}$ m ($\approx 200 \Delta z_{BL}$). Using these parameters, typically 19 grid lines bound the inlet boundary layer thickness of 1×10^{-3} m. An example grid (used in the MHD generator calculations of Section 3.6) is provided in Figure B-2; a close-up view of the near-wall region of the grid is provided in Figure B-3.

In summary, the algebraic grid generation algorithm provided in this Appendix is expected to adequately resolve the high Mach number flow fields studied in this work. The grid spatial-step sizes (axial and radial) used in this work are consistent with those found in the literature. Typically, a minimum of 5 grid lines are used to resolve the laminar sublayer (interpreted as that region $0 \leq z^+ \leq 11.6$ in the sample grid provided) and a minimum of 19 grid lines are used to resolve the boundary layer (1×10^{-3} m at the duct inlet).

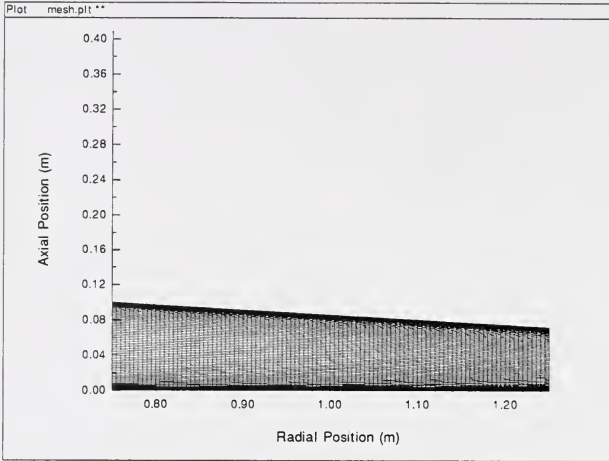


Figure B-2 Example Numerical Grid (used for Nonuniform Plasma Transport Property Generator Calculations in Section 3.6).

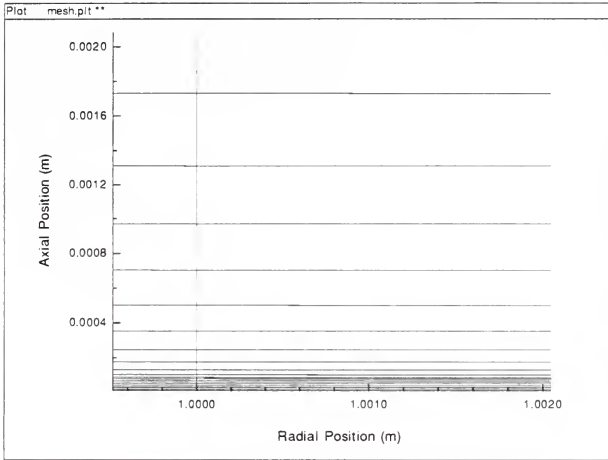


Figure B-3 Lower Wall Close-up View of Example Numerical Grid Shown in Figure B-2.

APPENDIX C

SHOCK CAPTURING

As reported throughout this work, the internal supersonic flow fields of this study are potentially complicated by oblique compression and rarefaction wave structure. The flow in the constant area duct geometry analyzed in Section 3.2.1 provides an example of a flow field with both compression and rarefaction waves that are induced by the duct geometry. After recognizing that what was thought to be an innocuous change in duct geometry, in the case of the constant area duct, could introduce significant wave structure to the flow field, it became necessary to investigate the shock capturing capabilities of the developed fluid solver.

This appendix reports on the effort to determine the degree to which the developed solution methodology is capable of correctly capturing shock waves. Two example duct geometries are considered; both geometries force the internal supersonic flow to undergo a five-degree compression turn. A five-degree compression corner is first considered; a smooth five-degree compression turn is then considered.

Five-Degree Compression Corner

Figure C-1 provides the duct geometry and resulting static pressure contour plot for the five-degree compression corner problem. Note that the inlet radius is

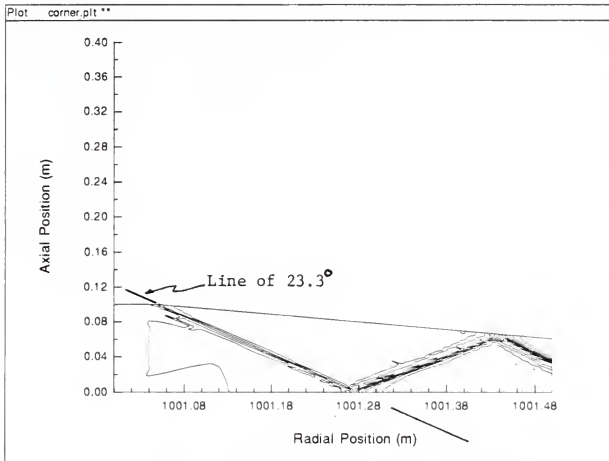


Figure C-1 Static Pressure Contour Plot for Supersonic Flow in Five-Degree Compression Corner Duct Geometry.

located at a radius of 1 km so that the $1/r$ cylindrical effects are inhibited. The duct walls are parallel at the duct inlet. Five centimeters into the duct, the top wall undergoes a (negative) five-degree change in direction and from this point, until the duct exit at 1001.5 m, the duct height is decreased linearly. The static pressure contour plot of Figure C-1 clearly shows that a shock wave is generated at the compression corner, is reflected off the lower and upper walls, and propagates downstream.

As a check for accuracy, the analytical relationship (see White, 1979, Shapiro, 1953, or other texts on gas dynamics)

$$\frac{2 \cot \beta (M_1^2 \sin^2 \beta - 1)}{M_1^2 (\gamma + \cos 2\beta) + 2} = \tan \theta \quad (C-1)$$

developed using the equations of gas dynamics applied to oblique shocks, is used to predict the shock angle (from the upper wall), β ; M_1 is the upstream Mach number (here $M_1 = 3$), θ is the angle of the corner (here 5°) and γ is the ratio of specific heats (here $\gamma = 1.482$). The predicted angle (negative from the parallel upper wall) β is 23.3° . The 23.3° is drawn on the static pressure contour plot in Figure C-1; clearly the shock is captured in the correct position and the correct orientation.

Figures C-2 and C-3 show the centerline radial Mach number and static pressure radial profiles, respectively. The radial positions where the shock wave and its reflections cross the duct centerline are clearly evident in these figures; the radial Mach number decreases across the oblique shocks waves; the static pressure increases across the shocks waves. The numerical oscillation in the

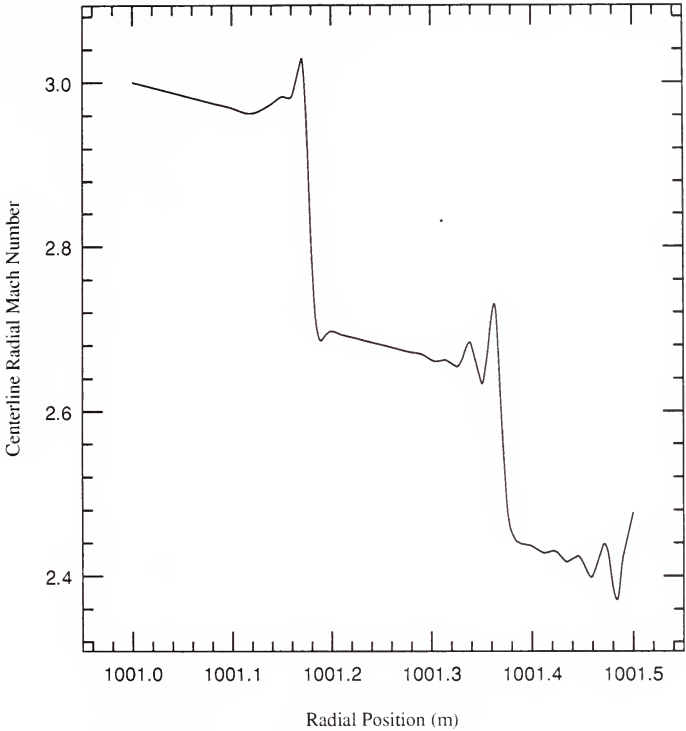


Figure C-2 Centerline Radial Mach Number as a function of Radial Position in Five-Degree Compression Corner Duct Geometry.

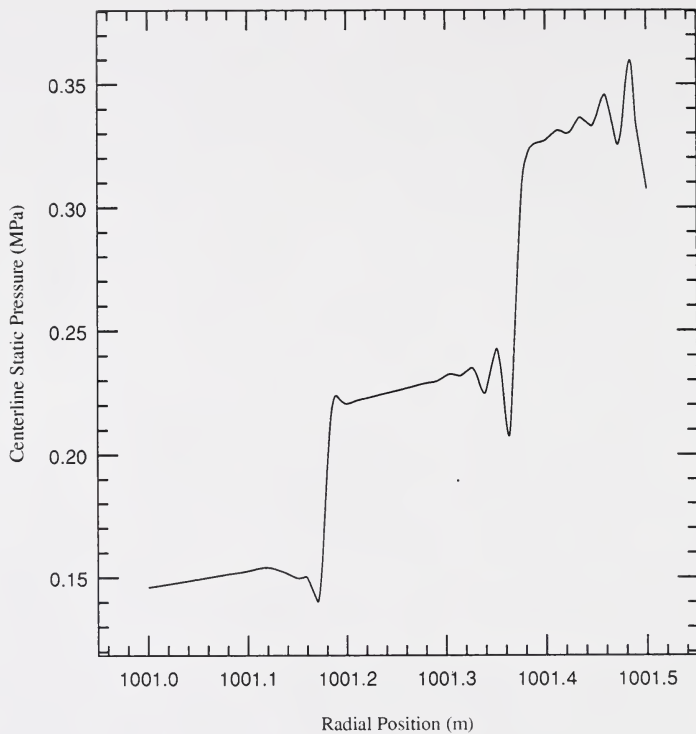


Figure C-3 Centerline Static Pressure as a function of Radial Position in Five-Degree Compression Corner Geometry.

vicinity of the oblique shock waves are substantial in spite of the artificial damping (see Section 3.1.2.) employed in the calculations.

The results of the compression corner calculation presented here suggest that the shock wave is captured correctly in terms of position and orientation. The shock wave also appears to correctly reflect off the upper and lower duct walls as the reflection proceeds downstream; however, the numerical oscillations seen in Figures C-2 and C-3 clearly indicate that the shock waves are not well resolved by the fluid solver. It should be noted that the oscillations to a large extent may be attributable to inadequate grid refinement in the radial (principal) flow direction; i.e., 5×10^3 m, or one-percent, of the 0.5 m duct is spanned by each grid space.

Smooth Five-Degree Compression Turn

Figure C-4 provides the duct geometry and static pressure contour plot for a second compression turn problem. In this example, the upper duct wall is parallel to the lower wall at the inlet ($r = 0.9$), and beginning at $r = 0.95$ makes a smooth transition between the parallel upper wall at $r = 0.95$ m to a negative 5° lofting at $r = 1.0$ m; the smooth transition is accomplished using a quadratic function. Note that cylindrical ($1/r$) effects influence the solution at the radial positions considered in the example.

Although the compression turn in this example is smooth, rather than the corner examined in the previous section, an oblique shock wave is generated at the compression turn, and reflects off the lower and duct walls as it propagates downstream. Again, the developed fluid solver captures the oblique shock wave.

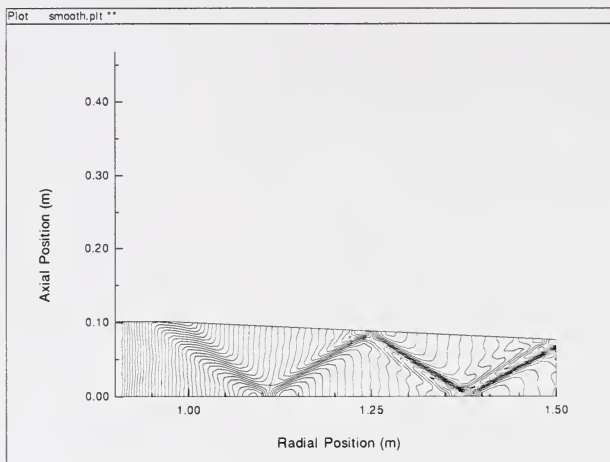


Figure C-4 Static Pressure Contour Plot for Supersonic Flow in Smooth Five-Degree Compression Turn Duct Geometry.

In summary, the developed fluid solver appears to correctly capture the position and angle of oblique shock waves generated in turning the supersonic flow at a compression turn. On the numerical grids with the level of grid refinement in the radial flow direction used in this work, the captured shock waves are not well resolved, but instead, are smeared over a large number of grid points.

LIST OF REFERENCES

- Anderson, D.A., Tannehill, J.C., and Pletcher, R.H. (1984). *Computational Fluid Mechanics and Heat Transfer*, McGraw-Hill, Inc., New York.
- Anderson, J.D., Jr. (1970). "A Time-Dependent Analysis for Vibrational and Chemical Nonequilibrium Nozzle Flows," *AIAA Journal*, Vol. 8, No. 3, March, pp. 545-550.
- Baldwin, B.S. and Lomax, H. (1978). "Thin Layer Approximation and Algebraic Model for Separated Turbulent Flows," *AIAA 16th Aerospace Sciences Meeting*, AIAA Paper 78-257, Huntsville, Alabama, January 16-18.
- Bird, R.B., Stewart, W.E., and Lightfoot, E.N. (1960). *Transport Phenomena*, John Wiley & Sons, Inc., New York.
- Boussinesq, J. (1877). "Essai Sur La Theorie Des Eaux Courantes," *Mem. Presentes Acad. Sci.*, Vol. 23, Paris, p. 46.
- Braun, J. (1965). "Linear Constant-Mach-Number MHD Generator With Nuclear Ionization. A Parametric Study," *Plasma Physics (Journal of Nuclear Energy Part C)*, Vol. 7, pp. 525-538.
- Brogan, T.R. (1963). "Electrical Properties of Seeded Combustion Gases," *Progress in Astronautics and Aeronautics*, Vol. 12, pp. 319-345.
- Cebeci, T. and Smith, A.M.O. (1974). *Analysis of Turbulent Boundary Layers*, Academic Press Inc.
- Celinski, Z.M., and Fisher, F.W. (1966). "Effect of Electrode Size in MHD Generators with Segmented Electrodes," *AIAA Journal*, Vol. 4, No. 3, March.
- Chapman, S. and Cowling, T.G. (1939). *The Mathematical Theory of Non Uniform Gases*, Cambridge University Press, Cambridge.
- Chapman, D.R. and Rubesin, M.W. (1949). "Temperature and Velocity Profiles in the Compressible Laminar Boundary Layer with Arbitrary Distribution of Surface Temperature," *Journal of the Aeronautical Sciences*, Vol. 16, No. 9, September, pp. 547-565.

- Crocco, L. (1965). "A Suggestion for the Numerical Solution of the Steady Navier-Stokes Equations," *ALAA Journal*, Vol. 3, No. 10, October, pp. 1824-1832.
- Crown, J.C. (1961). *Analysis of Magnetogasdynamic Generators Having Segmented Electrodes and Anisotropic Conductivity*, United Aircraft Research Laboratories Report R-1852-2.
- Degani, D. and Steger, J.L. (1983). "Comparison Between Navier-Stokes and Thin-Layer Computations for Separated Supersonic Flow," *ALAA Journal*, Vol. 21, No. 11, November, pp. 1604-1606.
- Douglas, J. and Rachford, H.H. (1956). "On the Numerical Solution of Heat Conduction Problems in Two and Three Space Variables," *Trans. Amer. Math. Soc.*, Vol. 82, pp. 421-439.
- Dugan, E.T. et al. (1988). *Gas Core Reactors: Neutronics, Energetics, and Magnetohydrodynamics. Final Report for period Sept. 12, 1985 - Sept. 30, 1988.* INSPI-FR-UF-88-001, Vol. 1 of 4, Innovative Nuclear Space Power Institute, University of Florida, December.
- Granville, P.S. (1987). "Baldwin-Lomax Factors for Turbulent Boundary Layers in Pressure Gradients," *ALAA Journal*, Vol. 25, No. 12, December, pp. 1624-1627.
- Hale, F.J. and Kerrebrock, J.L. (1964). "Insulator Boundary Layers in Magnetohydrodynamic Channels," *ALAA Journal*, Vol. 2, No. 3, March, pp. 461-469.
- Hasen, G.A. (1982). "Navier-Stokes Solutions for an Axisymmetric Nozzle," *ALAA Journal*, Vol. 20, No. 9, September, pp. 1219-1227.
- Hassan, H.A. and Deese, J.E. (1974). *Thermodynamic Properties of UF₆ at High Temperature*, NASA CR-2373, January.
- Hughes, W.F. and Young, F.J. (1966). *The Electromagnetodynamics of Fluids*, John Wiley & Sons, Inc., New York.
- Hurwitz, H., Jr., Kilb, R.W., and Sutton, G.W. (1961). "Influence of Tensor Conductivity on Current Distribution in an MHD Generator," *J. Appl. Phys.*, Vol. 32, pp. 205.
- Inui, Y., Hara, T., Ishikawa, M., and Umoto, J. (1989). "Two-Dimensional Simulation of Nonequilibrium Disk MHD Generator Using Helium Gas," *Proceedings of the 27th Symposium on Engineering Aspects of Magnetohydrodynamics*, Reno, Nevada, June 27-29, pp. 8.15-1 - 8.15-9.

James, R.K. (1980). *Joule Heating Effects in the Electrode Wall Boundary Layer of MHD Generators*, Ph.D. Dissertation, Stanford University, January. HTGL Report No. 115.

Jameson, A., Schmidt, W., and Turkel, E. (1981). "Numerical Solutions of Euler Equations by Finite Volume Method Using Runge-Kutta Time Stepping Scheme," AIAA-81-1259.

Kaye, J. (1954). "Survey of Friction Coefficients, Recovery Factors, and Heat-Transfer Coefficients for Supersonic Flow," *Journal of the Aeronautical Sciences*, Vol. 21, February, pp. 117-129.

Kerrebrock, J.L. (1960). "Non-equilibrium Effects on Conductivity and Electrode Heat Transfer in Ionized Gases," AFOSR 165 TN 4, Daniel and Florence Guggenheim Jet Propulsion Center, California Institute of Technology, Pasadena, November.

Kerrebrock, J.L. (1961). "Electrode Boundary Layers in Direct-Current Plasma Accelerators," *Journal of the Aerospace Sciences*, Vol. 28, No. 8, August, pp. 631-642.

Kerrebrock, J.L. (1962). "Conduction in Gases With Elevated Electron Temperatures," *Engineering Aspects of Magnetohydrodynamics*, Columbia University Press, New York, pp. 327-346.

Kerrebrock, J.L. (1965). "Magnetohydrodynamic Generators with Nonequilibrium Ionization," *AIAA Journal*, Vol. 3, No. 4, April, pp. 591-601.

Knight, D.D. (1981). "Improved Calculation of High Speed Inlet Flows: Part I. Numerical Algorithm," *AIAA Journal*, Vol. 19, No. 1, January, pp. 34-41.

Knoll, G.F. (1979). *Radiation Detection and Measurement*, John Wiley & Sons, Inc., New York.

Lear, W.E. Jr. (1984). *Performance and Electric Field Limitations in Inflow Disk MHD Generators*, Ph.D. Dissertation, Stanford University (September). HTGL Topical Report No. 242.

Li, C.P. (1973). "Numerical Solution of Viscous Reacting Blunt Body flows of a Multicomponent Mixture," *AIAA 11th Aerospace Sciences Meeting*, AIAA Paper No. 73-202, Washington, D.C., January 10-12.

Li, H. and Kroll, N. (1989). "Solution of One- and Two-Dimensional Euler Equations Using a TVD Scheme," Institut für Entwurfsaerodynamik, Braunschweig, IB 129-88/24, June.

- Louis, J.F. (1968). "Disk Generator," *AIAA Journal*, Vol. 6, No. 9, September, pp. 1674-1678.
- MacCormack, R.W. (1969). "The Effect of Viscosity in Hypervelocity Impact Cratering," *AIAA Hypervelocity Impact Conference*, AIAA Paper No. 69-354, Cincinnati, Ohio, April, 30 - May, 2.
- MacCormack, R.W. (1971). "Numerical Solution of the Interaction of a Shock Wave with a Laminar Boundary Layer," *Pro. Second Int. Conf. Num. Methods Fluid Dyn., Lecture Notes in Physics*, Vol. 8, Springer-Verlag, New York, pp. 151-163.
- MacCormack, R.W. (1976). *An Efficient Numerical Method for Solving the Time-Dependent Compressible Navier-Stokes Equations at High Reynolds Number*, NASA TM X-73-129; also in *Computing in Applied Mechanics*, Applied Mechanics Division, Vol. 18, pp. 49-64, Winter Annual Meeting of the ASME, New York, December 5-10.
- MacCormack, R.W. (1984). "Acceleration of Convergence of Navier-Stokes Calculations." ed. Parter, S.V. *Large Scale Scientific Computing*, Academic Press Inc., New York, pp. 161-193.
- MacCormack, R.W. (1985). "Current Status of Numerical Solutions of the Navier-Stokes Equations," *AIAA 23rd Aerospace Sciences Meeting*, AIAA Paper No. 85-0032, Reno, Nevada, January 14-17.
- MacCormack, R.W. (1989). *Computational Fluid Dynamics Short Course*, IBM CFD Short Course, Volume I, San Diego, California, April 3-7.
- MacCormack, R.W. and Baldwin, B.S. (1975). "A Numerical Method for Solving the Navier-Stokes Equations with Application to Shock-Boundary Layer Interactions," AIAA Paper No. 75-1, Pasadena, California.
- MacCormack, R.W. and Lomax, H. (1979). "Numerical Solution of Compressible Viscous Flows," *Ann. Rev. Fluid Mech.*, Vol. 11, pp. 289-316.
- Mitchner, M. and Kruger, C.H. (1973). *Partially Ionized Gases*. Wiley-Interscience, New York.
- Moffat, W.C. (1961). *Thermodynamic and Electrical Properties of Dissociated Combustion Gases*, MIT Magnetogasdynamics Lab. Rept. 5.
- Maya, I., Watanabe, Y., Appelbaum, J., and Diaz, N.J. (1991). "Fissioning Plasma Physics," *Ultrahigh Temperature Reactor and Energy Conversion Research Program, Annual Report for Period July 1990-September 1991*. INSPI-91-110, Vol. 5 of 6, Innovative Nuclear Space Power Institute, University of Florida, October.

- Nakamura, T. (1983). *A Quasi-One-Dimensional Calculation of the Open-Cycle MHD Disk Generator Performance*, HTGL Report No. 2783, Stanford University, July.
- Oliver, C.C. and Dugan, E.T. (1985). "Thermophysical Properties of UF_6 -He Mixtures Relevant to Circulating Gas Core Reactor Systems," *Nuclear Technology*, Vol. 69, May, pp. 161-169.
- Pai, Shih-I. (1965). *A Critical Survey of Magnetofluid Dynamics, Part III: Quasi-One Dimensional Analysis of Magnetogas Dynamics*, Aerospace Research Laboratories, Wright-Patterson Air Force Base, Ohio, ARL 63-175, Part III, December.
- Pai, Shih-I. (1981). *Modern Fluid Mechanics*, Science Press, Beijing.
- Peaceman, D.W. and Rachford, H.H. (1955). "The Numerical Solution of Parabolic and Elliptic Differential Equations," *J. Soc. Ind. Appl. Math.*, Vol. 3, pp. 28-41.
- Peyret, R. and Taylor, T.D. (1983). *Computational Methods for Fluid Flow*, Springer-Verlag, New York, Inc.
- Pullium, T.H., and Steger, J.L. (1980). "Implicit Finite-Difference Simulations of Three-Dimensional Compressible Flow," *AIAA Journal*, Vol. 18, No. 2, February, pp. 159-167.
- Pullium, T.H. (1986). *Efficient Solution Methods for the Navier-Stokes Equations*, Lecture Notes for the Von Karman Institute for Fluid Dynamics Lecture Series: Numerical Techniques for Viscous Flow Computation in Turbomachinery Bladings, Brussels, Belgium, January 20-24.
- Rankin, R.R. (1978). *Insulating Wall Boundary Layer in a Faraday MHD Generator*, Ph.D. Dissertation, Stanford University (April). HTGL Report No. 106.
- Roache, P.J. (1972). *Computational Fluid Dynamics*, Hermosa Publishers, Albuquerque.
- Roberts, G.O. (1971). "Computational Meshes for Boundary Layer Problems," *Lecture Notes in Physics*, Vol. 8, Springer-Verlag, New York, pp 171-177.
- Rosa, R.J. (1968). *Magnetohydrodynamic Energy Conversion*, McGraw-Hill Book Company, Inc., New York.
- Roseman, D.F. (1982). *Current Distribution and Nonuniformity Effects in MHD Disk Generators*, Ph.D. Dissertation, Stanford University (August). HTGL Report No. 231.

- Schlichting, H. (1955). *Boundary-Layer Theory*, McGraw-Hill Book Company, Inc., New York.
- Shapiro, A.H. (1953). *Compressible Fluid Flow* (Volume I). John Wiley & Sons, Inc., New York.
- Shapiro, A.H. (1954). *Compressible Fluid Flow* (Volume II). The Ronald Press Company, New York.
- Shih, T. I-P. (1990). Private Communication. Carnegie-Mellon University.
- Shirazi, S.A. and Truman, C.R. (1989). "Evaluation of Algebraic Turbulence Models for PNS Predictions of Supersonic Flow Past a Sphere-Cone," *AIAA Journal*, Vol. 27, No. 5, May, pp. 560-568.
- Stokes, G.G. (1845). "On the Theories of Internal Friction of Fluids in Motion," *Trans. Cambr. Phil. Soc.*, Vol. 8, pp. 287-305.
- Sutton, G.W. and Sherman, A. (1965). *Engineering Magneto hydrodynamics*, McGraw-Hill, Inc., New York.
- Thompson, J.F., Warsi, Z.U.A., and Mastin, C.W. (1985). *Numerical Grid Generation*, Elsevier Science Publishing Co., Inc., New York.
- van Driest, E.R. (1956). "On Turbulent Flow Near a Wall," *Journal of the Aeronautical Sciences*, Vol. 23, November, pp. 1007-1011, 1036.
- von Karman, T. (1931). "Mechanical Similitude and Turbulence," *NACA Tech. Memo.*, No. 611.
- Vinokur, M. (1974). "Conservation Equations of Gasdynamics in Curvilinear Coordinate Systems," *Journal of Computational Physics*, Vol. 14, pp. 105-125.
- Welch, G.E., Dugan, E.T., and Lear, W.E. Jr. (1988). "Disk MHD Generator for a Burst Power Gas Core Reactor," *Proceedings of the International Society for Optical Engineering Symposium on Space Structures, Power, and Power Conditioning*, Los Angeles, California, January. Vol. 871, pp. 42-47.
- Welch, G.E., Dugan, E.T., Lear, W.E., Jr., and Appelbaum, J.G. (1990). "Modeling and Analysis of the Disk MHD Generator Component of a Gas Core Nuclear Reactor/MHD Rankine Cycle Space Power System," *Proceeding of the 25th Intersociety Energy Conversion Engineering Conference (IECEC)*, Reno, Nevada, August, pp. 449-454.
- White, F.M. (1979). *Fluid Mechanics*, McGraw-Hill, Inc., New York.

Wilson, R.E. (1950). "Turbulent Boundary-Layer Characteristics at Supersonic Speeds--Theory and Experiment," *Journal of the Aeronautical Sciences*, Vol. 17, No. 9, September, pp. 585-594.

BIOGRAPHICAL SKETCH

Gerard Edward Welch was born on June 21, 1960, in Ancon, Canal Zone, in the country of Panama. He is the son of Gerard Joseph Welch and Mary Grace Welch and has one sister, Kathleen Anne Welch, and one brother, Christopher James Welch. The author lived in the beautiful Canal Zone for twenty years. In that time he was greatly influenced by his aunt, Dolores M. Welch. The author graduated from Balboa High School in 1978, and received an Associate of Science degree in mathematics from the Panama Canal College in 1980.

In August of 1980, the author moved to Gainesville, Florida, to attend the University of Florida. He received a Bachelor of Science (Nuclear Engineering) degree in 1983 and a Master of Engineering degree in 1985.

The author is a member of the Tau Beta Pi and Alpha Nu Sigma honorary societies; he is also a member of the Sigma Xi research society. He is active in the American Nuclear Society and is a member of the American Society of Mechanical Engineers.

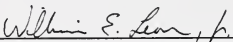
During his stay in Gainesville, the author was forever influenced by the liturgy and activities at the St. Augustine Catholic Student Center. He remembers most fondly his friends and family in the Children of the Light prayer community.

I certify that I have read this study and that in my opinion it conforms to acceptable standards of scholarly presentation and is fully adequate, in scope and quality, as a dissertation for the degree of Doctor of Philosophy.



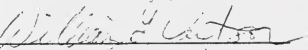
Edward T. Dugan, Chairman
Associate Professor of Nuclear
Engineering Sciences

I certify that I have read this study and that in my opinion it conforms to acceptable standards of scholarly presentation and is fully adequate, in scope and quality, as a dissertation for the degree of Doctor of Philosophy.



William E. Lear, Jr., CoChairman
Assistant Professor of Mechanical
Engineering

I certify that I have read this study and that in my opinion it conforms to acceptable standards of scholarly presentation and is fully adequate, in scope and quality, as a dissertation for the degree of Doctor of Philosophy.



William G. Vernetson
Associate Engineer, Nuclear
Engineering Sciences

I certify that I have read this study and that in my opinion it conforms to acceptable standards of scholarly presentation and is fully adequate, in scope and quality, as a dissertation for the degree of Doctor of Philosophy.



Alan M. Jacobs
Professor of Nuclear Engineering
Sciences

I certify that I have read this study and that in my opinion it conforms to acceptable standards of scholarly presentation and is fully adequate, in scope and quality, as a dissertation for the degree of Doctor of Philosophy.



Calvin C. Oliver
Professor of Mechanical
Engineering

I certify that I have read this study and that in my opinion it conforms to acceptable standards of scholarly presentation and is fully adequate, in scope and quality, as a dissertation for the degree of Doctor of Philosophy.



Robert J. Hanrahan
Professor of Chemistry

This dissertation was submitted to the Graduate Faculty of the College Engineering and to the Graduate School and was accepted as partial fulfillment of the requirements for the degree of Doctor of Philosophy.

May, 1992



Winfred M. Phillips
Dean, College of Engineering

Madelyn M. Lockhart
Dean, Graduate School

